

BROADBAND TRANSMIT PHASED ARRAY ANALYSIS AND DESIGN

by

LAILA FIGHERA MARZALL

B.S., Universidade Federal de Santa Maria, 2006

M.S., Instituto Tecnológico de Aeronáutica, 2009

A thesis submitted to the
Faculty of the Graduate School of the
University of Colorado in partial fulfillment
of the requirements for the degree of
Doctor of Philosophy
Department of Electrical and Computer Engineering
March 2022

This thesis entitled:
Broadband Transmit Phased Array Analysis and Design
written by Laila Figuera Marzall
has been approved for the Department of Electrical and Computer Engineering

Professor Zoya Popović

Professor Gregor Lasser

Date _____

The final copy of this thesis has been examined by the signatories, and we find that both the content and the form meet acceptable presentation standards of scholarly work in the above mentioned discipline.

Marzall, Laila Fighera (Ph.D., Electrical Engineering)

Broadband Transmit Phased Array Analysis and Design

Thesis directed by Professor Zoya Popović

This thesis has two parts with a common theme of broadband microwave circuit and antenna co-simulation and co-design for phased array front ends, where the prefix “co-” implies linear and nonlinear circuit, and full-wave electromagnetic methods. The thesis is organized around a 6–12 GHz 4-element active array. In the first part, the active sub-array radiating element with the microstrip-to-waveguide transition and power amplifier MMIC is presented, followed by the 4×1 spatial power combiner array design details. The study of this 4-element linear array when fed in phase as a spatial power combiner are performed over a broad frequency range (full octave), a wide range of input powers, and a wide range of PA drain voltages. Over-the-air (OTA) simulations and measurements show how these parameters affect efficiency and radiation pattern, as well as signal linearity. This study is then extended to a beam-steering phased array. The performance of the active beam-steering network and phase-shifter performance, steering angle versus progressive phase shift, and analysis of coupling effects as a function of supply-voltage amplitude tapering is presented, and an experimental array fabricated to validate the analysis. In the second part of the thesis, isolation components for simultaneous transmit-and-receive arrays are considered, with trade-offs in component design for octave bandwidth operation. Co-simulations, design and characterization is presented for three types of circulators with array integration as a goal. Ferrite circulators that use different magnetic biasing approaches to achieve miniaturization and reconfigurable bandwidth are shown, together with a comprehensive analysis of the effect of magnetization distribution on circulator design. The analysis is applied to obtain initial results in self-magnetized circulators with built-in shape anisotropy that can potentially be integrated with MMICs. Finally, a broadband active circulator, validated with measurements on a fabricated 7-13 GHz GaAs MMIC, is presented and the performance of this circulator in a phased array environment is analyzed. The thesis concludes with a list of contributions and an overview of exciting continuing and future work research topics.

DEDICATION

To my parents, my sister, my advisor.

ACKNOWLEDGMENTS

Advisor: Professor Zoya Popović

Ph.D. Committee: Professor Gregor Lasser, Professor Dejan Filipovic, Professor Jorge L. Salazar-Cerreno, Dr. Julio Navarro, Dr. Scott Schafer

Institutions/Sponsors: University of Colorado Boulder, ONR, CAPES, DARPA, Qorvo, ADI.

Colleagues: Shane Verploegh, Rob Streeter, Megan Robinson, Paige Danielson, Philip Zureck, Aman Samaiyar, Mauricio Pinto.

Professionals: Juliano Mogni (ANSYS), Mark Saffian (Cadence AWR), Mike Roberg (Qorvo).

University of Colorado Boulder staff: Adam Sadoff, Jarka Hladisova, Lori Meehan, Patricia Femrite.

Special thanks to Professor Dana Anderson.

CONTENTS

1	INTRODUCTION	1
1.1	BACKGROUND AND MOTIVATION	1
1.2	MAIN QUANTITIES, METRICS AND FIGURES OF MERIT	5
1.3	CHALLENGES IN OCTAVE-BANDWIDTH PHASED ARRAY COMPONENT DESIGN	7
1.3.1	ANTENNA ELEMENT AND ARRAY DESIGN	7
1.3.2	TRANSMIT-RECEIVE ISOLATION	10
1.3.3	POWER AMPLIFIER CHALLENGES	11
1.3.4	BEAMFORMING NETWORK CHALLENGES	13
1.4	CHALLENGES IN SYSTEM-LEVEL ANALYSIS AND CHARACTERIZATION	15
1.5	PHASED ARRAYS IN ELECTRONIC WARFARE APPLICATIONS	15
1.6	THESIS GOALS AND ORGANIZATION	19
2	ACTIVE ANTENNA ELEMENT DESIGN	21
2.1	CHAPTER INTRODUCTION	21
2.2	PASSIVE ANTENNA DESIGN	22
2.2.1	RIDGE WAVEGUIDE FEED AND AIR-FILLED HORN	23
2.2.2	EXPONENTIALLY-FLARED DIELECTRIC-LOADED SMALL-APERTURE HORN	25
2.2.3	INTEGRATION WITH MS-TO-WG TRANSITION	28
2.3	ACTIVE ANTENNA ELEMENT DESIGN	29
2.3.1	POWER AMPLIFIER CW CHARACTERIZATION	30
2.3.2	ACTIVE ANTENNA INTEGRATION, SIMULATION AND MEASUREMENTS	33

2.4	CHAPTER CONTRIBUTIONS AND CONCLUSION	37
3	SUPPLY-MODULATED SPATIAL POWER COMBINER	39
3.1	CHAPTER INTRODUCTION	39
3.2	PASSIVE ARRAY DESIGN	40
3.3	SUPPLY-MODULATED SPATIAL POWER COMBINER	48
3.3.1	CW SIMULATED AND MEASURED RESULTS	48
3.4	ACTIVE ARRAY PERFORMANCE UNDER MODULATED SIGNALS	53
3.5	CHAPTER CONTRIBUTIONS AND CONCLUSIONS	56
4	TRANSMIT PHASED ARRAY: ANALYSIS AND MEASUREMENTS	58
4.1	CHAPTER INTRODUCTION	58
4.2	BEAM STEERING RADIATION PATTERN ANALYSIS	59
4.2.1	ARRAY FACTOR AND GRATING LOBE ANALYSIS	60
4.3	PHASE SHIFTER SPECIFICATIONS AND PERFORMANCE ANALYSIS	64
4.4	ACTIVE TRANSMIT ARRAY BEAMFORMING NETWORK	66
4.5	EXPERIMENTAL PROTOTYPE AND MEASUREMENTS	69
4.6	CHAPTER CONTRIBUTIONS AND CONCLUSION	72
5	BACKGROUND IN FRONT-END ISOLATION COMPONENTS FOR STAR ARRAYS	77
5.1	CHAPTER OVERVIEW	77
5.2	FERRITE CIRCULATORS	78
5.3	SELF-BIASED CIRCULATORS	81
5.4	ACTIVE CIRCULATORS	82
5.5	CHAPTER CONTRIBUTIONS AND CONCLUSION	84
6	DESIGN OF FERRITE CIRCULATORS	85
6.1	CHAPTER INTRODUCTION	85
6.2	CAD-BASED DESIGN OVERVIEW	87

6.3	FERRITE BEHAVIOR AS A FUNCTION OF THE TOTAL INTERNAL FIELD AND FREQUENCY	90
6.4	EFFECTS OF HIGH-INTENSITY MBF ON CIRCULATOR BANDWIDTH	92
6.5	EFFECT OF FERRITE GEOMETRY ON DEMAGNETIZATION AND TOTAL INTERNAL FIELD	93
6.6	DISTRIBUTION OF THE APPLIED MAGNETIC BIAS FIELD	97
6.7	EXPERIMENTAL VALIDATION	98
6.7.1	BASELINE CIRCULATOR	99
6.7.2	MINIATURIZED DESIGN OPERATED BELOW SATURATION	100
6.7.3	DESIGN WITH NON-UNIFORM MBF	101
6.8	CHAPTER CONCLUSIONS AND CONTRIBUTIONS	104
7	SELF-BIASED CIRCULATORS	108
7.1	CHAPTER INTRODUCTION	108
7.2	MATERIAL PROPERTIES AND SIMULATIONS	109
7.3	MEASUREMENTS ON SAMPLES FROM ARGONNE NATIONAL LABS	113
7.4	CHAPTER CONCLUSION AND CONTRIBUTIONS	114
8	ACTIVE CIRCULATOR MMIC	119
8.1	CHAPTER INTRODUCTION	119
8.2	CIRCUIT TOPOLOGY AND MMIC DESIGN	120
8.2.1	BRANCH CIRCUIT DESIGN	120
8.2.2	ASYMMETRIC LANGE COUPLER	123
8.3	CIRCULATOR LAYOUT AND SIMULATED RESULTS	124
8.4	MEASURED RESULTS AND ANALYSIS	128
8.5	CONCLUSION AND CONTRIBUTIONS	131
9	SUMMARY, FUTURE WORK AND CONTRIBUTIONS	134
9.1	THESIS SUMMARY	134
9.2	FUTURE WORK	135

9.3	THESIS CONTRIBUTIONS	139
	BIBLIOGRAPHY	144
	APPENDICES	

LIST OF TABLES

1.1	Some IMD3 correction factors for calculating ACPR from IMD3 of a signal with n carriers	12
1.2	Estimated beam steering angle for different progressive phase shift configuration applied to the spatial power combiner of chapter 3 for 6, 9, 12 GHz, and respective horizon coverage for each scenario.	17
1.3	Table with initial array design specifications.	18
2.1	Comparison with Similar Horns	38
4.1	ADI HMC247 maximum phase shifting for 6–12 GHz considering a range of control voltages between 2–10 V. Maximum progressive phase shift Φ for a 4-element array.	66
4.2	Required control voltages for 3 values of the progressive phase shift for the 4-element array from 6–12 GHz.	66
4.3	Simulated power budget of the designed Wilkinson power combiner when two uncorrelated sources generating two tones spaced of 200 MHz and 30 dBm each are combined into a two-tones output signal.	73
5.1	Summary of commercially available ferrite circulators, manufacturers, and main specifications (collected in June 2019).	79
5.2	Examples of CMOS active quasi-circulators works from 2010 to 2020. Extracted from [125].	83
6.1	Validation circulator designs for different operating points using the same ferrite disk. . . .	99
6.2	Performance summary of circulators from Fig.6.24. BW is defined by $IL < 3$ dB, $ISO > 10$ dB and $RL > 10$ dB.	107

7.1	Material parameters used in simulation study and design.	111
8.1	Comparison of Active MMIC Circulator Performance [124]	133

LIST OF FIGURES

1.1	High-level block diagram of a phased array, where the beamforming can be done either in the digital or analog domains in transmit and/or receive. The isolation between TX and RX can be done either with circulators (full-duplex), switches for time-domain half-duplex, or filters for frequency-domain separation of TX and RX operation. The dotted arrows indicate coupling between the antenna elements, which affects isolation. The focus of this thesis is two-fold: (1) demonstrating octave-bandwidth analog components of broadband transmit arrays for beamforming, amplification, isolation; and (2) understanding interactions between the passive and active components at the array level through simulations and active over-the-air measurements. Shown in the expanded blocks with photographs are: GaAs MMIC phase shifter beamformer network; GaN MMIC power amplifiers; ferrite passive and MMIC active circulators; and broadband antennas with thermal handling capability.	3
1.2	Transmit ESA block diagram including: corporate feed network, phase shifters with control voltage V_{C1} , and power amplifiers with drain supply voltage V_{DD} directly connected to each array antenna element. The various parameters of interest are shown in blue font.	5
1.3	Beam steering mechanism in time and frequency domains.	7

1.4 Grating lobes in 1D for (a) $\Delta\Phi = 0$, and (b) $\Delta\Phi = -60^\circ$. The array factor can be read as the discrete Fourier transform in spatial domain of the current distribution of isotropic radiators. It has a periodicity that is dependent on the progressive phase shift $\Delta\Phi$, the frequency (inside the wavenumber k) and the distance between the elements. If the electrical distance between elements is above a certain limit (last equation) other maxima will appear, which we call grating lobes, and their direction is also dependent on the progressive phase shift and elements spatial sampling in wavelength. 8

1.5 Mutual coupling between antennas change active reflection coefficient according to scanning and tapering. 9

1.6 Mutual coupling between antennas change active reflection coefficient according to scanning and tapering. 9

1.7 Jamming radio link budget schematics used to evaluate phase shifter, minimum scan and loss requirements over frequency. 17

1.8 4x1 dielectric-loaded ridge horn active linear array geometry, where the input port (P_{IN}) is connected to a Wilkinson divider corporate network feeding broadband GaAs phase shifter and 6–12,GHz 2-W GaN power amplifiers. 19

2.1 Active antenna element geometry, showing the MMIC PA bonded to the microstrip circuit and the microstrip-to-waveguide transition feeding the ridge horn. 22

2.2 Passive double-ridge horn antenna element with WG-to-MS transition. The antenna is linearly polarized with the electric field in the z direction. 23

2.3 Dominant mode fractional bandwidth as a function of ridge height h_{rg} and ridge widths w_{rg} . 24

2.4 Simulated ridge waveguide wave impedance (Z_{wave}) and normalized guided wavelength (λ_g/λ_0) used for the design. 25

2.5 Reflection coefficient magnitude at waveguide feed (P_2) for different horn lengths, for a constant square aperture size $a = 21.27$ mm. 25

2.6 (a) Exponentially-tapered horn dimensions, and (b) lens geometry (dimensions in mm). . . . 26

2.7	Comparing $ S_{11} $ for each of the design steps from a linearly flared air filled horn towards a horn loaded with $\epsilon_r = 2.2$ slabs and lens.	27
2.8	Simulated H-plane radiation patterns at 6 GHz and 12 GHz for the linear air filled horn compared to the final design with dielectric loading and lens.	27
2.9	Geometry of the microstrip to single-ridge waveguide transition described in detail in [71]. The dimensions are given in mm.	28
2.10	Simulated $ S_{11} $ over bandwidth of horn with (solid) and without (dashed) coaxial-to-microstrip-to-waveguide transition.	28
2.11	Measured and simulated $ S_{11} $ (top) and gain (bottom) of the passive antenna element.	29
2.12	Measured (solid) and simulated (dashed) E- and H-plane radiation patterns at (a) 6 GHz, (b) 9 GHz, and (b) 12 GHz. The antenna is linearly polarized with a simulated cross-polarization ratio of 25 dB.	30
2.13	Active antenna element prototype. (a) Front view. (b) Back view. (c) MMIC PA and bias circuit close-up.	31
2.14	Schematics of load-pull simulations of Qorvo TGA2598 using measured X-parameters provided by the manufacturer.	31
2.15	Simulated PAE at $P_{IN} = 19$ dBm, {6, 9, 12} GHz for $V_{DD} = 24$ V (top) and 10 V (bottom).	32
2.16	(a) Simulated MMIC PA output power and power gain, over input power. The shaded areas show variation over 6–12 GHz. The VSWR of the load is kept ≤ 2.5 . Two supply voltages are shown: $V_{DD} = 10$ V (blue) and 24 V (red). (b) PAE range for same same frequency and impedance variation as in (a).	33
2.17	Procedure for EIRP estimation of the active antenna element. First, the radiating structure is divided into two parts at the plane where the power amplifier is inserted, and the two independent three-dimensional structures are full-wave simulated with HFSS. The S-parameters are then transferred to a nonlinear circuit simulator (AWR) allowing determination of the complex voltage excitation as a function of input power, supply, etc. This voltage is fed back into the full-wave simulator for calculating the total radiated field.	34

2.18	Active element measurement setup. To determine the active element system gain, P_{IN} is measured at the input of the passive antenna (dotted line) and active antenna, by calibrating all losses and gains in the input chain over the octave band. The output power is measured and the receiving antennas and feeds de-embedded.	34
2.19	Measured active element system gain over frequency for $P_{IN} = \{8, 14, 19\}$ dBm and $V_{DD} = \{10, 18, 24\}$ V. The measured passive element gain is shown in purple.	35
2.20	P_{OUT} and P_{GAIN} obtained through OTA (bold lines) and on-wafer measurements (shaded areas) at $\{6, 9, 12\}$ GHz.	35
2.21	Simulated and measured effective isotropic radiated power (EIRP) over input power and frequency, for $V_{DD} = \{10, 24\}$ V.	36
2.22	Simulated amplifier power-added efficiency (PAE) over input power and frequency, obtained from harmonic-balance (HB) simulations in AWR.	36
2.23	Measured amplifier power-added efficiency (PAE) over input power and frequency through OTA measurements.	37
3.1	Spatial power combiner geometry. A corporate feed network, based on 6–12 GHz three-section Wilkinson dividers, feeds 4 active elements described in the previous chapter.	40
3.2	Eigenmode simulations of mechanically synthesized dielectric material. (a) Cavity in HFSS; (b) parametric plot of average ϵ_r and $\tan \delta$ versus holes diameter; (c) Total E-field magnitude distribution on yz -plane, inside the cavity. The electric field is aligned to x -axis.	41
3.3	Geometry of in-phase uniformly excited horn array with lens loading (a). Active reflection coefficient variation for (b) outer and (c) inner array elements with lens relative permittivity varying from 1.6 to 1.8.	42
3.4	Simulated, normalized, H- and E-plane radiation patterns of passive array at $f_0 = 6, 9, 12$ GHz. The solid lines represent radiated power density of array without absorbers and dashed lines resulting radiation pattern with absorbers $\epsilon_r = 1, \mu_r = 1, \tan \delta = 0.7$ and magnetic loss tangent $\tan \delta_\mu = 0.7$	43

3.5	(a) Wilkinson power divider geometry and (b) measured S-Parameters. Input port reflection coefficient and isolation performance (left). Magnitude and phase transmission S-parameters (right).	44
3.6	(a) Schematic of Wilkinson power divider measured S-parameters and simulated array S-parameters with series inductance L modeling the connection between corporate feed network and microstrip-to-waveguide transition PCBs. (b) Simulated magnitude of reflection coefficients Γ_{in} (left) and reflection coefficient measured by gamma probes in MWO (GP) (right) for $L = \{0, 0.25, 0.5\}$ nH. (c) Array accepted power when corporate feed network input power is 0 dBm.	46
3.7	Prototype pictures: (a) front view, (b) Wilkinson power divider, and (c) back view. (d) Simulated and measured gain.	47
3.8	Spatial power combiner (a) photograph of prototype; (b) beamformer detail; (c) block diagram.	48
3.9	(a) $ \Gamma_A $ over frequency for all 4 elements uniformly biased with $V_{DDi} = \{10, 24\}$ V. (b) $ \Gamma_A $ with a nonuniform supply voltage of 10 V at external PAs and 24 V at the internal ones. . . .	49
3.10	Total delivered power to array: $V_{DD1,2,3,4} = 10$ V (left), $V_{DD1,2,3,4} = 10/24/24/10$ V (middle), and $V_{DD1,2,3,4} = 24$ V (right).	49
3.11	Simulated PAE_{avg} and η_{bf} over total delivered power to the antenna array for 6, 9, 12 GHz and $V_{DD} = 10/10, 10/24, 24, 24$ V.	51
3.12	Phase deviation between array input ports, normalized to port one and at $P_{IN} = 10$ dBm, traced over input power and at 6, 9, 12 GHz, for the three V_{DD} conditions.	52
3.13	Workflow for EIRP calculations in HFSS with HB co-simulations in Cadence AWR-MWO.	52
3.14	Normalized H-plane co-polarized radiation patterns at 6, 9 and 12 GHz for the drain voltage variations shown in the legend: uniform (red) and two levels of tapering (gray, blue).	53
3.15	Simulated EIRP for drain voltage tapering configurations shown in Fig.3.14.	53
3.16	Measured EIRP in dBm over frequency and input power for the 4-element combiner array. The color shading for all three plots is identical and color changes correspond to a 3 dB EIRP variation.	54

3.17	Simulated PAE (a) and IM3 (b) over output power for different frequencies within the octave bandwidth for a 2-tone, equal-amplitude, 10 MHz signal using the X-parameter MMIC PA model for $V_{DD} = 10, 24$ V. (c) Simulated OIP3 for the 2-tone excitation vs. frequency for two supply voltage levels.	54
3.18	Simulated array average PAE vs. output power for the 64-QAM 50-MHz signal and the 2-tone 10-MHz signal, using system-level co-simulations with Cadence VSS at (a) 6 GHz, (b) 8.4 GHz and (c) 12 GHz.	55
3.19	Array EIRP measured in the OTA setup over P_{IN} at 6, 8.5 and 12 GHz and for the three supply voltage configurations indicated in the legend.	55
3.20	Spectrum at 6, 8.5, and 12 GHz when amplifiers reach 34 dBm of total output power and the guardbands used to quantify the ACPR.	56
3.21	Array ACPR obtained from OTA measurements for the three different voltage combinations at {6,8.5,12} GHz.	56
4.1	Simulated array factor in the H-plane of a 4-element linear array across an octave, using the array spacing from the 4-element prototype. The cases for a uniform and 6-dB power taper are shown, as well as ideal steering with three different progressive phase shifts across the array, kept constant over frequency.	60
4.2	Left: Simulated Array factor (no antenna element) steering angle as a function of progressive phase shift across an octave. Right: maximum scanning for a grating-lobe free pattern vs. frequency for the array factor, or assuming an isotropic radiator element. The corresponding steering angle is also shown.	61
4.3	Simulated array geometry (a) and excitation scheme applied in HFSS (b).	61
4.4	Left: Simulated array beam steering angle θ_0 for constant progressive phase shift Φ over frequency. Center: Co-polar realized gain at beam steering direction. Right: Cross-polarization ration in beam direction.	62

4.5	Radiation pattern obtained from full-wave simulations in HFSS of geometry shown in 4.3 for $\{6, 7, 8, 9, 10, 11, 12\}$ GHz and $\Phi = \{0, -30, -60\}^\circ$ (red, black dashed, and blue dotted).	62
4.6	Magnitude of leakage power impinging (not flowing because we have output reflection coefficient) into each RF chain due to array coupling. (a) P_1 , (b) P_2 , (c) P_3 , (d) P_4 . Circuit simulation schematic (left) including the array 4×4 S-parameter matrix obtained from full-wave simulations. Expected backward power injected into the output ports of the four RF chains when each array port is excited with 0 dBm input power, over frequency and progressive phase shift Φ . One can observe symmetry between inner and outer elements. However, for a given progressive phase shift applied to the array, a different leakage level is observed at each element, as marked at 9 GHz and $\Phi = -30^\circ$ as an example.	64
4.7	Array scan reflection coefficient shown on a 50- Ω Smith chart for each port, traced for $\Phi = [-180, 0]^\circ$ and superimposed on simulated PAE when the PAs are biased at the specified quiescent point and input power of 19 dBm.	64
4.8	Active scan reflection calculated from measured coupling matrix, on a 50- Ω Smith chart for each port, traced for $\Phi = [-180, 0]^\circ$. One can observe that fabrication imperfections can cause a phase change (rotation) of Γ_A , and thus a change in expected PAE performance.	65
4.9	Magnitude of active array scan reflection over BW, calculated from measured coupling matrix, on a 50- Ω Smith chart for each port, for uniform excitation and traced for $\Phi = \{-72, 0\}^\circ$.	65
4.10	Simulated S-parameters of the ADI phase shifter using the manufacturer-provided model.	66
4.11	Beamforming network simulation schematics in AWR.	68
4.12	Beamforming network output power (solid) and system power gain (dashed) over input power for $f = \{6, 9, 12\}$ GHz, when the driver supply voltages are set to $V_{DD1,3,5,7} = 24$ V and the PA supply voltages are varied $V_{DD2,4,6,8} = \{10, 16, 24\}$ V. The top row shows the case for broadside radiation with phase shifter control voltages of $V_{Control1,2,3,4} = 2$ V, while the bottom row are simulated power and gain for phase shifter control voltages of $V_{Control1,2,3,4} = \{2, 3.8, 6.36, 9.99\}$ V. Generally, flat power behavior is observed over both frequency and steering angle.	70

4.13 Beamforming network output power over frequency for $P_{in} = 9 \text{ dBm}$, when $V_{DD1,3,5,7} = 24 \text{ V}$ and $V_{DD2,4,6,8} = \{10, 16, 24\} \text{ V}$. (a) Plot of output power for the case of broadside radiation and phase shifter control voltage of $V_{Control1,2,3,4} = 2 \text{ V}$. (b) Output power for phase shifter control voltages of $V_{Control1,2,3,4} = \{2, 3.8, 6.36, 9.99\} \text{ V}$ 71

4.14 (a) Simulated phase shift at ports 2,3 and 4 relative to the phase shift at the first element (E1), over frequency for phase shifter control voltages of $V_{Control1,2,3,4} = \{2, 3.8, 6.36, 9.99\} \text{ V}$ corresponding to the maximum scan at 12 GHz. (b) Calculated progressive phase shift over all elements. 71

4.15 Radiation patterns with complex excitations calculated from harmonic balance simulations of the active beamforming circuit in AWR-MWO for $P_{in} = 9 \text{ dBm}$ and all drain voltages set to 24 V. The solid blue line shows broadside radiation when the phase shifter voltages are $V_{Control1,2,3,4} = 2 \text{ V}$, while the dashed red curves are the resulting radiation patterns when phase shifters are set to maximum positive scan at 12 GHz with ($V_{Control1,2,3,4} = \{2, 3.83, 6.36, 9.89\} \text{ V}$). The cross-polarization ratio is better than 27 dB for all frequencies and θ at $\Phi = 0$, and better than 33 dB for $\theta \leq |60|^\circ$ 72

4.16 Maximum array directivity and realized gain (no beamforming included) over BW and $V_{Control1,2,3,4}$ set to a progressive phase shift of $\Phi = \{0, 24, 48, 72\}^\circ$ at 12 GHz. 73

4.17 EIRP (top) as a function of P_{in} and frequency for two progressive phase shifts. PAE (middle) and beamforming (BF) efficiency (bottom) as a function of EIRP and frequency. 74

4.18 Photographs of 4-element transmit phased array prototype. (a) Beamforming network, (b) bias circuit, and (c) microstrip-to-waveguide transition and small-horn array. 74

4.19 Closeup photograph of active element shown the three MMICs and bias circuit. 75

4.20 Simulation environment for determining the leakage between the ports and the power dissipated in the resistors for 0.2 GHz spaced two-tone signal. 75

4.21 (a) Photo of divider with additional isolation provided by circulators. (b) Measured S-Parameters. 76

4.22	Spectrum of two signals input into the array: a QAM signal with 50 MHz bandwidth centered at 10 GHz and single tone at 11 GHz.	76
5.1	Conventional geometry of a Y-junction ferrite circulator. The permanent magnets (PMs) produce a magnetic bias field (MBF) in the ferrite. A wave input at port P1 is transmitted to P2 with low insertion loss while P3 is isolated (counterclockwise circulation) or transmitted to P3 with P2 isolated (clockwise), depending on the resonator mode and direction of MBF. The microstrip junction is above the ferrite disk and the permanent magnets (shown here as an array) are placed immediately above and below the disk.	80
5.2	(a) Fabrication of plated magnetic nano-composite materials uses an aluminum oxide (AAO) porous template (a) filled with iron-nickel. (b) Photograph of circulator that uses a magnetic nano-composite (MNC) material as the non-reciprocal medium.	82
5.3	Block diagram of an active circulator topology implemented in this thesis in a GaAs MMIC. When port 1 (P1) is the input, P2 is the output and P3 isolated. The PA, LNA and antenna of the transmit-receive front end are shown for context.	84
6.1	Overall geometry of a Y-junction ferrite circulator. The permanent magnets (PMs) produce a magnetic bias field (MBF) in the ferrite. A wave input at port P1 is transmitted to P2 with low insertion loss while P3 is isolated (counterclockwise circulation) or transmitted to P3 with P2 isolated (clockwise), depending on the resonator mode and direction of MBF. The microstrip junction is above the ferrite disk and the permanent magnets (shown here as an array) are placed immediately above and below the disk.	86
6.2	Relevant dimensions of a Y-junction microstrip circulator: ferrite radius r_f and thickness t_f ; microstrip dielectric substrate thickness t_s ; microstrip line length l_i and width w_i . The magnets have radii r_m and thicknesses t_m and are h_m above and below the copper layers on the two sides of microstrip substrate.	88
6.3	Procedure for determining dimensions for a circular uniformly saturated ferrite disk, operating below FMR.	89

6.4 Steps for full-wave and magnetostatic simulations for microstrip circulators with nonuniform MBF at different levels of saturation resulting from realistic permanent magnets. 89

6.5 Real and imaginary parts of κ , μ and μ_{eff} over frequency for TT1-105 ferrite material parameters. The shaded area indicates the region of high absorption. 92

6.6 Simulated real (blue, triangle) and imaginary (yellow) effective relative permeability μ_{eff} for the Skyworks TT1-105 material over a frequency range $f = [1; 8]$ GHz and $H_0 = [1000; 3000]$ Oe. The 2D graphs in the insets illustrate the local behavior with one of the variables fixed. 93

6.7 Resonance analysis for $n = 1$ and $H_0 = \mu_0 M_s, 2\mu_0 M_s, 3\mu_0 M_s$ plotted with S -parameters, showing a relationship between the Eq.(6.4) zero crossing, bandwidth and MBF intensity. Three cases are traced: one considering μ_{eff} as a scalar isotropic quantity (red - solid) and two counter-propagating modes resulting from a tensor $[\mu]$ (dotted and dashed). The lower plot shows the S parameters resulting from the driven analysis for the three cases of the internal field. 94

6.8 Demagnetization factor in a cylindrical dielectric magnetic resonator as a function of radius and thickness. 95

6.9 Geometry for eigenmode simulations showing the empirically determined limits for the air box ($0.35\lambda_0 \times 0.35\lambda_0 \times 0.25\lambda_0$ at 3.5 GHz) and absorbing boundary condition boxes with the largest dimension of $0.65\lambda_0$ 96

6.10 Eigenmode analysis for resonant frequency and unloaded Q -factor for three canonical disk shapes as a function of disk thickness. A scalar μ_{eff} is used in the HFSS simulations, calculated from Skyworks TT1-105 material parameters and with $H_0 = 1750$ Oe at $f = 3.5$ GHz. For example, for a thickness of 1.0 mm (table), the circular disk is resonant at 3.9 GHz with a corresponding $Q=50.7$ 96

6.11 Parametric driven simulation for a variation of the disk thickness $t_f = [0.21; 1.41]$ mm. The disk has a circular cross section and is designed from equations given in (4) and (5). Material parameters are defined by Skyworks TT1-105 datasheet biased with a MBF $H_0 = 1750$ Oe. The grey arrow shows the shift in resonance as thickness increases. 97

6.12 Variation of magnitude and distribution of MBF in the ferrite disk region for two distances of a pair of PMs above the junction: $h_m = 0.01$ mm (left) and $h_m = 15$ mm (right). The PMs are $t_m = 3$ mm thick with diameters of $d_m = 18$ mm. The arrows in the cross-section indicate values of the dc magnetic field variation. 98

6.13 Simulated magnetic bias field generated by an array of 19 N50 grade permanent magnets, concentrically distributed and mirrored in the z -direction around the center plane of the substrate. The dimensions are $t_m = 1.106$ mm, $r_m = 0.79$ mm, $t_f = 1.249$ mm, $t_s = 1.524$ mm and, $h_m = 0.1$ mm. Magnetic field in the $x - z$ plane, including the PM volumes (left). The MBF inside the ferrite volume (right). 99

6.14 Baseline microstrip junction circulator design, where simulations are performed for a uniform MBF. 100

6.15 Baseline circulator simulated and measured performance of $|S_{11}|$, $|S_{21}|$, and $|S_{12}|$ 100

6.16 Photograph of fabricated microstrip circulator, showing the position of the PMs (one on the top, the other not visible below) [34]. The gray magnet holder is made of low-permittivity plastic and does not affect RF behavior. 101

6.17 S -parameters of a microstrip circulator designed to operate at 1.6 GHz. The ferrite disk dimensions are the same as in the previous design, centered at 4.3 GHz. To make the disk electrically smaller, a weaker MBF is applied by displacing the PMs apart. 101

6.18 Circulator operating in the UHF band having a reduced disk size by 40% [34]. The disk is initially designed to operate at 4.4 GHz when the ferrite is uniformly saturated. Foam spacers are used to define the distance from the disk. 102

6.19	Simulated S -parameters for different MBF distributions. Uniform MBF of $4\pi M_s = 1750$ G applied directly in HFSS (top), nonuniform MBF obtained through the magnetostatic co-simulations in Maxwell3D of a pair of cylindrical PMs (middle), and array of permanent magnets (bottom). The dashed boxes show the shift in frequency of the operating point as MBF distribution changes. All lines and ports are 50Ω , and the reference planes are de-embedded.	103
6.20	Photograph of third prototype presented in Fig.6.19. The circulator is designed to operate above FMR by applying a nonuniform MBF with an array of small PMs.	104
6.21	Simulated and measured S -parameters of the circulator shown in Fig. 6.20. The measurements were performed with a 2-Port VNA, so isolation is measured by $ S_{12} $. At 7.2 GHz, measured parameters are $ S_{11} = -21.8$ dB, $ S_{21} = -2.3$ dB and, $ S_{12} = -15.0$ dB.	104
6.22	Geometry for an asymmetric 3-D permanent magnet configuration.	105
6.23	Measured S -parameters of initial permanent magnetic array (2D) and the 3D-asymmetric array.	105
6.24	Summary of measured S -parameters of three microstrip circulators designed with the same ferrite disk. The different frequency bands are a result of different magnetization distributions. The response at the 4.3-GHz center frequency is a result of a design using a nearly uniformly saturated disk, while the response at 1.6-GHz center frequency is obtained when the magnetization is nonuniform and below saturation. The 7-GHz response is due to a very inhomogenous non-saturated ferrite obtained from an array of permanent magnets.	106
7.1	(a) Microscope photograph of porous alumina template filled with FeNi nanowires, from top (courtesy: Argonne National Labs). (b) Sketch of side cross-section showing the geometry and partial FeNi plating.	109

7.2	Measured hysteresis curves of two sister samples made in the same plating process with 85- μm FeNi nano-wire length and 30% alumina porosity. The corresponding FMR frequencies and linewidths are 9.1 and 14.6 GHz, and 470 and 920 Oe, respectively (courtesy: Argonne National Labs).	110
7.3	(a) Geometry of circularly shaped MNC material fabricated for a circulator. (b) Photograph of alumina (aluminum oxide) porous template substrate with plated FeNi in the shape of a circle with a 10-mm diameter.	110
7.4	Right: Calculated demagnetization profile of a cylindrical disc made of the material with properties in Table 7.1. Left: discretization for cylindrical circulator cavity simulations, where each shaded ring is treated as a uniform material with a different magnetization. . . .	111
7.5	Top (a) and full (b) view of a microstrip junction circulator assuming a MNC thin disk of self-biased material and 50- Ω ports directly connected to the junction.	112
7.6	Simulated S-parameters for a 5-mm radius FeNi MCN disc with uniform magnetic bias field of 0.4 T (left) and for three discrete concentric rings, with $H_{01}=0.4$ T, $H_{02}=0.16$ T and $H_{03}=0.06$ T, with the related radii of 3.5, 4.5 and 5 mm (right). Notice the change in circulation direction between the uniform and nonuniform field case, as well as increased loss and slight frequency shift.	112
7.7	Simulations for variations of M_s (top), FRM linewidth ΔH (middle) and Lande g-factor (bottom) over a range determined from MNC processing, given in Table 7.1.	115
7.8	Fabricated microstrip circulator that operates around 7 GHz. (a) Assembly drawing and (b) prototype photograph.	116
7.9	Measured vs. simulated results for the circulator from Fig. 7.8, where the simulations show data for a discretized model from Fig. 7.3. These measurements are done before external permanent magnets were applied to the disc.	116
7.10	Measured data for hybrid circulator from Fig. 7.8 for: (top) self-biased device, and (bottom) device with external field from a readily available rare-earth magnet.	117

7.11 Measured data for hybrid circulator with components shown in the photograph. The MCN sample in this case has the native copper ground layer used during the plating process. The sample was exposed to an external permanent magnet several days before the measurement. No external magnetic field was applied for the S-parameter data shown here. 118

8.1 Active circulator MMIC circuit topology. Nonreciprocal circulation is accomplished with gain-matched single-stage amplifiers. Each amplifier input is connected to a *through* port of one coupler while the output is connected to the *coupled* port of the following asymmetric Lange coupler. When port 1 (P1) is the input, P2 is the output and P3 isolated. 120

8.2 Gate and drain bias circuit layout with a feedback resistor of 200 Ω between the device gate and drain. Decoupling capacitors of 0.9 pF and bypass capacitors of 4 pF are used, with an RF choke implemented as a spiral inductor of 3.9 pF. 121

8.3 Unit amplifier layout, showing the 200 Ω feedback resistor and 0.9 pF blocking capacitors. The gate and drain bias circuits use 4 pF bypass capacitors and 3.9 nH spiral inductors. The maximum dimensions are 1050 μm×700 μm. Input and output matching networks are implemented with shunt inductors $L_1 = 0.45$ nH and $L_2 = 0.89$ nH, and a series inductor $L_3 = 2.12$ nH. 122

8.4 EM-simulated unit amplifier S-parameters from 7 – 13 GHz. The Qorvo PDK model is used for the transistor. 122

8.5 Lange coupler simulation model (top), and geometry (bottom).The main geometric parameters are the number of lines ($N = 4$), line widths $w = 5$ μm, line lengths $L = 900$ μm, and distance between lines $s = 3$ μm. 123

8.6 Lange coupler simulated S-parameter parametric study. Top: The coupler length is 2.5 mm ($\lambda_g/4$) and the line separations varies between 2 and 5 μm. Bottom: The coupler length is varied between 2.5 mm and 1 mm ($\lambda_g/10$) and the line separation kept at 3 μm. The nominal case with $l = 2.5$ mm and separation of 3 μm is shown in solid line. 124

8.7 Lange coupler EM-simulated S-parameters from 7 – 13 GHz. 125

8.8	Active circulator layout with perpendicular RF pads for ease of probing/packaging, and three sets of drain/gate bias pads.	125
8.9	Simulated S-parameters of the active circulator with the same amplifier, for a coupling coefficient of the couplers of $c = 3$ dB for two different coupled-line section lengths: $\lambda/4$ and $\lambda/10$	126
8.10	Simulated S-parameters of the active circulator with the same amplifier, using $c = 6$ dB couplers for two different coupled-line section lengths: $\lambda/4$ and $\lambda/10$	127
8.11	Simulated active circulator S-parameters from 7 to 13 GHz showing insertion gain with isolation $ S_{31} $ greater than 20 dB.	127
8.12	Stability analysis for complete active circulator under nominal bias and with all ports terminated in 50Ω	128
8.13	Photograph of a $2.5 \text{ mm} \times 2.5 \text{ mm}$ GaAs MMIC X-band implementation.	129
8.14	DC biasing board with chip mounted. Single layer and SMD capacitors are placed in the bias lines, connected with bondwires to on-chip DC pads. The gates bias lines are identified by G1, G2, G3 and drains D1, D2, D3, respectively. The RF ports are $150\text{-}\mu\text{m}$ GSG probe pads.	129
8.15	Measured and simulated S-parameters of the circuit from Fig.8.14.	130
8.16	Statistical analysis of gain and isolation on all three ports with process variation and loads within a VSWR=1.1 circle.	130
8.17	Block diagram of the active circulator and possible use in a transmission-reception (T/R) module. The three ports are connected to the output of the transmitter PA, antenna, and input of the receiver LNA.	131
8.18	Small-signal model extracted from transistor foundry nonlinear model and adapted to open-loop stability analysis.	131
8.19	Simulated loop gain for the three transistors (T1, T2, T3) when ports are terminated with loads within the VSWR=2 circle, from DC to 20 GHz.	132

8.20 Simulated loop gain for the three transistors (T1, T2, T3) when ports are terminated with loads within the VSWR=2 circle, from DC to 20 GHz, showing in detail the behavior within a magnitude of 1.5. The shaded regions show that the phase margin for this circuit is larger than 30° for all loads that fall within the VSWR=2 circle on all three ports, with a uniform statistical distribution of impedance values. 132

9.1 (a) Layout of a 6-W, 6–12 GHz power amplifier MMIC designed in the WIN Semiconductors NP15 GaN on SiC process, with broadband matching accomplished using multiple resonant *RLC* circuits. (b) Two-stage amplifier with input and output ports terminated in 50 *Omega* with no matching. The output of the first stage device is directly matched to the input of the second stage using resonant circuits. This quasi-MMIC has the flexibility to be matched at input and output using external matching circuits with different technical specifications from 6–12 GHz. 136

9.2 Simulated steady-state temperature throughout the brass mount when 4 heat sources the size of the 2-W MMICs are dissipating 2 W each. The brass and ceramic thermal properties are used, along with free convection coefficient of surrounding gases and dry vapors equal to 5 W/m², and with an external environmental temperature of 298 K (25°C). 137

9.3 Thermal simulations using the same sources as described in Fig. 9.2 but with MMICs remounted directly to the array chassis. (a) Mechanical structure used for simulation. (b) Simulated heat map. 137

9.4 Layout of a bidirectional power–low-noise amplifier (PALNA) implemented in the WIN Semiconductors PIH110 GaAs process for the 26–30 GHz 5G frequency band. Instead of switches for T/R, one possible solution is the use of switchless front-end bidirectional amplifiers. A PA and LNA (PALNA) are connected by a specialized matching network. Switching between transmit and receive paths is done by turning ON/OFF the drain and/or gate biases. The simulated two-stage LNA gain is about 20 dB with NF< 2.5 dB, the class-AB PA with a drain efficiency > 40 %. 139

CHAPTER 1

INTRODUCTION

CONTENTS

1.1	BACKGROUND AND MOTIVATION	1
1.2	MAIN QUANTITIES, METRICS AND FIGURES OF MERIT	5
1.3	CHALLENGES IN OCTAVE-BANDWIDTH PHASED ARRAY COMPONENT DESIGN	7
1.4	CHALLENGES IN SYSTEM-LEVEL ANALYSIS AND CHARACTERIZATION	15
1.5	PHASED ARRAYS IN ELECTRONIC WARFARE APPLICATIONS	15
1.6	THESIS GOALS AND ORGANIZATION	19

1.1 BACKGROUND AND MOTIVATION

Phased array antennas have penetrated a large application space, and in this thesis, some of the critical components for phased array front ends specifically focused on octave-bandwidth transmit arrays are discussed, illustrated in Fig.1.1. The components are demonstrated in the 6–12 GHz octave, but the methodology and component designs are scalable in frequency.

Over the past few decades, phased array applications have expanded from radar to wireless and satellite communications, as well as medical imaging and various sensing modalities. By tracking users with

individual high-gain beams, spatial multiplexing enables co-channel interference mitigation, enhancing signal levels and power management in wireless communications systems. For example, [1] shows a 64-element phased-array transceiver operating in the 28 GHz band with 52 dBm effective isotropic radiated power (EIRP) for 5G applications with up to 12 Gb/s of throughput. In satellite broadcasting and communication systems, phased array antennas enable beam shaping over countries and continents, tracking at the end-user side, and rain fading mitigation, e.g. [2]. In [3], advances in phased arrays for satellite applications developed at Lockheed Martin are described from an industry perspective. Scaling to higher frequencies, [4] demonstrates a system-level development of a 384-element, 16-tile, W-band phased array with 52 dBm EIRP in 0.18- μm SiGe BiCMOS technology.

Phased arrays also provide enhanced capabilities for airborne radar: power efficiency increase; adaptive beam forming to suppress jammers; space-time adaptive processing to suppress clutter return for more efficient GMTI (Ground Moving Target Indicator) functionality; multi-beam on receive capability for multi-static operation in stealth target detection; and higher system availability due to graceful degradation of array performance resulting in low life cycle cost [5]. For fast mobile applications, automotive radars are used as sensors for adaptive cruise-control (ACC), safety applications like blind-spot surveillance and collision mitigation/avoidance, backing/parking, and low-speed/stop-and-go ACC [6]. In [7], a system simulation using a phased-array frequency-modulated continuous-wave (FMCW) radar with beam steering controlled by environmental variables is implemented, demonstrating the advantages of increased range and providing more time for adaptation. The automotive environment presents design challenges, such as packaging and a harsh thermomechanical environment. In [6], automotive radar front-ends phased-array are analyzed, where RF MEMS are used as switches in a Rotman lens or in phase shifters, and optimized for RF and thermomechanical behavior.

For weather monitoring, phased array radar bring the capability of scanning larger volumes in shorter time intervals achieving update rates of < 1 min [8], where beam control and null generation enable collecting robust data for post statistical analysis [9]. Also, phased arrays have found applications in RFID for localization in the UHF range, e.g. [10], while in radioastronomy [11], adaptive nulling techniques help combat radio frequency interference [12]. More recently, beam-steering techniques have been extended to

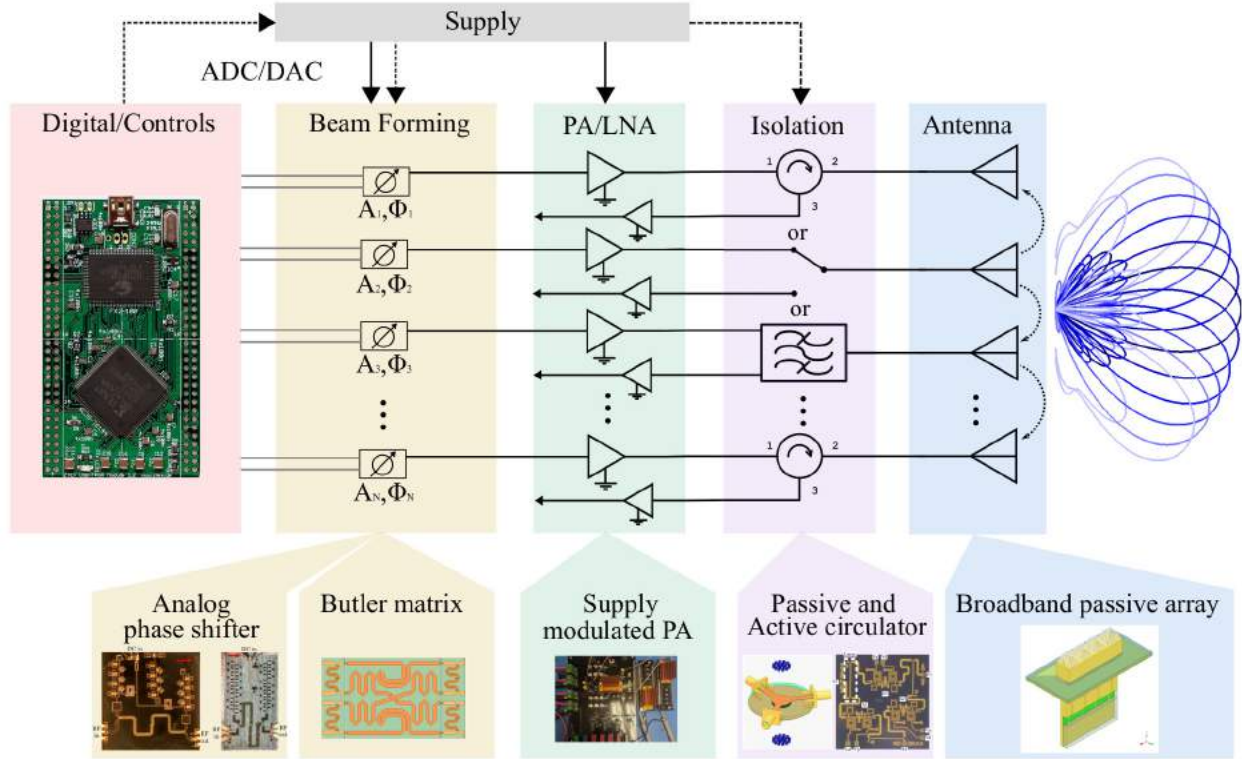


Figure 1.1: High-level block diagram of a phased array, where the beamforming can be done either in the digital or analog domains in transmit and/or receive. The isolation between TX and RX can be done either with circulators (full-duplex), switches for time-domain half-duplex, or filters for frequency-domain separation of TX and RX operation. The dotted arrows indicate coupling between the antenna elements, which affects isolation. The focus of this thesis is two-fold: (1) demonstrating octave-bandwidth analog components of broadband transmit arrays for beamforming, amplification, isolation; and (2) understanding interactions between the passive and active components at the array level through simulations and active over-the-air measurements. Shown in the expanded blocks with photographs are: GaAs MMIC phase shifter beamformer network; GaN MMIC power amplifiers; ferrite passive and MMIC active circulators; and broadband antennas with thermal handling capability.

biomedical devices [13]. Doppler-based non-contact vital-sign (NCVS) sensor systems are used to monitor heart and respiration rates of patients. The sensor accuracy can deteriorate quickly in a noisy or cluttered environment, and [14]- [15] reports on directive phased arrays for NCVS systems with considerably improved accuracy compared to fixed-beam Doppler radar. In [16], a 70-MHz near-field phased array provides 3-D SAR control and increases locoregional hyperthermia in tumor treatments, while in MRI systems signal-to-noise ratio, image contrast and resolution can be improved [17]. Phased array are also applied in wireless power transfer systems for maximizing power delivery to an intended location while minimizing leakage fields in other locations, e.g. [18, 19].

The growing variety of applications and system requirements lead to the need of scalable, modularized devices for transmit and receive chains. In this context, [20, 21], e.g., shows heterogeneously-integrated phased arrays for communication and sensor applications at Ku-band. In the transmit chain, spatial power combining is used to increase the EIRP, while enabling distributed integrated-circuit components, where each element or subarray is fed by an independent RF front-end circuit. This approach allows operation with multiple signals and beams using the same fixed antenna aperture, with trade-offs in size and performance requirements for high-power, wide-band operation [22]. Although it is an effective method to increase radiated power, size and generated heat remain key limitation as frequency increases and the $\lambda_0/2$ spacing of the antennas shrinks slower than the size of active elements. Therefore, power density and efficiency of the power amplifiers (PAs) favor the use of GaN over GaAs. The high breakdown voltage of GaN results in high peak power levels, and is accompanied by a robust SiC substrate with good thermal conductivity. Trends in active arrays for space and radar applications, with GaAs replaced by GaN PAs to increase EIRP with the same number of elements are discussed in [23] and [24].

Although most phased arrays are relatively narrowband, a number of broadband passive antenna arrays, e.g. [25], arrays with broadband optical beamforming, e.g. [26], [27], and CMOS true-time delay beamformers, e.g. [28], have been demonstrated. A comprehensive overview of digital and hybrid approaches can be found in, e.g. [29–31].

The focus of this thesis is two-fold: (1) demonstrating octave-bandwidth analog components of broadband transmit arrays for beamforming, amplification, isolation; and (2) understanding interactions between the passive and active components at the array level through simulations and active over-the-air measurements. Fig. 1.1 shows a high-level block diagram which outlines the components discussed in this thesis. The main blocks include the beamforming network, amplification stage with variable supply, isolation stage between transmit and receive, and the final radiating aperture. The digital control is not discussed here, but are an integral part of the system. The demonstrated components in Fig.1.1 focus on III-V semiconductor (GaAs and GaN) MMICs with potential for heterogeneous integration. The last component in the chain is the passive antenna itself, and its radiating and matching characteristics affect the entire system performance.

1.2 MAIN QUANTITIES, METRICS AND FIGURES OF MERIT

Starting from the radiating aperture in the block diagram of Fig.1.2, the main quantities include antenna radiation pattern (including beamwidth, steering angle and side-lobe level), gain, and polarization. The remaining part of this section discusses the various parameters from this figure shown in blue font. When an octave or larger bandwidth is considered, the element-to-element coupling has a large effect on antenna properties as well as front-end circuit performance. It is described by an active scan coefficient (Γ_A) which presents a non-50 Ω impedance to the circuit connected to the antenna [32].

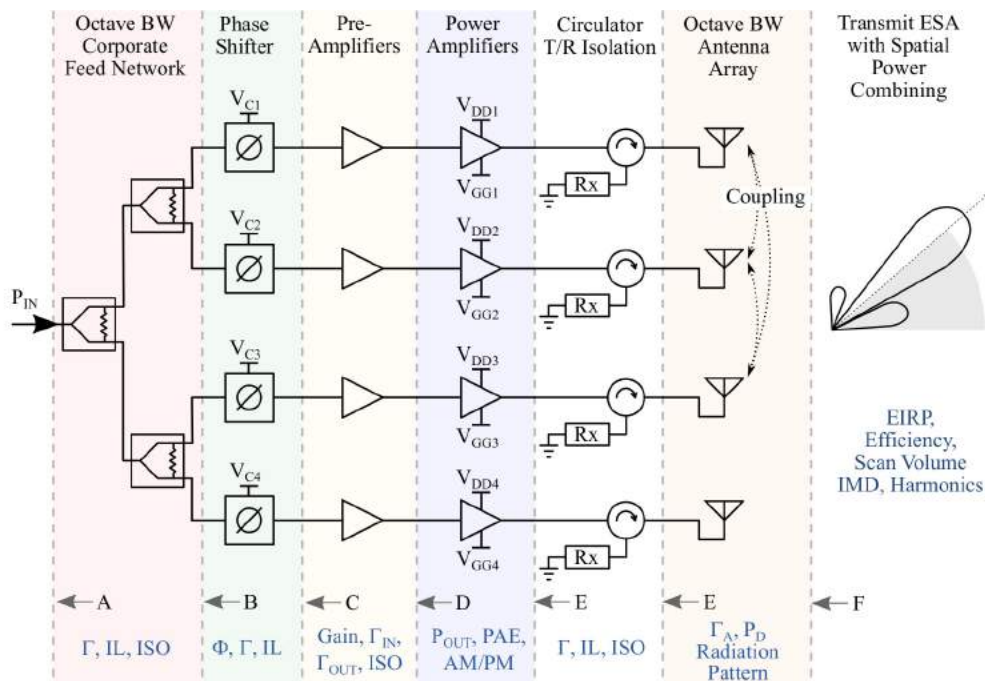


Figure 1.2: Transmit ESA block diagram including: corporate feed network, phase shifters with control voltage V_{C1} , and power amplifiers with drain supply voltage V_{DD} directly connected to each array antenna element. The various parameters of interest are shown in blue font.

The main Figures of Merit (FoMs) that are used in this thesis for transmit phased array, referring to Fig.1.2 are:

- Effective isotropic radiated power (EIRP), which depends on antenna array gain and power radiated by each element and is a function of frequency;
- Efficiency in continuous wave operation (CW), which includes the Power Added Efficiency (PAE) of

the power amplifiers (PAs), which in turn depends on the supply voltage, and overall beamforming efficiency.

- Average efficiency and power when multiple modulated signals are transmitted simultaneously across the octave band;
- Linearity, which can be described by harmonic radiation, intermodulation products (IMD) and in-band (error vector magnitude, EVM) as well as out-of-band (adjacent channel power ratio, ACPR) distortion. Importantly, linearity in the far field includes nonlinear interactions within the array.
- Maximum steering angle and scan volume across frequency.

The challenges in achieving specified performance across an octave bandwidth are attributed to both active and passive parts of the array. For example, for the active circuits, the matching, gain, efficiency, power and linearity are critical frequency-dependent parameters. On the other hand, isolation, insertion loss (IL), amplitude and phase imbalance and beam squint are difficult to maintain over a large bandwidth. In Fig.1.2, a 4-element linear active sub-array block diagram is shown, and such an array is used to demonstrate all the challenges quantitatively. For example, it is shown how the values of the above passive component parameters affect the transmitted radiation pattern, in terms of beam steering errors, degradation in sidelobe levels (SLL), distortion in modulated signals and reduction in overall efficiency. In terms of the active component parameters, for example, the PA design trades linearity and efficiency, and for high peak-to-average ratio (PAR) signals with wide instantaneous bandwidths (IBW), the efficiency is reduced. This leads to increased heat dissipation and a rise in PA active device junction temperature, leading to a drop in gain and output power. Likewise, a rise in temperature of the phase shifter circuits may change the progressive phase values and result in unexpected changes in the steering angle. It becomes obvious that complex calibration methods are needed to characterize and correct for these and other similar effects.

1.3 CHALLENGES IN OCTAVE-BANDWIDTH PHASED ARRAY COMPONENT DESIGN

Next, the specific challenges in broadband component design are discussed separately, followed by a discussion of their impact on system-level challenges.

1.3.1 ANTENNA ELEMENT AND ARRAY DESIGN

Although many possible octave-bandwidth antenna element types exist, a transmit phased array introduces specific constraints. There is a trade-off between grating lobes, beam squint, mutual coupling, integration level, and heat dissipation. The array design, including element and array factor analysis, will impact the beamforming (feed) network design and performance.

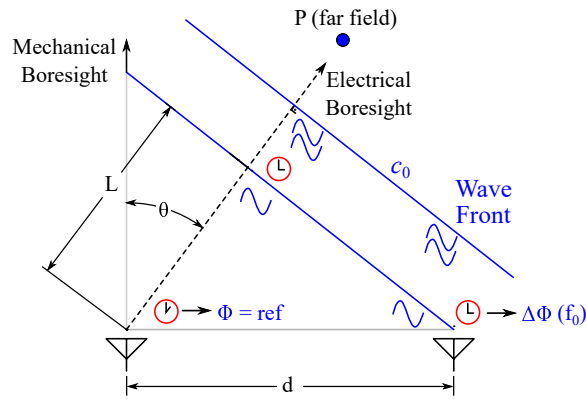


Figure 1.3: Beam steering mechanism in time and frequency domains.

Fig.1.3 shows a two-element array with relevant parameters. For steering in the θ direction, a delay d is required between elements which produces a progressive phase shift $\Delta\Phi$:

$$\Delta\Phi = 2\pi f \cdot \Delta t = 2\pi \frac{d \sin \theta}{\lambda_0} \quad (1.1)$$

since $L = c \cdot \Delta t = d \sin \theta$ and $\lambda_0 = c_0/f$. The array factor for a uniform array with an electrical period d/λ_0 introduces grating lobes which are a function of frequency and steering angle θ . The n -th grating lobe is found to be in the following direction:

$$\theta_{g,n} = \sin^{-1} \left(\sin \theta_0 \pm n \frac{\lambda}{d} \right) \quad (1.2)$$

where θ_0 is the main beam steering angle. If the first grating lobe is avoided by design, all the higher-order grating lobes will be eliminated. An illustration is shown in Fig.1.4 for an array factor of a four-element array with normalized electrical periods of 0.5, 0.75 and 1.0, covering an octave bandwidth, for $\Delta\Phi = 0$ and $\Delta\Phi = -60^\circ$. It is obvious that an array radiation pattern changes dramatically over an octave bandwidth.

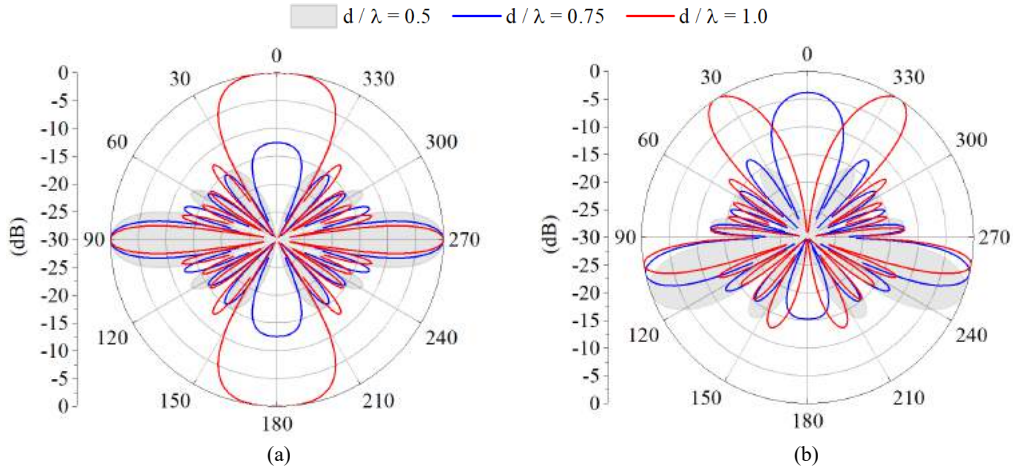


Figure 1.4: Grating lobes in 1D for (a) $\Delta\Phi = 0$, and (b) $\Delta\Phi = -60^\circ$. The array factor can be read as the discrete Fourier transform in spatial domain of the current distribution of isotropic radiators. It has a periodicity that is dependent on the progressive phase shift $\Delta\Phi$, the frequency (inside the wavenumber k) and the distance between the elements. If the electrical distance between elements is above a certain limit (last equation) other maxima will appear, which we call grating lobes, and their direction is also dependent on the progressive phase shift and elements spatial sampling in wavelength.

A related issue when operating over a large frequency range is beam squint, which refers to change in steering direction with frequency for a given $\Delta\Phi$ and d . For a progressive phase shift variation of $\delta\Phi$ which corresponds to a frequency change of Δf , there will be a change in steering angle of $\Delta\theta$:

$$\Delta\Phi + \delta\Phi = 2\pi \frac{d}{c_0} (f + \Delta f) \sin(\theta + \Delta\theta) \quad (1.3)$$

and there will be no beam squint ($\Delta\theta = 0$) if the following is satisfied:

$$\frac{\Delta\Phi + \delta\Phi}{f + \Delta f} = \text{constant} \quad (1.4)$$

This implies that for no beam squint, the progressive phase needs to change across frequency.

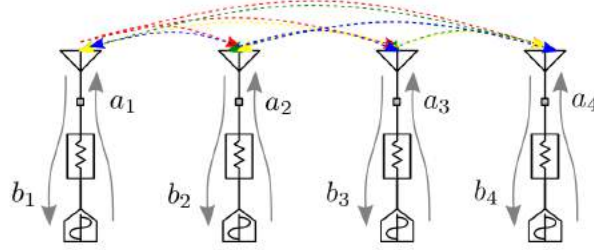


Figure 1.5: Mutual coupling between antennas change active reflection coefficient according to scanning and tapering.

Another relevant issue in phased array, especially if a broad bandwidth is considered, is coupling between elements and how it affects the impedance as the array beam is scanned. When a complex excitation is applied to all elements, the coupling is taken into account by defining the active reflection coefficients at all antenna element ports:

$$\Gamma_{m,a} = \sum_{n=1}^N S_{mn} \frac{a_n}{a_m} \quad (1.5)$$

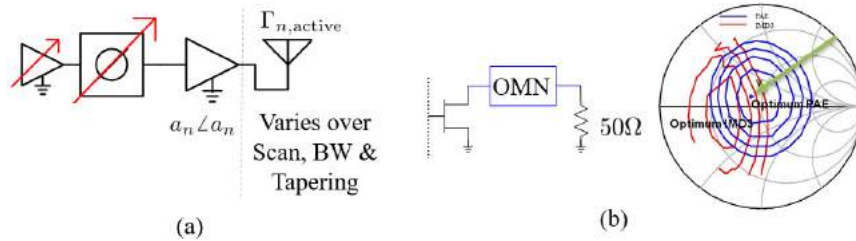


Figure 1.6: Mutual coupling between antennas change active reflection coefficient according to scanning and tapering.

This is illustrated in Fig.1.5. If we next consider that the antenna port is connected to the output of a PA in a transmit array, Fig.1.6a, there will be an effect on amplifier performance due to mismatch. Fig.1.6b shows an example of the efficiency-linearity tradeoff. The load-pull contours, obtained through harmonic balance simulations with a nonlinear device model, show constant efficiency (blue) and constant IMD3 (red). If the impedance presented to the device output, nominally matched to 50Ω for efficiency at one frequency at a single power level, one can observe a degradation in efficiency as well as linearity at that frequency, and

the effect is compounded when a wide bandwidth and a range of power levels are considered. In this thesis, the active scan array coefficient is quantified and its effects on the PA analyzed across bandwidth.

Circulators are often used to mitigate the variation of PA output impedance, but this leads to additional loss and mass, and limits the integration level and therefore physical separation between radiators as the frequency increases. Another space constraints comes from the fact that active circuits scale slower in size than the free-space wavelength, and that broadband matching implies either a lossy or large antenna element.

1.3.2 TRANSMIT-RECEIVE ISOLATION

Phased array are usually used to both transmit and receive, in which case some isolation method is required to protect the low-noise amplifier from saturating due to leakage from the transmitter. For non-simultaneous transmit and receive applications, switches can have high isolation and transmitter amplifier bias can be turned off during receive mode. For simultaneous transmit and receive (STAR), circulators or diplexers are used, depending on the frequency of the up/down links. For some calibration methods, a simplified receiving stage is usually implemented even for purely transmitting active antenna systems.

Often the required levels of isolation are greater than 100 dB and exceed what can be done by only one method, so several methods including e.g. antenna polarization are added, and have been demonstrated over a wide bandwidth, e.g. [33]. Circulators remain to be important components for circuit-level isolation, but are lossy and bulky. In this thesis, various designs of ferrite circulators are presented using the same ferrite disk size with different dc magnetic bias field distributions for frequency tuning and volume reduction. [34, 35]. A study of self-biased ferrite circulators is performed using magnetic nano-composite (MNC) materials for operation at X-band and below. These materials are under development at Argonne National Lab, using both electro-spinning and electro-plating fabrication techniques [36–38]. For higher levels of integration, MMIC circulators using the non-reciprocal nature of transistors can be used. In this thesis, design of an active circulator in a $0.25\ \mu\text{m}$ GaAs pHEMT monolithic microwave integrated circuit (MMIC) process [39] is presented, and the circulator performance in a phased-array-like environment is investigated [40].

1.3.3 POWER AMPLIFIER CHALLENGES

In a power amplifier design, output power, efficiency, linearity and bandwidth are always traded. The PA output power level directly governs the array transmitted power (EIRP), and is a determining parameter to estimate wireless system link budget and the effective communication range. The PA efficiency determines dc power consumption, heat dissipation, and consequently the thermal handling requirements and cooling technology which affects the total cost and form factor of a phased array. The power added efficiency (PAE) is the most conservative metric, since it takes into account the gain of the amplifier:

$$\text{PAE} = \frac{P_{out} - P_{in}}{P_{dc}} = \frac{P_{in}}{P_{dc}} (\text{Gain} - 1) \quad (1.6)$$

A theoretical study of the efficiency – bandwidth trade-off is derived in [41] from the Bode-Fano integrals, and applied to GaN PA design. It shows the counter-clockwise nature of maximum PAE behavior as frequency increases, which opposes the passive clockwise load input impedance behavior over bandwidth. In [42], a detail analysis of those trajectories is performed for the design of wideband PAs. In this thesis, the impact on the PAE of the broadband active reflection coefficient over scanning is quantified and a potential improved design approach is shown.

To achieve high efficiency, the transistor in a PA operates in the nonlinear region and introduces distortion of the amplified signal, both in and out of signal band. In a broadband PA, these distortions can fall within the operational bandwidth. The simplest metrics to evaluate PA nonlinearities are: AM to AM and AM to PM distortion. The former describes output amplitude variation against input power which depends in turn on PA gain compression. AM to PM distortion, or output phase variation against input power affects the phase modulated part of a signal. Intermodulation Distortion (IMD) occurs when two or more signals are amplified by a non-linear PA. The resulting spectrum will contain the sum and difference frequencies of the input signals, along with their harmonics. Since advanced phased arrays are expected to transmit multiple simultaneous complex modulated signals, which additionally may have nonconstant envelopes, other metrics also need to be considered. For example, Error Vector Magnitude (EVM) is a baseband (in-band) measure of how accurately a wireless system is transmitting symbols within its constellation. Adjacent Channel Power Ratio (ACPR) quantifies the channel leakage and is an out-of-band spectral metric. The relationships

between IMD and ACPR used throughout the thesis are detailed in [43–45] and described below:

- P_{tone} : output power per tone, dBm
- P_{out} : total output power, dBm
- $P_{tone,eq}$: equivalent power per tone of a two-tones signal when output power is P_{out} - IMD3: third order intermodulation distortion, dBc
- IM3: third order intermodulation product, dBm
- OIP3: Output interception point of fundamental and third order intermodulation product, dBm
- C_n : Correction factor from to obtain approximated calculation ACPR from IMD specification for a multi-tone signal, dB
- $ACPR_n$: Estimated ACPR for n tones signal, dB
- Equations operated directly in dB scale

$$IM3 = P_{tone} + IMD3 \quad (1.7)$$

$$OIP3 = \frac{3P_{tone} - IM3}{2} \quad (1.8)$$

$$P_{out} = P_{tone} + 10 \log n \quad (1.9)$$

$$P_{tone,eq} = P_{out} - 3 \quad (1.10)$$

$$ACPR_n = 2(P_{tone,eq} - OIP3) + C_n \quad (1.11)$$

Table 1.1: Some IMD3 correction factors for calculating ACPR from IMD3 of a signal with n carriers

# of Carriers	1	2	3	4	9
C_n (dB)	+3	+9	+11	+12	+13

In [46] an AM/AM and AM/PM semi-analytical model is derived for GaN HEMTs, and shows that the PA load impedance can be an additional source of AM/PM conversion when the output is mismatched. In [47], the relationships between phase distortion, bias point and load modulation in power amplifiers are experimentally evaluated for different GaN HEMT technologies. In [48], a design approach is presented to maximize the efficiency versus linearity trade-off in fixed and modulated load GaN PAs, by using the driver

stage as an AM/PM distorter to the power stage. While all these approaches are very insightful, they consider only the narrowband case.

Power amplifier solutions for broadband operation include multiple switched narrowband PAs [49], and architectures such as distributed, traveling-wave, feedback, and balanced configurations discussed in [50]. PAs with enhanced efficiency through dynamic power supplies (envelope tracking [51]) have been demonstrated at higher power levels, with higher efficiencies and at increased frequencies. An example PA designed for K-band satellite communications from 18–25 GHz is described in [52]. This 3-stage GaN MMIC fabricated in the Qorvo 150-nm process shows over 40% efficiency in CW with 4 W of output power from 18–24 GHz. The drain supply lines for the three stages can be accessed separately and by changing them dynamically with the envelope of a modulated signal, the average efficiency is improved. This approach of efficiency enhancement can be extended to high envelope bandwidths and multiple simultaneous signals over a large bandwidth.

In this thesis, a commercial broadband MMIC PA is integrated with the antenna array and the tradeoffs in EIRP, linearity and efficiency are analyzed in the array context using X-parameters. The implications of PA efficiency on thermal management within the array are also discussed.

1.3.4 BEAMFORMING NETWORK CHALLENGES

Beamforming can be achieved in many ways including discrete beams, such as Butler and Blass matrices, and Rotman and Luneburg lenses [32]. In the case of Rotman and Lunenburg lenses, the progressive phase shift is achieved by true-time delay feed networks, and beam squint (or beam pointing frequency distortion) is not observed. In this thesis, we aim to achieve continuous beam steering for small adjustments during operation. Thus, we investigate broadband phase shifters in a corporate feed network for beam steering and beamforming. In the 4×1 array, we consider broadband transmit chains in each element, consisting of a continuous phase shifter, driver and power amplifier. The input signal is divided with a corporate feed network, as shown in Fig.1.2.

A corporate feed network has a single input port. Multiple signals transmitted by the array must be combined beforehand. The design of the feed network requires minimized amplitude and phase imbalances

across a wide bandwidth, and a high isolation. In this thesis, an isolated Wilkinson divider is designed with 3 sections to cover the octave band and phase shifters can be integrated in the four output ports.

A phase shifter provides a known amount of controllable phase shift at the RF carrier. It can be realized by a connecting reactive elements in series or shunt to a transmission line, and there are two main classes: constant phase shift difference, and true-time-delay (TTD), or constant time difference. The implementations can use PIN diodes, varactors or FETs [53].

In the case of broadband phased arrays, beam squint can be mitigated using true-time delay beamforming, which can be done in the optical or microwave domains. Common microwave true-time delay phase shifters include loaded lines [54] and switched delay lines [55]. These are difficult to design with simultaneous wide bandwidth and low loss. Loaded transmission lines can provide a true time delay over as much as a decade bandwidth, where the phase is varied using varactors [55], MEMS [54] or ferroelectrics [56] and are typically limited by return loss variation over frequency. Reflective phase shifters with different hybrids are presented in [57,58], and the variable reflective loads can be implemented with MEMS or varactors. Large continuous phase shifts in [59,60], are accomplished with two cascaded phase shifters. In [61] 6-12 GHz designs are presented, which combine a reflective topology with a loaded-line variable reactance implemented in WIN Semiconductors' GaAs enhancement (E-) mode PIH10 and GaN depletion (D-) mode NP15-00 pHEMT processes. It is shown that the GaN phase shifter is more linear and has higher power handling.

The phase shift does not typically vary with frequency in a way that is beneficial for phased arrays to compensate for beam squint, especially over a large bandwidth. In this thesis, the beam steering is quantified for a commercial state-of-the-art GaAs continuous phase shifter and its model is used in the transmit chain with the broadband horn array to evaluate far-field radiation patterns.

The phase shifters and PAs require a multitude of bias lines, and in this work, they are built in the microstrip-to-waveguide transition PCB. Many challenges are associated with the biasing: decoupling capacitors tend to be large for high voltages required by GaN devices; many dual polarity dc voltages need to be separately routed to each circuit (e.g. from -5 to 25 V in the prototype array); stability capacitors and resistors need to be included to prevent oscillations; and proper bias sequencing must be implemented.

1.4 CHALLENGES IN SYSTEM-LEVEL ANALYSIS AND CHARACTERIZATION

Useful simulations need to include the interaction of all the components in the feed network an antenna, presenting numerous challenges. For example, the following needs to be accounted for: effects of the corporate feed network line lengths and isolation between ports; phase-shifter mismatch and nonlinearities; AM/AM and AM/PM and IMDs of the PAs over bandwidth and power level; effects of antenna element coupling and cross-talk; and finally effects of component failure. In this thesis full wave electromagnetic simulations (Ansys HFSS) are used in conjunction with linear and nonlinear harmonic-balance circuit simulations (Cadence MWO) and system-level signal simulations (Cadence VSS).

Experimental characterization presents its own unique challenges as well: the input is a coaxial connector while the outputs are one or more plane waves; nonlinearities propagate through the active front-end chain and are modified by the antenna frequency and spatial selectivity; in PA characterization through over-the-air (OTA) measurements pre-characterization of the passive array has to be performed [62], etc. In this thesis, the measured active array is presented in Chapter X, while details of the calibration and other measurement routines are given in Appendix A1.

1.5 PHASED ARRAYS IN ELECTRONIC WARFARE APPLICATIONS

The research in this thesis is aimed at enabling friendly forces dynamic access to the RF part of the electromagnetic spectrum while denying enemy use, through a reconfigurable broadband transmit phased array. One of the applications of an octave-bandwidth phased array is electronic warfare, specifically for active jammers. The technical objective of the research is to show improved performance of the transmit front end, gained from integrated design and associated tradeoffs in a scalable architecture. The modular and scalable front end can adaptively support several operating modes simultaneously with the transmit unit element described in detail in Chapter 2 as a building block. For example, the beamwidth, center frequency, and power (EIRP) can be independently adjusted in different beams, and each beam can operate in a different jamming mode, e.g.:

- A beam can operate over the full spectrum in swept CW mode, which does not require supply-modulation or power re-configurability, is very efficient, and allows the full 2:1 instantaneous bandwidth.
- Other beams can transmit signals with higher PARs simultaneously.
- Supply modulation at the element or sub-array level can be used for enhancing efficiency.
- An example of the above scenario is a beam that carries a signal that is symmetric around an arbitrary center frequency with a total bandwidth of twice the supply modulator bandwidth.
- Alternatively, the beam could be used to simultaneously jam several narrow portions of the full octave in a sum-of-envelope supply modulation mode [63].

It is instructive to examine a jammer link budget using a spatial power combiner topology, with beam steering functionality. The following scenario is assumed for a link budget analysis [64], [65]. We consider a monostatic radar with self-protection against electronic attack. The jammer beam is placed on the target aircraft, assuming a constant gain and a threshold for jamming to signal ratio of $J/S = 10$ dB. The block diagram used for calculating the link budget is shown in Fig. 1.7, where P_{RTx} is the radar output power, G_{aR} is the radar transmit antenna gain, FSL is the free space loss, G_{aJaRx} is the jammer receive antenna gain, G_{Ja} is the jammer beamforming network gain, G_{aJaTx} is the jammer transmit antenna gain, $GRCS$ is the aircraft radar cross section (RCS), and $PRRx$ is the sum of jamming signal plus radar echo.

The following scenario was considered for link budget calculations Range between radar and aircraft: 30 km; frequency 9 GHz, $P_{RTx}=70$ dBm, $G_{aR}=45$ dBi, $G_{aJaRx}=2$ dBi, $RCS: 9$ m². The calculated transmit phased array system gain ($G_{Ja} \times G_{aJaTx}$) for $J/S = 10$ dB is 58 dB. Table 1.2 shows four configurations of progressive phase shift that will result in a maximum scanning angle for 6, 9, 12 GHz for an array of isotropic radiators, uniform excitation and distance distance between elements of 25 mm. The coverage ranges on the horizon line and at a distance of 30 km. The information obtained in the table combined with link budget calculations is key for the definition of beamformer topology, and thus for the components associated with beam steering functionality.

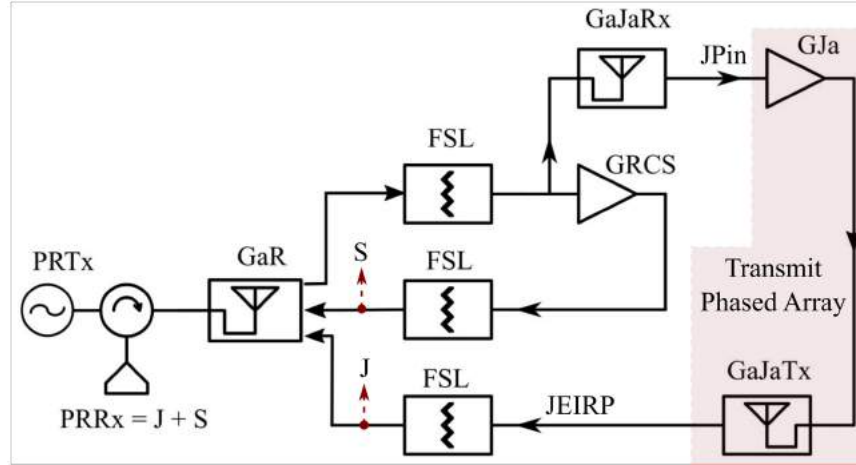


Figure 1.7: Jamming radio link budget schematics used to evaluate phase shifter, minimum scan and loss requirements over frequency.

Table 1.2: Estimated beam steering angle for different progressive phase shift configuration applied to the spatial power combiner of chapter 3 for 6, 9, 12 GHz, and respective horizon coverage for each scenario.

Phase excitation at each element (°)	Beam steering angle (°) / Horizon coverage at 30 km distance (km)		
	6 GHz	9 GHz	12 GHz
0/15/30/45	8.0 / 4.2	3.0 / 1.6	2.0 / 1.0
0/30/60/90	14.0 / 7.3	6.0 / 3.1	4.5 / 2.4
0/60/120/180	24.0 / 12.2	11.5 / 6	9 / 4.7
0/75/150/225	27.5 / 13.9	14.0 / 7.3	11.0 / 5.7

As a result of the above discussion, some notional specifications were set as a guideline for the research approach. Since the usual 2–18 GHz EW band is almost a decade wide and very challenging, we consider first an octave contained within this band, namely the 6–12 GHz band. We choose an antenna element that can meet the octave bandwidth match, pattern and lattice spacing. An element-level initial power level of 1-2 W is a good initial goal, since a 4-element array would give on the order of 50 dBm for the EIRP. Table 1.3 shows further details on the specifications that guide this work.

Table 1.3: Table with initial array design specifications.

Parameter	Range	Unit	Other requirements / comments
System			
Frequency	6–12	GHz	
EIRP	50	dBm	
RF Input	0-10	dBm	Single input.
Minimum steering angle	7.5	deg	Continuous, electronically controlled.
Radiating subsystem			
Antenna element type	Broadband		<ul style="list-style-type: none"> - High gain > 5 dBi (preferred). - High X-pol. - RP symmetry at main planes in between +/- 30 deg. - Integratable with MMICs. - Provides heat sinking.
Antenna element size	< 25 x 25	mm ²	lambda0/2 at 6 GHz.
Array size	4 X 1	elements	Minimal array size to demonstrate required functionalities.
Maximum distance between elements	25 mm		
Beamforming subsystem			
Corporate feed network	1 input 4 outputs		<ul style="list-style-type: none"> - Minimal phase and amplitude imbalance. - Isolation between ports >15 dB is desired.
Progressive phase shift component	0-225	deg	<ul style="list-style-type: none"> - Voltage-controlled phase shifting. - Insertion loss between 4 and 8 dB over BW. - Low variation of insertion loss and matching control voltages.
Pre-amplifier gain	20	dB	Linear at output power levels close to 20 dBm.
Power amplifier gain	15	dB	<ul style="list-style-type: none"> - Output power > 33 dB at 1-dB saturation point. - PAE > 25% (matched). - MMICs with preferably one bias and one supply pad.

1.6 THESIS GOALS AND ORGANIZATION

This thesis has two parts with a common theme of broadband microwave circuit and antenna co-simulation and co-design for phased array front ends, where the prefix “co-” implies linear and nonlinear circuit, and full-wave electromagnetic methods. The thesis is organized around a 6–12 GHz 4-element, dielectric-loaded ridge horn active linear array, which is designed to be scalable, shown in Fig.1.6. A broadband ridge-waveguide small-aperture horn element with transitions to microstrip enables direct MMIC integration in the antenna assembly with a low-resistance thermal path. GaAs MMIC phase shifters and GaN MMIC PAs are used as the active elements. Distributed scaling across sub-arrays is enabled by an element-based architecture, to overcome the electronics limitations driven by tighter prime power budgets and reduced form factors of smaller unmanned system classes. The architecture is modular and scalable in terms of power per element and number of elements.

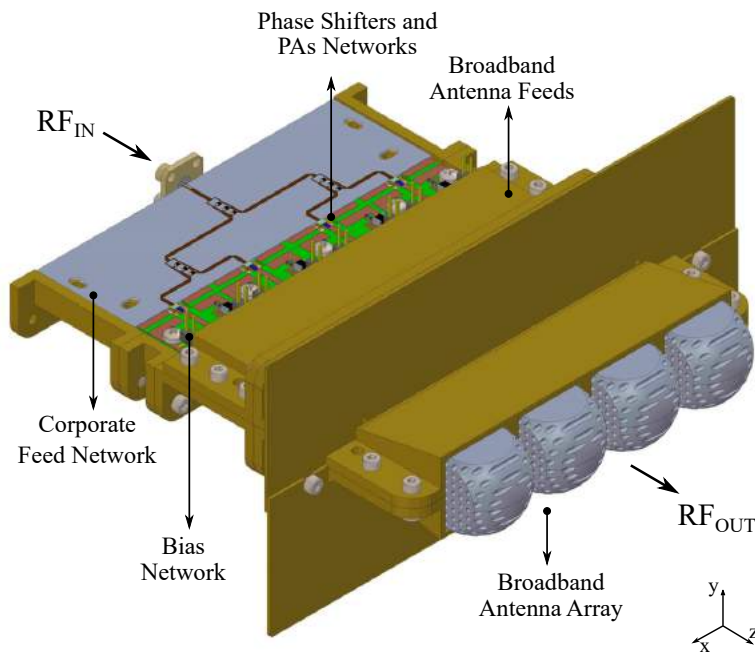


Figure 1.8: 4×1 dielectric-loaded ridge horn active linear array geometry, where the input port (P_{IN}) is connected to a Wilkinson divider corporate network feeding broadband GaAs phase shifter and 6–12,GHz 2-W GaN power amplifiers.

The thesis is organized as follows.

- Chapter 2 shows design and measurements of the active sub-array fundamental part: the radiating element with the microstrip-to-waveguide transition and power amplifier MMIC.
- Chapter 3 details the 4×1 spatial power combiner array design, including a broadband Wilkinson divider feed network, expected radiation patterns, as well as measured array performance when the 4 elements are fed in phase.
- Chapter 4 details the co-simulated performance of the active beam-steering network and phase-shifter, steering angle versus progressive phase shift (PPS), and analysis of coupling effects as a function of PPS and supply-voltage amplitude tapering.
- In Chapter 5, background in simultaneous transmit-and-receive arrays is given, and integration is discussed, particularly the trade-offs in component design for octave bandwidth operation.
- Chapters 6, 7 and 8 present analysis, design and characterization of three types of circulators with a goal of integration into an array. Chapter 6 show design and measurement of ferrite circulators that use different magnetic biasing approaches to achieve miniaturization and reconfigurable bandwidth, while Chapter 7 shows some initial results in self-magnetized circulators that can potentially be integrated with MMICs.
- Chapter 8 shows a broadband GaAs MMIC full-circulator design. The performance of this circulator in a phased array environment is simulated statistically, and design improvements are a topic of future work described in Chapter 9. Other research topics that are initiated by this thesis include power scaling, distributed supply modulation, design for improved thermal performance, a broadband matching approach for PA MMICs, and a bias-switched integrated PA and LNA. Finally the thesis concludes with a summary of contributions.

CHAPTER 2

ACTIVE ANTENNA ELEMENT DESIGN

CONTENTS

2.1	CHAPTER INTRODUCTION	21
2.2	PASSIVE ANTENNA DESIGN	22
2.3	ACTIVE ANTENNA ELEMENT DESIGN	29
2.4	CHAPTER CONTRIBUTIONS AND CONCLUSION	37

2.1 CHAPTER INTRODUCTION

Antenna arrays that cover octave bandwidths require broadband elements with a geometry that takes into account the element-to-element spacing tradeoff between coupling and array factor effects. Traditional wideband elements, such as Vivaldi endfire tapered slots, can cover bandwidths ($>5:1$), as described in [66]. On the other hand, ridge horns typically cover less BW ($>2:1$, e.g. [67]), but have higher power handling and heat dissipation properties, which is desired for transmit arrays with integrated beamforming networks. A 4-10 GHz open ridge waveguide array is presented in [68], and an X-band dual-polarized open-ended ridge waveguide monopulse array is shown in [69]. Millimeter-wave circular corrugated horn arrays with greater than octave bandwidths from 120-270 GHz and 80-180 GHz are demonstrated in [70].

This chapter presents the design and characterization of an octave-bandwidth, small-aperture, linearly-polarized, high-gain active horn antenna, operating in the 6-12 GHz, shown in Fig.2.1. The feed network hybridly integrates a 2-W MMIC PA and its biasing network. The active element demonstrates a system gain between about 21 and 30 dB over the octave band for 12 dBm of input power at 24 V supply voltage.

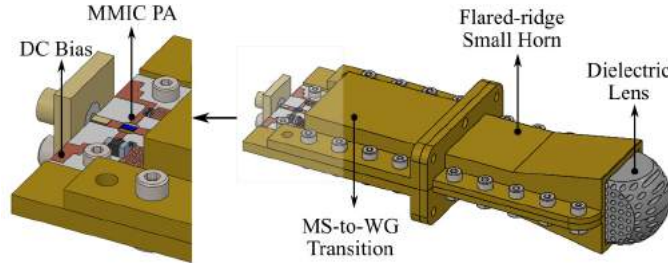


Figure 2.1: Active antenna element geometry, showing the MMIC PA bonded to the microstrip circuit and the microstrip-to-waveguide transition feeding the ridge horn.

The physical aperture size of the small horn element is a tradeoff between bandwidth due to ridge waveguide cutoff frequency at the lower end, and grating lobe appearance at the higher frequency end. These constraints affect the input reflection coefficient, which load-pulls the power amplifier (PA) integrated in the feed network. This in turn will change the PA and active system. The load-pulled, nonlinear system performance is estimated from Cadence AWR Microwave Office (MWO) harmonic-balance (HB) and Ansys HFSS full-wave co-simulations.

2.2 PASSIVE ANTENNA DESIGN

The radiating element is an E-plane flared horn with an exponential double ridge fed by a low-loss waveguide-to-microstrip transition 2.2, eliminating the need for additional connections between the antenna elements and the beamforming and amplification circuits. The horn is loaded with a synthesized dielectric with $1 < \epsilon_r < 2.2$, which lowers the cutoff frequency and improves phase distribution over the aperture, and therefore the radiation pattern.

The lens and feed loading structure are designed together to improve matching without degrading the radiation pattern. The antenna element is designed to enable straightforward integration with active transmit/receive components, with a feed that includes a low-loss double-ridge waveguide-to-microstrip

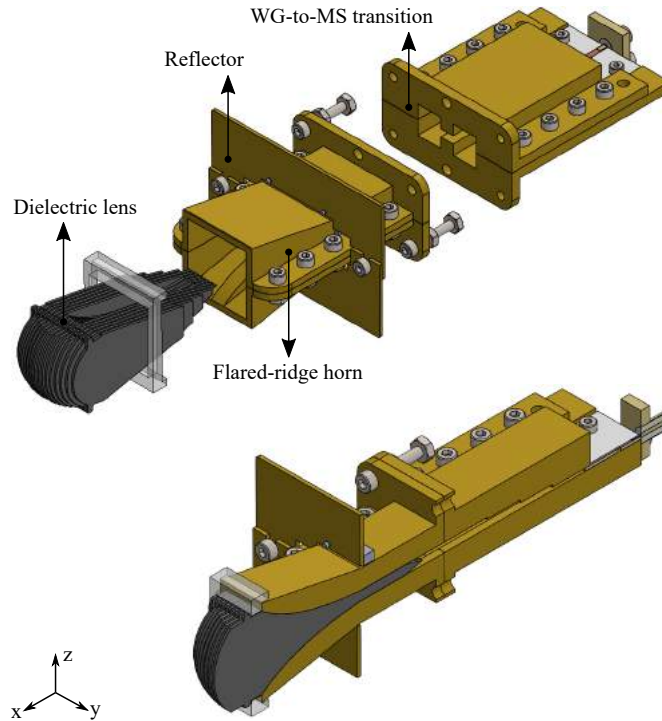


Figure 2.2: Passive double-ridge horn antenna element with WG-to-MS transition. The antenna is linearly polarized with the electric field in the z direction.

transition [71]. The aperture is a square of size $a = 21.27$ mm, which is about $\lambda_0/2$ at the lower edge of the band and λ_0 at the upper edge. Figure 2.2 shows the main parts of the single linearly-polarized antenna element. A cross-sectional view in the xz -plane describes the final assembly with transition, flare and lens details. A prototype is fabricated in brass using split-block machining, and the lens is machined from 16 parallel dielectric slabs 0.762 mm thick with $\epsilon_r = 2.2$. The measurements are performed with the integrated microstrip transition.

2.2.1 RIDGE WAVEGUIDE FEED AND AIR-FILLED HORN

This subsection discusses aspects of waveguide feed selection. Next, the limitations of an air-filled linearly flared horn related to the lower-frequency limit are discussed, leading to the design approach and final geometry of the passive radiating element. Standard rectangular waveguides do not cover an octave, resulting in a choice of a ridge waveguide feed which reduces the fundamental mode cutoff frequency. Single, double and quad ridge waveguides have all been shown to increase bandwidth, e.g. [72] [73]. A

double-ridge waveguide feed is chosen as a tradeoff between complexity and radiation pattern symmetry of the horn. Fig.2.3 shows the dominant mode fractional bandwidth of a parametric simulation for waveguide sizes $a_{wg} = 21.27$ and $b_{wg} = 9.9$ mm, where the two symmetrical ridge widths and heights are varied. From the plot, $w_{rg} = 4.47$ mm and $h_{rg} = 3.63$ mm are manufacturable and result in the largest ratio of the lower cutoff frequency to the frequency where the next higher order mode starts propagating.

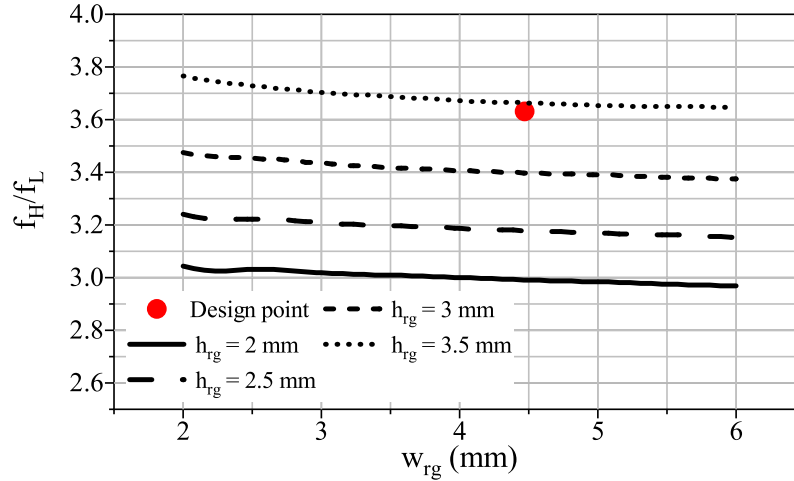


Figure 2.3: Dominant mode fractional bandwidth as a function of ridge height h_{rg} and ridge widths w_{rg} .

As a starting point, the feed is flared with a linear ridge taper for a compact air-filled horn element. An air-filled horn will have a reduced bandwidth compared to the feed itself, following the reasoning in [74] for a standard rectangular waveguide. This can be understood from the dominant-mode impedance and normalized guided wavelength for this specific double-ridge design, shown in Fig. 2.4, as simulated using *Ansys HFSS*. The wave impedance is calculated by integrating the transverse electric field of the fundamental mode to find the voltage ($Z_{wave} = V^2/P$). The dispersive wave impedance, which varies from 160-120 Ω in the 6-12 GHz range, leads to the first design constraint. Namely, the horn has to match this waveguide impedance to the constant 377- Ω free-space impedance. The second constraint can be inferred from the normalized guided wavelength (dashed line in Fig.2.4). A well-matched antenna requires reducing the guided wavelength in the lower part of the band to maintain a constant normalized propagation constant and therefore delay.

The feed from Fig.2.4 is next flared with a linear taper. To understand the performance limitations of a small-aperture air-filled horn, we plot the reflection coefficient as a function of the horn length h for a

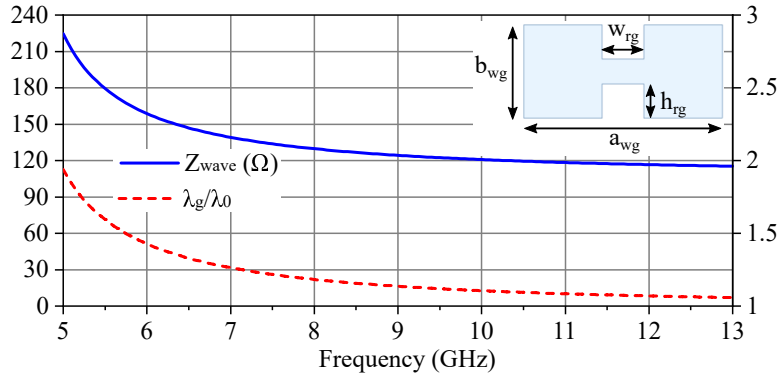


Figure 2.4: Simulated ridge waveguide wave impedance (Z_{wave}) and normalized guided wavelength (λ_g/λ_0) used for the design.

constant square aperture size of $a = 21.27$ mm. Fig. 2.5 shows the de-embedded reflection coefficient from port P_1 to port P_2 when loaded with an air-filled, E-Plane flared horn, for various values of horn height h . The waveguide feed length is 50 mm. One can observe that the cut-off frequency does not significantly vary with changes in the horn length, and we address this in the next section.

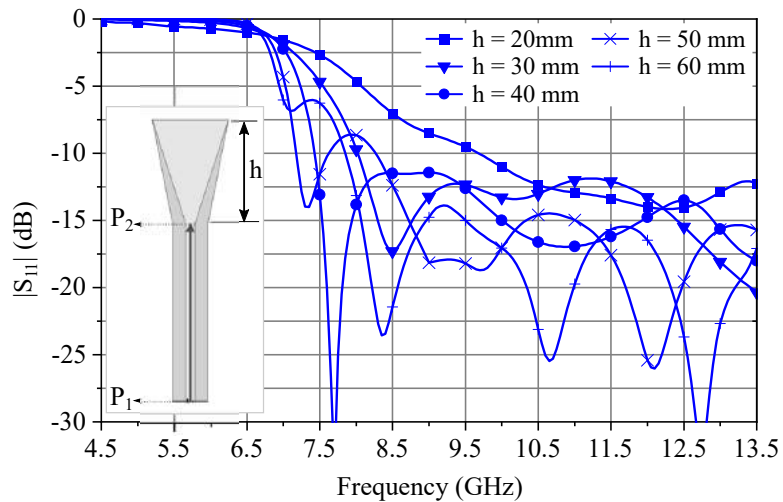


Figure 2.5: Reflection coefficient magnitude at waveguide feed (P_2) for different horn lengths, for a constant square aperture size $a = 21.27$ mm.

2.2.2 EXPONENTIALLY-FLARED DIELECTRIC-LOADED SMALL-APERTURE HORN

Aperture efficiency enhancement of small horns by PTFE loading is shown in [75], with an application to limited scan-angle arrays. Dielectric loading of circular and rectangular horns is also discussed in [76] and [77] for improving radiation patterns. In [78], it is shown that dielectric loading can improve the reflection

coefficient of a horn array. A short horn using low-loss anisotropic meta-material transverse loading is shown to improve gain in [79]. In an analogous manner, in order to improve the match at the waveguide feed of the horn from Fig.2.2, an exponential taper of the ridge is introduced, with a final profile obtained with *Ansys HFSS* simulations. Figure.2.6a shows the horn cross-sections in the xz and yz cuts. The aperture size is 21.27 mm, corresponding to $0.425 \lambda_0$, $0.638 \lambda_0$, and $0.851 \lambda_0$ at $f_0 = 6, 9, 12$ GHz, respectively. Because this antenna element is designed for an active transmit array, a design that allows air flow is preferable. This is obtained by replacing the solid $\epsilon_r = 1.6$ dielectric lens by a mechanically synthesized one build from 16 parallel dielectric slabs of Rogers Duroid RT5880, $\epsilon_r = 2.2$, 0.762-mm thick, and spaced 0.55 mm apart, shown in Fig. 2.6b.

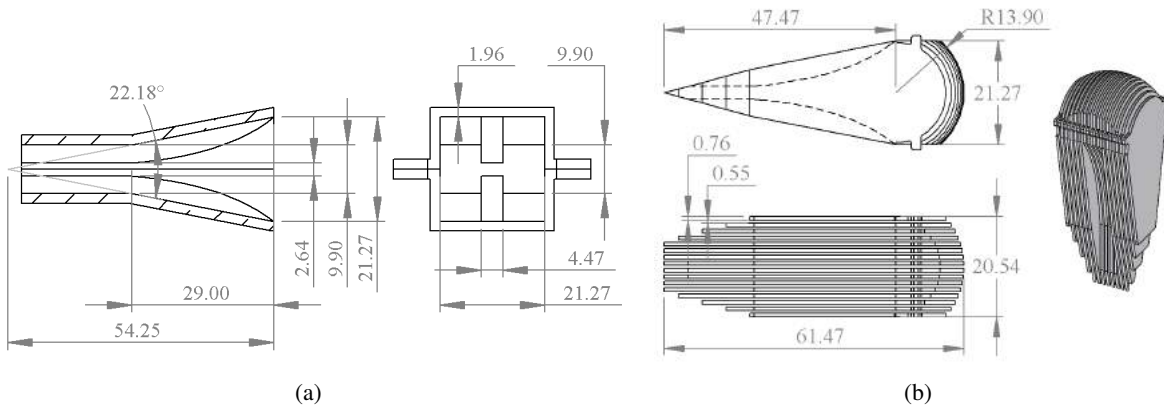


Figure 2.6: (a) Exponentially-tapered horn dimensions, and (b) lens geometry (dimensions in mm).

To understand how the taper, dielectric filling of the feed and the dielectric lens impact antenna performance, we next show the evolution of the design that achieves an improvement in impedance bandwidth at the lower frequency end without radiation pattern degradation. Figure 2.7 gives a comparison between the air-filled linear (solid black line) and exponential (dashed line) tapers, showing an improved match at the lower frequency end. Further improvement is obtained with a solid dielectric filling with a flat aperture surface and, slab filled exponential taper then the final design with lens incorporated to the dielectric structure.

The replacement of a solid filled exponential taper with $\epsilon_r = 1.6$ and the slab filled exponential taper show very similar performance in return loss. Finally, instead of a planar aperture, the dielectric slabs are extended to form a lens (Fig.2.2), and this further improves the match across the band (red line in Fig.2.7).

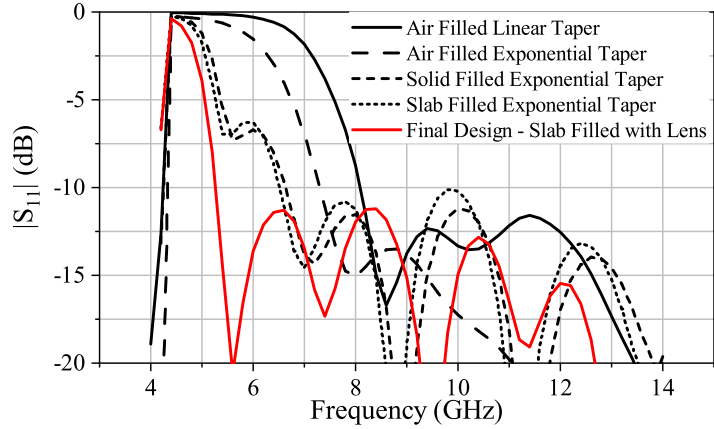


Figure 2.7: Comparing $|S_{11}|$ for each of the design steps from a linearly flared air filled horn towards a horn loaded with $\epsilon_r = 2.2$ slabs and lens.

Normalized H-plane radiation patterns in Fig.2.8 compare the first and final designs at 6 and 12 GHz. At the lower frequencies, performance was improved in the final design due to the better matching from the addition of the loading and lens. At the higher frequencies, there was also an increase in gain as large as 1.7 dB at 9 GHz.

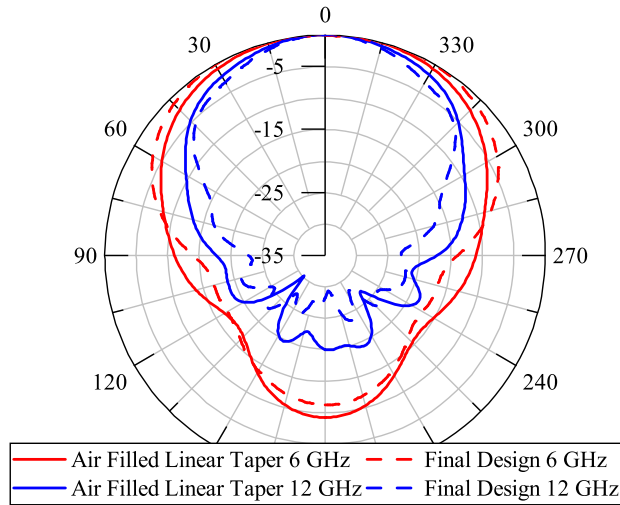


Figure 2.8: Simulated H-plane radiation patterns at 6 GHz and 12 GHz for the linear air filled horn compared to the final design with dielectric loading and lens.

2.2.3 INTEGRATION WITH MS-TO-WG TRANSITION

The WG-to-MS transition design used for integration with an active array is detailed in [71], with geometry shown in Fig.2.9. A comparison between simulated $|S_{11}|$ over bandwidth of the horn with (solid) and without (dashed) coaxial-to-microstrip-to-waveguide transition shows a final VSWR=2 BW from 5.2 to 12.7 GHz, plotted in Fig. 2.10. The degradation above 12.5 GHz is due to the coaxial-to-microstrip transition mismatch. Furthermore, an increased back radiation the E plane around 250° is expected based on the results in [71], and is due to the open microstrip transition.

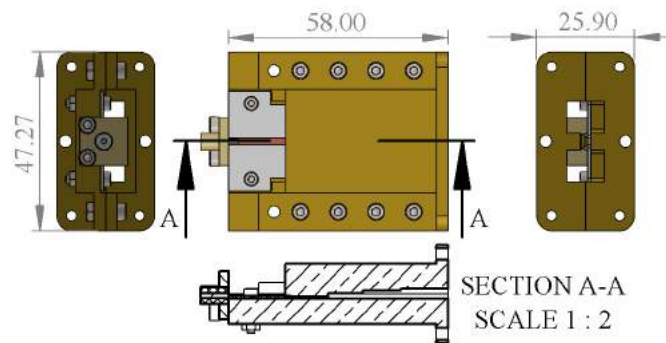


Figure 2.9: Geometry of the microstrip to single-ridge waveguide transition described in detail in [71]. The dimensions are given in mm.

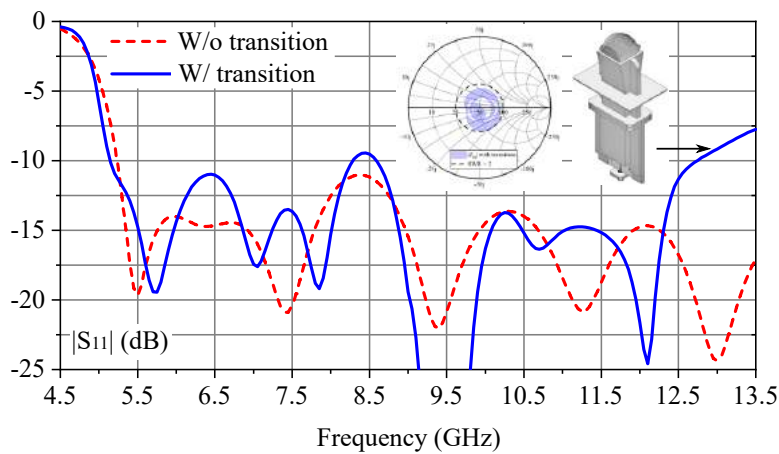


Figure 2.10: Simulated $|S_{11}|$ over bandwidth of horn with (solid) and without (dashed) coaxial-to-microstrip-to-waveguide transition.

Figure 2.11 shows the measured and simulated $|S_{11}|$ (top) and gain (bottom) of the passive antenna element. As expected, the measured $|S_{11}|$ deviation from simulation is more pronounced at higher frequen-

cies, as is the difference between the two measured prototypes. Nonetheless the measured input reflection coefficient is below -9 dB over the entire range for both prototypes, following the simulated performance. The gain was measured in an in-house built anechoic chamber, using the two prototypes and assuming the gains are the same. A photograph of one of the prototypes is shown in the inset. In the measurement setup, the feed cable is in the 180° direction, contributing to reflections and errors in the back lobe data, which is seen e.g. in the 6-GHz measured patterns at that angle. The measured radiation patterns compared to simulated ones are shown in Fig.2.12.

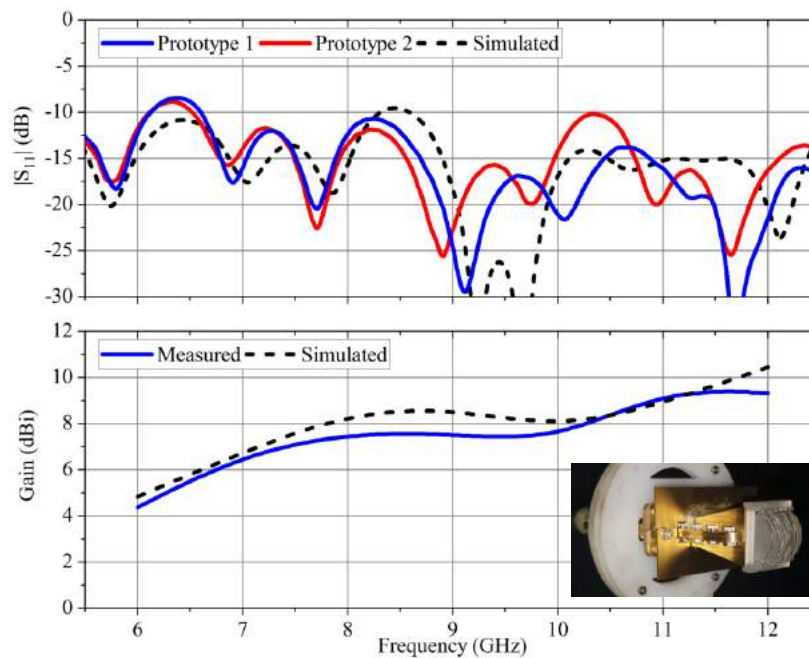


Figure 2.11: Measured and simulated $|S_{11}|$ (top) and gain (bottom) of the passive antenna element.

2.3 ACTIVE ANTENNA ELEMENT DESIGN

This subsection presents the design and characterization of octave-bandwidth, small-aperture, linearly-polarized, high-gain active horn antenna, operating in the 6-12 GHz, shown in Fig.2.13. The feed network hybridly integrates a 2-W TGA2598 GaN MMIC PA and biasing network. The PA is fabricated in the Qorvo 0.25- μ m GaN on SiC process, with a specified P_{SAT} = 33 dBm, PAE > 30% @ 50- Ω , 21 dB small signal gain and IM3 < -17 dB @ 28 dBm per tone over 6–12 GHz. The PA is first characterized in subsection 2.3.1

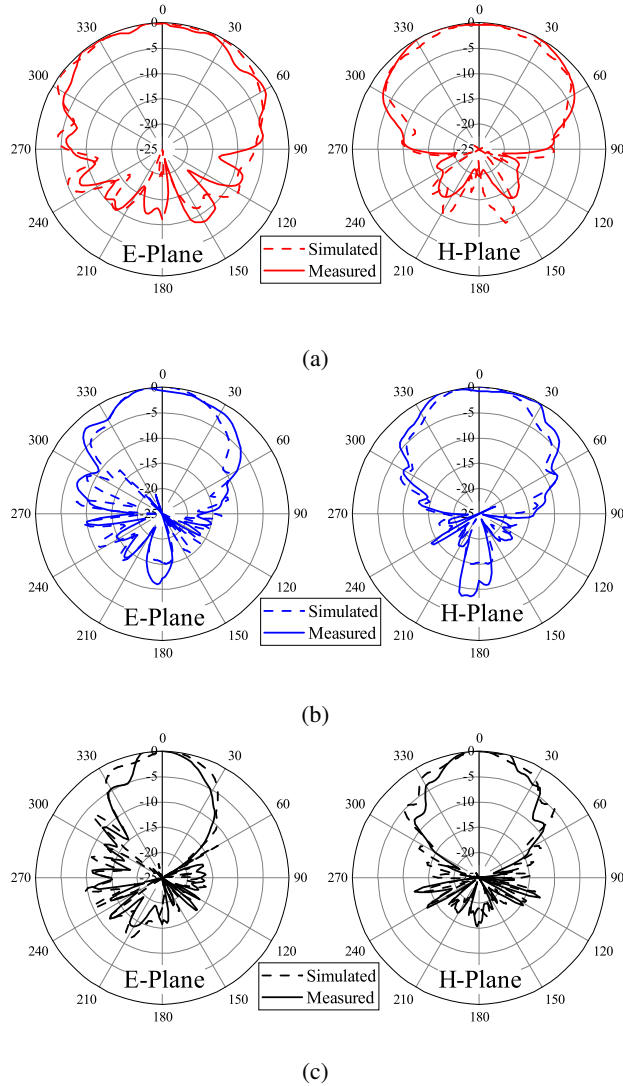


Figure 2.12: Measured (solid) and simulated (dashed) E- and H-plane radiation patterns at (a) 6 GHz, (b) 9 GHz, and (b) 12 GHz. The antenna is linearly polarized with a simulated cross-polarization ratio of 25 dB.

with harmonic balance simulations, using a X-Parameters based nonlinear model provided by the foundry. Subsection 2.3.2 describes active antenna integration details, system CW simulation and measurements. The X-parameter model is limited in frequency from 5–13 GHz (CW, 1-Tone), $P_{IN} = [-10, 24]$ dBm and $V_{DD} = [10, 24]$ V.

2.3.1 POWER AMPLIFIER CW CHARACTERIZATION

For estimating performance boundaries of the selected PA over frequency, power, drain voltage and output load impedance, HB simulations are carried out in MWO and described in Fig. 2.14. The RF source

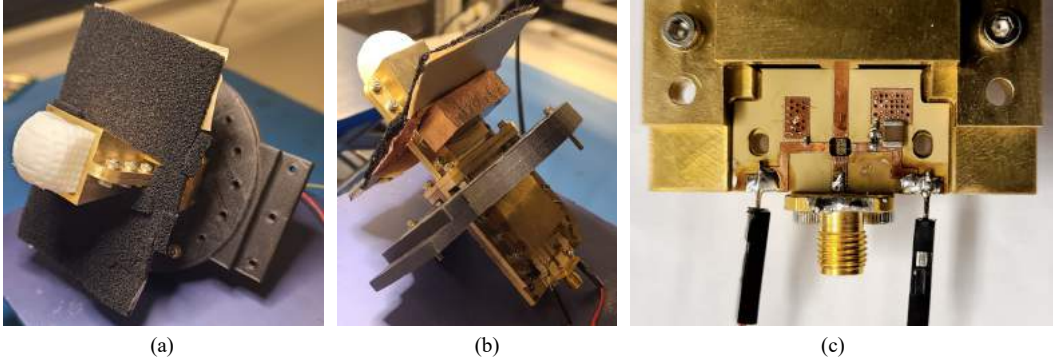


Figure 2.13: Active antenna element prototype. (a) Front view. (b) Back view. (c) MMIC PA and bias circuit close-up.

(P_{IN}) is varied to emulate back-off under signal transmission and amplitude tapering effects. The drain supply voltage (V_{DD}) is also varied to emulate slow supply modulation for PA efficiency enhancement for $V_{DD} = 10\text{--}24\text{ V}$. The output tuner models changes in antenna impedance in an array environment, over scan angle and bandwidth. The output reflection coefficient lies inside the $VSWR < 2.5$ circle, a smaller value than suggested by [80], since the expected scanning angles of the array design under study are smaller than 60° .

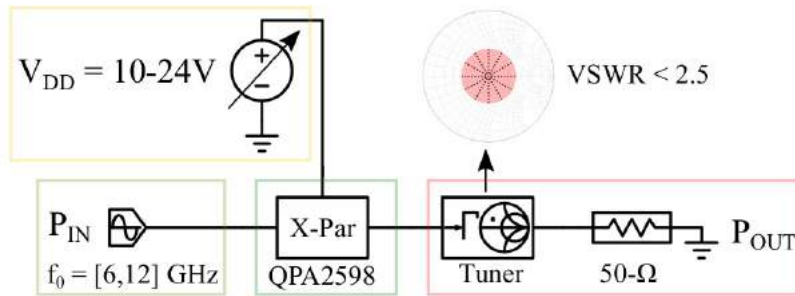


Figure 2.14: Schematics of load-pull simulations of Qorvo TGA2598 using measured X-parameters provided by the manufacturer.

Fig.2.15 shows simulated load-pull PAE at $\{6, 9, 12\}$ GHz $V_{DD} = \{10, 24\}$ V, within $VSWR \leq 2.5$. It is observed that the peak PAE moves to the edges of the VSWR circle with increasing frequency, although we would expect that the MMIC operates best at $50\ \Omega$. On the other hand, the plots suggest that the design was tuned for presenting a flat PAE close to 30% over the octave bandwidth. Further, between two bias points, the region of best efficiency moves dramatically. For example, at 6 GHz, the impedance for best efficiency at

$V_{DD} = 24$ V is inductive, while it becomes capacitive at the lower bias.

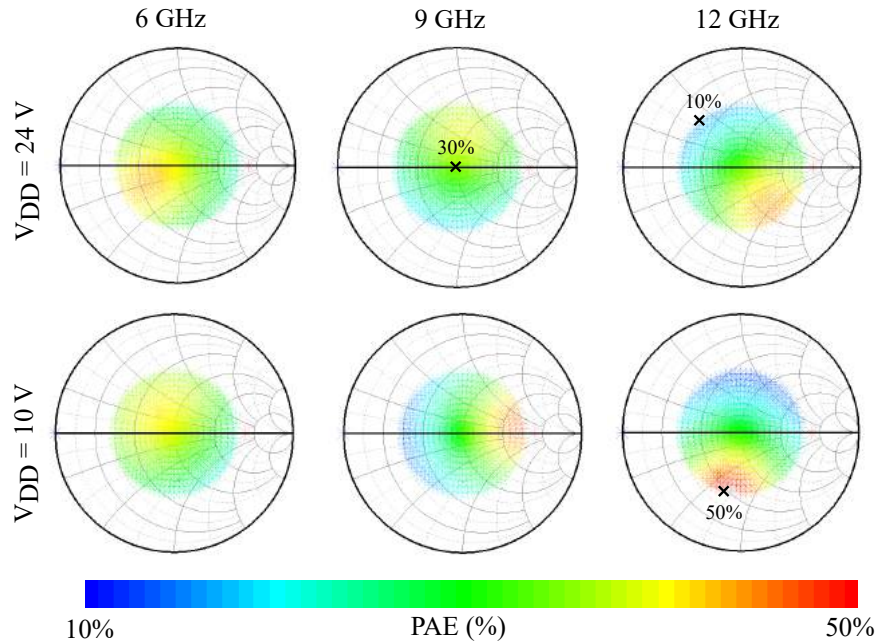


Figure 2.15: Simulated PAE at $P_{IN} = 19$ dBm, $\{6, 9, 12\}$ GHz for $V_{DD} = 24$ V (top) and 10 V (bottom).

Figure 2.16a shows the simulated range of P_{OUT} P_{GAIN} . The solid and dashed lines show the maximum and minimum parameter values for the range of Γ_{OUT} and $f_0 = [6, 12]$ GHz. Blue plots show the simulated performance for $V_{DD} = 10$ V and red for $V_{DD} = 24$ V. An overall decrease in power gain and output power is observed for the same input power as V_{DD} decreases, as expected. This behavior can be used as a second tuning parameter for array tapering, the first being supply voltage. The compression point appears to evenly move with drain voltage changes, which indicates that it is possible to implement a systematic optimization of PAE over different tapering scenarios.

Simulated power-added efficiency PAE is shown in Fig. 2.16b. The shaded areas show variation over the octave band, 6–12 GHz and for $VSWR = \leq 2.5$ for $V_{DD} = 10$ V (blue) and $V_{DD} = 24$ V (red). Filled marker traces show the best case, and hollow markers the worst case. The dotted lines shows the PAE when the PA is matched. One can observe that higher PAE values occur for $V_{DD} = 10$ V, which indicates that the device was design for improved performance at back-off operation. Furthermore, the variation in PAE with drain voltage changes indicates the potential of using slow supply modulation to enhance efficiency.

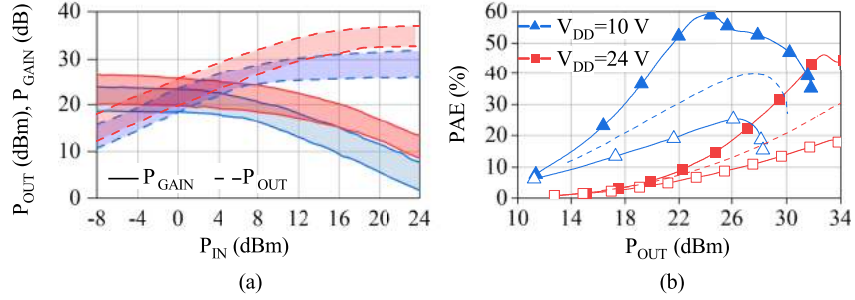


Figure 2.16: (a) Simulated MMIC PA output power and power gain, over input power. The shaded areas show variation over 6–12 GHz. The VSWR of the load is kept ≤ 2.5 . Two supply voltages are shown: $V_{DD} = 10$ V (blue) and 24 V (red). (b) PAE range for same same frequency and impedance variation as in (a).

2.3.2 ACTIVE ANTENNA INTEGRATION, SIMULATION AND MEASUREMENTS

The active transmit element shown in Fig.2.1 is a structure that connects a modified version of the passive antenna design presented in [81] followed by a Qorvo TGA2598 GaN MMIC PA. Figure 2.17 illustrates the analysis method used for obtaining EIRP of the active antenna element. First, the radiating three-dimensional structure is divided into two parts at the plane where the power amplifier is inserted, and the two independent structures are full-wave simulated (with Ansys HFSS). The S-parameters of the coaxial-to-microstrip transition and the antenna with the microstrip-to-waveguide feed are imported into a nonlinear circuit simulator (Cadence AWR), where the complex voltage excitations over input power, bandwidth, and various drain voltages are calculated. The radiating structure efficiency varies over bandwidth due to absorbers added for sidelobe level and back radiation reduction. The voltage at the feed point of the radiating element is fed back to the full-wave simulator for post-processing to find the total radiated power and maximum gain.

An over-the-air (OTA) measurement is used to characterize the active element with the MMIC initially biased at $V_{DD} = 25$ V and $I_{DQ} = 70$ mA with a gate bias of -2.5 V. Figure 2.18 shows the schematics and setup photograph. First the passive element absolute gain is measured using the three antenna method described in [62], and then used for indirect gain and PAE calculations.

The active element system gain (Fig.2.19) over bandwidth for (a) $P_{IN} = 8$ dBm, (b) $P_{IN} = 14$ dBm (b), and (c) $P_{IN} = 19$ dBm at $V_{DD} = \{10, 18, 24\}$ V is compared to the passive element gain (purple). The insets

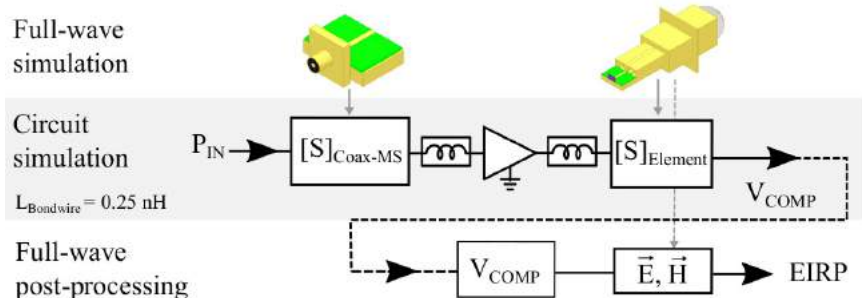


Figure 2.17: Procedure for EIRP estimation of the active antenna element. First, the radiating structure is divided into two parts at the plane where the power amplifier is inserted, and the two independent three-dimensional structures are full-wave simulated with HFSS. The S-parameters are then transferred to a nonlinear circuit simulator (AWR) allowing determination of the complex voltage excitation as a function of input power, supply, etc. This voltage is fed back into the full-wave simulator for calculating the total radiated field.

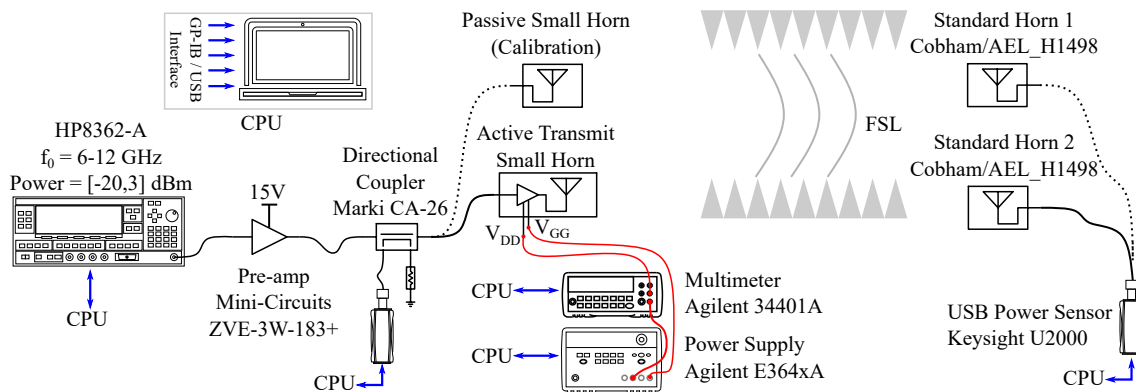


Figure 2.18: Active element measurement setup. To determine the active element system gain, P_{IN} is measured at the input of the passive antenna (dotted line) and active antenna, by calibrating all losses and gains in the input chain over the octave band. The output power is measured and the receiving antennas and feeds de-embedded.

show the average measured input power at the antenna SMA connector. It is observed that input power does not change considerably with V_{DD} , which suggests that input matching remains reasonably constant for different supply conditions.

The measured active element system gain has a larger variation over V_{DD} range for lower input powers. It is nonuniform over frequency and V_{DD} . The system gain varies by 6 dB at 6 GHz and around 10 dB at 11 GHz. As the PA approaches compression, system gains for $V_{DD} = 18$ and $V_{DD} = 24$ V are almost the same.

Figure 2.20 shows the PA output power and power gain over input power, obtained from $50 - \Omega$, on-

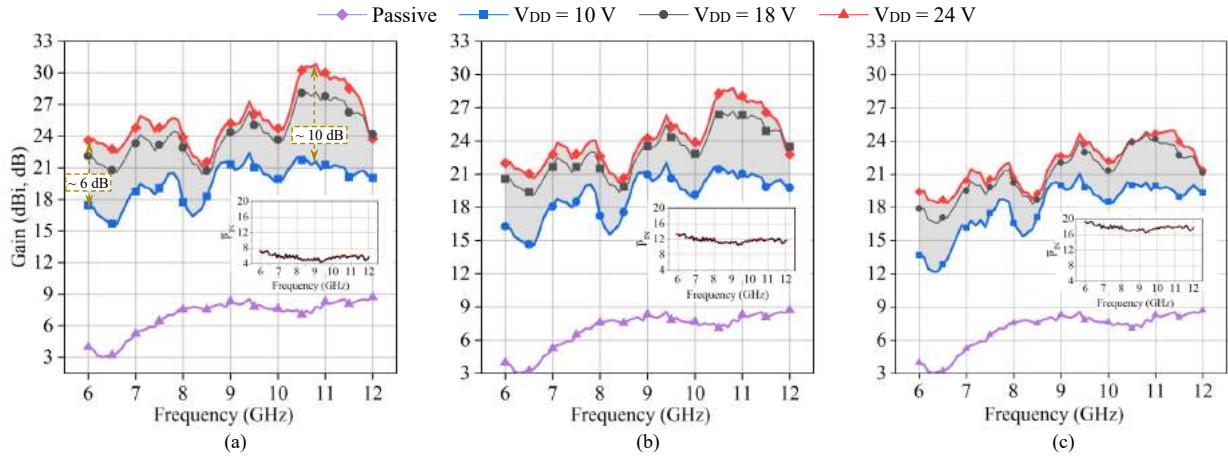


Figure 2.19: Measured active element system gain over frequency for $P_{IN} = \{8, 14, 19\}$ dBm and $V_{DD} = \{10, 18, 24\}$ V. The measured passive element gain is shown in purple.

wafer measurements (shaded area) and through the indirect over-the-air (OTA) measurement setup (solid colored lines). A better agreement between curves at 6 GHz and at smaller power levels is observed. The discrepancies become evident towards higher frequencies. Also, the on-wafer measurements were not as carefully calibrated, since the more relevant ones for an active antenna are over the air.

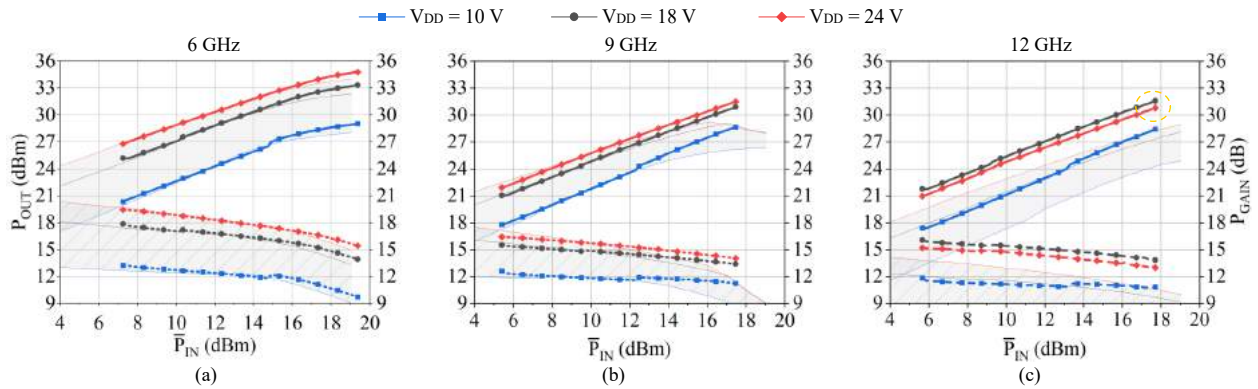


Figure 2.20: P_{OUT} and P_{GAIN} obtained through OTA (bold lines) and on-wafer measurements (shaded areas) at $\{6, 9, 12\}$ GHz.

The EIRP depends on how much power the PA is delivering to the antenna, which in turn depends on matching and nonlinear characteristics, as well as the antenna aperture efficiency, and thus maximum antenna element gain. The simulated EIRP over input power and frequency is shown in Fig. 2.21a for $V_{DD} = 10$ V, and in Fig. 2.21b for $V_{DD} = 24$ V. The corresponding measured parameters are plotted in Figs. 2.21c,d respectively. The agreement between simulated and measured results is better for $V_{DD} = 24$ V.

The discrepancies between simulated and measured results at $V_{DD} = 10$ V suggest that model accuracy degrades at lower supply voltages. It is also noted that the device starts to compress earlier around 11 GHz, agreeing with system gain calculations.

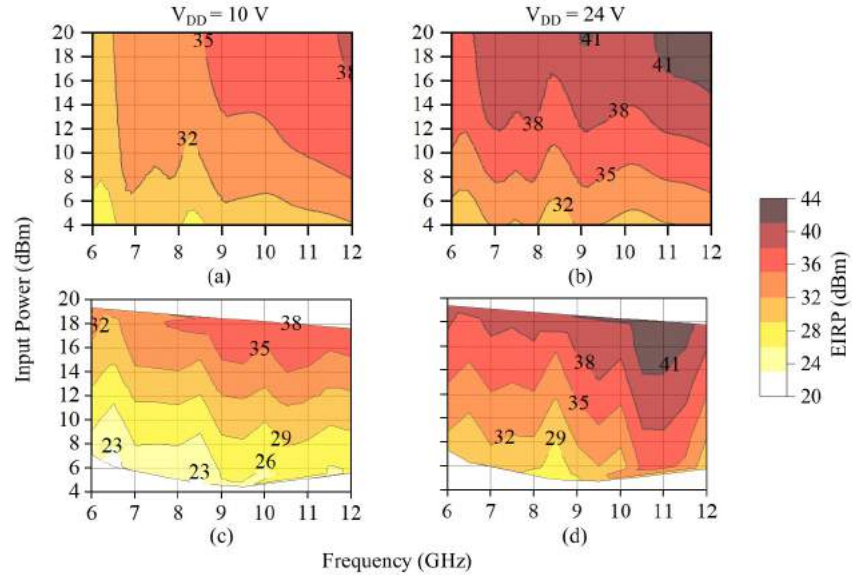


Figure 2.21: Simulated and measured effective isotropic radiated power (EIRP) over input power and frequency, for $V_{DD}=\{10,24\}$ V.

The simulated amplifier PAE over input power and frequency is obtained by using the procedure from Fig.2.17 with the antenna connected to the output of the PA. The results of the simulation are shown in Fig.2.22. Best average performance over frequency occurs around $P_{IN} = 10$ dBm and $V_{DD} = 10$ V, confirming that the circuit is likely designed for improved performance at power backoff.

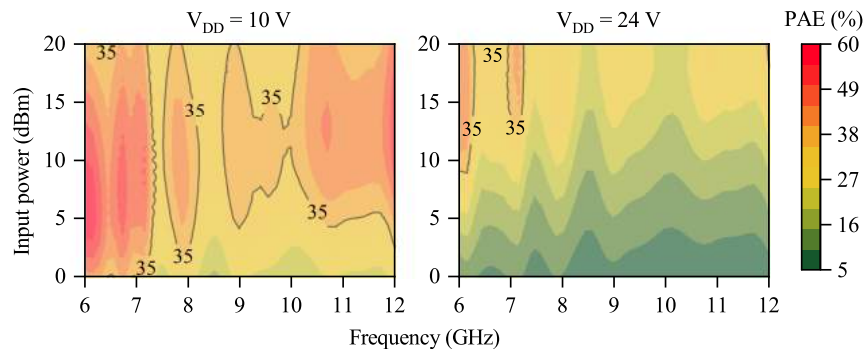


Figure 2.22: Simulated amplifier power-added efficiency (PAE) over input power and frequency, obtained from harmonic-balance (HB) simulations in AWR.

Figure 2.23 shows the measured and simulated PAE over output power for three drain supply voltages at three frequencies. The performance trends agree with the X-parameter MMIC PA model, but with an overall performance degradation, as expected. For instance, at 6 GHz and 10 V the maximum PAE drops from 60% (Fig.2.16) to 43% due to mismatch in the transitions and losses of the passives. The ripple over frequency is due to the horn input impedance variation over the octave bandwidth, as shown in [81]. Note that the peak efficiency moves to lower output powers as the drain supply voltage is reduced. This is exploited in later chapters in the context of sidelobe tapering of an array and maintaining efficiency in backoff when signals with varying PAPR are amplified.

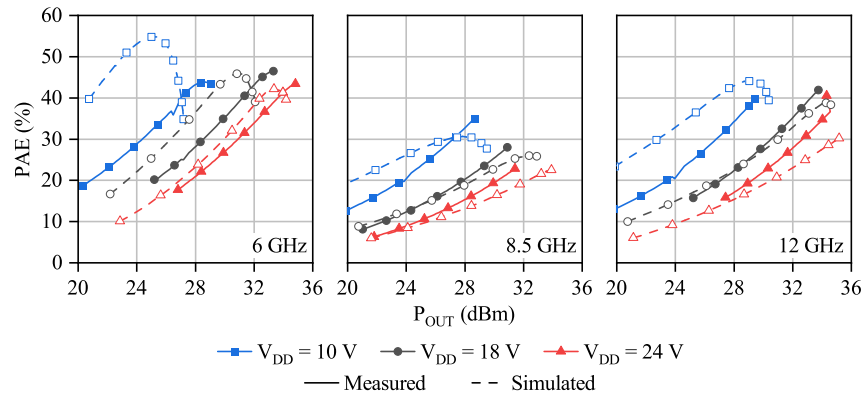


Figure 2.23: Measured amplifier power-added efficiency (PAE) over input power and frequency through OTA measurements.

2.4 CHAPTER CONTRIBUTIONS AND CONCLUSION

In conclusion, this chapter presents the design procedure, prototype construction and characterization of a small octave-bandwidth linearly-polarized transmit amplified horn antenna element, suitable for array integration. Related to the passive antenna design, Table 2.1 shows a comparison between passive horn antennas with similar bandwidths, concluding that the horn element presented in this chapter achieves comparable gain across an octave with a $0.56\lambda_0^2$ element spacing at the center frequency. The horn aperture efficiency depends on the illumination uniformity provided by the ridge horn geometry, dielectric loading and spherical lens, and it is indeed a hot topic for further exploration and improvement.

Table 2.1: Comparison with Similar Horns

Ref	Type	BW (GHz)	Aperture (λ_0^2)	Gain (dBi)
[69]	Open-ended WG	8 - 12	0.54	9.7 - 14
[82]	Horn fed by dipole array	1.5 - 4.5	8.9	11 - 20
[83]	Dielectric-loaded horn	8 - 16	29, conical	n/a
[84]	Metamaterial-loaded	3.7 - 7	7.28	16 - 24
[85]	3D-printed horn array	29 - 37	0.5	8
[81]	Ridge waveguide, dielectric-loaded horn	6 - 12	0.56	5 - 10

The feed is implemented in ridge waveguide and includes a transition to a 50- Ω microstrip line, allowing direct integration with active circuits with a common thermal and RF ground. A dielectric-slab lens extends the lower-frequency impedance matched region without significantly affecting the radiation pattern.

The active horn performance is simulated for varying drain supply voltages of the MMIC PA, and shows a performance trade-off between EIRP and PAE. The PAE is shown to be higher at lower drain voltages, which leads to lower active element system gain and EIRP. The active element EIRP with calibrated OTA measurements depends on the power delivered to the antenna by the PA, which in turn depends on matching and nonlinear characteristics of the PA. The EIRP also depends on antenna aperture efficiency, and thus maximum antenna gain.

The contributions contained in this chapter are published in [71], [81], [86] and [87] (accepted).

CHAPTER 3

SUPPLY-MODULATED SPATIAL POWER COMBINER

CONTENTS

3.1	CHAPTER INTRODUCTION	39
3.2	PASSIVE ARRAY DESIGN	40
3.3	SUPPLY-MODULATED SPATIAL POWER COMBINER	48
3.4	ACTIVE ARRAY PERFORMANCE UNDER MODULATED SIGNALS	53
3.5	CHAPTER CONTRIBUTIONS AND CONCLUSIONS	56

3.1 CHAPTER INTRODUCTION

In the previous chapter, the design and characterization of an active antenna element are presented. As the element is designed with an aperture size that is within a free-space wavelength at the highest frequency of the octave bandwidth, a 4-element transmit array, with all element fed in phase, is designed as a spatial power combiner. This chapter presents the analysis of this active octave-bandwidth transmit array, focusing on maintaining EIRP and efficiency across the band. Four GaN amplifier MMICs are fed with a broadband microstrip Wilkinson divider and power combine upon radiation from ridged-waveguide dielectric-loaded small-aperture horn antennas.

The supply voltage of individual MMIC PAs is used as a variable, quantifying how efficiency, power and linearity of the combiner depend on the dc drain voltages. The chapter presents a simulation and experimental study with CW and QAM-64 50-Mbaud modulated signals input to the combiner. Sidelobe level control with supply variation is also investigated and shows that it is possible to reduce sidelobes without significantly degrading EIRP. The array is shown in Fig.3.1 and is a simplified version of the phased array shown in Fig.1.6, where phase shifters and pre-amplifiers are not included.

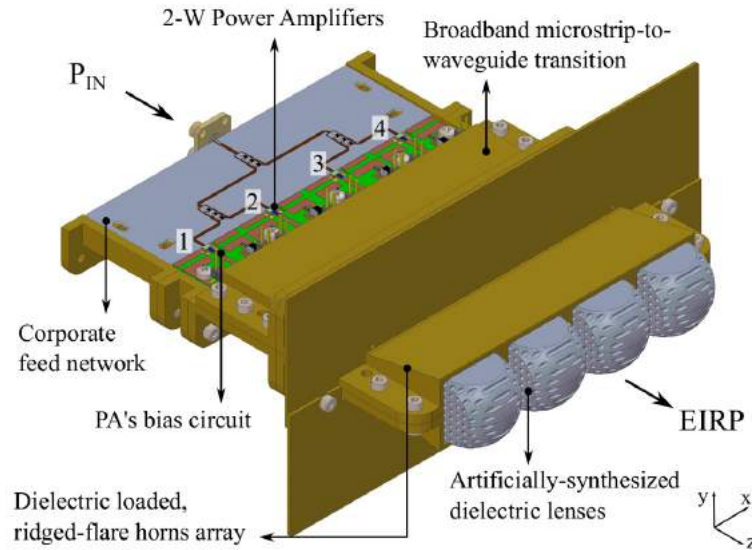


Figure 3.1: Spatial power combiner geometry. A corporate feed network, based on 6–12 GHz three-section Wilkinson dividers, feeds 4 active elements described in the previous chapter.

In Section 3.2, the passive array design and main results are presented. Section 3.3 shows the active spatial power combiner topology and prototype details, while Section 3.4 presents CW simulated and measured results. In Section 3.5, the system performance with modulated signals (2-tone and 64-QAM) is presented.

3.2 PASSIVE ARRAY DESIGN

The array element is the small ridged horn described in Chapter 2 and [81]. It is made of brass using split-block machining and connected with flanges. The aperture is a square with sides of 21.27 mm and the walls are 3-mm thick for mechanical stability. The array spatial sampling is $0.5\lambda_0$ @ 6 GHz and $1\lambda_0$ @ 12 GHz. The cutoff frequency of the element geometry limits the element/array operation in the lower

frequency range, while grating lobes limit the upper frequency of operation.

The array elements also have dielectric lenses, however to simplify the lens fabrication, a different artificial dielectric than the one in Chapter 2 and [81] is designed using bulk PTFE with $\epsilon_r = 2.1$. Air-filled sub-wavelength cylindrical holes are machined in the bulk PTFE. The average permittivity of the mechanically synthesized dielectric is calculated with eigenmode simulations in HFSS, by comparing the fundamental frequency of a 23.2 mm side, vacuum-filled a cubic cavity $f_0 = 8.76$ GHz to the same cube filled with the engineered material. The average permittivity is calculated from $\epsilon_{r,avg} = (f_0/f_1)^2$ and loss tangent calculated $\tan \delta = 1/Q_{factor}$ of the loaded cavity. Figure 3.2 shows the geometry of the material and relative permittivity and $\tan \delta$ as a function of cylindrical hole diameter.

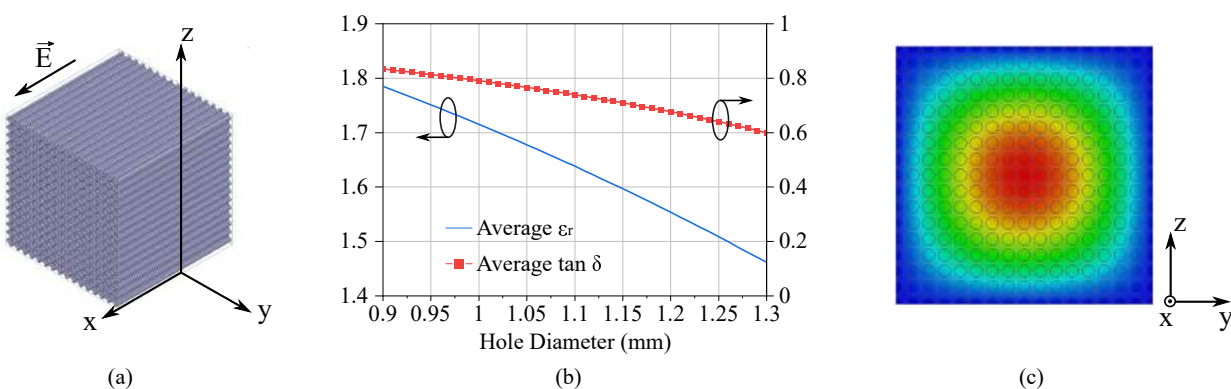


Figure 3.2: Eigenmode simulations of mechanically synthesized dielectric material. (a) Cavity in HFSS; (b) parametric plot of average ϵ_r and $\tan \delta$ versus holes diameter; (c) Total E-field magnitude distribution on yz -plane, inside the cavity. The electric field is aligned to x -axis.

Even though the 5D milling simplifies the array assembly, the imperfect drilling process resolution causes variation in the relative permittivity between lenses. Figure 3.3 shows active reflection coefficient variation for the inner and outer horn elements loaded with solid dielectric lenses with permittivity in the range $\epsilon_r = [1.6, 1.8]$ and with uniform in-phase excitation. The plot shows that the reflection coefficient is not sensitive to the relative permittivity within over 10% variation.

The array radiation patterns are improved by placing 3-mm thick material RF absorber layers on the reflector, microstrip-to waveguide transition back opening, and corporate power divider area, as shown in Fig.3.3(a). The prototype was built using Leader Tech EA-LF125-XX wideband RF absorber foam sheets. Figure 3.4 shows simulated, normalized, H- and E-plane radiation patterns of the passive array at

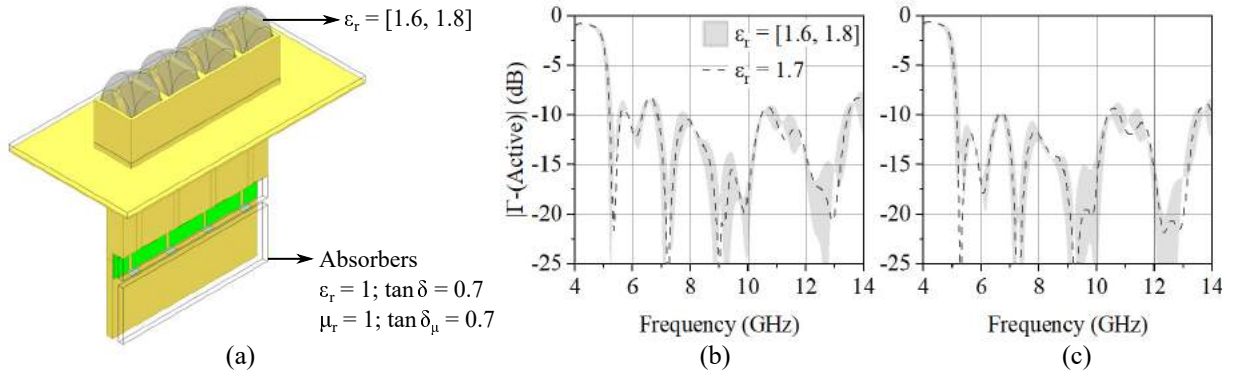


Figure 3.3: Geometry of in-phase uniformly excited horn array with lens loading (a). Active reflection coefficient variation for (b) outer and (c) inner array elements with lens relative permittivity varying from 1.6 to 1.8.

$f_0 = 6, 9, 12$ GHz. The solid lines represent radiated power density of array without absorbers, while the dashed lines show radiation patterns when absorbers with $\epsilon_r = 1$, $\mu_r = 1$, $\tan \delta = 0.7$ and magnetic loss tangent $\tan \delta_\mu = 0.7$ are placed in the relevant surfaces. The radiation pattern improves more obviously at higher frequencies due to the electrical dimensions of reflector. The E-plane asymmetry increases towards 12 GHz due to MS-to-WG transition leakage, as described in [71]. Finally, the forward radiation is not highly impacted by the absorbers, but slightly improves the angular (spatial) ripple at 12 GHz.

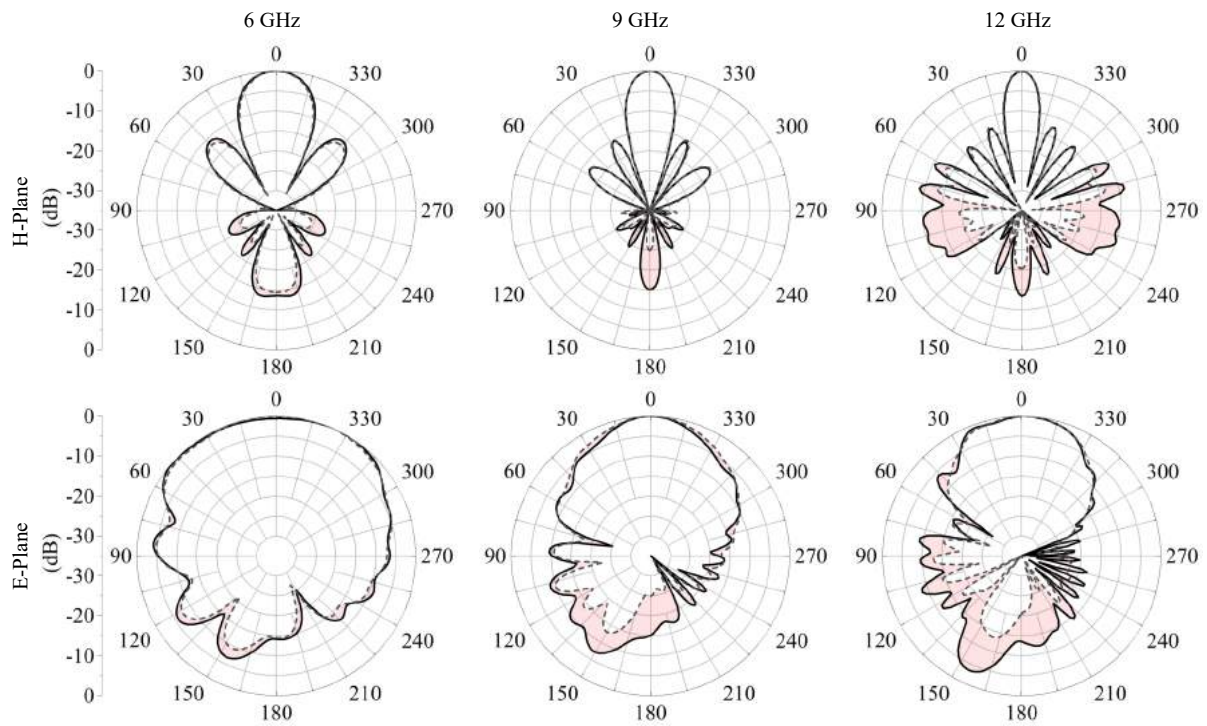


Figure 3.4: Simulated, normalized, H- and E-plane radiation patterns of passive array at $f_0 = 6, 9, 12$ GHz. The solid lines represent radiated power density of array without absorbers and dashed lines resulting radiation pattern with absorbers $\epsilon_r = 1$, $\mu_r = 1$, $\tan \delta = 0.7$ and magnetic loss tangent $\tan \delta_\mu = 0.7$.

The corporate feed network is implemented with three-section Wilkinson dividers, fabricated on Rogers TMM6 substrate. The measured performance using a coaxial calibration is shown in Fig. 3.5, showing an insertion loss that ranges from 0.5–2.5 dB over the octave bandwidth. The return loss and isolation are better than 14 and 20 dB, respectively. Insertion loss and phase imbalance are better than 1 dB and better than 10° between inner and outer branches.

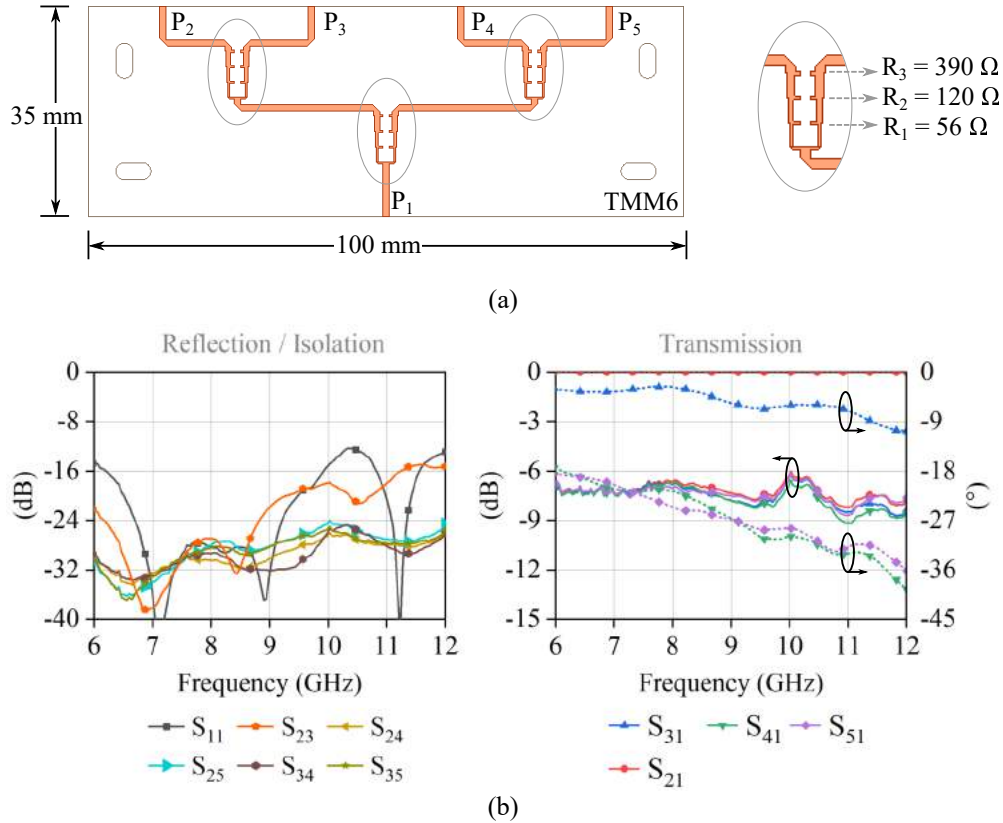


Figure 3.5: (a) Wilkinson power divider geometry and (b) measured S-Parameters. Input port reflection coefficient and isolation performance (left). Magnitude and phase transmission S-parameters (right).

Figure 3.6(a) shows the schematic of Wilkinson power divider measured S-parameters and simulated array S-parameters, with the series inductance L added to model the connection between corporate feed network PCB (TMM6) and microstrip-to-waveguide transition PCB (TMM3). The simulated reflection coefficient magnitudes are plotted in Fig. 3.6(b) for $L = \{0, 0.25, 0.5\}$ nH. The left plot shows the array reflection coefficient at the input port (Γ_{in}). A degradation is observed around 8 and 10 GHz, where Γ_{in} approaches -5 dB, which means a mismatch loss of approximately 1.6 dB at the array reference plane. This

can lead to EIRP and efficiency degradation. The righthand plot shows the magnitude of the reflection coefficient (measured by gamma probes (GP) in MWO) in the direction of the array, showing mismatch around 8 and 10 GHz. Mismatches at the output of the Wilkinson power divider will affect matching at the amplifiers input ports, compromising gain and overall active network efficiency. Figure 3.6(c) shows the array accepted power when corporate feed network input power is 0 dBm, and this is directly related to mismatch losses at all ports.

Figure 3.7(a-c) shows the passive array prototype obtained by connecting the Wilkinson power divider and array. Figure 3.7d shows the simulated gain with a feed implemented directly in HFSS (no corporate feed network) and measured results calibrated using the three-antenna method [62].

After characterizing the gain of the passive portion of the array, power amplifiers are included in the beamformer network and the power is combined spatially, after radiation by each antenna element.

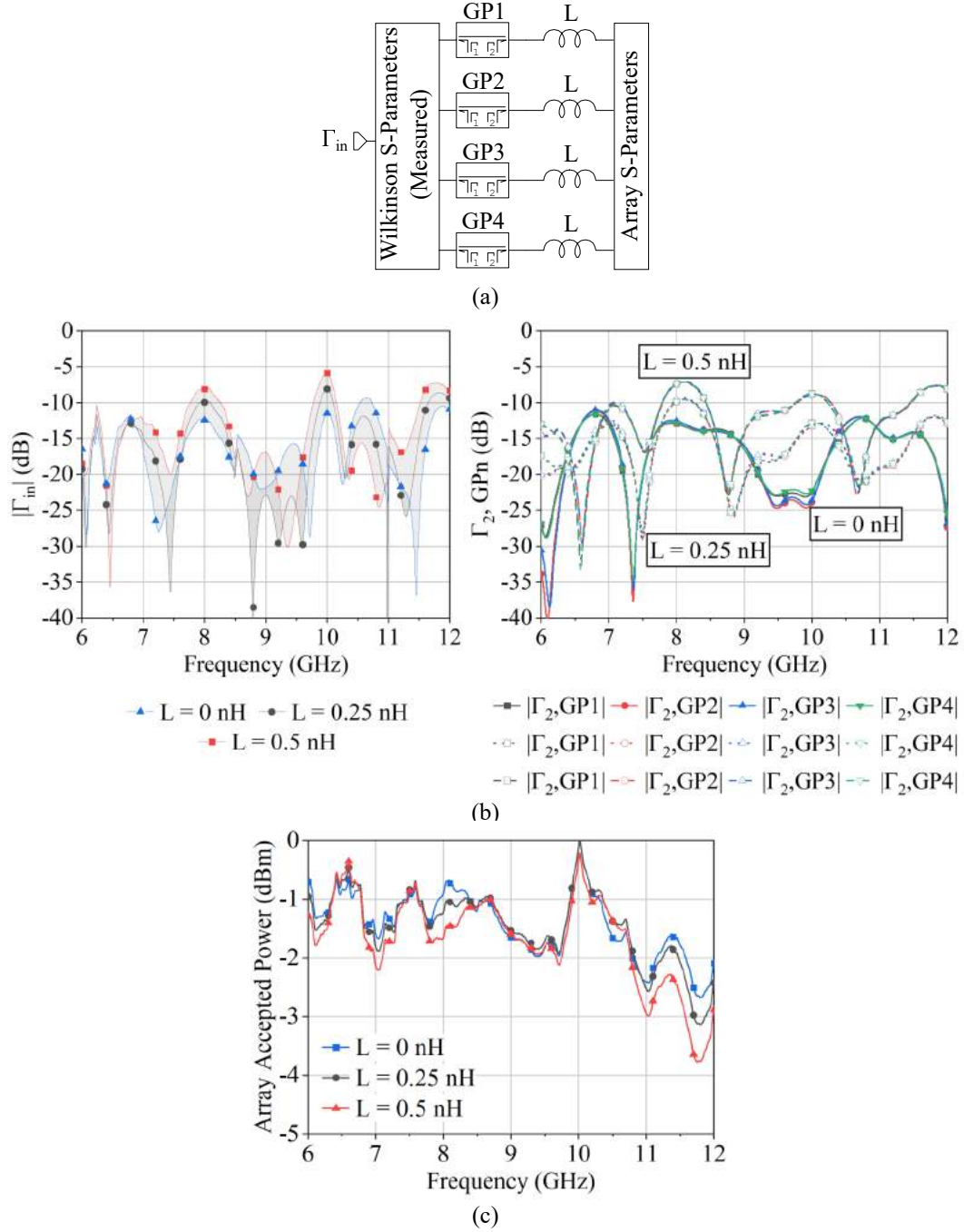


Figure 3.6: (a) Schematic of Wilkinson power divider measured S-parameters and simulated array S-parameters with series inductance L modeling the connection between corporate feed network and microstrip-to-waveguide transition PCBs. (b) Simulated magnitude of reflection coefficients Γ_{in} (left) and reflection coefficient measured by gamma probes in MWO (GP) (right) for $L = \{0, 0.25, 0.5\}$ nH. (c) Array accepted power when corporate feed network input power is 0 dBm.

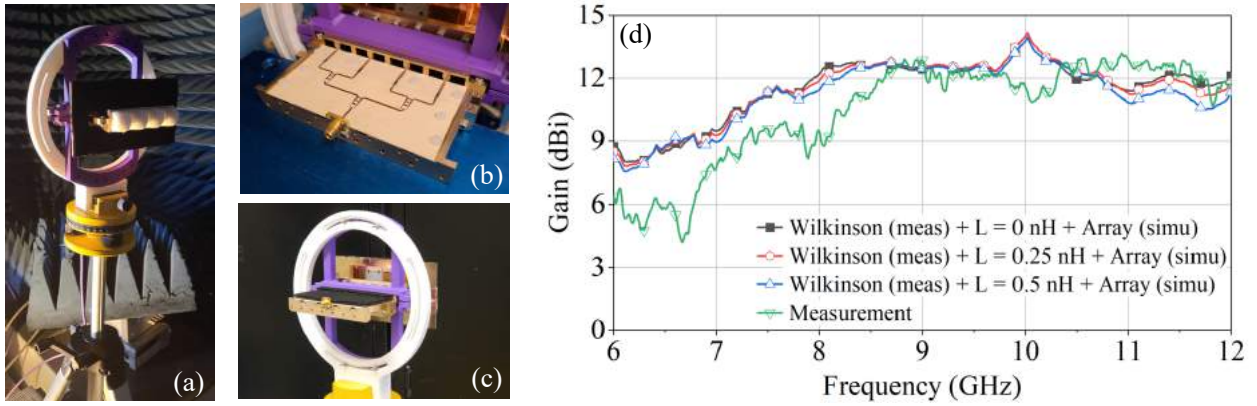


Figure 3.7: Prototype pictures: (a) front view, (b) Wilkinson power divider, and (c) back view. (d) Simulated and measured gain.

3.3 SUPPLY-MODULATED SPATIAL POWER COMBINER

The spatial power combiner geometry prototype shown in Fig.3.8(a) is a modified version of the passive array presented in section 3.2, where the beamformer shown in Fig.3.8(b) includes a 2-W, Qorvo QPA2598 GaN MMIC PA in each element between the Wilkinson power divider output and the antenna element feed, as in the block diagram shown in Fig. 3.8(c). The gate bias voltages are adjusted for a fixed quiescent current of $I_{DQ} = 70$ mA at each amplifier. The array is characterized in CW for three supply voltage combinations:

1. $V_{DD1,2,3,4} = \{10,10,10,10\}$ V motivated by improving PAE in backoff when envelope tracking is used;
2. $V_{DD1,2,3,4} = \{10,24,24,10\}$ V for sidelobe level reduction; and
3. $V_{DD1,2,3,4} = \{24,24,24,24\}$ V for maximized EIRP.

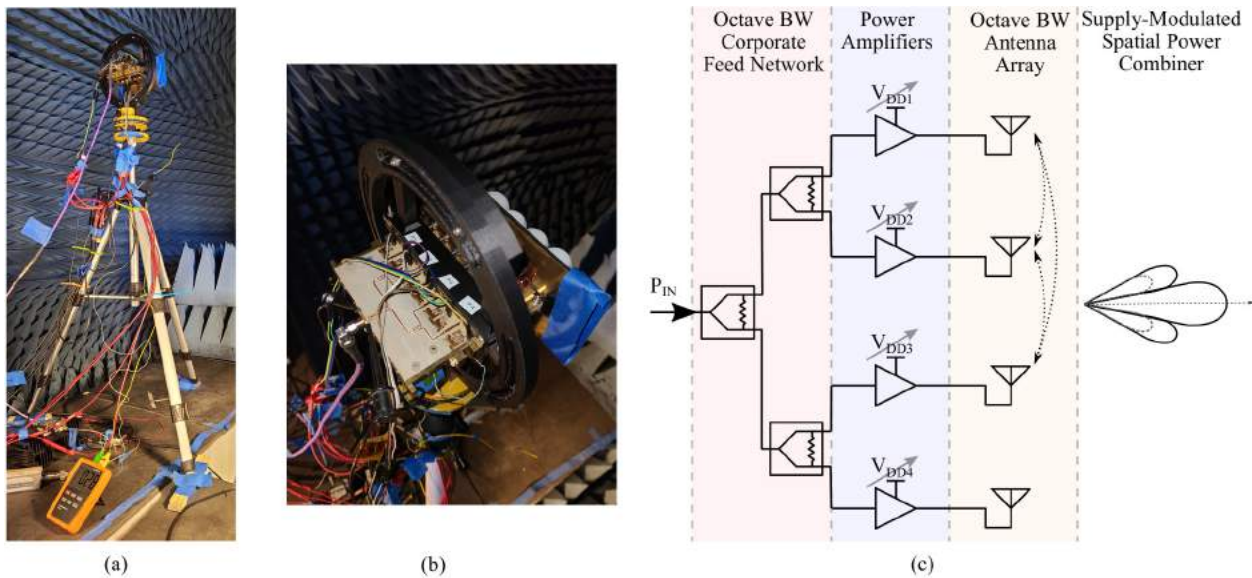


Figure 3.8: Spatial power combiner (a) photograph of prototype; (b) beamformer detail; (c) block diagram.

3.3.1 CW SIMULATED AND MEASURED RESULTS

The simulated element active impedances $|\Gamma_A|$ as a function of the drain voltage V_{DD} and frequency are shown in Fig.3.9(a) for all 4 elements uniformly biased with $V_{DDi} = \{10, 24\}$ V, where there is no observable

difference between the two supply voltage cases or with different input powers. Figure 3.9(b) shows $|\Gamma_A|$ for $P_{IN} = 10$ (dashed) and 30 dBm (solid), with a nonuniform supply voltage of 10 V applied to the edge-element PAs and 24 V at the internal ones. The array coupling affects the inner elements more than the outer elements at lower frequencies. As a nonuniform supply voltage is applied to the branches, the PA gain amplitude and phase variations interact with the array coupling, thus producing active input impedance variation across the elements.

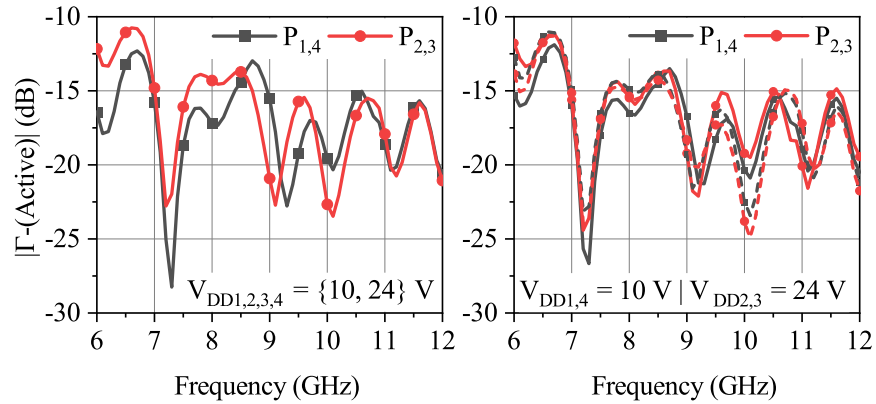


Figure 3.9: (a) $|\Gamma_A|$ over frequency for all 4 elements uniformly biased with $V_{DDi} = \{10, 24\}$ V. (b) $|\Gamma_A|$ with a nonuniform supply voltage of 10 V at external PAs and 24 V at the internal ones.

Figure 3.10 shows the total delivered power to the antenna array over frequency and beamformer input power P_{IN} for the three considered V_{DD} configurations. For a fixed input power, the delivered power varies over frequency by at least ± 3 dB. This variation is a result of the $|\Gamma_A|$ behavior over frequency shown in 3.9, as well as PA frequency dependence.

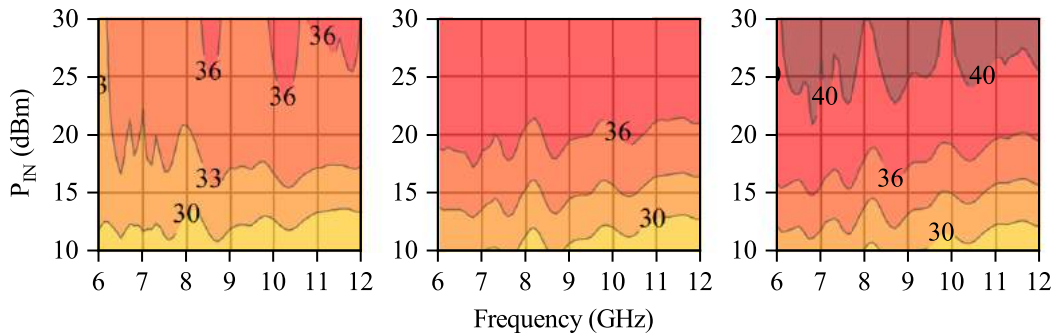


Figure 3.10: Total delivered power to array: $V_{DD1,2,3,4} = 10$ V (left), $V_{DD1,2,3,4} = 10/24/24/10$ V (middle), and $V_{DD1,2,3,4} = 24$ V (right).

The individual PAs have a PAE that is dependent on V_{DD} and the complex output load impedance, given by $|\Gamma_A|$ at each element. On the other hand, the total beamforming efficiency η_{BF} is affected by the Wilkinson power divider performance. The average PAE for all PAs, as a metric of beamformer efficiency, is here defined as:

$$PAE_{avg} = \frac{\sum P_{out,PA_s} - \sum P_{in,PA_s}}{\sum P_{dc}} \quad (3.1)$$

and the beamformer efficiency is then defined by:

$$\eta_{bf} = \frac{\sum P_{array} - P_{in,net}}{\sum P_{dc}} \quad (3.2)$$

Figure 3.11 shows simulated PAE_{avg} and η_{BF} simulated for 6, 9, 12 GHz, and previously given V_{DD} variations. The corporate feed network effects on efficiency is more evident at higher power levels when drain voltages are lower, what coincides with the peak efficiency achievable. Furthermore, curves at 6 GHz show efficiency levels of at least 10 percentage points (pp) higher at peak if compare to center and highest frequencies, but with a faster decay over power. This is due to the higher gain and earlier compression of the amplifiers associated with the lower corporate feed network losses at lower frequencies.

The nonlinearity of the PAs, e.g. AM-to-PM distortion, is both power and frequency dependent, but also depends on the drain supply level. Additionally, coupling between elements in the antenna array will lead to phase differences between PAs in each element. Figure 3.12, shows the simulated phase deviation between array input ports, normalized to port one and at $P_{IN} = 10$ dBm, traced over input power and at 6, 9, 12 GHz for the three V_{DD} conditions. One can observe a symmetric phase deviation of up to 10° between inner and outer elements, at 6 GHz, reduced somewhat at 9 GHz. For uniform V_{DD} (top and bottom), the phase difference is constant over P_{IN} . For the tapered V_{DD} (middle), the phase of inner and outer elements changes slope. At 12 GHz, there is negligible phase deviation, probably due to the fact the PAs are not being compressed, and the coupling is lower. The importance of this investigation is the effects of phase differences on steering angle and possible sidelobe level increase. Additionally, the nonuniform variation of AM-to-PM distortion over the elements will lead to total intermodulation products of four PAs in an array environment that is different from the nonlinearity of single matched PA.

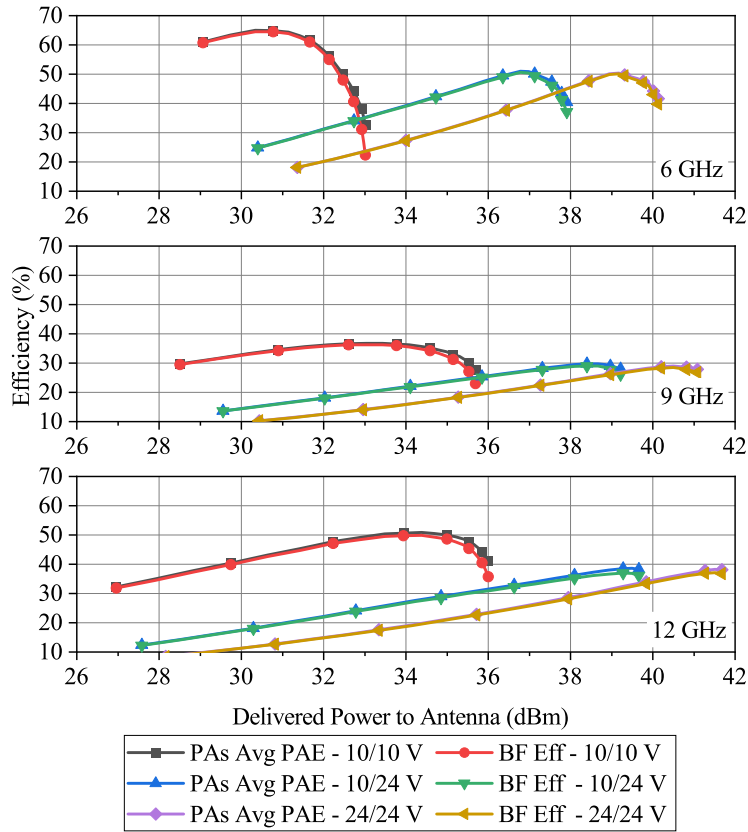


Figure 3.11: Simulated PAE_{avg} and η_{bf} over total delivered power to the antenna array for 6, 9, 12 GHz and $V_{DD} = 10/10, 10/24, 24, 24$ V.

Co-simulations with HFSS and AWR-MWO are used to calculate radiation patterns. This is done by exporting excitations from beamforming harmonic balance circuit simulations into the full-wave analysis, as illustrated in Fig.3.13. Figure 3.14 shows the normalized co-polarized H-plane radiation pattern over frequency for drain voltage combinations in the set of (10, 16 and 24 V) discrete levels. A tapering effect is observed (blue and black), where the first side lobe levels (SLL) is reduced and main beam is widened. The side lobes appearing at 12 GHz close to 90° and 270° are a result of the entrance of grating lobes into the visible region, and can thus not be controlled by tapering.

Figure 3.15 shows the simulated EIRP and realized array gain over frequency corresponding to the three simulated supply voltage combinations. Fig. 3.16 shows the measured EIRP for different input powers and frequencies corresponding to the three simulated supply voltage combinations. The color shading for all three plots is identical and color changes correspond to a 3 dB EIRP variation. This measurement is performed in an over-the-air setup (OTA) in a far-field anechoic chamber, with all losses calibrated and using the

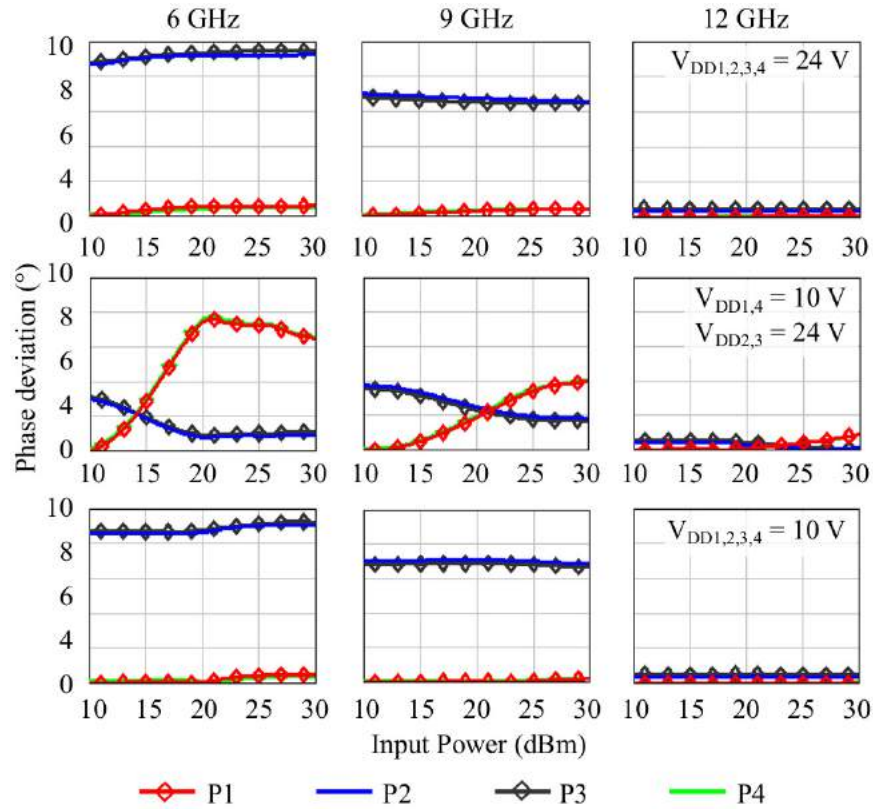


Figure 3.12: Phase deviation between array input ports, normalized to port one and at $P_{IN} = 10$ dBm, traced over input power and at 6, 9, 12 GHz, for the three V_{DD} conditions.

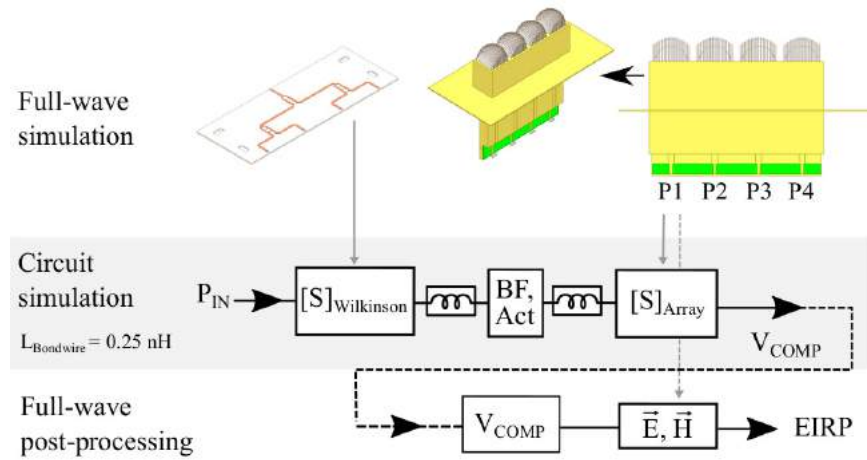


Figure 3.13: Workflow for EIRP calculations in HFSS with HB co-simulations in Cadence AWR-MWO.

three-antenna method. The EIRP is relatively flat across the band. The highest EIRP is obtained at 12 GHz because of the highest antenna gain. At 6.5 GHz and around 10 GHz, there is a drop in EIRP, following the

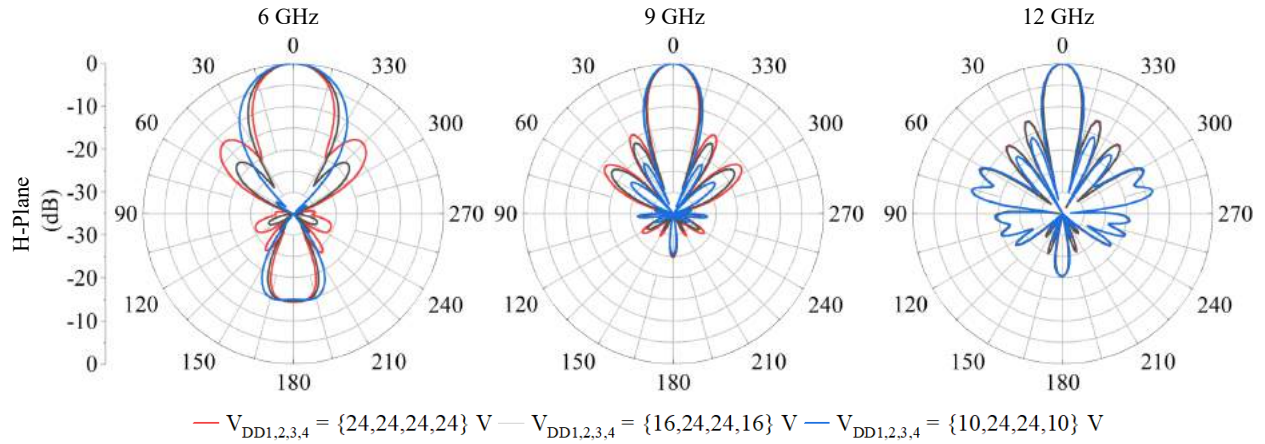


Figure 3.14: Normalized H-plane co-polarized radiation patterns at 6, 9 and 12 GHz for the drain voltage variations shown in the legend: uniform (red) and two levels of tapering (gray, blue).

drop in antenna gain. The antenna gain is also lower at 6 GHz but the PA gain increase compensates for it.

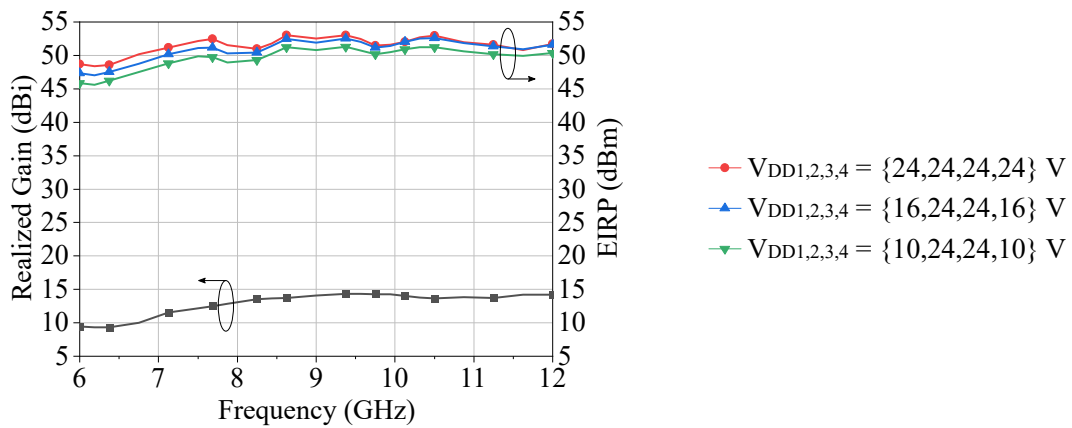


Figure 3.15: Simulated EIRP for drain voltage tapering configurations shown in Fig.3.14.

3.4 ACTIVE ARRAY PERFORMANCE UNDER MODULATED SIGNALS

The array is next characterized for linearity metrics under two types of modulated signals: a 2-tone signal with 10 MHz tone spacing, and a 64-QAM 50 MHz instantaneous bandwidth signal. The metrics used to characterize the nonlinear behavior are the third-order intermodulation (IM3) and the third-order intercept (OIP3), defined in eqs.(1.7,1.8).

Figure 3.17 (a) and (b) shows simulated PAE and IM3 over output power for the 2-tone signal using the

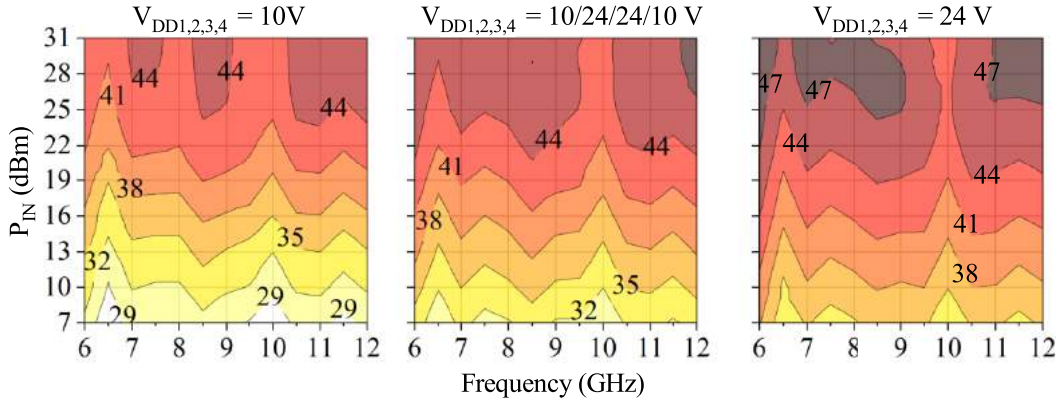


Figure 3.16: Measured EIRP in dBm over frequency and input power for the 4-element combiner array. The color shading for all three plots is identical and color changes correspond to a 3 dB EIRP variation.

X-parameters for the MMIC PA obtained from Qorvo, for several frequencies within the octave band. The total system efficiency is higher for the lower voltage due to the PA characteristics, and compresses earlier with a worse linearity. The higher supply voltage compresses at higher input power, and results in lower efficiency with better linearity. Fig. 3.18 presents system-level co-simulation results using Cadence VSS, together with HFSS and MWO HB, with a 64-QAM 50-MHz input signal input to the array, compared to the 2-tone signal. The simulated PAE shows substantially better efficiency under the 64-QAM signal for all three supply voltages, as compared to a 2-tone input.

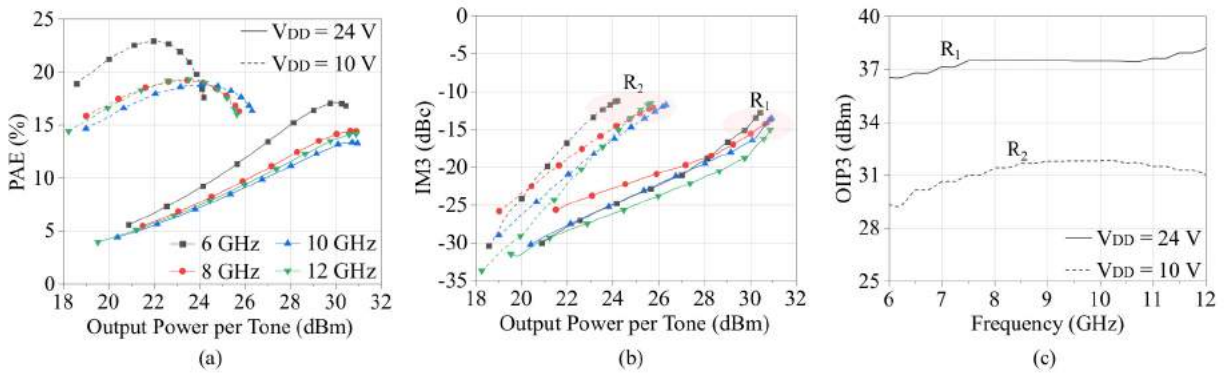


Figure 3.17: Simulated PAE (a) and IM3 (b) over output power for different frequencies within the octave bandwidth for a 2-tone, equal-amplitude, 10 MHz signal using the X-parameter MMIC PA model for $V_{DD} = 10, 24$ V. (c) Simulated OIP3 for the 2-tone excitation vs. frequency for two supply voltage levels.

Next, measurements are performed to validate the simulation trends. The active array is tested with a with a 64-QAM, 50-Mbaud signal, filtered by a root-raised cosine filter with $\alpha = 0.35$. The modulated signal is

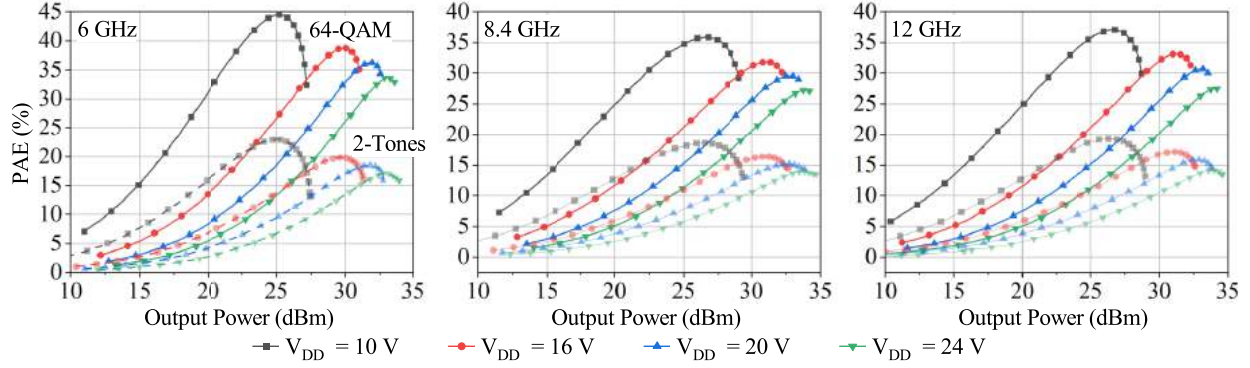


Figure 3.18: Simulated array average PAE vs. output power for the 64-QAM 50-MHz signal and the 2-tone 10-MHz signal, using system-level co-simulations with Cadence VSS at (a) 6 GHz, (b) 8.4 GHz and (c) 12 GHz.

created using an Agilent PSG E8267D, followed by a Mini-Circuits ZVE-3W-83+ pre-amplifier which allows output powers up to 27 dBm with an ACPR > 35 dB. Fig.3.19 shows the EIRP measured in an OTA setup for different input powers P_{IN} and the same voltage supply combinations as described previously. We observe that the total gain variation using the modulated signal follows similar trends to the gain measurements obtained previously with CW signals, and an EIRP of 50 dBm is reached at all frequencies.

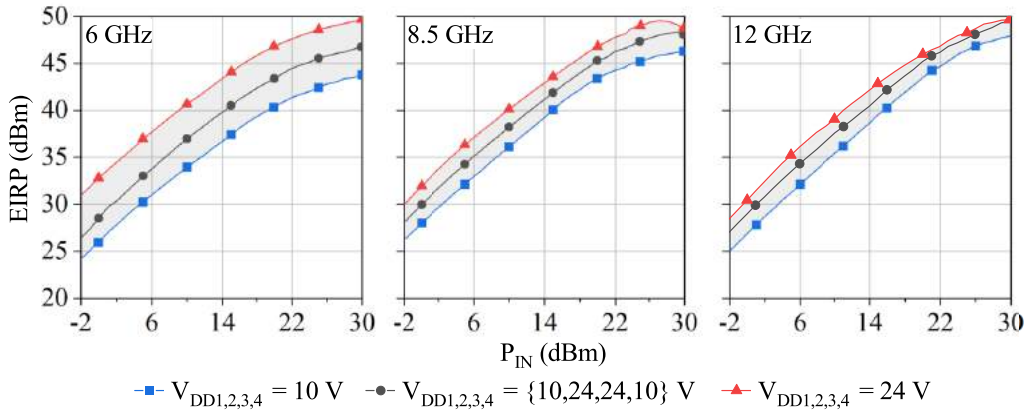


Figure 3.19: Array EIRP measured in the OTA setup over P_{IN} at 6, 8.5 and 12 GHz and for the three supply voltage configurations indicated in the legend.

The linearity is evaluated using OTA spectrum measurements. Here a channel bandwidth of 50 MHz and a channel spacing of 55 MHz are used for ACPR computations. The ACPR and its relationship to IM3 is defined in Chapter 1, eq.(1.11). The spectrum and the guardbands used to quantify the ACPR are shown in Fig.3.20. Fig.3.21 shows the measured ACPR for different measured EIRP levels at three frequencies

$f = \{6, 8.5, 12\}$ GHz and for the three supply voltage cases. The constant supply case of $V_{DD} = 24$ V shows the most linear behaviour, and as expected the case where all drain voltages are set to 10 V is the least linear one. The ACPR degradation for the mixed drain voltage operation is between these cases but closer to the 24 V case.

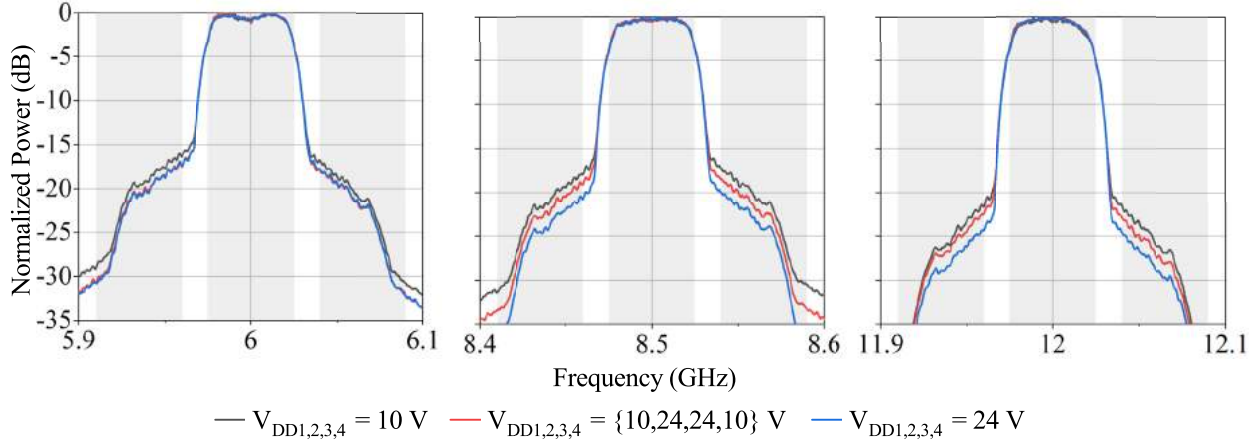


Figure 3.20: Spectrum at 6, 8.5, and 12 GHz when amplifiers reach 34 dBm of total output power and the guardbands used to quantify the ACPR.

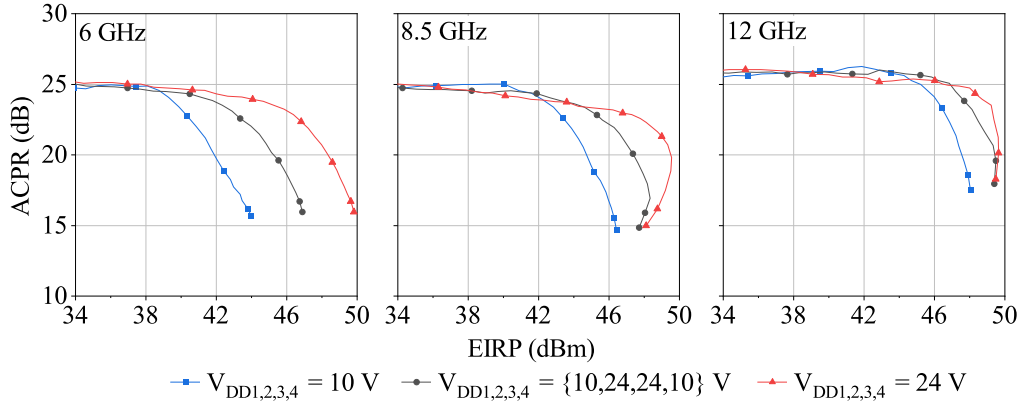


Figure 3.21: Array ACPR obtained from OTA measurements for the three different voltage combinations at $\{6, 8.5, 12\}$ GHz.

3.5 CHAPTER CONTRIBUTIONS AND CONCLUSIONS

This chapter presents a detailed analysis of an octave-bandwidth active transmit array as a spatial power combiner, including nonlinear co-simulations of EIRP, efficiency, sidelobe control and nonlinearities when

the drain supply voltage is varied across amplifiers in the combiner. The co-simulations are performed with full-wave simulations (HFSS) for the passive antenna array and feed portion, Cadence MWO harmonic balance simulations for the circuit portion, and system simulations for linearity under modulated signals. Over-the-air (OTA) measurements are performed on the prototype to validate the simulation approach, and an EIRP of 50 dBm is achieved across the 6–12 GHz octave, in agreement with simulations. The linearity is evaluated using a 64QAM 50 MHz signal, showing that the ACPR gracefully degrades when the supply voltage of the outer elements is reduced in order to improve the array sidelobe level. The measured linearity trends with frequency, supply voltage and signal follow the simulation trends.

The analysis in this chapter unveils the challenges in transmit arrays that result from the complex dependence between output power, efficiency, linearity and inter-element coupling when a full octave bandwidth is considered. Although the demonstrated 4-element array is a small linear sub-array, it is implemented in a modular metal-based architecture with good heat sinking properties, which lends itself to further scaling in EIRP, and the presented analysis can easily be extended to larger arrays.

The contributions from this chapter are reported in [87](accepted), [86], [88](accepted), [89](accepted) and [90](to be submitted).

CHAPTER 4

TRANSMIT PHASED ARRAY: ANALYSIS AND MEASUREMENTS

CONTENTS

4.1	CHAPTER INTRODUCTION	58
4.2	BEAM STEERING RADIATION PATTERN ANALYSIS	59
4.3	PHASE SHIFTER SPECIFICATIONS AND PERFORMANCE ANALYSIS	64
4.4	ACTIVE TRANSMIT ARRAY BEAMFORMING NETWORK	66
4.5	EXPERIMENTAL PROTOTYPE AND MEASUREMENTS	69
4.6	CHAPTER CONTRIBUTIONS AND CONCLUSION	72

4.1 CHAPTER INTRODUCTION

In the previous chapter, an active transmit array with elements fed in phase is presented. It performs far-field spatial power combining, with an EIRP reaching 50 dBm over an octave bandwidth. In this chapter, the array is extended into a transmit phased array with the additional functionality of beamsteering across the 6–12 GHz octave. In active phased arrays, the antenna impedance changes with steering and affects the

main FoMs such as effective isotropic radiated power (EIRP), average power-added efficiency (PAE), total beamforming network efficiency (η_{BF}), adjacent channel power ratio (ACPR) and radiation pattern. These inter-dependencies are analyzed in previous publications from different perspectives, some of them already cited in Chapter 1 [1], [4]. Here, a comprehensive analysis, which extends the co-simulation results from the previous chapter, is presented, along with measurements that validate the models.

The broadband scalable front end described in Chapter 3 can adaptively support several jamming modes simultaneously. For example, the beamwidth, center frequency, and power (EIRP) can be independently adjusted for different beams, and each beam can operate in a different jamming mode. One example includes a beam that operates over the full spectrum in swept CW mode, which would not require supply-modulation or power re-configurability, is very efficient, and allows the full 2:1 instantaneous bandwidth. Another example is a beam that can transmit signals with higher PARs and use supply modulation for efficient operation at the element or sub-array level. Another example is a means that can simultaneously jam several narrow portions of the full octave bandwidth and is operated with sum-of-envelope supply modulation as demonstrated in the 2–4 GHz band in [63].

In this chapter, first the steering radiation pattern of the 4-element array is analyzed across the octave bandwidth. This informs phase shifter specifications, which are followed by a phase shifter analysis in the array context. A beamforming network that includes broadband phase shifters, and GaN pre-amplifiers and power amplifiers is analyzed, fabricated and characterized.

4.2 BEAM STEERING RADIATION PATTERN ANALYSIS

In this section, an analysis of the array factor and array radiation patterns are presented for the passive array from Chapter 2, with added beamsteering. This section serves as background to set the stage for nonlinear array analysis and to provide a step-by-step insight into the operation of an octave-band array.

4.2.1 ARRAY FACTOR AND GRATING LOBE ANALYSIS

The first step in array radiation pattern analysis is determination of limits on steering angles, grating lobes, and beam squint associated with the array spacing only (not taking the element into account) and across frequency. Fig. 4.1 shows the simulated array factor corresponding to the actual array prototype, for several progressive phase shifts Φ across the array (held constant across frequency) and for two different tapers on the elements (achieved in our case with drain supply variation). The plots show the appearance of grating lobes at the higher frequencies and scan angles, which cannot be affected by the taper. Figure 4.2 shows the array factor steering angle as a function of progressive phase shift from 6 to 12 GHz. The steering (scan) angle will vary across frequency for the same progressive phase shift. The grating-lobe free maximum scan angle is shown as a function of frequency, as well as the corresponding steering angle for a given progressive phase shift, in this case -60° . These simulations are done using standard equations implemented in Mathematica.

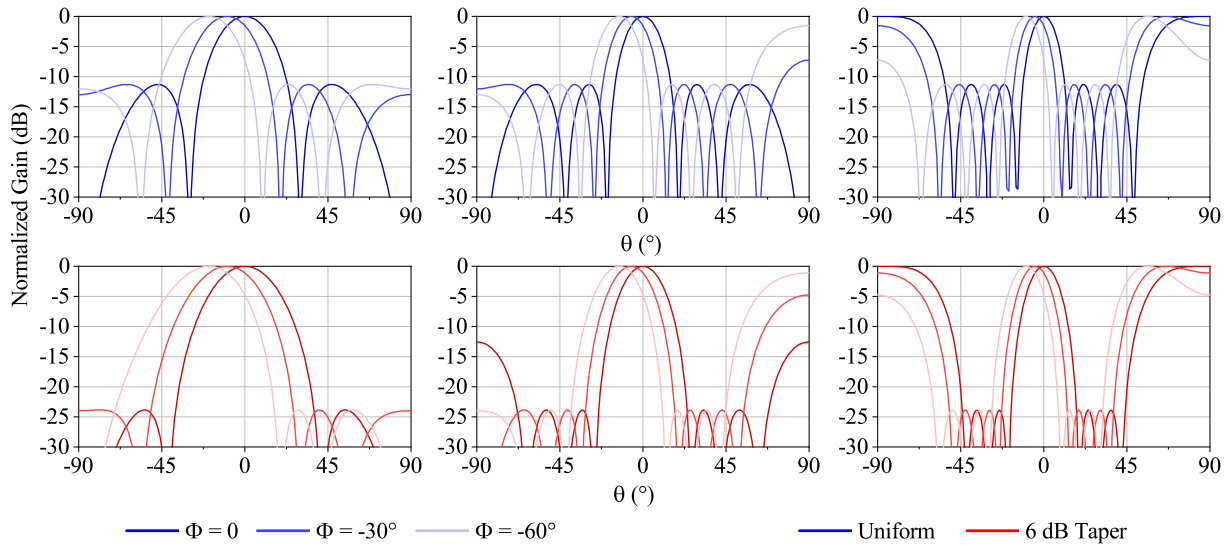


Figure 4.1: Simulated array factor in the H-plane of a 4-element linear array across an octave, using the array spacing from the 4-element prototype. The cases for a uniform and 6-dB power taper are shown, as well as ideal steering with three different progressive phase shifts across the array, kept constant over frequency.

Next, the element radiation pattern is included and the radiation patterns simulated in HFSS. Fig. 4.3 shows the array geometry and the 4 ports, showing the applied ideal progressive phase shift. Fig. 4.4 shows the resulting simulation results for the steering angle, co-polarized gain and cross-polarization level across

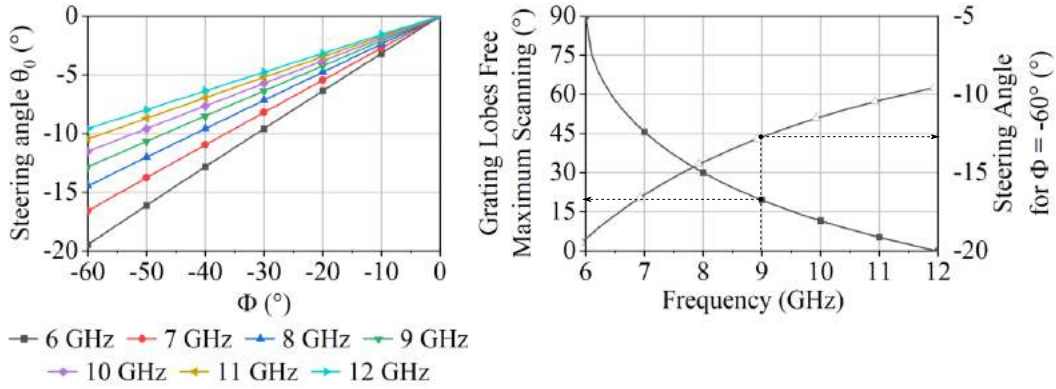


Figure 4.2: Left: Simulated Array factor (no antenna element) steering angle as a function of progressive phase shift across an octave. Right: maximum scanning for a grating-lobe free pattern vs. frequency for the array factor, or assuming an isotropic radiator element. The corresponding steering angle is also shown.

the octave bandwidth, while Fig. 4.5 shows the full-wave simulated radiation patterns over frequency and for three progressive phase shifts.

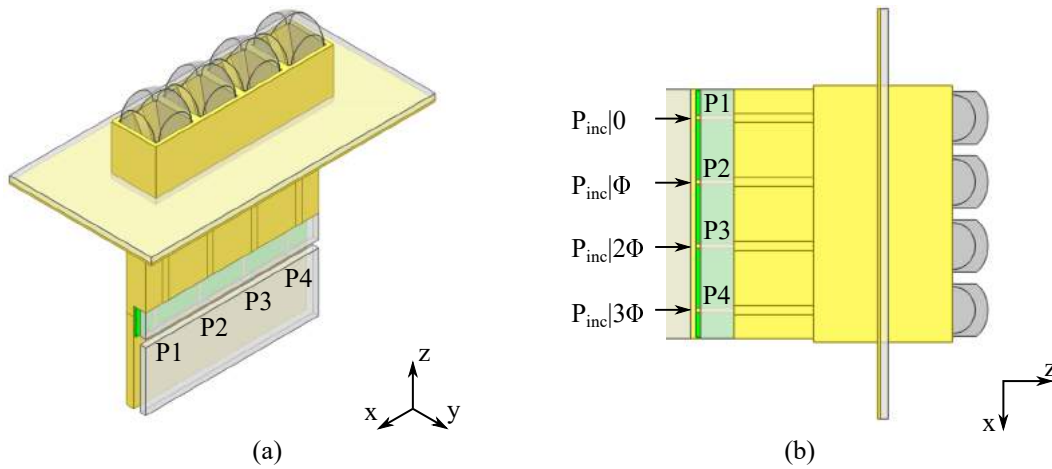


Figure 4.3: Simulated array geometry (a) and excitation scheme applied in HFSS (b).

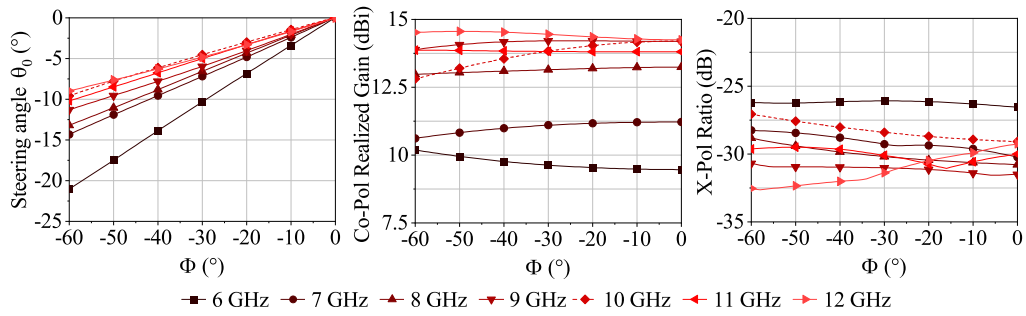


Figure 4.4: Left: Simulated array beam steering angle θ_0 for constant progressive phase shift Φ over frequency. Center: Co-polar realized gain at beam steering direction. Right: Cross-polarization ration in beam direction.

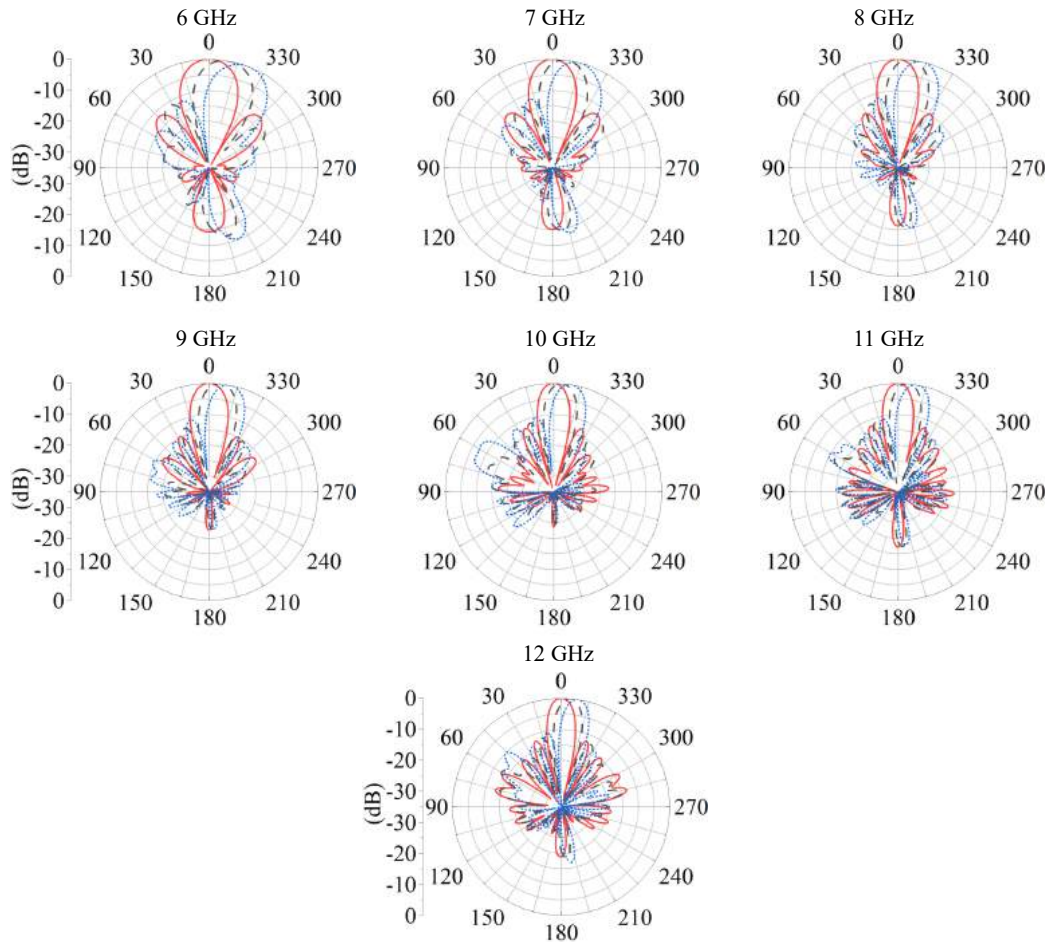


Figure 4.5: Radiation pattern obtained from full-wave simulations in HFSS of geometry shown in 4.3 for $\{6, 7, 8, 9, 10, 11, 12\}$ GHz and $\Phi = \{0, -30, -60\}^\circ$ (red, black dashed, and blue dotted).

As the beam is scanned, the coupling between elements changes, resulting in a change in the active scan impedance presented to the power amplifier. This in turn affects the efficiency, EIRP and linearity of the PAs in the array. Fig. 4.6 shows the results of the coupling analysis starting from the antenna elements. Fig. 4.6 shows the schematic implemented in MWO for coupling simulations when $P_d = 0$ dBm at each port, over frequency and for a varying progressive phase shift $\Phi = [-60, 60]^\circ$. The magnitude of the complex scattered power at each port consists of the reflected power and that coupled from other ports. For a fixed, uniform excitation across the elements, changes in coupling levels will depend on the array geometry and phases applied to each port, requiring both full-wave and circuit simulations. The reflected power due to self-impedance mismatch at each port remains the same. The simulated scattered power due to mutual coupling is shown for each RF chain P_1 to P_4 in Fig. 4.6. One can observe symmetric performance between inner and outer elements. For a given progressive phase shift applied to the array, different scattered power is observed at each element, an example shown with a cross symbol at 9 GHz and $\Phi = -30^\circ$. This has an effect on PA performance and on the entire RF transmit chain, and is important quantitative information when multiple signals are transmitted simultaneously through an active array, possibly on different beams.

Figure 4.7 is a plot of the simulated PAE of when the PAs are biased at the specified quiescent point and input power of 19 dBm (colors are used to show impedances that result in a constant PAE). The Smith charts are normalized to $50\ \Omega$ and only a part of the unity-radius Smith chart is shown, approximately to a VSWR=2.5. Superimposed on the PAE are trajectories of the array scan reflection coefficient traced for $\Phi = [-180, 0]^\circ$. One can observe that at 6 GHz and for moderate progressive phase shifts, the active scanning reflection coefficient falls in the region of highest PAE, but degrades fast towards wide scanning angles. At 9 GHz a flattened behavior of Γ_A is expected for all elements, falling in a region of the Smith chart where the expected PAE is around 35%. At 12 GHz the coupling levels are low and Γ_A does not substantially change with scanning angle. The elements also show a good impedance match to $50\ \Omega$, where the expected PAE is 30% around this frequency.

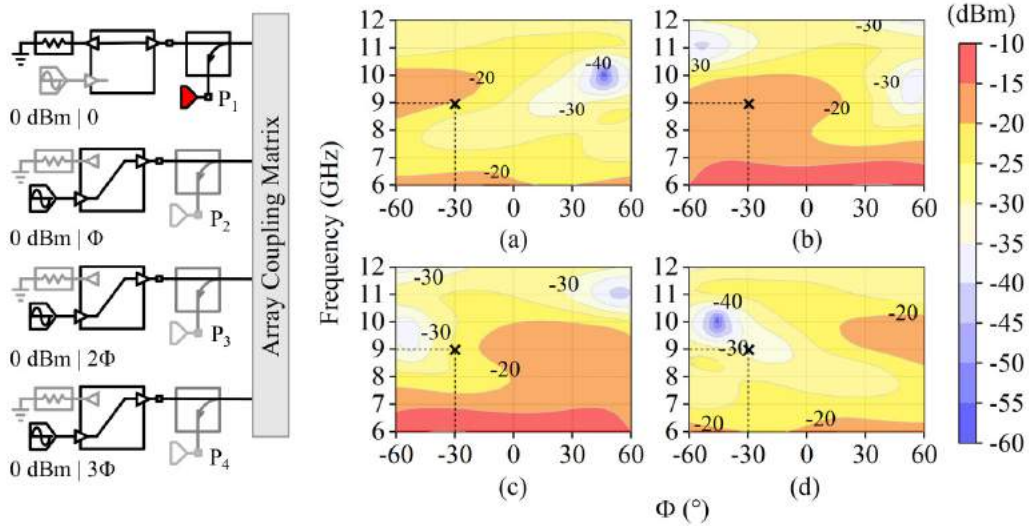


Figure 4.6: Magnitude of leakage power impinging (not flowing because we have output reflection coefficient) into each RF chain due to array coupling. (a) P₁, (b) P₂, (c) P₃, (d) P₄. Circuit simulation schematic (left) including the array 4×4 S-parameter matrix obtained from full-wave simulations. Expected backward power injected into the output ports of the four RF chains when each array port is excited with 0 dBm input power, over frequency and progressive phase shift Φ . One can observe symmetry between inner and outer elements. However, for a given progressive phase shift applied to the array, a different leakage level is observed at each element, as marked at 9 GHz and $\Phi = -30^\circ$ as an example.

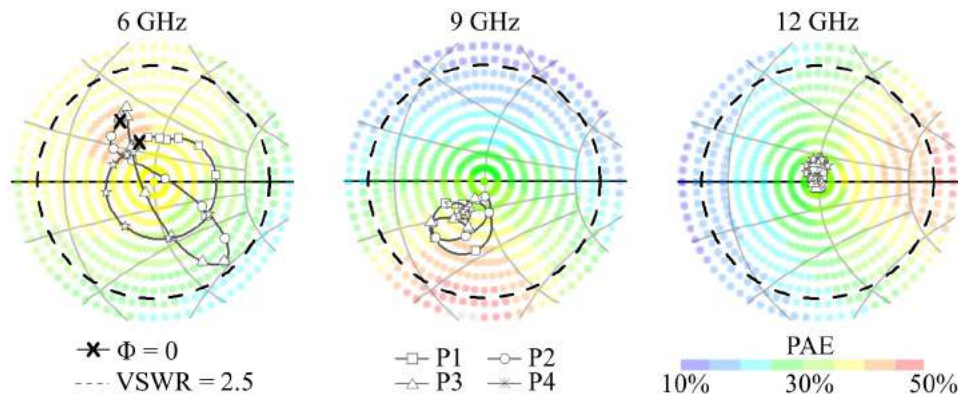


Figure 4.7: Array scan reflection coefficient shown on a 50- Ω Smith chart for each port, traced for $\Phi = [-180, 0]^\circ$ and superimposed on simulated PAE when the PAs are biased at the specified quiescent point and input power of 19 dBm.

4.3 PHASE SHIFTER SPECIFICATIONS AND PERFORMANCE ANALYSIS

For a 6–12 GHz array, the beamforming network based on phase shifters requires a broadband design. The Wilkinson-divider corporate feed is described in Chapter 3. A commercial phase shifter MMICs with the best

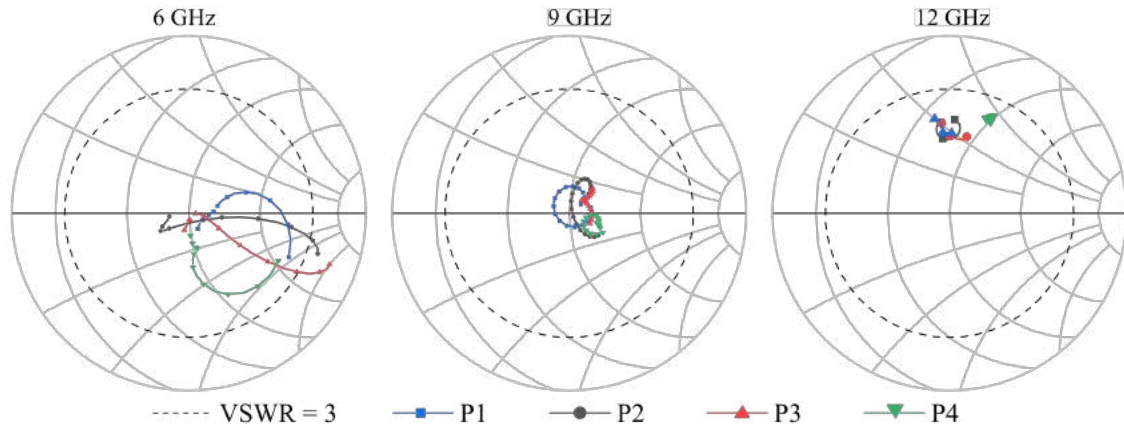


Figure 4.8: Active scan reflection calculated from measured coupling matrix, on a 50- Ω Smith chart for each port, traced for $\Phi = [-180, 0]^\circ$. One can observe that fabrication imperfections can cause a phase change (rotation) of Γ_A , and thus a change in expected PAE performance.

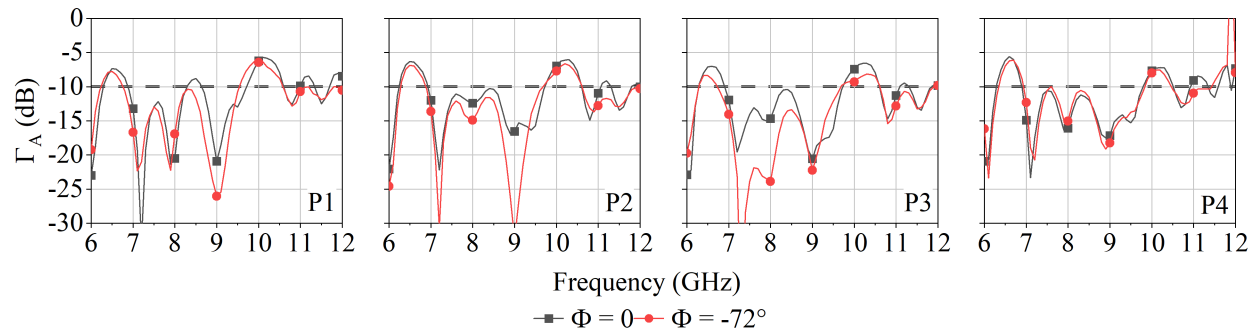


Figure 4.9: Magnitude of active array scan reflection over BW, calculated from measured coupling matrix, on a 50- Ω Smith chart for each port, for uniform excitation and traced for $\Phi = \{-72, 0\}^\circ$.

performance over the octave was identified. The Analog Devices HCM247 GaAs analog phase shifter MMIC has 400° of continuously variable phase shift from 5–18 GHz with a 0-10,V control voltage. The size of the die is 2.3×1.6 mm on a standard $100 \mu\text{m}$ thick GaAs substrate. The manufacturer-provided S-parameters of the phase shifter as a function of frequency are shown in Fig. 4.10 for several control voltages. This model is used for full array simulations. Table 4.1 summarizes the phase shift as a function of frequency and the progressive phase shift obtained for the 4-element array. Table 4.2 shows the required control voltages for three progressive phase shifts, which are used for both simulations and measurements of beam scanning.

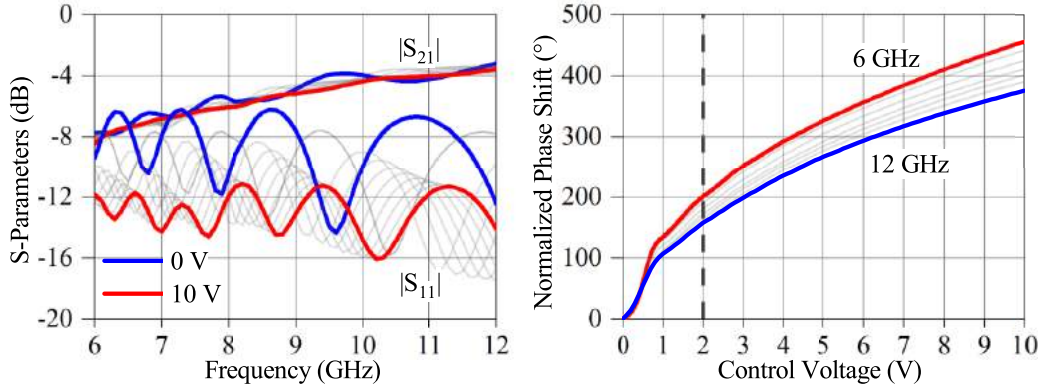


Figure 4.10: Simulated S-parameters of the ADI phase shifter using the manufacturer-provided model.

Table 4.1: ADI HMC247 maximum phase shifting for 6–12 GHz considering a range of control voltages between 2–10 V. Maximum progressive phase shift Φ for a 4-element array.

Frequency (GHz)	6	7	8	9	10	11	12
Maximum phase shift (°)	255	251	244	238	235	230	218
Maximum progressive phase shift Φ (°)	85	84	81	79	78	77	73

Table 4.2: Required control voltages for 3 values of the progressive phase shift for the 4-element array from 6–12 GHz.

Frequency (GHz)	$\Phi = 24^\circ$				$\Phi = 48^\circ$				$\Phi = 72^\circ$			
	V_{C1}	V_{C2}	V_{C3}	V_{C4}	V_{C1}	V_{C2}	V_{C3}	V_{C4}	V_{C1}	V_{C2}	V_{C3}	V_{C4}
6	2.00	2.47	2.92	3.51	2.00	2.92	4.13	5.61	2.00	3.51	5.61	8.29
7	2.00	2.48	2.96	3.52	2.00	2.96	4.13	5.64	2.00	3.52	5.64	8.41
8	2.00	2.50	3.00	3.56	2.00	3.00	4.20	5.69	2.00	3.56	5.69	8.64
9	2.00	2.50	3.01	3.62	2.00	3.01	4.30	5.81	2.00	3.62	5.81	8.84
10	2.00	2.51	3.03	3.65	2.00	3.03	4.31	5.92	2.00	3.65	5.92	9.00
11	2.00	2.54	3.10	3.70	2.00	3.10	4.44	6.01	2.00	3.70	6.01	9.26
12	2.00	2.58	3.18	3.83	2.00	3.18	4.58	6.36	2.00	3.83	6.36	9.89

4.4 ACTIVE TRANSMIT ARRAY BEAMFORMING NETWORK

As previously mentioned in Chapter 1, here we use the best commercially available broadband phase shifters to investigate small-angle beam steering with a goal to quantify nonlinear effects due to the interactions between all components in the transmit chain. Due to the phase shifter limitations, only small beam-steering angles are possible with this specific implementation at the higher frequencies, and therefore this array does not have a full octave bandwidth when larger steering angles are considered. As mentioned in Chapter 1, true

time delay beamforming networks have been successfully implemented and are a commercially available solution. For a true octave-bandwidth transmit array, broadband lens-based beam-forming networks, e.g. a Rotman lens, could be designed to replace the phase shifter based corporate feed discussed next. The beamforming network consists of the broadband Wilkinson corporate combiner with integrated ADI GaAs MMIC phase shifters, driver amplifiers (1,3,5,6) and power amplifiers (2,4,6,8). Both driver and PA use the Qorvo 2-W TGA2598 GaN MMIC described in the active unit element in Chapter 2 and in the active array in Chapter 3. Fig. 4.11 shows the circuit schematic of the beamforming network simulation in Cadence AWR Microwave Office.

Figure 4.13 shows the simulated output power (solid line) and gain (dashed line) vs. input power to the phase shifter when the driver is biased at 24 V and for three drain supply voltages of the PA. It can be observed that the output power is constant over input power and steering angle and increases slightly with frequency, while the gain decreases with input power, as expected. The losses of the phase shifter increase in frequency, contributing to the output power flatness. The output power remains constant at different drain supply voltages of the PA stage, and is reduced by approximately 5 dB when the supply is reduced from 24 V to 10 V. This implies that the supply voltage of the output stage can be used for controlling the radiation pattern and EIRP of the array.

Figure 4.13 shows simulated output power at the antenna element feeds over frequency for a constant $P_{in} = 9$ dBm, for two steering angles. Fig. 4.14 shows the simulated phase shift across frequency at ports 2,3 and 4 relative the phase of the first element (port 1), for phase shifter control voltages that correspond to the maximal scan angle at 12 GHz. The progressive phase shift across the 4 elements is calculated and shown in Fig. 4.14(b) along with the standard deviation.

Fig. 4.15 displays simulated radiation patterns with complex excitations calculated from harmonic balance simulations of the active beamforming circuit from Fig. 4.11 for $P_{in} = 9$ dBm and all drain voltages set to 24 V. The solid blue line shows broadside radiation when the phase shifter voltages are $V_{Control1,2,3,4} = 2$ V, while the dashed red curves are the resulting radiation patterns when phase shifters are set to maximum positive scan at 12 GHz. The cross-polarization ratio is better than 27 dB for all frequencies and θ at $\Phi = 0$, and better than 33 dB for $\theta \leq |60|^\circ$. The maximum directivity of the array and the realized gain with no

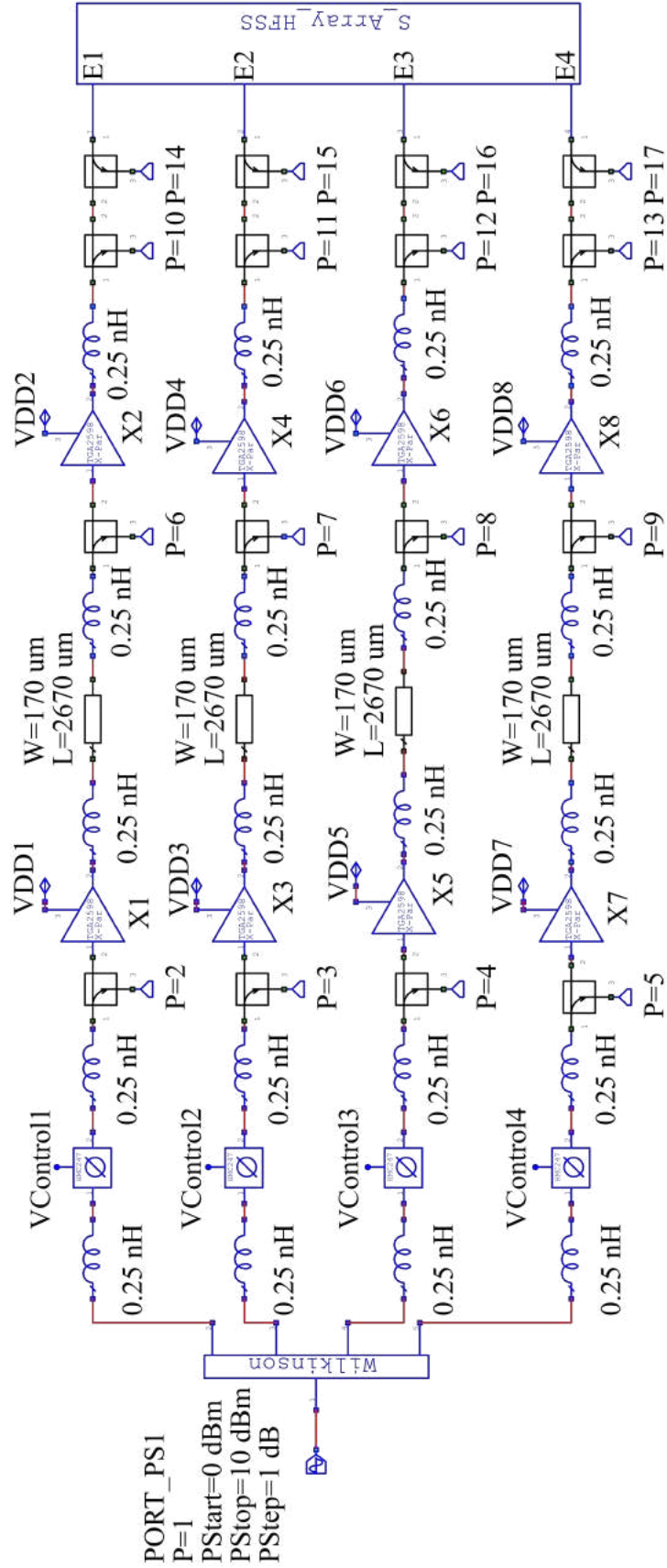


Figure 4.11: Beamforming network simulation schematics in AWR.

beamforming is shown in Fig. 4.16 across frequency, along with the gain using control voltages on the phase shifters for a specific progressive phase shift at 12 GHz. The antenna efficiency shows degradation due to the use of absorbers for sidelobe level and back radiation control, which reduces the total radiated power. Also, matching losses are taken into account (Realized Gain measurement), contributing to the difference between directivity and gain. The EIRP is calculated in Cadence AWR from the power incident on the array ports (output power from beamforming network) and the realized gain found from full-wave HFSS calculations, and is plotted in Fig. 4.17(top) as a function of P_{in} and frequency for two progressive phase shifts. The EIRP exceeds 50 dBm and has similar values at broadside and when scanning. Fig. 4.17(middle) and (bottom) show the PAE and beamforming efficiency, respectively, as a function of EIRP and frequency. Both efficiencies drop with increasing frequency. Even though the drop in PAE and beamforming efficiency follow the same profiles, with a shift in magnitude, the nature of both efficiencies is slightly different: the PAE takes into account the power received from the pre-amplifiers, the beamforming network efficiency includes the array input matching performance, and sometimes may not result in a scaled version of PAE.

4.5 EXPERIMENTAL PROTOTYPE AND MEASUREMENTS

The experimental prototype of the transmit phased array is shown in Fig. 4.18, showing the beamformer network and bias line board, as well as the small-horn lens antenna array. A close-up photograph of the active element is shown in Fig. 4.19. The three MMICs are mounted on a CuMo carrier with an alumina connection between the two amplifiers. The chips are bonded to each other and the external bias and control lines using 1-mil gold bondwires. Off-chip, single layer capacitors of 1000 pF are directly connected to the chip for both mechanical and electrical stability and to create a wider area for wire bonding to the PCB bias lines. SMD 5- Ω resistors and 0.01 μ F capacitors are used on the gates and drains for low-frequency decoupling and 1 μ F capacitors are added for compensating the inductance introduced from the long cables to connect the dc power supplies to the beamforming network.

Measurements of the prototype are performed in an over-the-air setup implemented in a non-commercial anechoic chamber that allows a distance of 2 m between the antenna under test (AUT) and a commercial

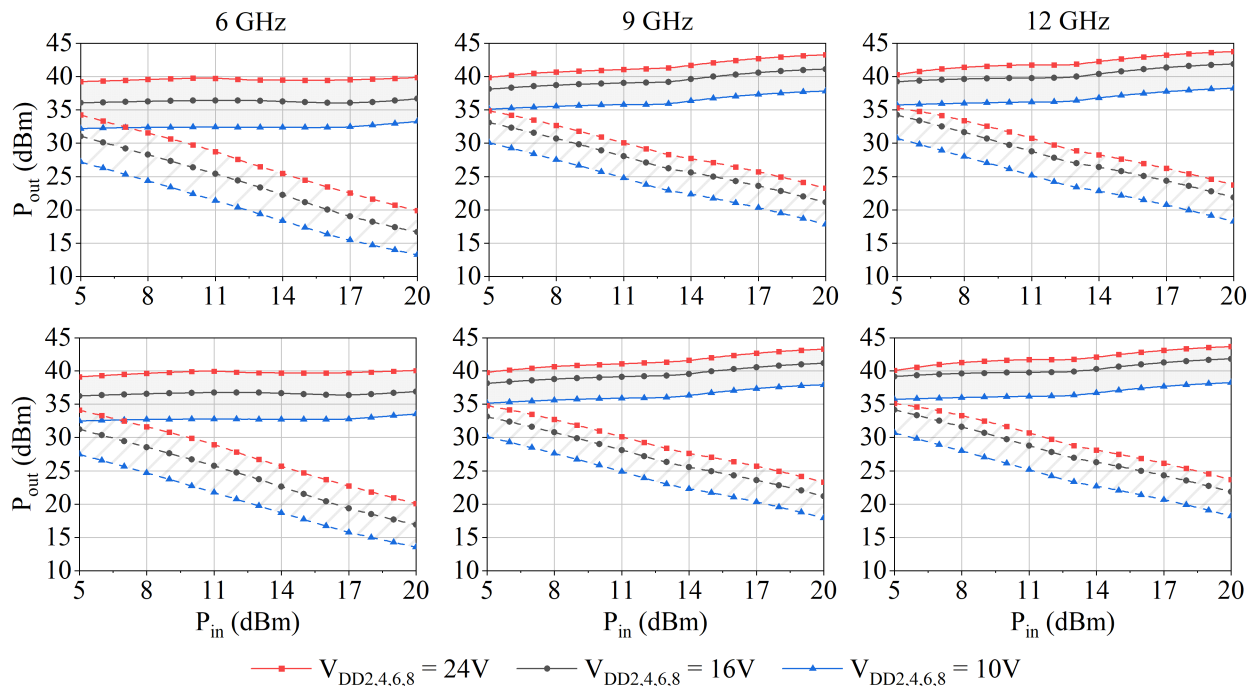


Figure 4.12: Beamforming network output power (solid) and system power gain (dashed) over input power for $f = \{6, 9, 12\}$ GHz, when the driver supply voltages are set to $V_{DD1,3,5,7} = 24$ V and the PA supply voltages are varied $V_{DD2,4,6,8} = \{10, 16, 24\}$ V. The top row shows the case for broadside radiation with phase shifter control voltages of $V_{Control1,2,3,4} = 2$ V, while the bottom row are simulated power and gain for phase shifter control voltages of $V_{Control1,2,3,4} = \{2, 3.8, 6.36, 9.99\}$ V. Generally, flat power behavior is observed over both frequency and steering angle.

standard gain antenna pre-calibrated in the final measurement configuration using the absolute-gain three antenna method. The average antenna input power is obtained in every measurement cycle through power samples at coupler ports and de-embedded by the measured S-parameters. Different signal profiles are obtained from vector and analog generators and amplified by high-linearity broadband instrumentation amplifiers. Laboratory-grade dc power supplies are used for voltage control and current monitoring. All equipment control and measurement routines are implemented through MATLAB codes.

Since the array is broadband, it is of interest to test its performance with more than one concurrent signals. The setup built for generating concurrent signals uses one vector signal generator for generating a 64-QAM, 50-Mbaud signal and one analog signal generator to provide a amplitude or frequency modulated signal in arbitrary carriers and amplitudes in the 6-12 GHz range. Both signals are amplified by linear drivers and input in a high-isolation power combiner composed of two ferrite isolators connected to a two-inputs

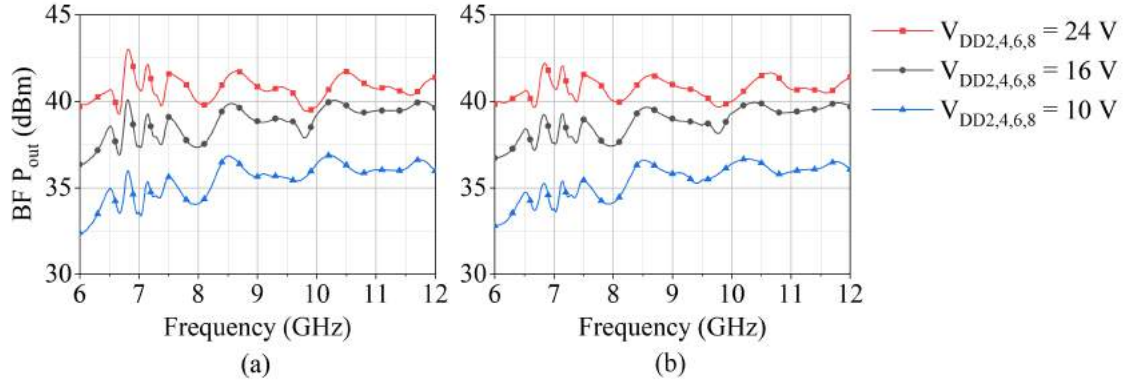


Figure 4.13: Beamforming network output power over frequency for $P_{in} = 9$ dBm, when $V_{DD1,3,5,7} = 24$ V and $V_{DD2,4,6,8} = \{10, 16, 24\}$ V. (a) Plot of output power for the case of broadside radiation and phase shifter control voltage of $V_{Control1,2,3,4} = 2$ V. (b) Output power for phase shifter control voltages of $V_{Control1,2,3,4} = \{2, 3.8, 6.36, 9.99\}$ V.

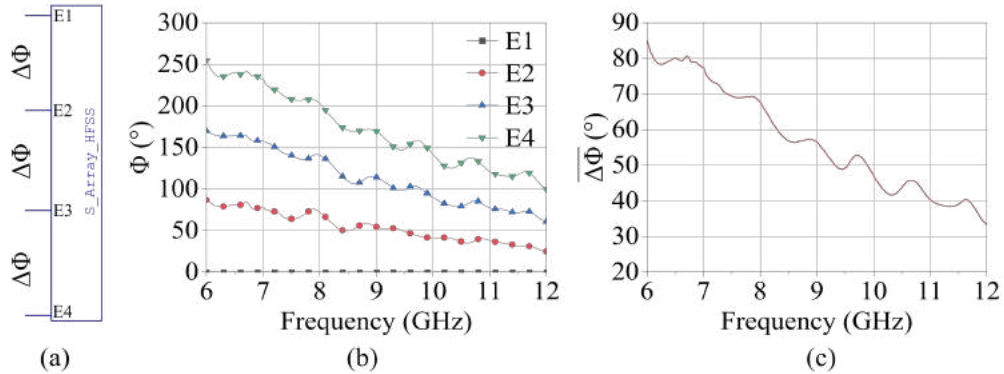


Figure 4.14: (a) Simulated phase shift at ports 2,3 and 4 relative to the phase shift at the first element (E1), over frequency for phase shifter control voltages of $V_{Control1,2,3,4} = \{2, 3.8, 6.36, 9.99\}$ V corresponding to the maximum scan at 12 GHz. (b) Calculated progressive phase shift over all elements. (c) Calculated progressive phase shift over all elements.

Wilkinson power combiner. The isolators provide an isolation between the two input ports of 19 dB and the Wilkinson adds a minimum of 14 dB isolation, resulting in an isolation better than 37 dB between the two sources. In order to perform dual-signal measurements, the Wilkinson divider network required careful calibration. Fig. 4.20 shows the simulation environment used to determine leakage between the ports to verify power dissipation in the resistors of the Wilkinson divider circuits. Table 4.3 shows the resulting power budget when two uncorrelated sources generating two tones spaced by 200 MHz and with 30 dBm power each are combined into a two-tone input signal. A photograph of the combiner and circulators that provide additional isolation is shown in Fig. 4.22, as well as the measured S-parameters.

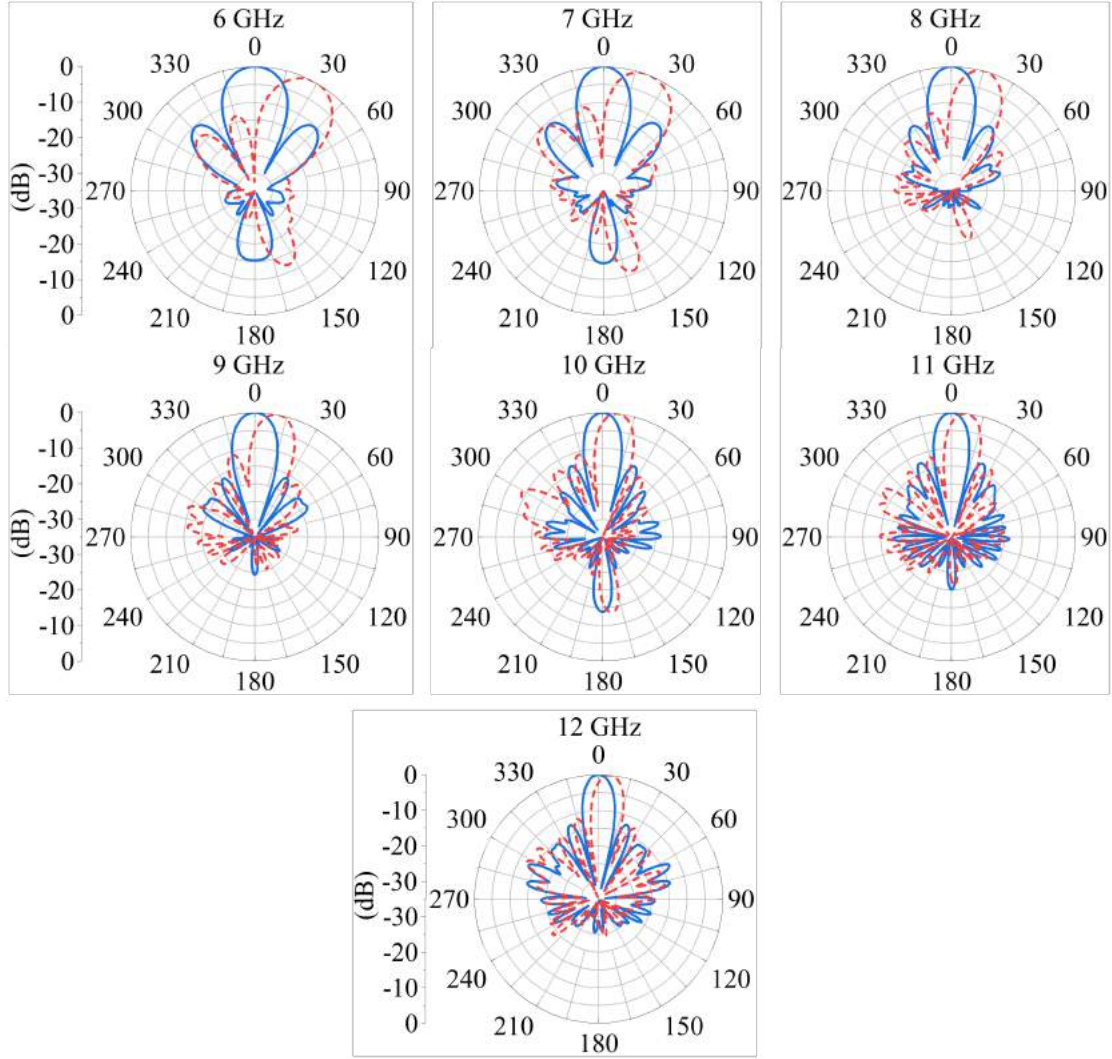


Figure 4.15: Radiation patterns with complex excitations calculated from harmonic balance simulations of the active beamforming circuit in AWR-MWO for $P_{in} = 9$ dBm and all drain voltages set to 24 V. The solid blue line shows broadside radiation when the phase shifter voltages are $V_{Control1,2,3,4} = 2$ V, while the dashed red curves are the resulting radiation patterns when phase shifters are set to maximum positive scan at 12 GHz with $(V_{Control1,2,3,4} = \{2, 3.83, 6.36, 9.89\}$ V). The cross-polarization ratio is better than 27 dB for all frequencies and θ at $\Phi = 0^\circ$, and better than 33 dB for $\theta \leq |60|^\circ$.

4.6 CHAPTER CONTRIBUTIONS AND CONCLUSION

In this chapter, the active array analysis from Chapter 3 is extended to include GaAs MMIC broadband continuous phase shifters in the beamformer network. Since the phase shifters are lossy, a driver amplifier is included in the chain. The active array is analyzed in an over-the-air simulation environment starting from signal generation at the system level, following with nonlinear circuit simulations (harmonic balance

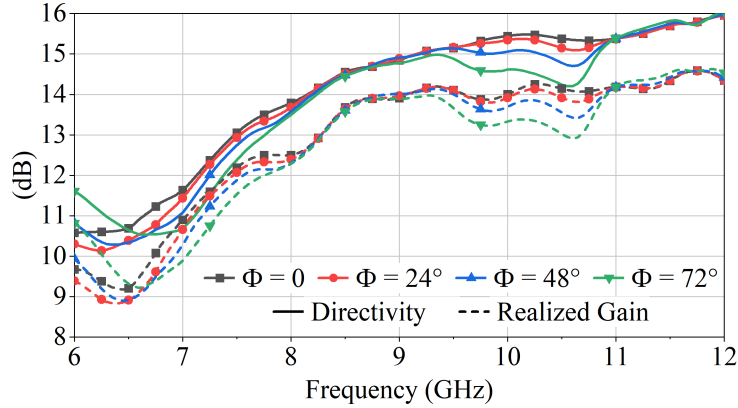


Figure 4.16: Maximum array directivity and realized gain (no beamforming included) over BW and $V_{\text{Control}1,2,3,4}$ set to a progressive phase shift of $\Phi = \{0, 24, 48, 72\}^\circ$ at 12 GHz.

Table 4.3: Simulated power budget of the designed Wilkinson power combiner when two uncorrelated sources generating two tones spaced of 200 MHz and 30 dBm each are combined into a two-tones output signal.

Parameter (dBm)	Frequency (GHz)						
	6	7	8	9	10	11	12
Total power @ Port1	29.8	29.7	29.6	29	29.1	29.1	29.2
Power tone 1 @ Port1	26.7	26.7	26.6	26.1	26	26.1	26.2
Power tone 2 @ Port1	26.8	26.7	26.6	25.9	26.2	26	26.3
Power dissipated R1 = 56 Ohms	22.7	22.5	22.5	22.6	22.9	23.4	23.9
Power dissipated R2 = 120 Ohms	26.7	26.8	26.9	26.9	26.8	26.6	26.1
Power dissipated R3 = 390 Ohms	24.6	24.6	24.6	24.4	24.3	24.3	24.5

in Cadence AWR MWO), with full-wave EM co-simulations in Ansys HFSS starting from the output of the final PAs to the far field of the antenna array. A large number of variables is included in the analysis to gain an understanding of array behavior: frequency (6–12 GHz); input power to each element (10–33 dBm); phase shift through control voltage in each element for beam steering (maximum value depends on frequency); drain supply voltage on each PA (for beam tapering, and later efficiency enhancement); signals transmitted through the array (single CW and two widely spaced modulated signals).

The array is designed to be modular, and an active module containing the phase shifters, drivers and PAs, and the accompanying control and bias circuit, is added for experimental demonstration of the analysis. At the time of writing, the array coupling matrix is measured showing a rotation in the scan active reflection coefficient at 6 GHz, a well matched behavior at 9 GHz and an inductive, flat behavior at 12 GHz. Also, a

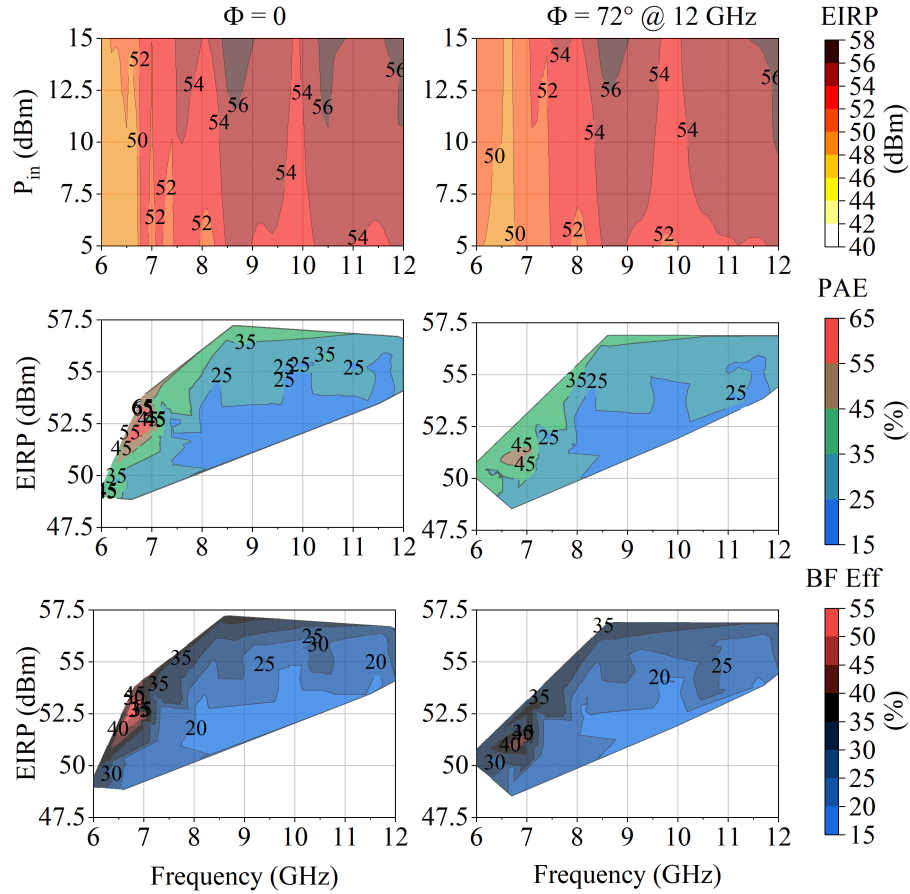


Figure 4.17: EIRP (top) as a function of P_{in} and frequency for two progressive phase shifts. PAE (middle) and beamforming (BF) efficiency (bottom) as a function of EIRP and frequency.

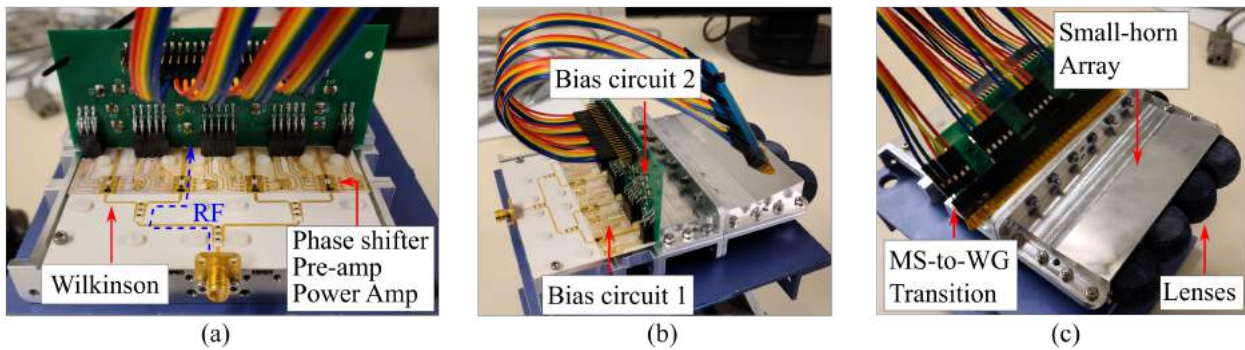


Figure 4.18: Photographs of 4-element transmit phased array prototype. (a) Beamforming network, (b) bias circuit, and (c) microstrip-to-waveguide transition and small-horn array.

broadband, high-isolation power combiner is designed and measured, allowing combining two concurrent signal for the array nonlinear characterization. A prototype is built integrating the antennas, transitions,

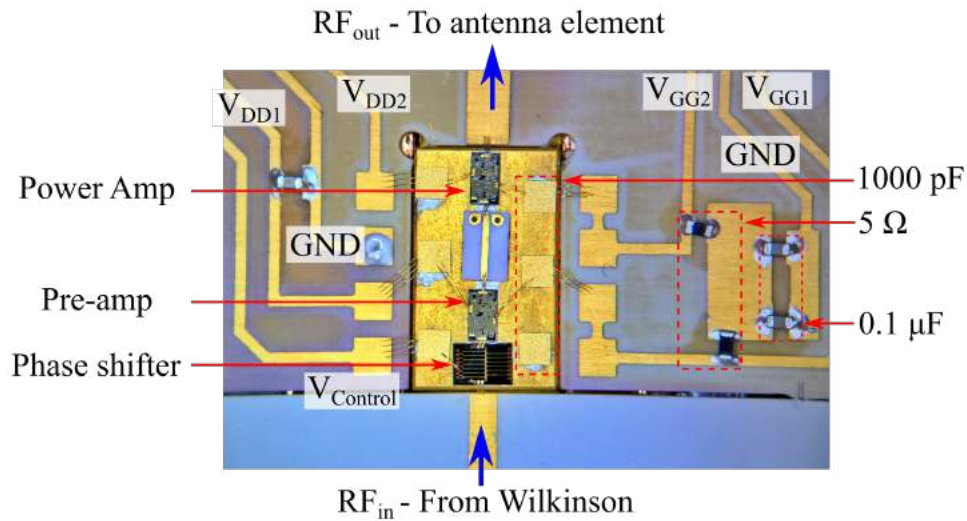


Figure 4.19: Closeup photograph of active element shown the three MMICs and bias circuit.

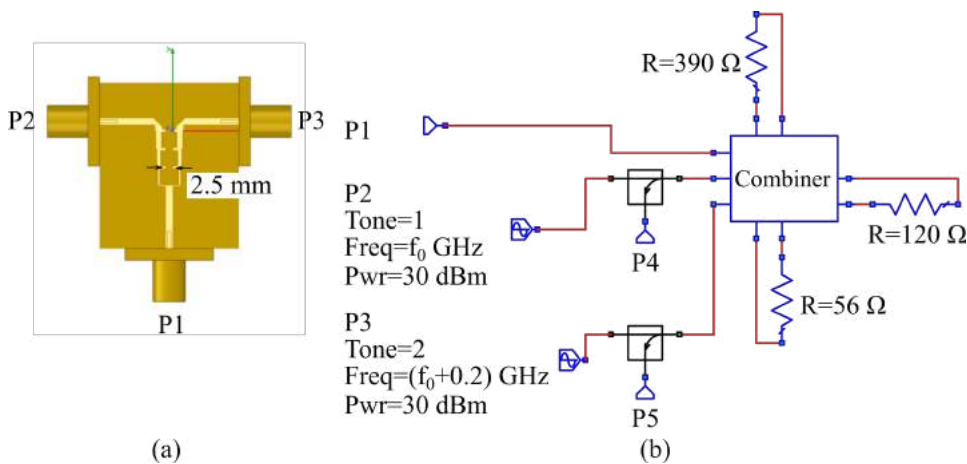


Figure 4.20: Simulation environment for determining the leakage between the ports and the power dissipated in the resistors for 0.2 GHz spaced two-tone signal.

beamforming network and bias circuits in a compact, scalable configuration. An OTA measurement setup is implemented for wideband, concurrent signals and supply-controlled measurements. NOTE: due to supply-chain delays, at the time of writing, a few hardware components necessary for final measurements were still not delivered. These measurements will be completed and added to a remaining journal publication otherwise ready for submission. The contributions of this chapter are included in [86], [87] (accepted), [89] (accepted) and [90](to be submitted).

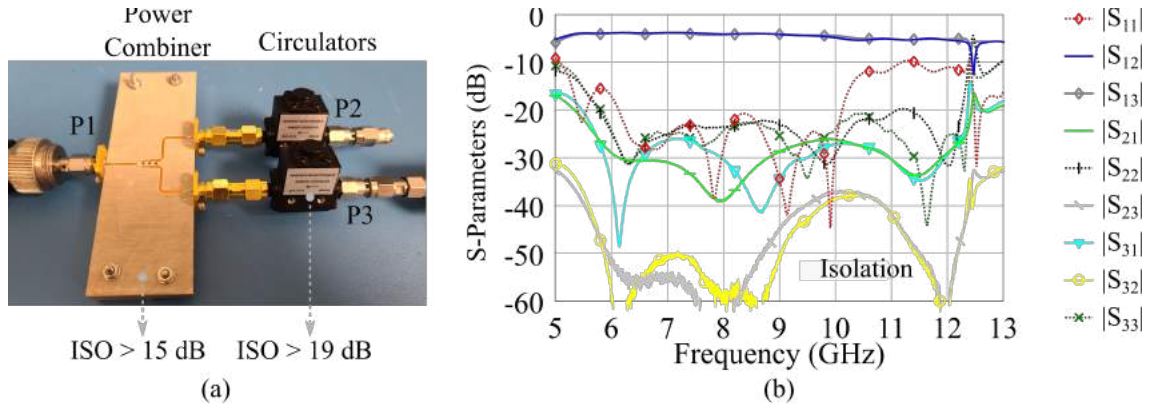


Figure 4.21: (a) Photo of divider with additional isolation provided by circulators. (b) Measured S-Parameters.

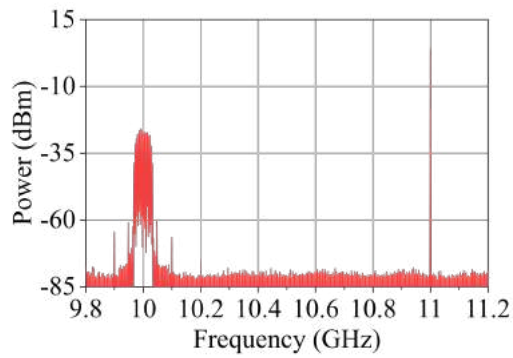


Figure 4.22: Spectrum of two signals input into the array: a QAM signal with 50 MHz bandwidth centered at 10 GHz and single tone at 11 GHz.

CHAPTER 5

BACKGROUND IN FRONT-END ISOLATION COMPONENTS FOR STAR ARRAYS

CONTENTS

5.1	CHAPTER OVERVIEW	77
5.2	FERRITE CIRCULATORS	78
5.3	SELF-BIASED CIRCULATORS	81
5.4	ACTIVE CIRCULATORS	82
5.5	CHAPTER CONTRIBUTIONS AND CONCLUSION	84

5.1 CHAPTER OVERVIEW

In the previous chapters, a detailed analysis of an active transmit phased array is presented, in both co-simulations and OTA measurements. Phased array are usually used to both transmit and receive, and several modes of operation are possible, as described in Chapter 1. When simultaneous transmit and receive at the same frequency is required by the application (continuous radar and some communication modes), the high-power transmitter interferes with the receiver through both free-space coupling and circuit-level

coupling. This can lead to instabilities, receiver LNA saturation translating to signal distortion, and excess noise, as well as ADC saturation after downconversion. Therefore, some isolation method is required to protect the receiver from transmitter leakage. Fundamentally, nonreciprocity is required to provide this type of isolation, and can be done either with a nonreciprocal medium, such as a ferrite, or with non-reciprocal circuit elements, such as transistors. Classical circulators implemented with magnetic nonreciprocity have been in use for a long time in microwave systems and remain essential components for transmit/receive front-ends, e.g. [91], [92]. However, commercial circulators require permanent magnets and can be bulky at the circuit level. Additionally, they are usually narrowband and broadband low-loss circulators are difficult to achieve. Therefore, integratable, chip form-factor solutions with low insertion loss have been the topic of research in the past decade.

This chapter introduces the second part of this thesis, focused on new design approaches of 3-ports circulators, and presents background needed to understand the designs presented in the next three chapters. The main goal is to achieve compact, low-loss components with high isolation over a wide bandwidth, amenable to integration in broadband phased arrays. The contributions are grouped in three main areas: weakly nonuniformly biased ferrite circulators; self-biased circulators with shape anisotropy; and active circulators using transistors and implemented in a MMIC.

This chapter is organized as follows. Section 5.2 describes the literature background on ferrite circulators and introduces the studies done in Chapter 6. Section 5.3 overviews a collection of works published on self-biased circulators and describes a new material used on experiments of Chapter 7. Finally, Section 5.4 introduces the active circulator design described in Chapter 8, and presents an overview of previous work done in transistor-based circulators and quasi-circulators.

5.2 FERRITE CIRCULATORS

This section provides a brief historical overview of ferrite circulator development. Early ferrite circulators employed Faraday rotation in metal waveguide technology, and a rich literature exists in this area. In this thesis, the focus is on more compact lower-power planar microstrip and stripline implementations. Externally

Table 5.1: Summary of commercially available ferrite circulators, manufacturers, and main specifications (collected in June 2019).

Manufacturer	Lowest BW		Highest BW		All products		
	Frequency (MHz)	BW (%)	Frequency (GHz)	BW (%)	Max VSWR	IL range (dB)	Isolation range (dB)
Centric RF	390 - 460	17%	8 - 18	77%	1.5	0.5 - 1.0	14 - 20
Wenteq	24 - 40	3%	6 - 18	100%	1.9	0.4 - 1.5	10 - 30
MCLI	180 - 225	22%	35 - 40	13%	1.8	0.3 - 1.3	10 - 35
Ditom	400 - 500	22%	37 - 40	8%	2.1	0.3 - 2.1	9 - 23
Teledyne Microwave	500 - 1000	100%	13 - 26.5	100%	1.5	0.5 - 0.8	16 - 20
Fairview Microwave	698 - 960	32%	18 - 26.5	38%	1.4	0.5 - 1.0	14 - 20
Cobham	62 - 72	15%	13.95 - 14.55	4%	1.25	0.25 - 0.6	18 - 25
Rf-Ci	800 - 2000	86%	2.7 - 6.2	79%	1.58	0.4 - 1.4	14 - 21
Trak	490 - 710	37%	18 - 26.5	38%	1.78	0.5 - 1.2	13 - 22
M2Global	2000 - 4000	100%	12.4 - 18	37%	1.35	0.4 - 0.5	15 - 20
Sierramicrowave	225 - 400	200%	26.5 - 40	41%	1.5	0.4 - 2.0	13 - 23

biased ferrite circulators were first studied in the 1950s, e.g. [93]. The theoretical framework for circulator design was established in the 60's [94], [95], and a dyadic Green's function based analysis is discussed in, e.g. [96]. Stripline circulators were first treated in the early 1960s, e.g. [94], [95], [97], [98]. Wideband designs with over 50% fractional bandwidth using different disk shapes are discussed in [99]. A ferrite circulator integrated with a Low-Temperature Co-fired Ceramic (LTCC) stripline circuit is simulated using full-wave numerical tools in [100]. Microstrip circulator design is presented in [101], [102] with broadband approaches discussed in [103] and including antenna-circulator integration in [104], [105]. For example, a 7-GHz microstrip circulator in a LTCC substrate using ferrite tape is shown in [106]. Thin-film devices have also been demonstrated, e.g. in [107].

In traditional designs, the magnetic bias is produced by a pair of cylindrical permanent magnets (PMs), in general larger than the ferrite disk, as shown in Fig.5.1. When the ferrite is fully saturated, the phase velocity is different in two directions of circulation due to the anisotropy. Therefore, a wave input at port 1 (P1) splits in two directions, and constructively interferes at P2, while cancelling at P3. The nonidealities introduce insertion loss between P2 and P1, and limited isolation between P3 and P1.

The analysis presented in Chapter 6 allows for more complex 3D permanent magnet configurations,

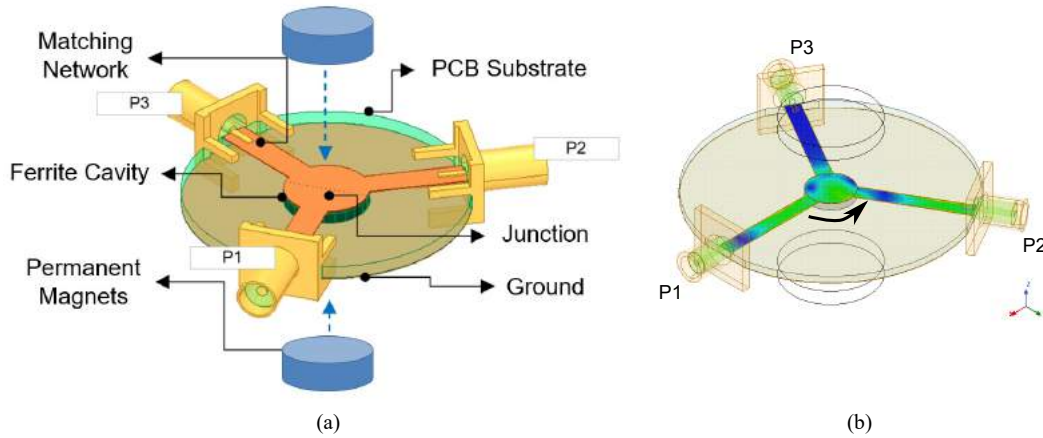


Figure 5.1: Conventional geometry of a Y-junction ferrite circulator. The permanent magnets (PMs) produce a magnetic bias field (MBF) in the ferrite. A wave input at port P1 is transmitted to P2 with low insertion loss while P3 is isolated (counterclockwise circulation) or transmitted to P3 with P2 isolated (clockwise), depending on the resonator mode and direction of MBF. The microstrip junction is above the ferrite disk and the permanent magnets (shown here as an array) are placed immediately above and below the disk.

such as the small-magnet arrays, which allows the same ferrite resonator to be used for circulators at frequencies across more than two octaves. The nonuniform magnetization that results from the configuration of permanent magnets shown in Fig.6.1 can lead to weakly-biased regions inside the ferrite cavity, as will be discussed in Chapter 6. Most of the high-end, full-wave EM simulators, such as HFSS, use Polder's model to calculate the ferrite permeability tensor $[\mu]$, which assumes that the ferrite is operated in saturation. In general, however, the net magnetization can vary from point to point within the ferrite, and the Polder model used in HFSS becomes inaccurate. In order to best use the full-wave analysis tool, we recognize this limitation and set the external magnetic bias field (MBF) at a lower value than M_s where the ferrite is not fully saturated. With this approximation, we find that the analysis agrees well with measurements, while allowing us to take advantage of the power of full-wave simulations of a ferrite disk with matching networks and the real magnetic bias structure.

As discussed above, the MBF is generally not constant throughout the disk and the strength of the magnets may not be sufficient to fully saturate the ferrite. Unsaturated ferrites are discussed in [108], and partially magnetized ones are studied in [109], [110]. The effect of demagnetization is further discussed in [111], [112], [96]. A reduction in bandwidth due to a nonuniform magnetic field is detailed in [113] and validated at X-band. In [114], a comparison is performed between a computed nonuniform MBF and full-

wave electromagnetically simulated uniform one (using Ansys HFSS), showing that nonuniformity should be taken into account.

5.3 SELF-BIASED CIRCULATORS

The largest drawback of ferrite circulators is the need for a fairly strong external dc magnet. This has made it impossible to integrate them in semiconductor processes and make them more compact. Therefore, a significant amount of research has been devoted to developing self-biased ferrites, which have a built-in magnetization without the presence of an applied magnetic field. Different fabrication methods include sintering process of hexaferrites and electro- spinning and plating of magnetic nano-composite (MNC) materials [115]. One of the technologies that has been commercialized is based on thin-film hexaferrites [116]. These materials are useful for circulators and isolators at Ka-band and above with isolation limited to 15 dB [117], and have not been demonstrated at lower microwave frequencies and in the band of interest in this thesis (6–12 GHz).

Other materials that enable low-temperature fabrication compatible with front and backside MMIC processing have especially become a focus of research for full integration in, e.g. a GaN-on-SiC, leading to the potential integration with amplifiers in monolithic microwave integrated circuits (MMICs) [118]- [119]. Unlike hexaferrites [116], [120], magnetic nano-composite (MNC) materials have the advantage of operating at X-band and below. These materials are under development at Argonne National Lab, using both electro-spinning and electro-plating fabrication techniques [115, 121, 122]. Briefly, a ceramic substrate, such as alumina (aluminum oxide), is micro-machined with vertically-oriented cylindrical holes, roughly 50 nm in diameter, which are then filled with a magnetic material such as iron nickel. The material is then poled with a permanent magnet, and retains magnetization which is now anisotropic due to its geometry, referred to as shape anisotropy. The process is not fully developed, resulting in material properties that are generally nonuniform. As a result, the ferrite disk can operate in unsaturated conditions. This gives further motivation to investigate the impacts of nonuniform biasing and non-saturated magnetization on circulator performance.

Chapter 7 presents a circulator design approach using initial results on electro-plated MNC materials.

Figure 5.2 shows the hybridly integrated microstrip circulator packaging design that uses a 0.1-mm thick MNC iron-nickel plated sample. The implemented circulator operates in X-band, and the design process includes a sensitivity simulation study and experimental results showing non-reciprocal behavior without external dc magnetic biasing.

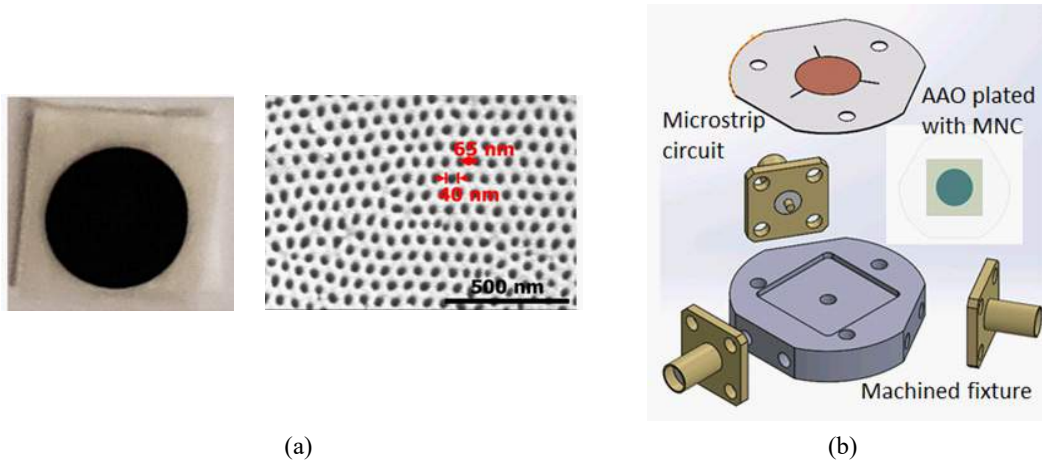


Figure 5.2: (a) Fabrication of plated magnetic nano-composite materials uses an aluminum oxide (AAO) porous template (a) filled with iron-nickel. (b) Photograph of circulator that uses a magnetic nano-composite (MNC) material as the non-reciprocal medium.

5.4 ACTIVE CIRCULATORS

Non-reciprocal behavior of transistors can be used to achieve circulation and was first presented in 1965 [123]. Later, a variety of architectures were further explored, e.g. [124]. In these devices, the distinction is made between active 3-way circulators with full rotational symmetry as in a ferrite device, and quasi-circulators that have isolation between two of the ports but do not have full circulation. An excellent overview of CMOS-based quasi-circulators is given in [125], with a summary table adapted in Table 5.2. Active circulators are also demonstrated in GaAs, e.g. [126], [127], [128], and recently in GaN [129].

In [130] a mixed integrated active circulator based on a GaN MMIC power amplifier design and Wilkinson power dividers implemented in PCB and connected with bond wires is reported. It claims the advantages of high integration, small circuit size and high power capacity. Power and noise limitations are discussed in [131].

Table 5.2: Examples of CMOS active quasi-circulators works from 2010 to 2020. Extracted from [125].

Ref Year	Process	Parameter										
		Freq (GHz)	BW (%)	S31 (dB)	S21 (dB)	S32 (dB)	S23 (dB)	S12 (dB)	S13 (dB)	S11 (dB)	S22 (dB)	S33 (dB)
[136] 2010	180-nm CMOS	29 - 31	7	12	4–6	7.2–7.9	24	22	35	6	5	11.5
[137] 2017	45-nm CMOS SOI	22.7 - 27.7	20	18.5	3.3	3.2	5	7	8	10	10	14
[135] 2017	45-nm CMOS SOI	5.3 - 7.3	32	30	10.5 (gain)	5	NA	25	NA	10	10	10
[138] 2018	180-nm CMOS	0.8 - 6.8	158	27	8–10	9–12	28	20	15	3	5	5
[139] 2019	180-nm CMOS	1 - 7	150	36	10	9	30	15	30	6	10	11
[140] 2020	180-nm CMOS	1 - 8	156	34	8	2.5	16	34	33	8.5	11	8.5

CMOS circulators are mostly done in a quasi-circulator topology and have trade-offs between power handling and noise figure. For example, a comprehensive diagram shown in [125] depicts that most of the state-of-the-art works do not exceed $IP1dB=22$ dBm in the Tx-Antenna path. The tradeoff between power handling and noise in CMOS technology can be observed in some recently published works. In [132], an X-band quasi circulator is implemented with a low-noise amplifier (LNA) in 65-nm CMOS process, presenting Rx noise figure $NF=1.05$ dB and $IP1dB=-15$ dBm. In [133], a 0.914–1.086 GHz $IP1dB=34$ dBm and Rx $NF=2.5$ dB is presented. In [134], a combination of common-source, common-gate and common-drain configurations is applied to the design of a 180-nm CMOS quasi-circulator presenting $IL \leq 6$ dB and isolation better than 18 dB over the 1.5–9.6 GHz. Port mismatch is better than 5 dB from 4.5–9.6 GHz. In [135], a tunable distributed topology build on 45-nm CMOS SOI technology is reported, presenting isolation better than 30 dB, $IL=5.0$ dB, $IP1dB=18$ dBm, and Antenna-RX $NF=20$ dB for a 5.3–7.3 GHz tuning range.

Chapter 8 describes an active MMIC circulator design, where circulation is accomplished by connecting three unconditionally stable, gain-matched, single-stage equal amplifiers with three asymmetric Lange couplers. Figure 5.3 shows the circuit schematic in the context of a transmit-receive front-end module. The circuit is designed in a closed loop configuration where the *through* ports are connected to the amplifier inputs, and the *coupled* ports to the outputs. The isolated ports are terminated in $50\text{-}\Omega$ resistors and the

Lange coupling coefficient specified to achieve a trade-off between backward isolation ($|S_{31}|$) and forward gain ($|S_{21}|$), while ensuring stability. The forward gain of the circulator is proportional to the amplifier gain, reduced by the *coupling* and *through* attenuation of the Lange couplers. Although a PA, LNA and antenna are shown in Fig. 5.3, the component is a full (not quasi) circulator as it has rotational symmetry. Chapter 8 further details the design in a MMIC manufactured in a Qorvo 250-nm GaAs process.

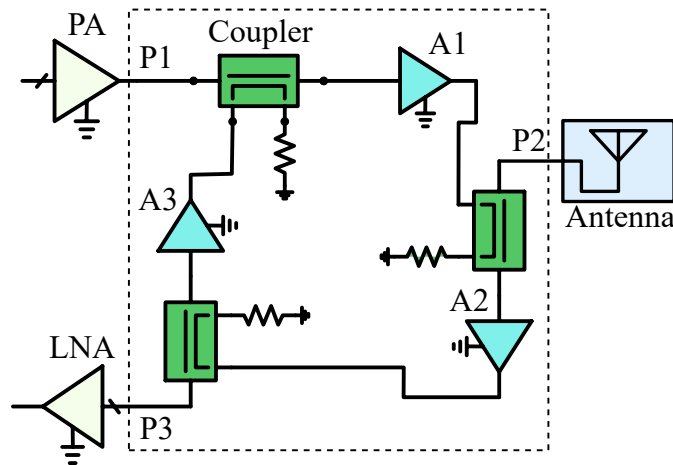


Figure 5.3: Block diagram of an active circulator topology implemented in this thesis in a GaAs MMIC. When port 1 (P1) is the input, P2 is the output and P3 isolated. The PA, LNA and antenna of the transmit-receive front end are shown for context.

5.5 CHAPTER CONTRIBUTIONS AND CONCLUSION

This chapter presents background on circulator topologies that potentially enable better integration in transmit-receive front ends for STAR phased arrays, and provides motivation for material presented in the second part of the thesis in Chapters 6, 7, and 8, which deal with isolation between transmit and receive paths in the front-end module. Parts of this chapter are reported in [34], [141], [142], [35], [39], [143].

CHAPTER 6

DESIGN OF FERRITE CIRCULATORS

CONTENTS

6.1	CHAPTER INTRODUCTION	85
6.2	CAD-BASED DESIGN OVERVIEW	87
6.3	FERRITE BEHAVIOR AS A FUNCTION OF THE TOTAL INTERNAL FIELD AND FREQUENCY	90
6.4	EFFECTS OF HIGH-INTENSITY MBF ON CIRCULATOR BANDWIDTH	92
6.5	EFFECT OF FERRITE GEOMETRY ON DEMAGNETIZATION AND TOTAL INTERNAL FIELD	93
6.6	DISTRIBUTION OF THE APPLIED MAGNETIC BIAS FIELD	97
6.7	EXPERIMENTAL VALIDATION	98
6.8	CHAPTER CONCLUSIONS AND CONTRIBUTIONS	104

6.1 CHAPTER INTRODUCTION

This chapter presents a study of the impact of different external magnetic bias field distributions on Y-junction microstrip ferrite circulator performance. For a fixed standard commercially-available ferrite disk, it is shown that applying different MBF distributions, implemented with various permanent magnet (PM) configurations, can result in a wide range of performance parameters. Aspects such as operating frequency,

bandwidth, matching, insertion loss, and isolation are analyzed and compared. It is important to highlight that this study does not intend to demonstrate state-of-the-art circulator performance, but rather to give insights to the designer of how to use available CAD tools and the MFB distribution for achieving specific design parameters.

In analogy to the co-simulations with system-level, nonlinear circuit and full-wave tools used in Chapters 2, 3, and 4, co-simulations are done in this chapter with magneto-static, full-wave and circuit commercial simulation tools. This enabled design using a circular ferrite disk, with several permanent magnet (PM) configurations for unsaturated and nonuniform bias conditions. Eigenmode simulations are used to analyze the circulator bandwidth over a range of magnetic bias field intensities. It is shown in simulations and experiments that different bias conditions can result in an operating frequency range from 1.5 to 7 GHz using the same 9.7-mm diameter commercial ferrite disk resonator. A general geometry of the microstrip ferrite circulator is shown in Fig.6.1. Here we allow different permanent magnet geometries, such as the array of small magnets shown in the figures.

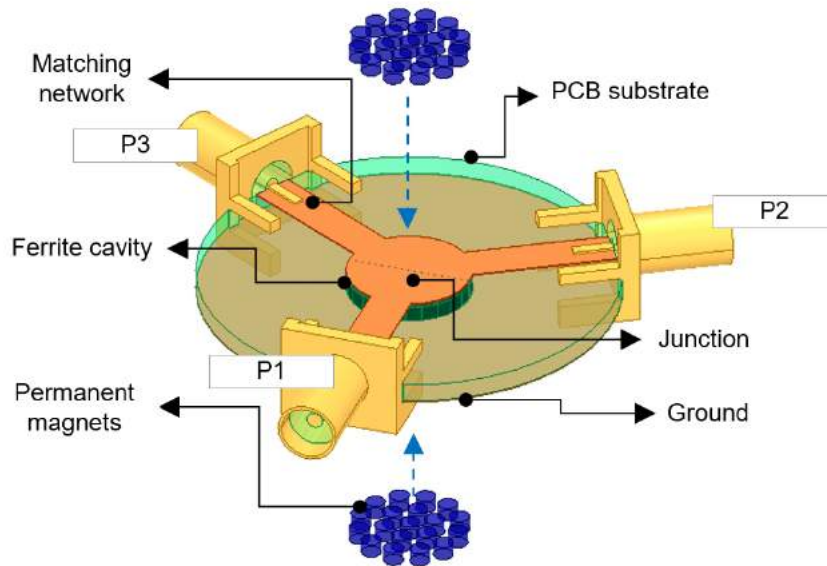


Figure 6.1: Overall geometry of a Y-junction ferrite circulator. The permanent magnets (PMs) produce a magnetic bias field (MBF) in the ferrite. A wave input at port P1 is transmitted to P2 with low insertion loss while P3 is isolated (counterclockwise circulation) or transmitted to P3 with P2 isolated (clockwise), depending on the resonator mode and direction of MBF. The microstrip junction is above the ferrite disk and the permanent magnets (shown here as an array) are placed immediately above and below the disk.

In Section 6.2, a CAD-based design approach using commercial tools is overviewed. Section 6.3

discusses the ferrite effective permeability behavior over magnetic field bias and frequency. In section 6.4, the effects on circulator behavior are analyzed when a magnetic bias field above saturation is applied. Section 6.5 discusses the influence of disk geometry on demagnetization and the effects on the total internal magnetic field. Section 6.7 introduces non-traditional biasing geometries and a study of the distribution of the applied MBF for different PM physical configurations. The theoretical and simulation results are validated in Section 6.8 by measurements of three prototype designs that use the same commercial ferrite disc but operate in three distinct bands around 1.6, 4.3, and 7 GHz.

6.2 CAD-BASED DESIGN OVERVIEW

Figure 6.2 gives more details pertaining to the main geometric parameters of a microstrip ferrite circulator from Fig.6.1. The ferrite disk is embedded in the PCB substrate on top of the ground plane and is in general thinner than the substrate. Ferrite materials are extensively discussed in the literature, e.g. [144]. The main parameters given for a commercial ferrite material are magnetization saturation ($4\pi M_s$ usually in Gauss), ferromagnetic (FMR) linewidth (ΔH in oersted), relative permittivity (ϵ_r) and initial relative permeability (μ_r). The parameters that are chosen or determined during the design are the external magnetic bias field (MBF), internal magnetic field (H_0 in Oe), Larmor or free-precession frequency (f_0), the ferromagnetic (FMR) resonant frequency (f_r), the permeability tensor [μ] and the effective (scalar) permeability (μ_{eff}).

Figure 6.3 illustrates a simplified flowchart for determining dimensions of a microstrip circulator, for a baseline design which assumes a uniformly saturated ferrite with an operating bandwidth below the FMR. Then, assuming an infinite material, we set $\text{FMR}=f_0$ and calculate the resulting internal field as

$$H_0 = f_0/\gamma, \quad (6.1)$$

where $\gamma = 2.8 \text{ MHz/Oe}$. Then we set $\text{MBF}=H_0$, giving a saturation magnetization $4\pi M_s = H_0$ in the CGS system of units where $\mu_0 = 1$ and M_s is in gauss. Now a material can be chosen based on the specified value of M_s , and the FMR linewidth ΔH is then also given. For example, given a center frequency of 3.8 GHz, the calculated $\text{FMR}=4.9 \text{ GHz}$ and $M_s = 1750 \text{ G}$. The Skyworks TT1-105 ferrite material has this value of M_s

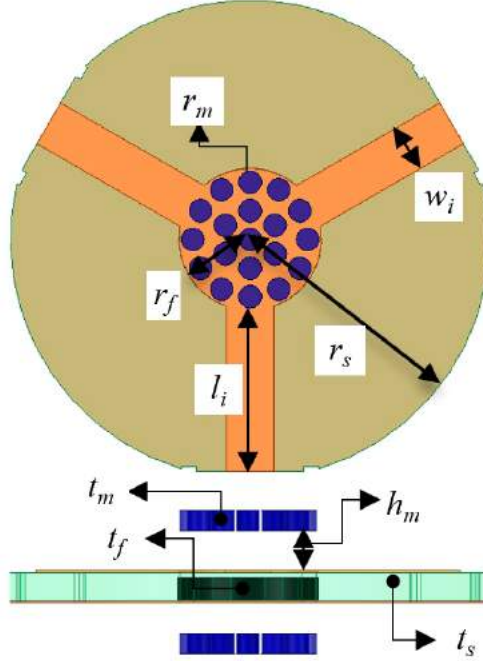


Figure 6.2: Relevant dimensions of a Y-junction microstrip circulator: ferrite radius r_f and thickness t_f ; microstrip dielectric substrate thickness t_s ; microstrip line length l_i and width w_i . The magnets have radii r_m and thicknesses t_m and are h_m above and below the copper layers on the two sides of microstrip substrate.

and losses characterized by $\Delta H = 280$ Oe [145]. The ferrite disk initial dimensions are next calculated from $[\mu]$ and μ_{eff} according to standard equations given in, e.g. [146]. For the given center operating frequency, the FMR is placed about 30% higher, and the disk thickness is chosen to be 10% of its diameter, which is the minimum commercially available thickness.

Now that the radius of the ferrite resonator is determined, we perform electromagnetic simulations towards a baseline design of a microstrip circulator, as illustrated in Fig.6.4. A driven full-wave simulation is next performed with a uniform MBF. In HFSS, for instance, we suggest starting with an internal MBF of $\vec{H}_0 = \mu_0 \vec{M}_s$, converted from CGS to SI units. In this simulation, a substrate with a minimum thickness equal to that of the ferrite disk can be used, and the junction geometry (top microstrip metal) is placed immediately above the disk and initially has the same radius. The realistic nonuniform MBF is introduced through magneto-static co-simulations with a tool such as Ansys Maxwell3D. The nonuniformity can result in a frequency shift, increase in insertion loss and degradation in isolation, requiring design modifications.

Additional eigenmode analysis can be performed to evaluate the effect of nonuniform MBF due to

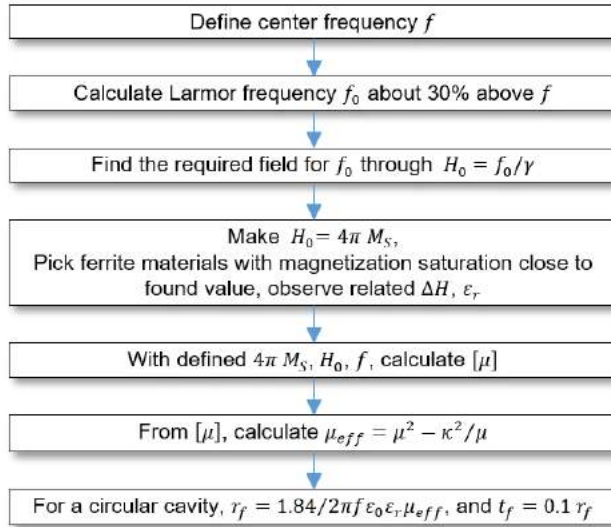


Figure 6.3: Procedure for determining dimensions for a circular uniformly saturated ferrite disk, operating below FMR.

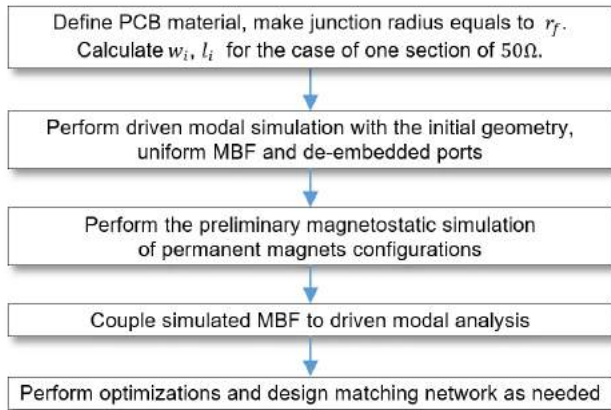


Figure 6.4: Steps for full-wave and magnetostatic simulations for microstrip circulators with nonuniform MBF at different levels of saturation resulting from realistic permanent magnets.

demagnetization for different ferrite shapes. Coupled magneto-static and full-wave RF simulations are useful in the trade-off between size and performance, and will be discussed in detail in the next section. The design is performed with 50- Ω ports and microstrip lines which are de-embedded to determine the complex impedance at the edge of the ferrite disk. An impedance-matching network is then designed to trade off return loss, isolation and bandwidth.

6.3 FERRITE BEHAVIOR AS A FUNCTION OF THE TOTAL INTERNAL FIELD AND FREQUENCY

One way to examine ferrite behavior in the context of a microstrip circulator is first to consider an infinite material approximation and evaluate μ_{eff} as a function of frequency and total internal field. The well-known expression of the scalar complex effective permeability depends on the relationship between the magnetization vector \vec{M} , the magnetic flux density \vec{B} , and permeability tensor $[\mu]$:

$$\vec{B} = \mu_0(\vec{H} + \vec{M}) = \mu_0(\vec{H} + [\chi]\vec{H}) = [\mu]\vec{H} \quad (6.2a)$$

$$[\chi] = \begin{bmatrix} \frac{f_0 f_m}{f_0^2 - f^2} & j \frac{f f_m}{f_0^2 - f^2} & 0 \\ -j \frac{f f_m}{f_0^2 - f^2} & \frac{f_0 f_m}{f_0^2 - f^2} & 0 \\ 0 & 0 & 0 \end{bmatrix} \quad (6.2b)$$

$$[\mu] = \mu_0(I + [\chi]) = \begin{bmatrix} \mu & j\kappa & 0 \\ -j\kappa & \mu & 0 \\ 0 & 0 & \mu_0 \end{bmatrix} \quad (6.2c)$$

$$\mu_{eff} = \frac{\mu^2 - \kappa^2}{\mu} \quad (6.2d)$$

where $[\chi]$ is the susceptibility tensor for an infinite material, f_0 is the Larmor frequency and f_m is the precession frequency at saturation. When the RF frequency $f = f_0$, the disk is close to resonance (FMR) and all RF power is transferred to the spins [147]. If the material shows no loss, the permeability tensor components experience a singularity at this frequency. However, damping exists and is characterized by ΔH . The loss can be taken into account when computing the permeability tensor components by defining a complex resonant frequency \hat{f}_0 :

$$\hat{f}_0 = f_0 + j \frac{\Delta H \mu_0 \gamma}{2 f_{FMR,m}} \cdot f \quad (6.3)$$

where $f_{FMR,m}$ is the frequency where ΔH is measured.

Figure 6.5 shows the behavior of $[\mu]$ components and μ_{eff} over frequency for the TT1-105 ferrite

material, with $M_s = 1750$ G, $\Delta H = 280$ Oe and $f_{FMR,m} = 9.4$ GHz. The figure illustrates the regions below and above the FMR for a fixed and uniform $H_0 = 1750$ Oe. The singularity points do not reach infinite values since ΔH is different from zero. There is also a 2-GHz shift in the zero crossings of components of $[\mu]$ and μ_{eff} , resulting from the Larmor and FMR frequencies. This plot is useful for design since it points to the frequency ranges that should be avoided to achieve low-loss operation, but it only gives an indication for one fixed value of the MBF.

Off-the-shelf ferrite materials typically have values for M_s in the range 90 to 5000 G, ΔH from 0.5 to 2500 Oe and can operate between 0.02 and 94 GHz [148]. By observing Fig.6.5, we notice that there is a frequency shift in μ_{eff} relative to the Larmor frequency, and therefore we study the dependence of the complex μ_{eff} on frequency and H_0 to identify high absorption regions. An example is shown in Fig.6.6 for the TT1-105 material. The real (blue) and imaginary (yellow) effective permeability μ_{eff} is shown over a frequency range $f = [1; 8]$ GHz and for a theoretical internal magnetic field of $H_0 = [1000; 3000]$ Oe. The graph clearly shows the low-loss regions above and below the FMR. The 2D plots illustrate the local behavior with one of the variables fixed. Note that the μ_{eff} approach is restricted to geometries where the RF wave propagation is transverse to the bias, as in the case of a microstrip circulator.

At this point, it is worth clarifying the nomenclature adopted for the regions of operation of a circulator throughout this paper: in the circulator industry, a below-resonance circulator operates below FMR and is also referred to as a weakly-biased circulator. An above-resonance circulator operates above FMR and is also referred to as a strongly-biased circulator. However, we understand that, no matter what the level of magnetization is, an FMR region will occur and it is simultaneously frequency and magnetization dependent, as seen in Fig.6.6. Thus, we chose the nomenclature “above” and “below FMR” by splitting the operation regions based on the high loss area in multi-parameter space. Even though Fig.6.6 shows the concurrent dependence of μ_{eff} using Polder’s model, the same analysis can be done by using models for weakly biased ferrites, available in [149], [109], and [150].

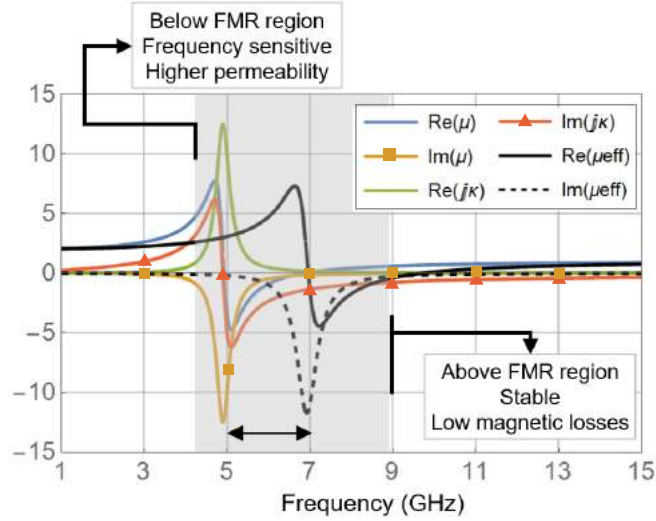


Figure 6.5: Real and imaginary parts of κ , μ and μ_{eff} over frequency for TT1-105 ferrite material parameters. The shaded area indicates the region of high absorption.

6.4 EFFECTS OF HIGH-INTENSITY MBF ON CIRCULATOR BANDWIDTH

The effects of MBF with intensities higher than the magnetization saturation are next studied through a comparison between modal analysis and driven simulations. A thin disk is biased with a uniform internal field in the z -direction and has the internal magnetic flux density radial dependence proportional to Bessel functions [94]:

$$B_{\pm n} \propto J'_n(k\rho) \pm \frac{n\kappa}{k\rho\mu} J_n(k\rho) \quad (6.4)$$

where n is the mode number, $J_n(k\rho)$ is the n -th order Bessel function, and k is the wavenumber.

The sum of Bessel functions given in Eq.(6.4) can be plotted as a function of frequency, and is shown in Fig. 6.7. The plot shows resonances (zeros) for $n = \pm 1$ and $H_0 = \mu_0 M_s$, $2\mu_0 M_s$ and, $3\mu_0 M_s$. We observe that the zero-crossings are closer to the resonances calculated with μ_{eff} (scalar - green line) as the MBF increases. This result is expected since the ratio κ/μ decreases. The corresponding S -parameters are shown in the lower plot. Note that the optimum MBF is not the highest one. In fact, there is a decrease in bandwidth with increasing MBF, indicating that the distance between zero-crossings is affected by the bias field magnitude, and therefore affects device bandwidth. This can be seen in the driven simulation by

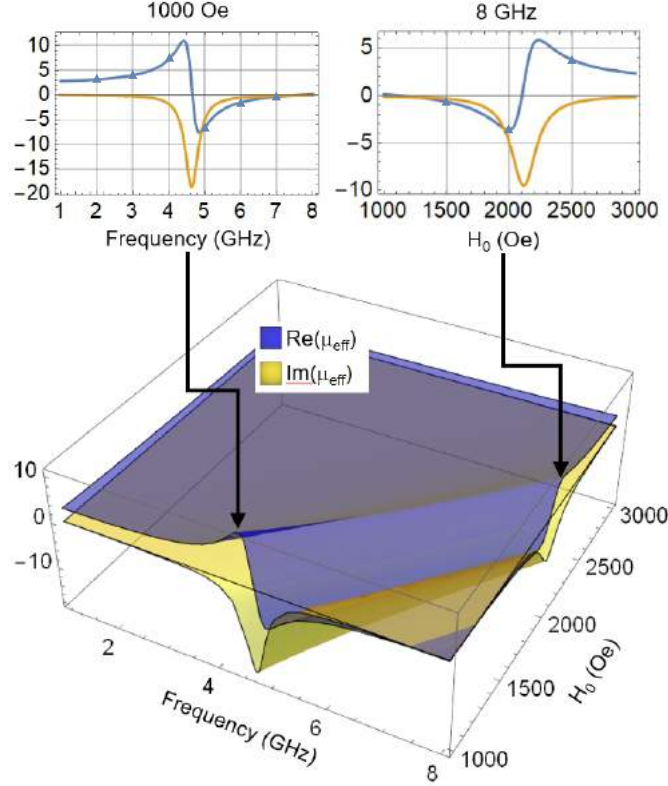


Figure 6.6: Simulated real (blue, triangle) and imaginary (yellow) effective relative permeability μ_{eff} for the Skyworks TT1-105 material over a frequency range $f = [1; 8]$ GHz and $H_0 = [1000; 3000]$ Oe. The 2D graphs in the insets illustrate the local behavior with one of the variables fixed.

observing the S -parameters of the device obtained under the different MBF conditions.

6.5 EFFECT OF FERRITE GEOMETRY ON DEMAGNETIZATION AND TOTAL INTERNAL FIELD

For a finite ferrite size, boundary conditions must be met at the edges of the disk, resulting in a demagnetizing field which varies within the ferrite volume [112] and changes the magnetization vector. It can be described as a tensor, with components referred to as *demagnetization factors*. The relationship between the demagnetization field and factors is given by

$$\vec{H}_i^{(dem)} = 4\pi \sum_j N_{ij} \vec{M}_j \quad (6.5)$$

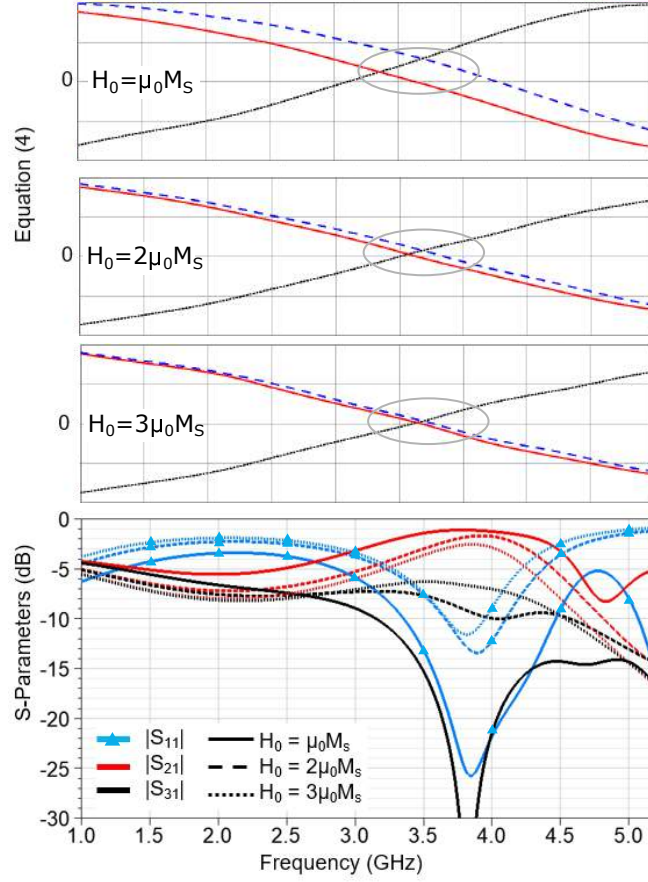


Figure 6.7: Resonance analysis for $n = 1$ and $H_0 = \mu_0 M_s, 2\mu_0 M_s, 3\mu_0 M_s$ plotted with S -parameters, showing a relationship between the Eq.(6.4) zero crossing, bandwidth and MBF intensity. Three cases are traced: one considering μ_{eff} as a scalar isotropic quantity (red - solid) and two counter-propagating modes resulting from a tensor $[\mu]$ (dotted and dashed). The lower plot shows the S parameters resulting from the driven analysis for the three cases of the internal field.

where i is the component of the demagnetizing field, \vec{M}_j refers to the (ρ, ϕ, z) or (x, y, z) components of the magnetization vector, and N_{ij} are the demagnetization factors. The total internal field, H_0 (in Oe) depends on the applied MBF and the demagnetization factors. For a ferrite disk, we assume a z -oriented magnetization of magnitude $M_z = M_s$. For a thin disk the expression for the internal field is given by [151]:

$$H_0 = MBF - H_i^{dem} \quad (6.6)$$

To illustrate, the demagnetization for a 5-mm radius cylindrical ferrite is plotted in Fig.6.8 as a function of radius and for different thicknesses t_f using equations established in [112]. It shows that thinner cavities exhibit a more uniform demagnetization factor over the cross section, but with a higher magnitude.

The demagnetizing fields change the FMR according to the Kittel relationship [152] causing a drift in

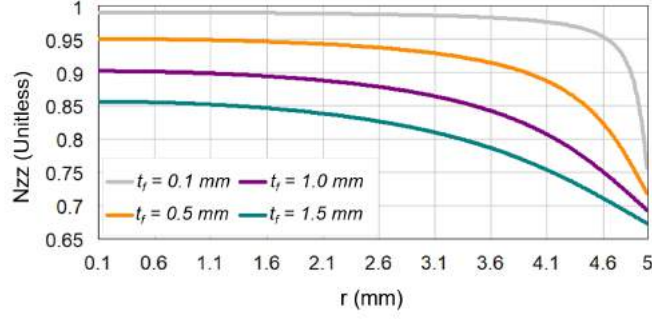


Figure 6.8: Demagnetization factor in a cylindrical dielectric magnetic resonator as a function of radius and thickness.

frequency:

$$f_r = \gamma \sqrt{[H_z + (N_y - N_z)M_z] \times [H_z + (N_x - N_z)M_z]}$$

$$= \gamma [H_0 - N_{zz}M_s]$$

for $N_y = N_x = 0$, $N_z = N_{zz}$, $H_z = H_0$, $M_z = M_s$.

The effects of thickness variation are addressed by eigenmode simulations. This type of CAD analysis, by its nature, does not include the excitation. For a useful eigenmode analysis, we first calculate the normalized tensor $[\mu]/\mu_0$ at the center frequency, and then assign the values to the μ_{eff} field in the material properties. Perfect electric boundaries are applied on top and bottom faces of the disk. The size of the air box is a trade-off between convergence speed and minimum frequency of simulation to avoid overlap with air-box resonances, as illustrated in Fig.6.9. An eigenmode analysis (e.g. in HFSS) can give insight into the behavior of the disk alone.

Fig.6.10 presents the result of such an analysis for different ferrite disk shapes, which will result in different demagnetization profiles. The analysis is performed using the relative permeability as a scalar μ_{eff} , calculated from the Skyworks TT1-105 material parameters and $H_0 = 1750$ Oe at $f = 3.5$ GHz. The plot shows the resonant frequency and Q -factor for a square, circular and triangular thin ferrite, as a function of the thickness. As thickness increases, there is an upward shift in frequency, as well as an increase in unloaded Q -factor and it can be explained through the fact that demagnetization factors and phase velocity inside the disk change with geometry. The triangular case shows the most pronounced effect of

demagnetization.

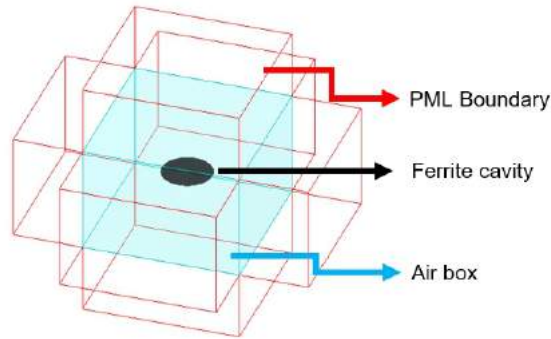


Figure 6.9: Geometry for eigenmode simulations showing the empirically determined limits for the air box ($0.35\lambda_0 \times 0.35\lambda_0 \times 0.25\lambda_0$ at 3.5 GHz) and absorbing boundary condition boxes with the largest dimension of $0.65\lambda_0$.

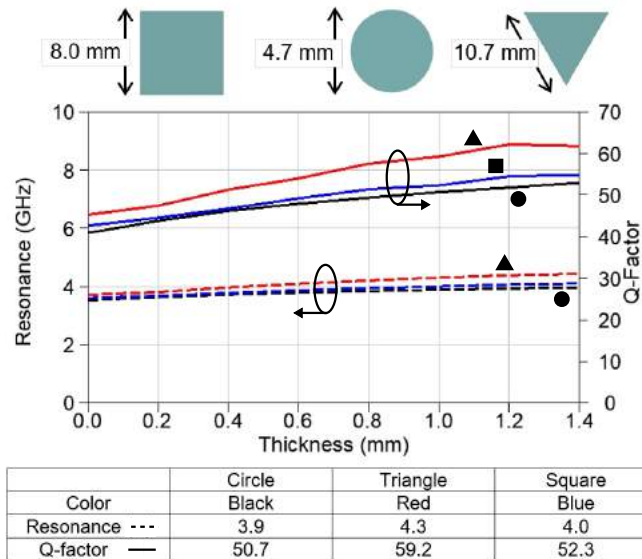


Figure 6.10: Eigenmode analysis for resonant frequency and unloaded Q -factor for three canonical disk shapes as a function of disk thickness. A scalar μ_{eff} is used in the HFSS simulations, calculated from Skyworks TT1-105 material parameters and with $H_0 = 1750$ Oe at $f = 3.5$ GHz. For example, for a thickness of 1.0 mm (table), the circular disk is resonant at 3.9 GHz with a corresponding $Q=50.7$.

Thickness variations can also substantially change the relation between dielectric and conductor losses, resulting in frequency shifts and increased insertion loss. Figure 6.11 shows the simulation results for a thickness variation of $t_f = [0.21; 1.41]$ mm. A shift to higher frequencies can be observed as thickness increases, agreeing with the results obtained by eigenmode simulations from Fig.6.10. Furthermore, an increase in $|S_{21}|$ and improvement in $|S_{31}|$ and $|S_{11}|$ is observed for larger t_f , consistent with the Q -factor

increase with larger disk volume.

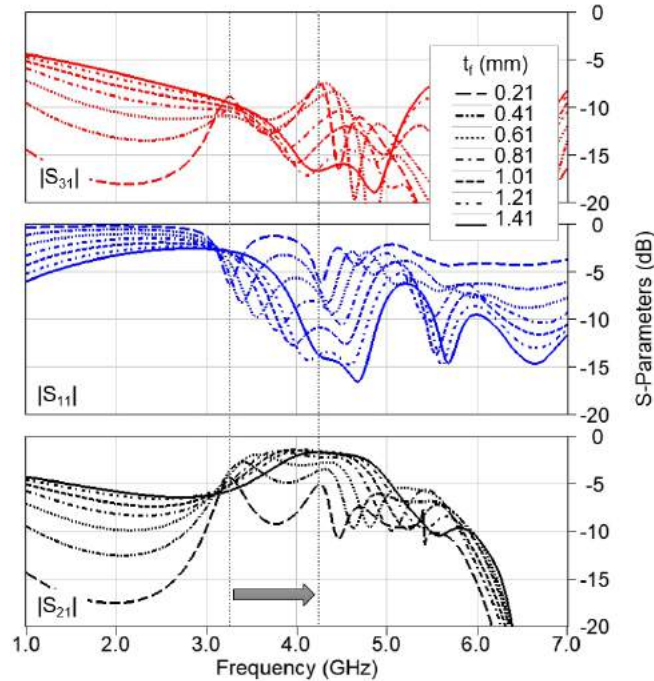


Figure 6.11: Parametric driven simulation for a variation of the disk thickness $t_f = [0.21; 1.41]$ mm. The disk has a circular cross section and is designed from equations given in (4) and (5). Material parameters are defined by Skyworks TT1-105 datasheet biased with a MBF $H_0 = 1750$ Oe. The grey arrow shows the shift in resonance as thickness increases.

6.6 DISTRIBUTION OF THE APPLIED MAGNETIC BIAS FIELD

The MBF distribution generated by permanent magnets (PMs) depends on factors such as grade, shape, and distance from the ferrite disk. This distribution will affect RF performance. For example, Fig.6.12 shows MBF distributions with the change in distance h_m of a pair of cylindrical rare-earth PMs *HKCM* NdFeB-N35 [153] with a thickness $t_m = 3$ mm and diameter $d_m = 18$ mm. The MBF distribution is simulated for two cases: $h_m = 0.01$ and $h_m = 15$ mm. The top of Fig. 6.12 shows that the total variation of the magnetic bias field goes from 260 to 30 kA/m as the PMs are separated. The bottom of the figure shows the magnetic flux density distribution, where the weaker field appears in the center for $h_m = 0.01$ mm, while the intensity is higher in the center for $h_m = 15$ mm.

Next, we consider a different PM distribution in the shape of two arrays of 19 small magnets on the two

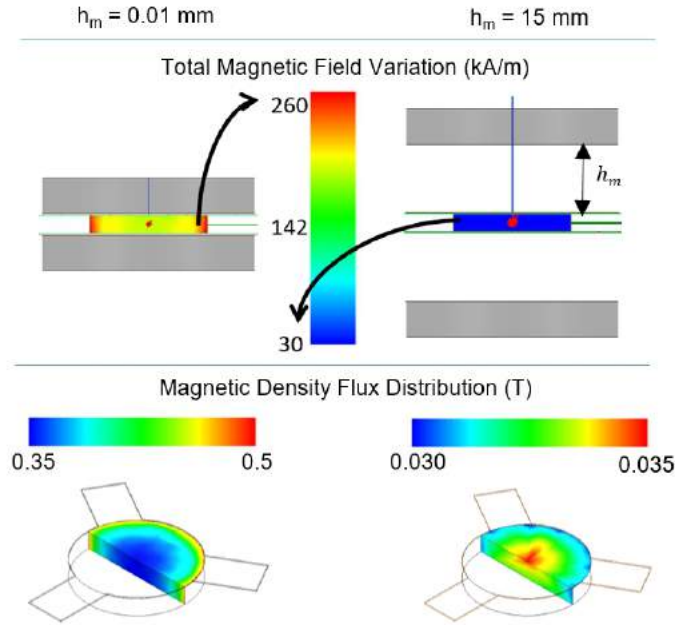


Figure 6.12: Variation of magnitude and distribution of MBF in the ferrite disk region for two distances of a pair of PMs above the junction: $h_m = 0.01$ mm (left) and $h_m = 15$ mm (right). The PMs are $t_m = 3$ mm thick with diameters of $d_m = 18$ mm. The arrows in the cross-section indicate values of the dc magnetic field variation.

sides of the junction. In this case, the resulting magnetic bias field distribution, obtained by magneto-static simulations, is shown in Fig.6.13. The MBF shows no symmetry, is very nonuniform, and the ferrite is saturated only in a few small isolated parts.

In Figs. 6.12 and 6.13, the simulated magnetostatic field distributions show that the synthesis of a certain MBF is highly dependent on the permanent magnet geometries and distance from the ferrite disk. In some cases, it will completely change the internal field distribution and hence impact the magnetization levels at every point in the ferrite.

6.7 EXPERIMENTAL VALIDATION

To validate the above analysis experimentally, three circulators using the same ferrite disk are designed, fabricated and characterized, and their main characteristics are summarized in Table 6.1.

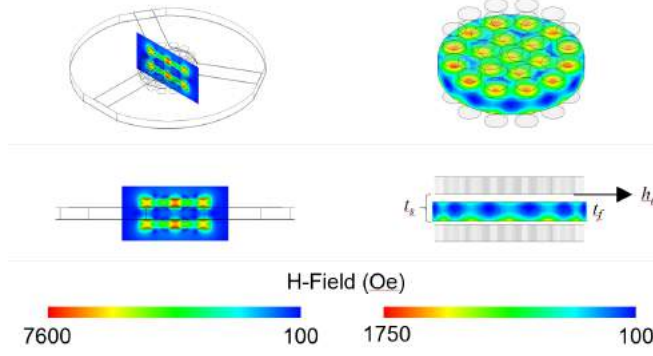


Figure 6.13: Simulated magnetic bias field generated by an array of 19 N50 grade permanent magnets, concentrically distributed and mirrored in the z -direction around the center plane of the substrate. The dimensions are $t_m = 1.106$ mm, $r_m = 0.79$ mm, $t_f = 1.249$ mm, $t_s = 1.524$ mm and $h_m = 0.1$ mm. Magnetic field in the $x-z$ plane, including the PM volumes (left). The MBF inside the ferrite volume (right).

Table 6.1: Validation circulator designs for different operating points using the same ferrite disk.

Bias Strategy	f_0 (GHz)	Goal
Unsaturated nonuniform	1.6	Miniaturization
Saturated uniform	4.4	Baseline
Unsaturated nonuniform with array of PMs	7.2	Tuning at frequencies above FMR

6.7.1 BASELINE CIRCULATOR

Since the the applied magnetic bias field determines the distribution and level of magnetization inside the ferrite and it can also vary with PM geometry and relative position to the ferrite disk, a baseline circulator is first implemented for comparison purposes. Using a traditional design approach, a circulator is implemented as shown in Fig.6.14. The disk has a 5-mm radius and is made of TT1-105 ferrite material, same radius microstrip circular junction, thickness of both ferrite and substrate of $t_s = t_f = 1.524$ mm, substrate dielectric constant $\epsilon_r = 3.6$ (Rogers RO4350C), and microstrip line width of 3.5 mm corresponding to 50Ω .

The performance in Fig.6.14 is simulated for a uniform MBF of 1750 G. The measured performance shown in Fig.6.15 shows a shift in frequency from 3.8 GHz to 4.3 GHz (dashed lines). The solid lines show simulated results with a nonuniform MBF obtained as in [34]. The implemented circulator is shown in Fig.6.16 and uses two rare-earth commercially-available magnets with a thickness of $t_m = 3$ mm and diameter $d_m = 15.85$ mm, with specifications for the commercially available *HKCM* NdFeB-N35 material [153].

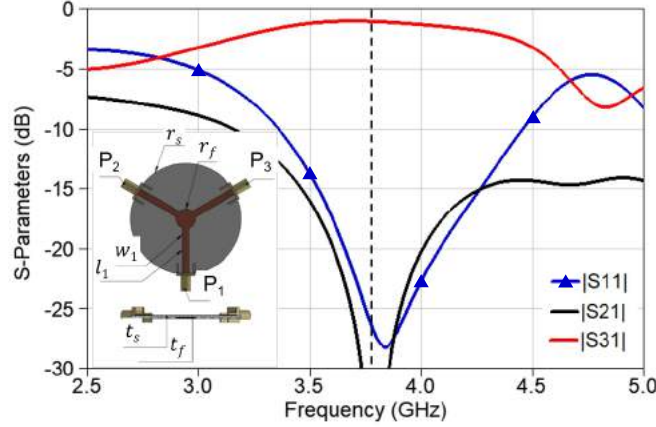


Figure 6.14: Baseline microstrip junction circulator design, where simulations are performed for a uniform MBF.

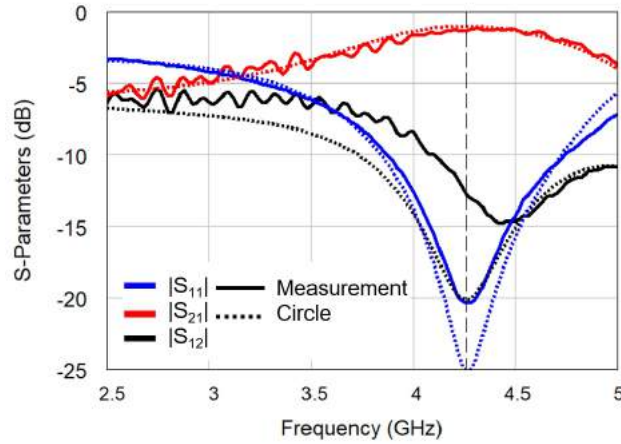


Figure 6.15: Baseline circulator simulated and measured performance of $|S_{11}|$, $|S_{21}|$, and $|S_{12}|$.

6.7.2 MINIATURIZED DESIGN OPERATED BELOW SATURATION

A second variation of the design is studied with a MBF below saturation magnetization to test frequency change. This is accomplished by moving the PMs away from the disk as simulated in Fig.6.12. As H_0 decreases, μ_{eff} increases, resulting in electrically smaller cavities. This can be used for miniaturization at the cost of bandwidth reduction. Figure 6.17 plots simulated S -parameters corresponding to $h_m = 15$ mm and with the same ferrite disk size. A frequency shift from 4.3 GHz to 1.6 GHz is observed, resulting in a reduction of electrical size by 63%. A bandwidth reduction from 25% to 10% is also seen, validating the analysis. The S -parameters in Fig.6.17 are plotted for a junction with 50- Ω microstrip lines connected

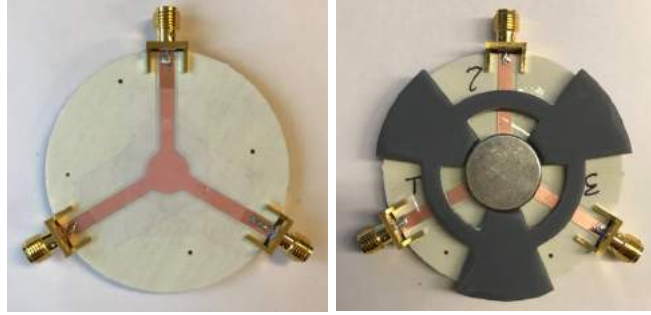


Figure 6.16: Photograph of fabricated microstrip circulator, showing the position of the PMs (one on the top, the other not visible below) [34]. The gray magnet holder is made of low-permittivity plastic and does not affect RF behavior.

to the ports. In [34], impedance matching is shown to improve bandwidth, and an example of impedance matching that results in improved simulated and measured isolation and bandwidth is shown in Fig.6.18. The microstrip matching network shown in the photo can easily be designed with surface-mount lumped elements for further size reduction.

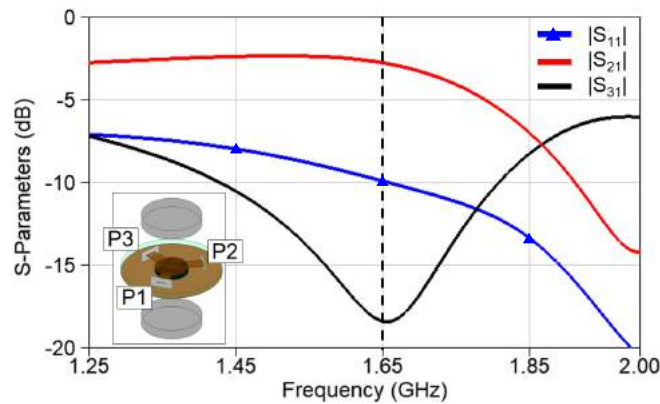


Figure 6.17: S -parameters of a microstrip circulator designed to operate at 1.6 GHz. The ferrite disk dimensions are the same as in the previous design, centered at 4.3 GHz. To make the disk electrically smaller, a weaker MBF is applied by displacing the PMs apart.

6.7.3 DESIGN WITH NON-UNIFORM MBF

To validate the theory related to an extremely nonuniform MBF, another design variation is studied by substituting the traditional pair of big PMs by nonuniform arrays of small magnets (Fig.6.13). The idea is to add a degree of freedom to the design by changing the MBF distribution, and isolating the effects of

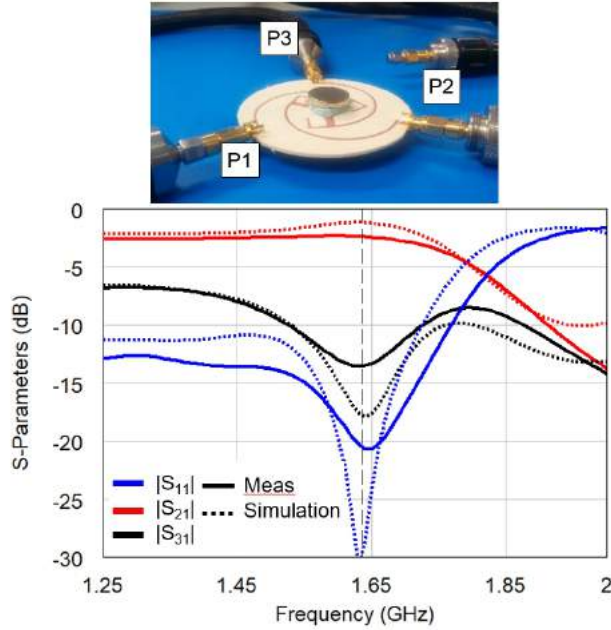


Figure 6.18: Circulator operating in the UHF band having a reduced disk size by 40% [34]. The disk is initially designed to operate at 4.4 GHz when the ferrite is uniformly saturated. Foam spacers are used to define the distance from the disk.

matching networks. Fig.6.19 shows the S -parameters for the same previous disk for three configurations: an ideal uniform MBF of $4\pi M_s = 1750$ G applied directly in HFSS; nonuniform MBF obtained through the magnetostatic co-simulations in Maxwell3D of a pair of cylindrical PMs; and the different nonuniform MBF generated by an array of small magnets. The two larger PMs are of a grade N50 material with radii $r_m = 7.145$ mm, thicknesses $t_m = 0.79$ mm and $h_m = 0.1$ mm. Two arrays of 19 magnets in a circular lattice with $r_m = 0.79$ mm, $t_m = 0.553$ mm, and $h_m = 0.1$ mm are placed on the two sides of the microstrip substrate. When the disk has a theoretical uniform MBF, the first mode is dominant and at a frequency associated with the ferrite diameter. When a nonuniform MBF is generated by the two larger PMs, a shift in frequency is observed, since a variation in the magnetic bias field distribution will change the internal field, and thus the effective permeability. As in an ordinary dielectric cavity with fixed geometry, if ϵ_r and μ_r change, the resonances in the ferrite disk will drift. When the MBF distribution is modified by an array of small permanent magnets, the operating frequency is shifted above FMR and the direction of circulation flips.

The prototype with small-magnet arrays is shown in Fig.6.20. Two pieces made of RO4350C were CNC

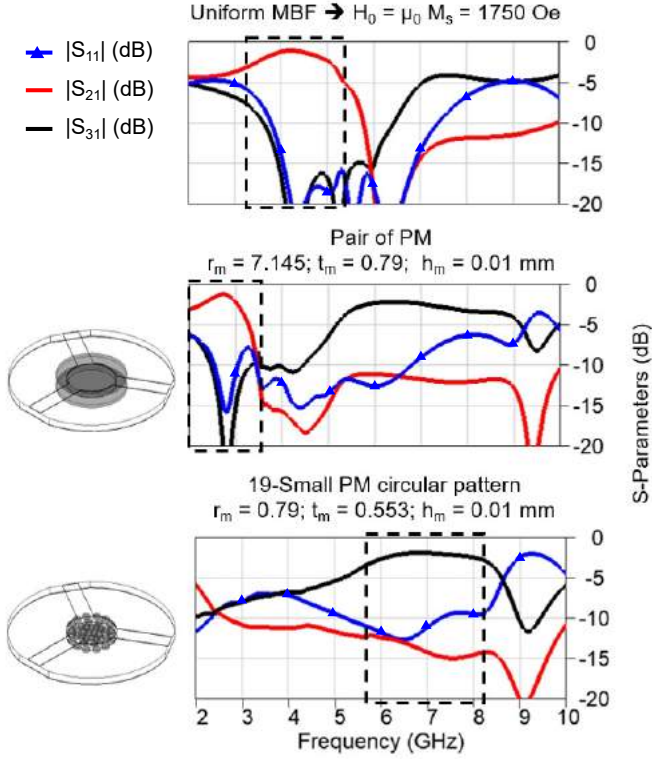


Figure 6.19: Simulated S -parameters for different MBF distributions. Uniform MBF of $4\pi M_s = 1750$ G applied directly in HFSS (top), nonuniform MBF obtained through the magnetostatic co-simulations in Maxwell3D of a pair of cylindrical PMs (middle), and array of permanent magnets (bottom). The dashed boxes show the shift in frequency of the operating point as MBF distribution changes. All lines and ports are 50Ω , and the reference planes are de-embedded.

machined to mechanically support the small magnets. Bottom and top arrays were then aligned as shown in the lower image. Fig. 6.21 shows agreement between simulated and measured S -parameters. As expected, the circulator operates around 7.2 GHz. Although the trend is the same, the measured results show lower bandwidth than simulated, and this is attributed to fabrication tolerances.

Further exploration of this novel approach is performed experimentally by varying the PM array geometry. For example, when an additional magnet with $r_{m2} = 2$ mm and $t_{m2} = 0.01$ mm is placed on the top of the small-magnet array (Fig.6.22, making the MBF asymmetric in the z -direction, the S -parameters improve as shown in Fig.6.23. Such result suggests that the asymmetric structure of a microstrip circulator demands asymmetric MBF for overall compensation.

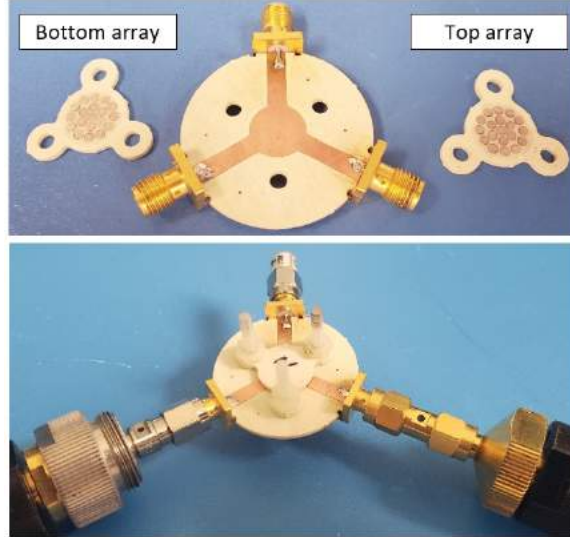


Figure 6.20: Photograph of third prototype presented in Fig.6.19. The circulator is designed to operate above FMR by applying a nonuniform MBF with an array of small PMs.

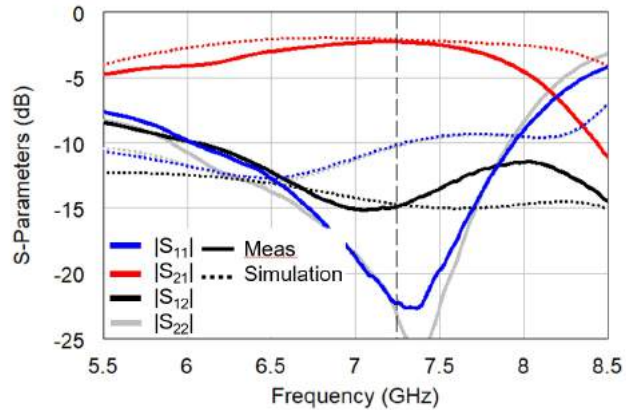


Figure 6.21: Simulated and measured S -parameters of the circulator shown in Fig. 6.20. The measurements were performed with a 2-Port VNA, so isolation is measured by $|S_{12}|$. At 7.2 GHz, measured parameters are $|S_{11}| = -21.8$ dB, $|S_{21}| = -2.3$ dB and, $|S_{12}| = -15.0$ dB.

6.8 CHAPTER CONCLUSIONS AND CONTRIBUTIONS

This chapter presents a detailed study of design of microstrip ferrite circulators by controlling the magnetic bias field (MBF). The studies are carried out by using full-wave EM and magnetostatic co-simulations (using HFSS and Maxwell3D, respectively) with variations of the MBF are presented for several permanent magnet configurations. To the best of the author's knowledge, the only other related work for a saturated ferrite disk

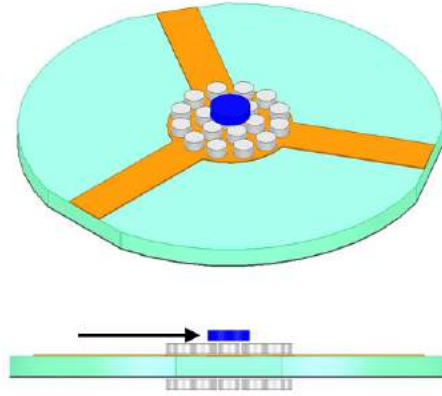


Figure 6.22: Geometry for an asymmetric 3-D permanent magnet configuration.

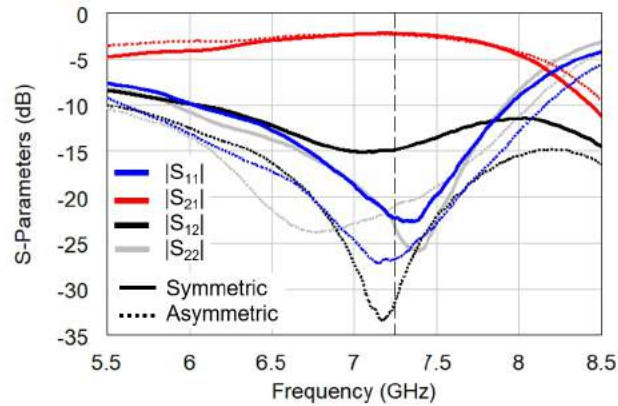


Figure 6.23: Measured S -parameters of initial permanent magnetic array (2D) and the 3D-asymmetric array.

is presented in [154]. The approach in this thesis includes numerical modal analysis, as well as eigenmode and driven simulations to understand the impact of magnetization levels and distribution on circulators electromagnetic performance. The contributions related to this chapter are published in [155], [35], [34], [141], [156].

A graphical study is developed to characterize the real and imaginary parts of the effective permeability, as a simultaneous function of MBF intensity and frequency. It shows that the low-loss region can be avoided even with a weak MBF. On the other hand, eigenmode analysis combined with driven simulations show the effects on circulator bandwidth when applied a magnetic bias field with higher magnitudes than the ferrite magnetization saturation. The total internal field distribution changes when the same MBF is applied to different ferrite geometries, due to boundary field modification. A parametric study of the resonance and Q-

factor of the disk as a function of shape and thickness quantifies this effect, and the results are confirmed with driven full-wave simulations. Finally, the nonuniformity of different PM bias geometries is characterized using magnetostatic and full-wave co-simulations in order to observe changes in the operation point (above or below FMR), which in turn results in a shift in direction of circulation and frequency.

The analysis is validated using a commercially-available ferrite disk (Skyworks TT1-105). The variations on the MBF allows design of three circulators: a 4.3 GHz device with PMs positioned to produce nearly uniform saturation; a 1.6 GHz device when the same PMs are placed further from the ferrite disk and result in weak biasing; and a 7 GHz device non-uniformly biased with a reduced-volume array of small magnets. The co-simulations match measured results, which are summarized in Fig.6.24 and Table 6.2, showing the greater than two octaves difference in center operating frequencies. Since the impedance at the resonator ports is in general complex, external matching circuits can improve bandwidth, but can also be used to introduce other functions such as filtering, as demonstrated in [156].

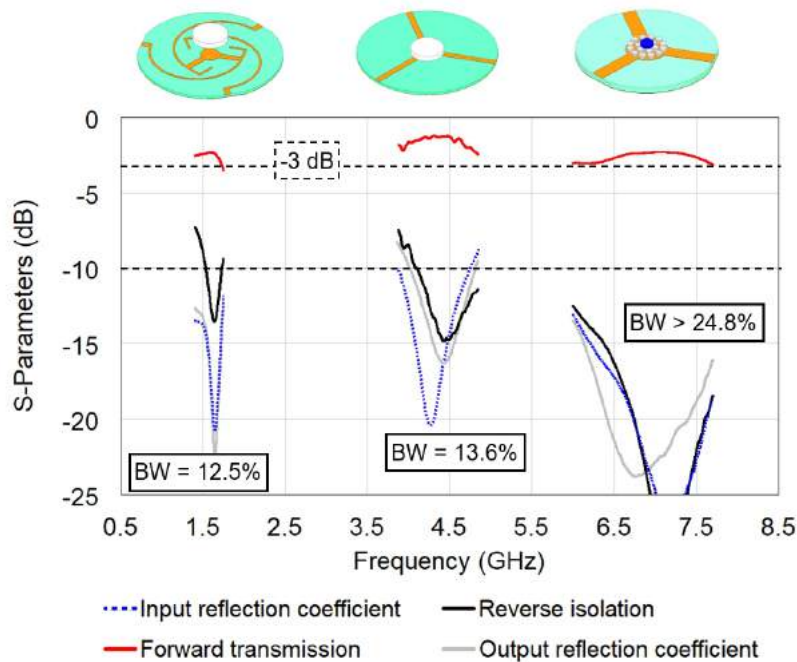


Figure 6.24: Summary of measured S -parameters of three microstrip circulators designed with the same ferrite disk. The different frequency bands are a result of different magnetization distributions. The response at the 4.3-GHz center frequency is a result of a design using a nearly uniformly saturated disk, while the response at 1.6-GHz center frequency is obtained when the magnetization is nonuniform and below saturation. The 7-GHz response is due to a very inhomogenous non-saturated ferrite obtained from an array of permanent magnets.

Table 6.2: Performance summary of circulators from Fig.6.24. BW is defined by $IL < 3$ dB, $ISO > 10$ dB and $RL > 10$ dB.

Bias Strategy	f_0 (GHz)	BW (%)	IL (dB)	ISO (dB)	RL (dB)
Unsaturated, PM pair	1.6	12.5	2.5	17.5	20
Saturated, PM pair	4.4	13.6	< 1	20	15
Unsaturated, PM array	7.2	24.8	2.5	30	25

The two first circulator designs from Fig.6.24 are operated below the absorptive FMR region, while the third is operated above the FMR with opposite direction of circulation. The study of designs below FMR is motivated by self-biased circulator constraints, i.e., low volumes, nonuniform and unsaturated cavities. The same analysis presented here can be applied to investigating circulators with materials characterized by shape anisotropy, e.g. hexaferrites [157] and magnetic nano-wires, e.g. [158]. These materials operate below the FMR with no external magnets and have the potential of monolithic integration with active circuits [158], and are investigated in the next chapter.

CHAPTER 7

SELF-BIASED CIRCULATORS

CONTENTS

7.1	CHAPTER INTRODUCTION	108
7.2	MATERIAL PROPERTIES AND SIMULATIONS	109
7.3	MEASUREMENTS ON SAMPLES FROM ARGONNE NATIONAL LABS	113
7.4	CHAPTER CONCLUSION AND CONTRIBUTIONS	114

7.1 CHAPTER INTRODUCTION

This chapter describes initial results with a hybrid microstrip circulator operating in the lower part of X-band and designed with self-biased nano-composite materials with shape anisotropy, obtained from Argonne National Labs in a collaboration through a DARPA M3IC program. With this new synthetic material introduced briefly in Chapter 5, a study is performed on the effect of saturated magnetization, remnant magnetization, dielectric loss and ferro-magnetic resonance (FMR) on circulator performance, following the methods developed in Chapter 6. The next section discusses material fabrication and properties, as well as how they impact the simulations and circulator design. Proof-of-concept measurements are described next, and demonstrate non-reciprocal behavior around 7 and 8 GHz and are obtained with and without external

bias field, and before and after material magnetization.

7.2 MATERIAL PROPERTIES AND SIMULATIONS

The magnetic material with shape anisotropy is an artificial material, obtained by plating iron-nickel nanowires in a quasi-periodic mold. An alumina (Aluminum oxide) 100- μm thick substrate, with 40-nm pore size, 65-nm pitch distance, and a porosity of 30-35% is used as the template, shown in the photo in Fig. 7.1(a) and with a cross-section illustrated in Fig.7.1 (b). The length of the iron-nickel magnetic nano-wires is 85 μm , and this partial fill is taken into account in simulations and design presented in the remainder of the paper. The periodicity is on the 65-nm scale, but as seen from the photo it is not exactly periodic. The significant sub-wavelength scale for a circulator in X-band or below justifies the approximation of treating this material as continuous.

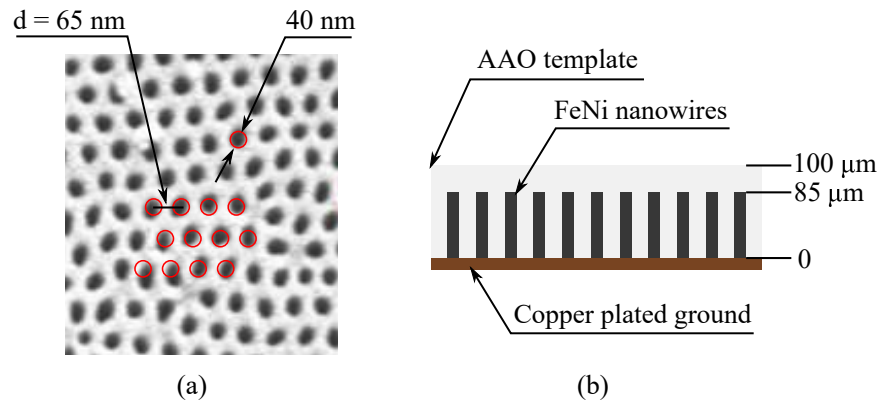


Figure 7.1: (a) Microscope photograph of porous alumina template filled with FeNi nanowires, from top (courtesy: Argonne National Labs). (b) Sketch of side cross-section showing the geometry and partial FeNi plating.

The alumina pores with plated FeNi give a shape anisotropy such that the Ni content can be controlled during plating to modulate the saturated magnetization M_s , with a ferromagnetic resonance around 12 GHz. The measured hysteresis curves of two sister samples are shown in Fig. 7.2. These are made in the same plating process, with 85- μm FeNi nano-wire length and 30% alumina porosity, as described above. It is observed that the measured FMR frequencies and linewidths vary between 9.1 and 14.6 GHz, and 470 and 920 Oe, respectively.

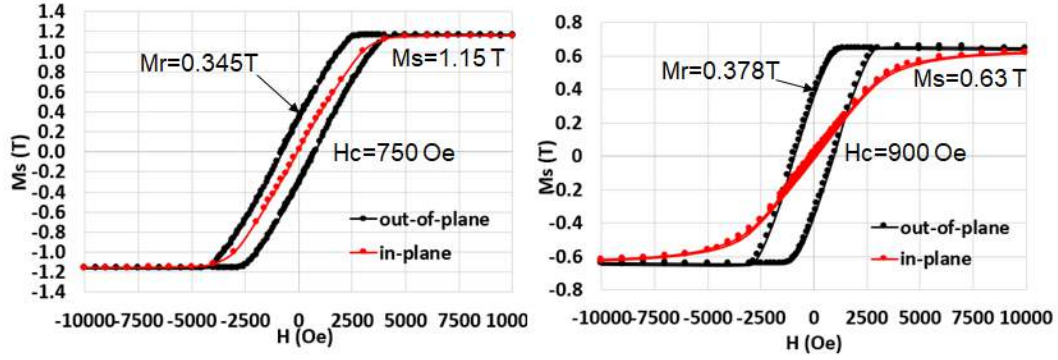


Figure 7.2: Measured hysteresis curves of two sister samples made in the same plating process with 85- μm FeNi nano-wire length and 30% alumina porosity. The corresponding FMR frequencies and linewidths are 9.1 and 14.6 GHz, and 470 and 920 Oe, respectively (courtesy: Argonne National Labs).

After the artificial anisotropic material is characterized, the circulator shape is defined by a 10-mm circular, selective plating mask, as shown in Fig. 7.3. The relevant parameters for circulator design include the dimensions, relative permittivity of the material measured to be 5.9 with $\tan\delta = 0.08$, a remnant magnetization $M_r = 0.4\text{ T}$, a FMR linewidth $\Delta H = 600\text{ Oe}$ and a Lande g-factor of 2. These parameters can vary due to the fabrication process immaturity, and a sensitivity analysis enables diagnostics and more accurate circulator design.

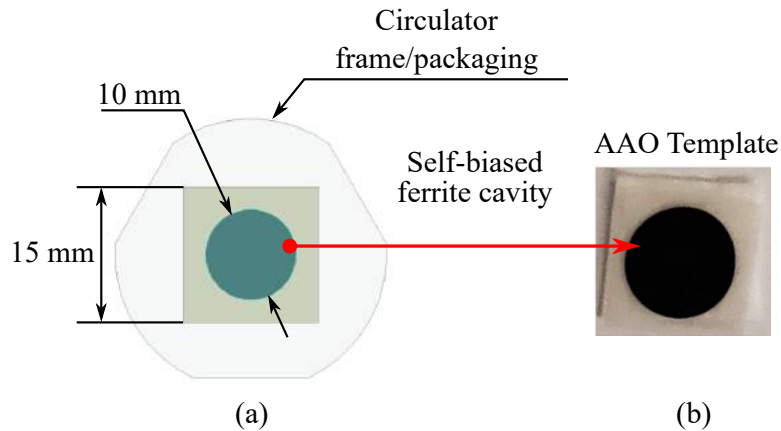


Figure 7.3: (a) Geometry of circularly shaped MNC material fabricated for a circulator. (b) Photograph of alumina (aluminum oxide) porous template substrate with plated FeNi in the shape of a circle with a 10-mm diameter.

In this work, the self-biased MNC is modeled as a ferrite cavity. The cavity shape introduces a demagnetization factor, and results in a non-uniform distribution of the magnetic bias field, as described

in [112], where the demagnetization factor for a disc with a radius a and thickness L is given by the following integral:

$$N_{zz}(r, z) = \frac{a}{2} \int_0^\infty J_0(tr) J_1(ta) \{e^{-iz} + e^{-t(L-z)}\} dt \quad (7.1)$$

and the Bessel functions of zero-th and first order are a result of the cylindrical geometry. This equation is used to calculate the demagnetization factor as a function of radial distance for a disc with a radius $a = 5$ mm and for several thicknesses, shown in Fig. 7.4. We model this variation by dividing the ferrite cavity into smaller regions with a uniform magnetic bias field H_0 and with a different amplitude applied to each volume, as illustrated with rings of different shades in the figure. The plot in Fig. 7.4 shows the expected effect of non-uniform magnetization. The parameters listed in Table 7.1 are used for design and simulations, with $M_r = \mu_0 H_0$.

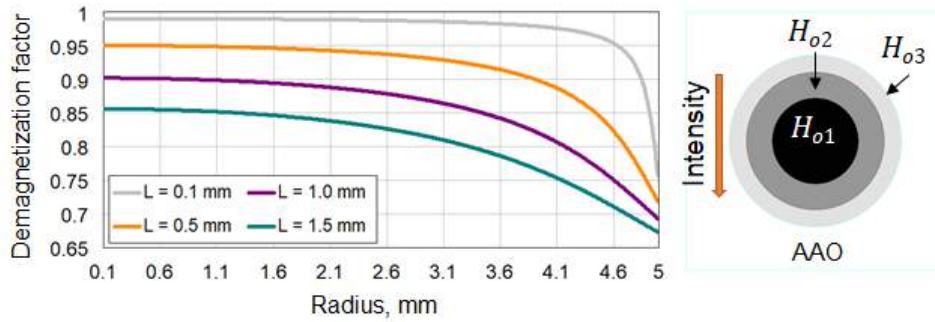


Figure 7.4: Right: Calculated demagnetization profile of a cylindrical disc made of the material with properties in Table 7.1. Left: discretization for cylindrical circulator cavity simulations, where each shaded ring is treated as a uniform material with a different magnetization.

Table 7.1: Material parameters used in simulation study and design.

Parameter	Reference	Case 1	Case 2	Case 3
$\epsilon_r, \tan\delta$	5.9, 0.08	5.9, 0.08	5.9, 0.08	5.9, 0.08
M_s (T)	1.2	0.6, 1.1, 1.6	1.2	1.2
M_r (T)	0.4	0.4	0.4	0.4
FMR	12.5	12.5	12.5	12.5
ΔH (Oe)	600	600	100, 600, 1200	600
Lande factor	2	2	2	1.5, 2, 2.5

This discretized model results are then imported into a full-wave electromagnetic simulator (Ansys HFSS) and used to design a circulator using the MNC circular disc from Fig. 7.3. With no external matching (50- Ω microstrip lines on a TMM6 substrate) the device geometry is shown in Fig. 7.5 and simulations show nominal operation around 7.6 GHz with a 2.3 dB insertion loss, 9 dB isolation and 15 dB return loss. The simulation results in Fig. 7.7 clearly show the difference in S-parameters for a microstrip circulator between a uniformly magnetized cavity and a discretized cavity with 3 uniformly magnetized rings and with a decrease in the magnetic bias field.

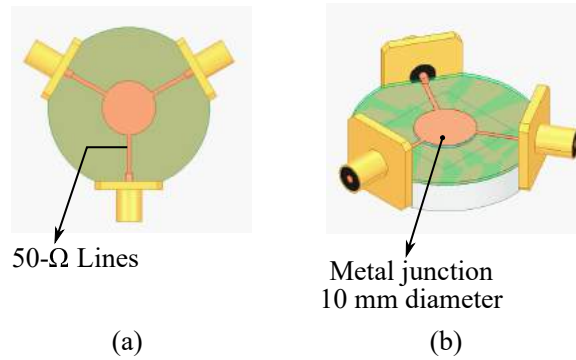


Figure 7.5: Top (a) and full (b) view of a microstrip junction circulator assuming a MNC thin disk of self-biased material and 50- Ω ports directly connected to the junction.

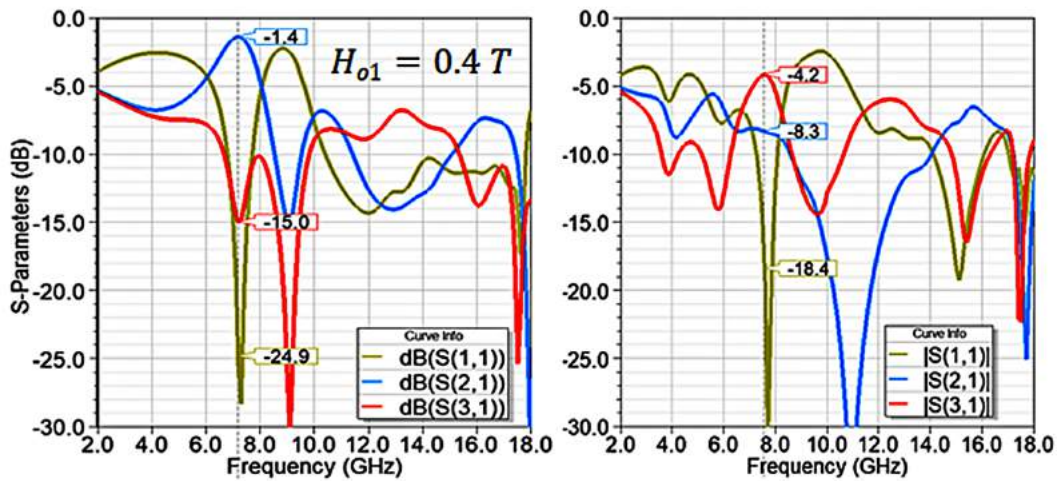


Figure 7.6: Simulated S-parameters for a 5-mm radius FeNi MCN disc with uniform magnetic bias field of 0.4 T (left) and for three discrete concentric rings, with $H_{01}=0.4$ T, $H_{02}=0.16$ T and $H_{03}=0.06$ T, with the related radii of 3.5, 4.5 and 5 mm (right). Notice the change in circulation direction between the uniform and nonuniform field case, as well as increased loss and slight frequency shift.

These results show not only a slight shift in frequency and increase in insertion loss, but also a change in circulation direction. This is initially surprising, but can possibly be explained by considering the following relation [120]:

$$H_0 = H_a + H_k - 4\pi M_s N_z z \quad (7.2)$$

where the demagnetization factor from 7.2 is used to establish a region of operation, H_k is an effective internal field, and H_a is the external field, which is in our case zero. Therefore, H_0 can become negative if $4\pi M_s N_z z > H_k$, thus shifting the circulation direction.

The plating process allows tuning the ratio M_r/M_s between 0.25 and 0.95 without applying an external field. In order to verify effects of process variation on circulator behavior, a sensitivity analysis is performed according to the values in Table 7.1. It is seen that the value of M_s affects the frequency as well as the S-parameters, while ΔH does not have a pronounced effect due to the separation of the operating frequency from the FMR resonance of 12.5 GHz. The Lande factor affects frequency and bandwidth. The sensitivity analysis is briefly summarized in Fig. 7.7.

7.3 MEASUREMENTS ON SAMPLES FROM ARGONNE NATIONAL LABS

A circulator is designed using the described method with available 1-mm thin circular MNC plated 100- μ m thick material, assembled using hybrid integration as shown in Fig.7.8. The starting point for the design is based on classical approach from Bosma's stripline circulator paper [94]. The microstrip port lines are fixed at 50 Ω , with no additional impedance matching, differing from, e.g. [34]. Fig. 7.9 shows measured results compared to simulations using a 3-ring discretized model, showing that the trends are adequately modeled and closer to measurements than for the uniform model. The loss is within 0.2 dB and the frequency shift is 10%, while the isolation is about 11 dB with a bandwidth of 5%.

Figure 7.10 shows another set of measurements for a different sample, and in this case we investigate the effect of adding an external magnetic field in addition to the built-in field. By applying an external field, as expected the frequency shifts and the loss decreases. The measurements show a frequency of operation of

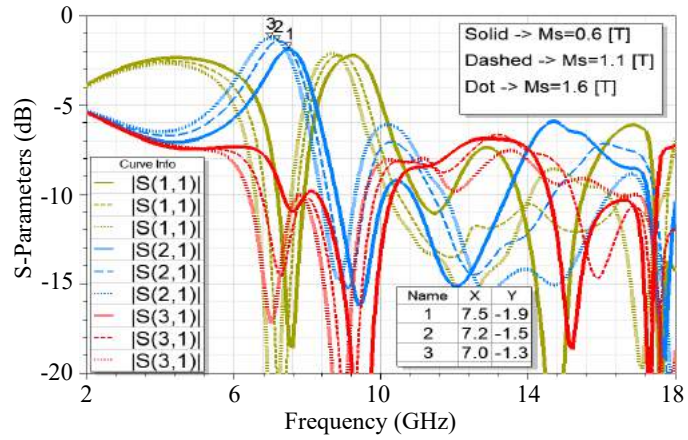
the self-biased material at 7.1 GHz, with an isolation of 10 dB and a return loss of 12 dB, which compares well with the simulation. For the samples demonstrated above, the copper layer that is used during the plating process has been removed and the circulator relies on the microstrip ground and aluminum fixture.

Next, we investigated the effect of leaving the initial copper layer used during the fabrication process of the MCN sample. These samples have improved mechanical stability. Fig. 7.11 shows measured results for a sample with the native copper layer and without an external magnet. The sample was exposed to a strong external dc magnetic field several days before the measurements were performed, showing that the self-biasing field remains.

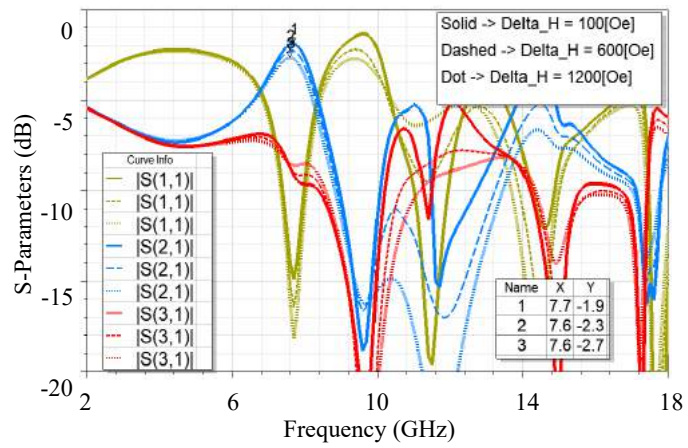
7.4 CHAPTER CONCLUSION AND CONTRIBUTIONS

This chapter presents simulations and measured initial results for hybrid microstrip circulators operating in the lower part of X-band with no external permanent magnets. The devices are enabled by a iron-nickel plating process of porous alumina, developed at Argonne National Labs, synthesizing an artificial magnetic material with shape anisotropy. Starting from this new material measured electro-magnetic properties, a study is performed on the effect on device performance of parameters such as saturation magnetization, FMR linewidth and Lande g-factor, which vary over a range expected from process analysis. The demagnetization of the material is a function of sample geometry and results in a non-uniform self-bias field. This effect was analyzed showing improved agreement with measured results, indicating that it needs to be taken into account during the design process.

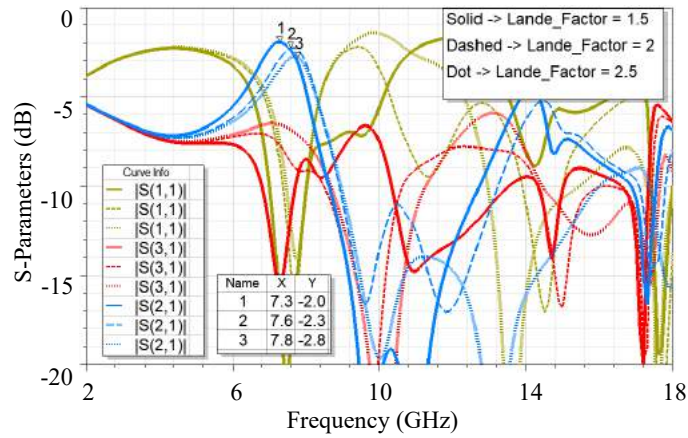
Proof-of-concept measurements that demonstrate non-reciprocal behavior around 7 and 8 GHz are obtained with and without external bias field, and before and after material magnetization. These demonstrations, described in [142], are the first demonstrations of self-magnetized connectorized MNC circulators below 10 GHz, to the best of the author's knowledge.



(a)



(b)



(c)

Figure 7.7: Simulations for variations of M_s (top), FRM linewidth ΔH (middle) and Lande g-factor (bottom) over a range determined from MNC processing, given in Table 7.1.

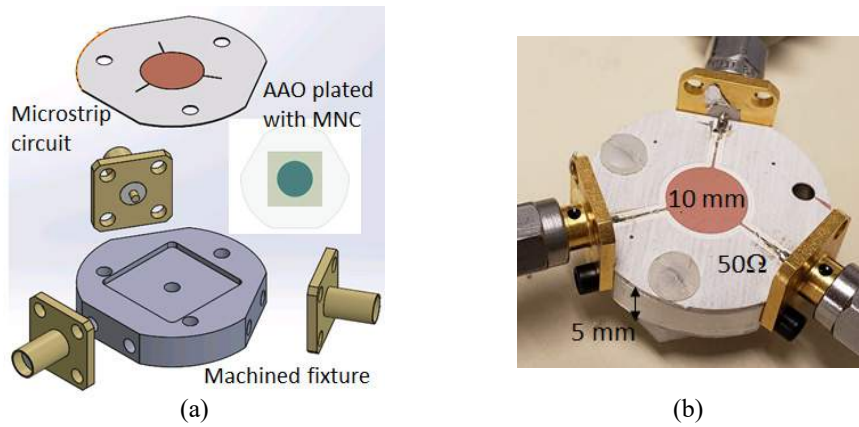


Figure 7.8: Fabricated microstrip circulator that operates around 7 GHz. (a) Assembly drawing and (b) prototype photograph.

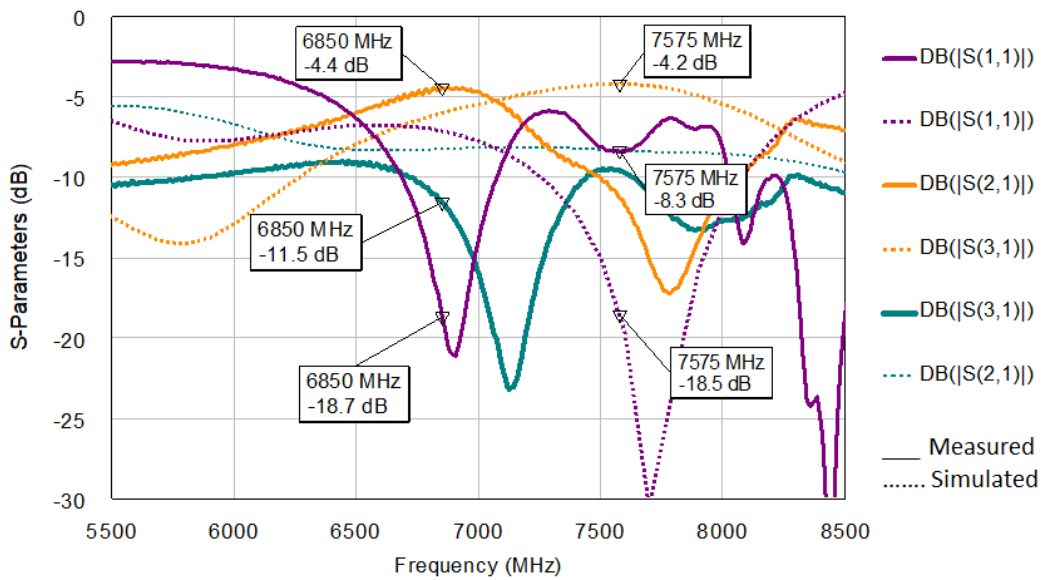


Figure 7.9: Measured vs. simulated results for the circulator from Fig. 7.8, where the simulations show data for a discretized model from Fig. 7.3. These measurements are done before external permanent magnets were applied to the disc.

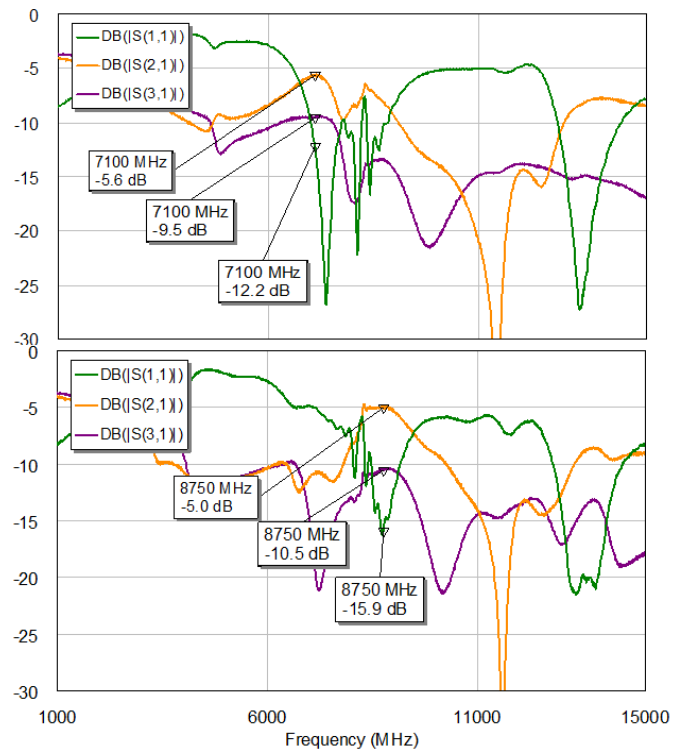


Figure 7.10: Measured data for hybrid circulator from Fig. 7.8 for: (top) self-biased device, and (bottom) device with external field from a readily available rare-earth magnet.

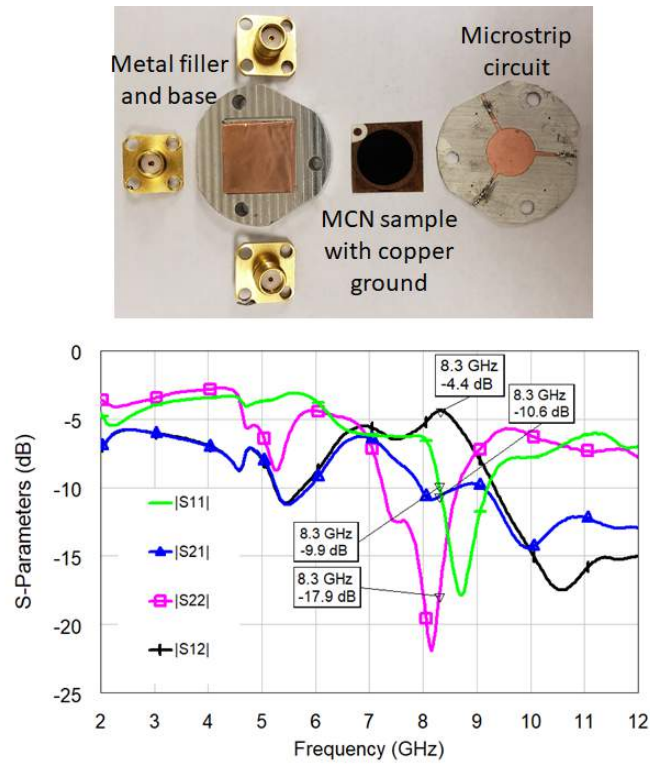


Figure 7.11: Measured data for hybrid circulator with components shown in the photograph. The MCN sample in this case has the native copper ground layer used during the plating process. The sample was exposed to an external permanent magnet several days before the measurement. No external magnetic field was applied for the S-parameter data shown here.

CHAPTER 8

ACTIVE CIRCULATOR MMIC

CONTENTS

8.1	CHAPTER INTRODUCTION	119
8.2	CIRCUIT TOPOLOGY AND MMIC DESIGN	120
8.3	CIRCULATOR LAYOUT AND SIMULATED RESULTS	124
8.4	MEASURED RESULTS AND ANALYSIS	128
8.5	CONCLUSION AND CONTRIBUTIONS	131

8.1 CHAPTER INTRODUCTION

This chapter presents the design of a 8-12 GHz active circulator fabricated in a 0.25 μm GaAs pHEMT monolithic microwave integrated circuit (MMIC) process. The circuit consists of three Lange couplers which connect gates and drains of three equal gain-matched amplifiers, as illustrated in Fig. 8.1. The coupling factor of the unequal-split Lange coupler is designed to achieve an isolation higher than 20 dB over a 40% bandwidth, with a return loss of better than 10 dB and an insertion gain of 2.4 dB across the band. The layout includes bias networks for the three amplifiers and occupies a 2.5 mm \times 2.5 mm die. Measurements in a 50- Ω environment are shown to be in good agreement with simulations. Since this compact quasi-

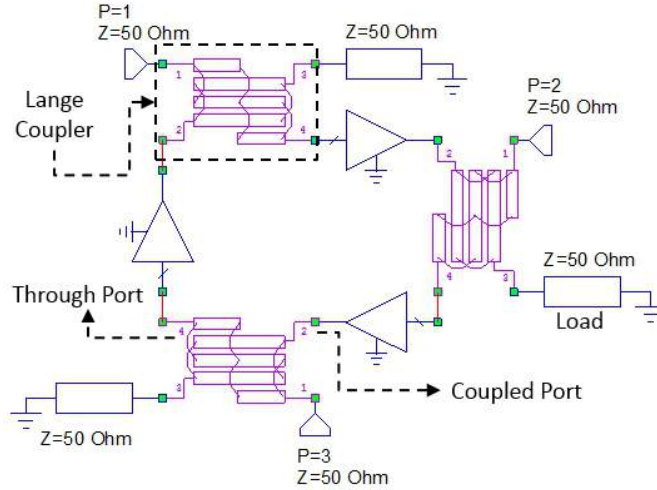


Figure 8.1: Active circulator MMIC circuit topology. Nonreciprocal circulation is accomplished with gain-matched single-stage amplifiers. Each amplifier input is connected to a *through* port of one coupler while the output is connected to the *coupled* port of the following asymmetric Lange coupler. When port 1 (P1) is the input, P2 is the output and P3 isolated.

circulator is intended for use in full-duplex phased array front ends, an analysis is then performed assuming the circulator is presented with an active scan coefficient corresponding to that in earlier chapters.

8.2 CIRCUIT TOPOLOGY AND MMIC DESIGN

The design of an active circulator circuit topology from Fig.8.1 is performed. Simulations for 50- Ω loads at the ports show insertion gain of up to 3 dB across 6–14 GHz with isolation $|S_{31}| > 13$ dB. The design is implemented in a Qorvo 0.25 μm GaAs PHEMT MMIC process for operation in the 7–13 GHz band. During the design process, the Lange coupler length is varied to reach a trade-off between isolation ($|S_{31}|$) and transmission gain ($|S_{21}|$), while ensuring stability. The forward gain of the circulator is proportional to the amplifier gain, reduced by the *coupling* and *through* attenuation of the Lange couplers. The sub-circuits required in each branch of the design are the unit amplifier and an asymmetric Lange coupler, detailed below.

8.2.1 BRANCH CIRCUIT DESIGN

A $6 \times 50 \mu\text{m}$ depletion-mode HEMT biased at $V_D = 5.4$ V and $V_G = -0.4$ V is used for the unit small-signal amplifier. The metal layer in this MMIC process supports a maximum current of 18 mA/ μm , and the dc

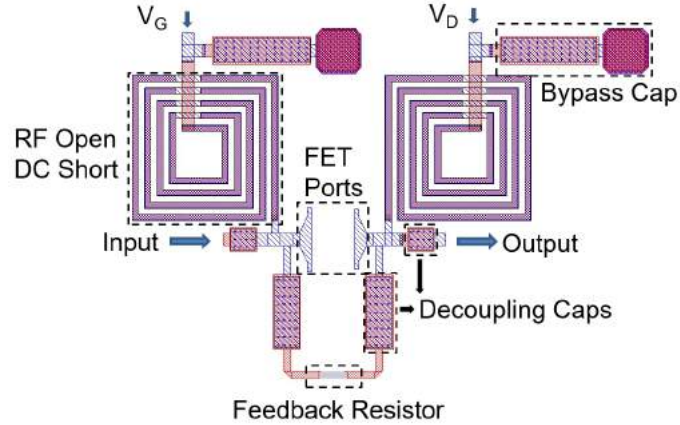


Figure 8.2: Gate and drain bias circuit layout with a feedback resistor of $200\ \Omega$ between the device gate and drain. Decoupling capacitors of $0.9\ \text{pF}$ and bypass capacitors of $4\ \text{pF}$ are used, with an RF choke implemented as a spiral inductor of $3.9\ \text{pF}$.

drain current at the quiescent point is $39.5\ \text{mA}$. Line widths greater than $4\ \mu\text{m}$ are used to meet the current handling requirement of $72\ \text{mA}$ with a safety margin. The biasing circuits are implemented with $3.95\ \text{nH}$ spiral inductor RF chokes, $4\ \text{pF}$ bypass and $0.9\ \text{pF}$ blocking capacitors. To improve stability and increase bandwidth, a $R = 200\ \Omega$ feedback resistor is connected with high-impedance short lines between gate and drain terminals. The dc bias network layout shown in Fig. 8.2 is fully EM-simulated and used to define gain-matched input and output reflection coefficients.

To design the gate and drain-side matching circuits, ideal tuners are connected to the input and output RF ports indicated in Fig. 8.2, to include the transistor and the bias lines. The output tuner is first swept to achieve a good match. This value is then fixed and the input tuner swept. After fine tuning, an input match $\Gamma_{IN} = 0.57\angle 116^\circ$ and $\Gamma_{OUT} = 0.137\angle 94^\circ$ are obtained. Matching networks are then designed with lumped elements because of size constraints. Figure 8.3 shows the unit amplifier layout, with maximum dimensions of $1050\ \mu\text{m} \times 700\ \mu\text{m}$. Input and output matching networks are implemented with shunt inductors $L_1 = 2.1\ \text{nH}$ and $L_2 = 0.89\ \text{nH}$, and a series inductor $L_3 = 0.45\ \text{nH}$. The EM-simulated S -parameters are plotted in Fig. 8.4, showing $|S_{11}|$ and $|S_{22}|$ below $-10\ \text{dB}$, $|S_{21}| > 8\ \text{dB}$ and $|S_{12}| < -15\ \text{dB}$ over $8 - 12\ \text{GHz}$.

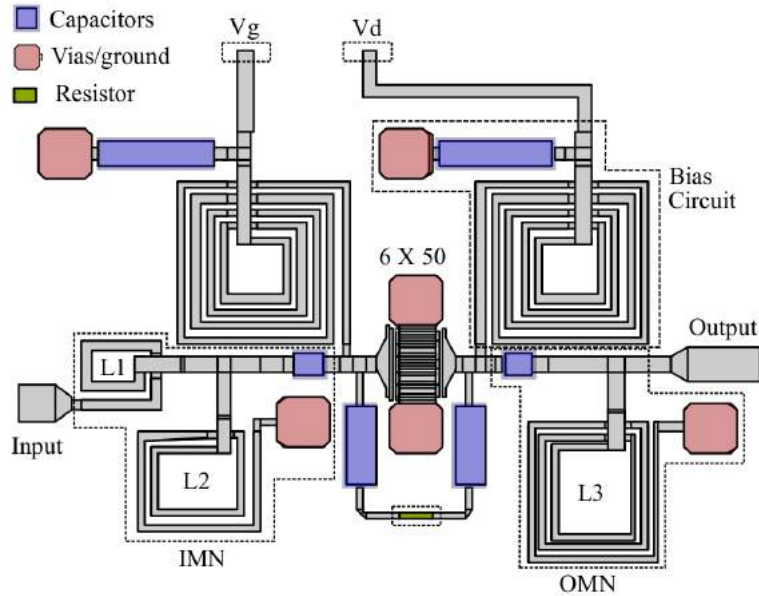


Figure 8.3: Unit amplifier layout, showing the $200\ \Omega$ feedback resistor and $0.9\ \text{pF}$ blocking capacitors. The gate and drain bias circuits use $4\ \text{pF}$ bypass capacitors and $3.9\ \text{nH}$ spiral inductors. The maximum dimensions are $1050\ \mu\text{m} \times 700\ \mu\text{m}$. Input and output matching networks are implemented with shunt inductors $L_1 = 0.45\ \text{nH}$ and $L_2 = 0.89\ \text{nH}$, and a series inductor $L_3 = 2.12\ \text{nH}$.

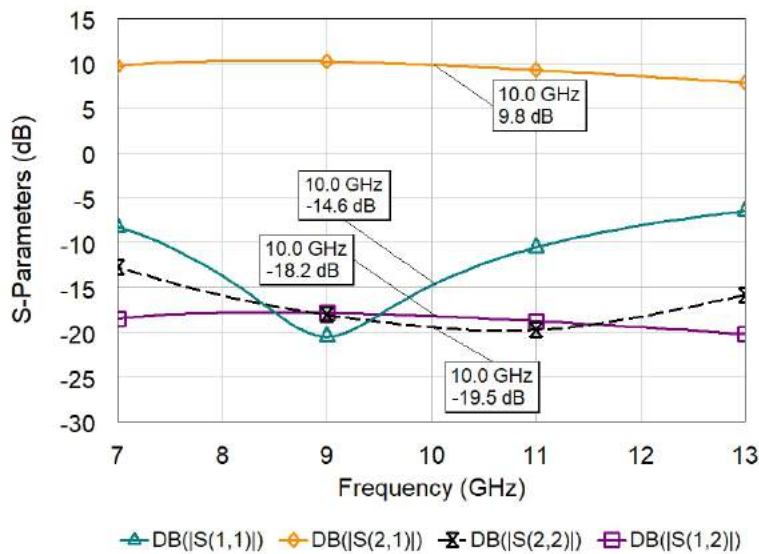


Figure 8.4: EM-simulated unit amplifier S -parameters from 7 – 13 GHz. The Qorvo PDK model is used for the transistor.

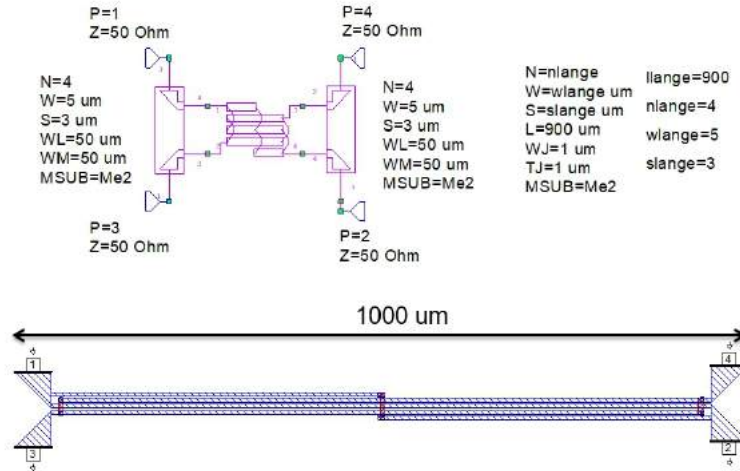


Figure 8.5: Lange coupler simulation model (top), and geometry (bottom). The main geometric parameters are the number of lines ($N = 4$), line widths $w = 5 \mu\text{m}$, line lengths $L = 900 \mu\text{m}$, and distance between lines $s = 3 \mu\text{m}$.

8.2.2 ASYMMETRIC LANGE COUPLER

The Lange coupler parameters are determined by adjusting the coupling coefficient to achieve the best circulator overall performance. The schematic and layout are shown in Figure 8.5. The EM-simulated results are plotted in Figure 8.7 from 7 – 13 GHz showing an asymmetric power division with a relative high *through* of -1.4 dB to the direct port (P2) and a *coupled* level of -5.9 dB to P3. Match and isolation ($|S_{11}|$ and $|S_{41}|$) are below -30 dB over the band. The main geometric parameters are the number of lines ($N = 4$), line widths $w = 5 \mu\text{m}$, line lengths $L = 900 \mu\text{m}$, and distance between lines $s = 3 \mu\text{m}$.

The Lange coupler S-parameters depend on length and coupling coefficient, illustrated in Fig. 8.6. For a coupler length of 2.5 mm ($\lambda_g/4$ on the MMIC substrate) and with 4 fingers, a parametric simulation is performed with line separations between 2 and 5 μm and shown in Fig.8.6(top). When the coupler length is varied between 2.5 mm and 1 mm ($\lambda_g/10$) and with a line separation of 3 μm , the results are shown in Fig. 8.6(bottom). The implication of this study is that even for couplers with the same coupling coefficient, the isolation can vary depending on length, and will impact circulator isolation and bandwidth. For the final design, we adopt a Lange coupler $l=1$ mm long with a spacing of 3 μm between each of the 4 lines, resulting in $|S_{21}| \approx -1.4$ dB and $|S_{31}| \approx -5.9$ dB, with a match and isolation better than -30 dB over 8-12 GHz after

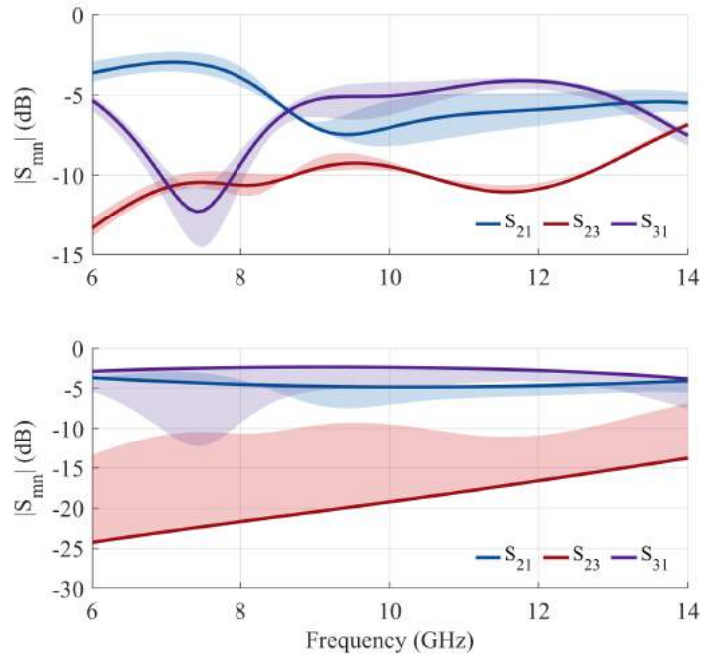


Figure 8.6: Lange coupler simulated S -parameter parametric study. Top: The coupler length is 2.5 mm ($\lambda_g/4$) and the line separations varies between 2 and $5\mu\text{m}$. Bottom: The coupler length is varied between 2.5 mm and 1 mm ($\lambda_g/10$) and the line separation kept at $3\mu\text{m}$. The nominal case with $l = 2.5\text{ mm}$ and separation of $3\mu\text{m}$ is shown in solid line.

full-wave simulations (Fig. 8.7).

8.3 CIRCULATOR LAYOUT AND SIMULATED RESULTS

The final circulator layout is displayed in Fig. 8.8. The RF GSG pads are connected by 50Ω lines. The layout is adjusted to keep amplifier input and output lines the same length. Amplifier port geometries are individually remodeled so the layout fits in a $2.5 \times 2.5\text{ mm}^2$ area. The EM-simulation responses of each sub-circuit are placed in a schematic environment with transmission line models synthesizing interconnections and the circulator overall performance is simulated.

To understand the impact of the coupler on circulator parameters, consider an idea matched coupler with S -parameters analytically expressed analytically as:

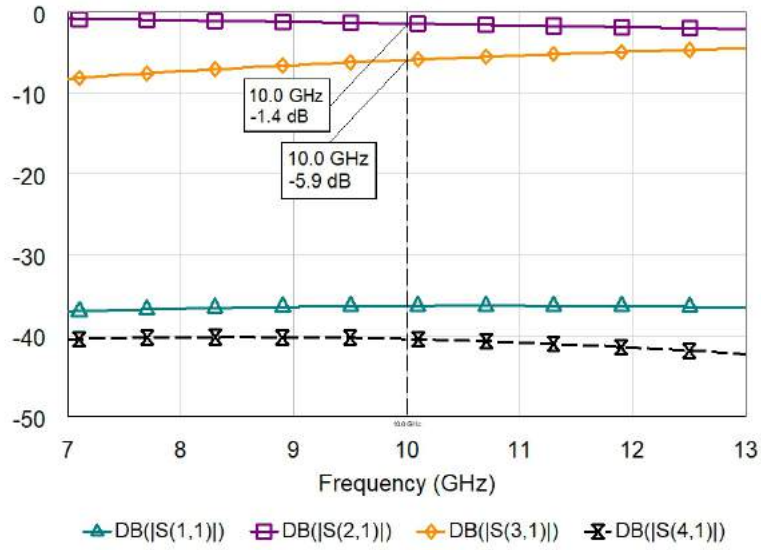


Figure 8.7: Lange coupler EM-simulated S -parameters from 7 – 13 GHz.

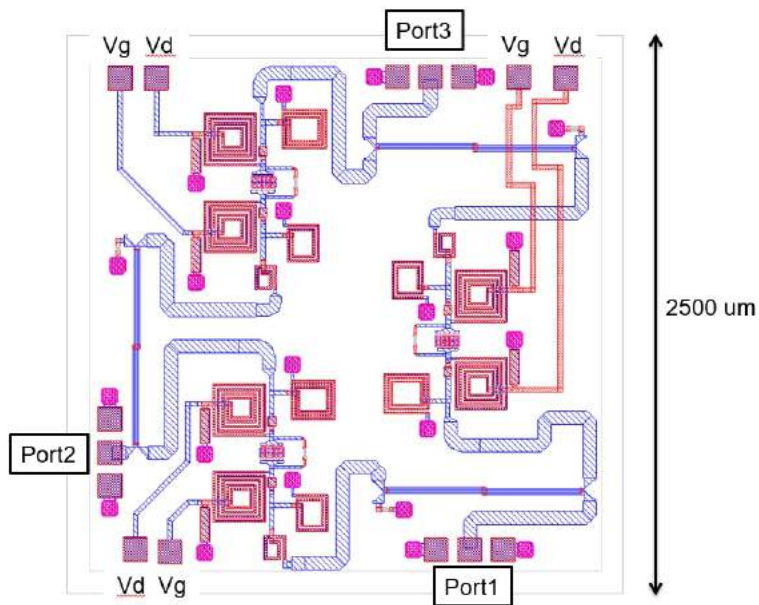


Figure 8.8: Active circulator layout with perpendicular RF pads for ease of probing/packaging, and three sets of drain/gate bias pads.

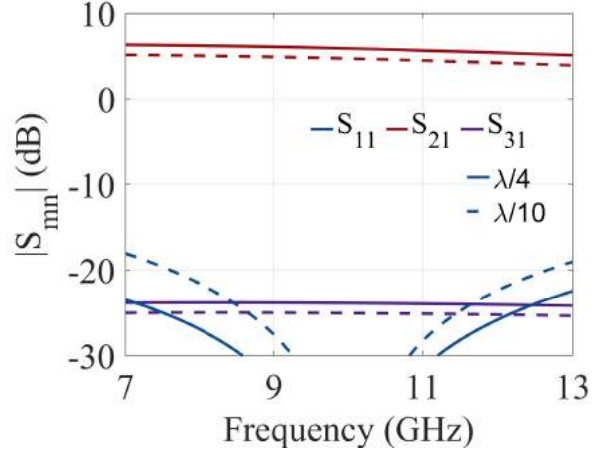


Figure 8.9: Simulated S-parameters of the active circulator with the same amplifier, for a coupling coefficient of the couplers of $c = 3$ dB for two different coupled-line section lengths: $\lambda/4$ and $\lambda/10$.

$$a = \frac{\sqrt{1 - c^2}}{\sqrt{1 - c^2 \cos \beta l + j \sin \beta l}} \quad (8.1)$$

$$b = \frac{j c \tan \beta l}{\sqrt{1 - c^2 + j \tan \beta l}} \quad (8.2)$$

where the coupling coefficient c is a value between 0 and 1, βl is the electrical length of the coupled-line section. The circulator behavior is affected by both the coupling coefficient and the length of the coupler. Fig. 8.9 shows the simulated S-parameters for 3-dB couplers, while Fig. 8.10 shows the case for 6-dB couplers. Two line lengths are considered: $\lambda/4$ and $\lambda/10$, showing that the circulator gain and isolation are affected by either the coupling coefficient or the length of the line, while the match and bandwidth are not dramatically affected. In particular, the isolation is high because of the ideality of the coupler, and depends on S_{12} of the amplifiers in the circulator.

The simulation results for the final design are shown in Fig. 8.11. A gain of 2.4 dB at 10 GHz is observed between each pair of ports, with a return loss (RL) better than 14 dB and isolation (IS) better than 20 dB from 8 – 12 GHz, or an operating bandwidth of 40%. In this circulator configuration, stability is a factor that needs to be carefully verified. The final design was EM-simulated over a wide frequency range and the stability factors K and $B1$ (determinant) analyzed from DC to 20 GHz and is shown in Fig. 8.12. Both parameters meet the unconditional stability condition ($K > 1$, $B1 > 0$) over the wide band for small-signal

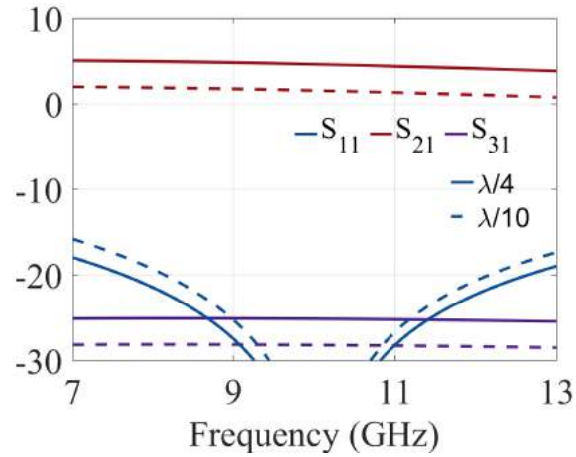


Figure 8.10: Simulated S-parameters of the active circulator with the same amplifier, using $c = 6$ dB couplers for two different coupled-line section lengths: $\lambda/4$ and $\lambda/10$.

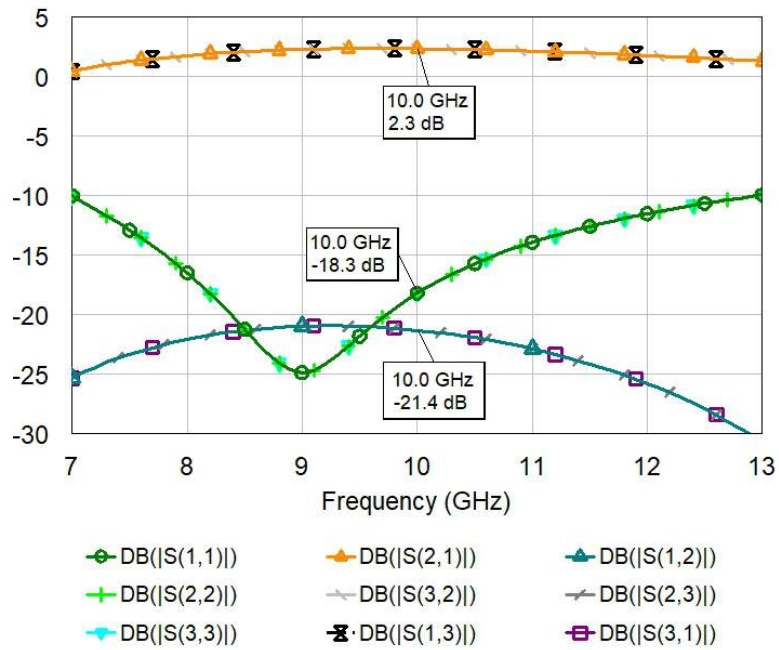


Figure 8.11: Simulated active circulator S-parameters from 7 to 13 GHz showing insertion gain with isolation $|S_{31}|$ greater than 20 dB.

operation.

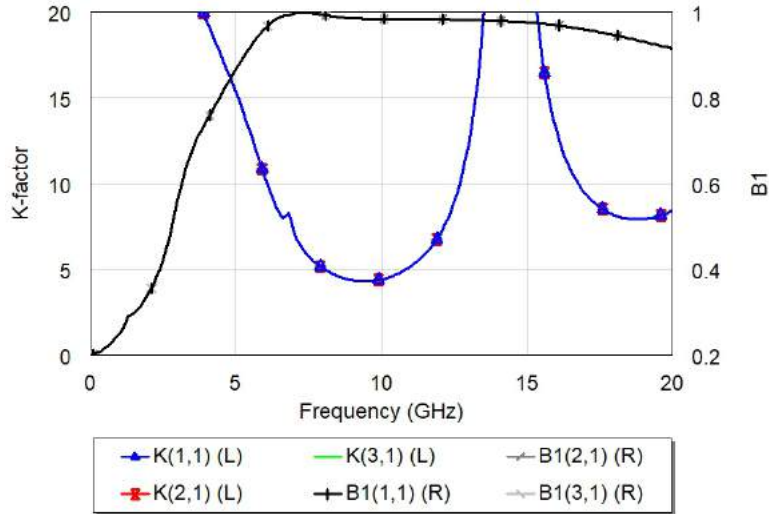


Figure 8.12: Stability analysis for complete active circulator under nominal bias and with all ports terminated in $50\ \Omega$.

8.4 MEASURED RESULTS AND ANALYSIS

A photograph of the fabricated MMIC is shown in Fig. 8.13, while Fig. 8.14 shows the chip mounted in a biasing fixture. The on-chip dc pads are wire-bonded to external bias lines. To avoid low frequency instabilities, single layer and SMD capacitors are connected in shunt to the bias lines. The RF ports are $150\text{-}\mu\text{m}$ GSG pads. A chip was chosen from a production batch for mounting, and measured using a multiport PNA with with a 3-port calibration done to the coaxial connector of the probes. The measured S-parameters are compared to simulations in Fig. 8.15 at the nominal bias. The gain (and matching, not shown) agrees well, but the isolation is degraded over the band. To understand this, a statistical analysis is performed with information provided by Qorvo for their process variation, and with additional load mismatch on all three ports inside the $\text{VSWR}=1.1$ circle with a normal distribution of impedances. The results are shown in Fig. 8.16. Note that this analysis shows a large spread in the three isolation parameters, and that for some values of process parameters and load impedances, the degradation in the measurement is predicted.

The $2.5\ \text{mm} \times 2.5\ \text{mm}$ chip shown in Fig.8.4 is analyzed in terms of behavior when integrated in a phased array environment, where the port impedances vary and where process variations impact device performance, as discussed above. The three-port active circulator topology is intended to be inserted in a phased array

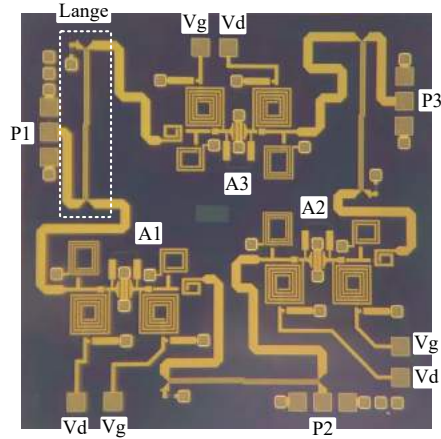


Figure 8.13: Photograph of a 2.5 mm × 2.5 mm GaAs MMIC X-band implementation.

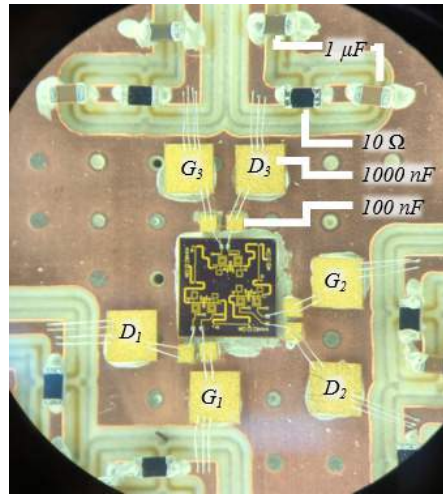


Figure 8.14: DC biasing board with chip mounted. Single layer and SMD capacitors are placed in the bias lines, connected with bondwires to on-chip DC pads. The gates bias lines are identified by G1, G2, G3 and drains D1, D2, D3, respectively. The RF ports are 150- μ m GSG probe pads.

front end as shown in Fig.8.17, where $|S_{31}|$ and $|S_{23}| \approx 1$, $|S_{13}|$, $|S_{32}|$ and $|S_{21}| \approx 0$, with all three ports matched. In normal operation, a circulator is connected to three different loads (PA, LNA and antenna. In an active electronically-steered phased array, these loads can vary, so it is important to investigate stability under different load impedance variations.

The closed-loop topology from Fig. 8.17 requires careful stability analysis, because odd-mode oscillations can occur but will not be detected by K -factor analysis. An open-loop gain analysis [159] is performed by extracting the locally linearized, intrinsic small-signal model of the device (Fig. 8.18) and using it in the

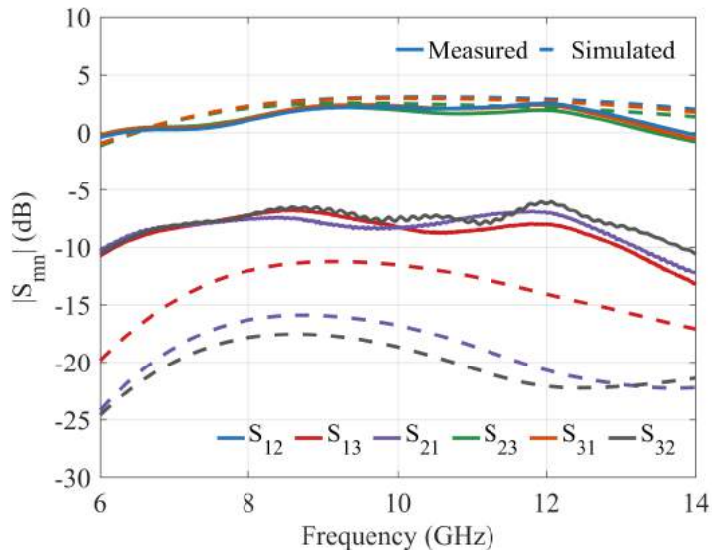


Figure 8.15: Measured and simulated S-parameters of the circuit from Fig. 8.14.

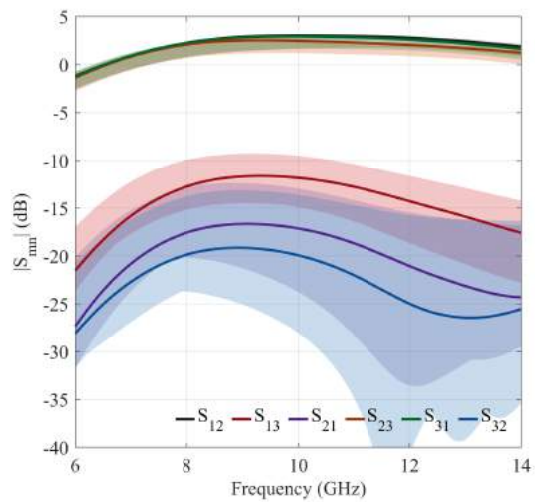


Figure 8.16: Statistical analysis of gain and isolation on all three ports with process variation and loads within a VSWR=1.1 circle.

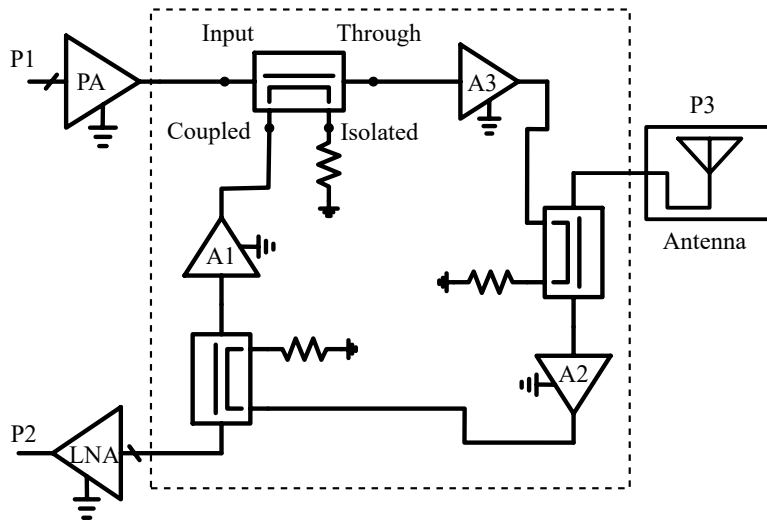


Figure 8.17: Block diagram of the active circulator and possible use in a transmission-reception (T/R) module. The three ports are connected to the output of the transmitter PA, antenna, and input of the receiver LNA.

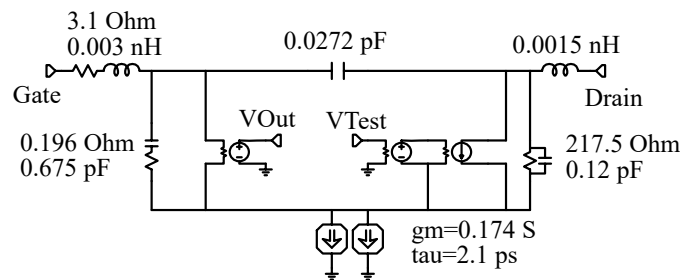


Figure 8.18: Small-signal model extracted from transistor foundry nonlinear model and adapted to open-loop stability analysis.

EM-simulated circuit in place of the foundry model. The polar plot in Fig. 8.19 shows the feedback voltage gain for the three devices over frequency and with external port impedances of 50Ω (solid lines). Stability is ensured when V_{Out}/V_{Test} does not cross the positive horizontal axis for amplitudes larger than unity. The shaded regions in Fig. 8.20 show that the phase margin for this circuit is larger than 30° for all loads that fall within the VSWR=2 circle on all three ports, with a uniform statistical distribution of impedance values.

8.5 CONCLUSION AND CONTRIBUTIONS

The design of an active circulator MMIC with gain is presented with a sensitivity analysis emulating the application in a phased-array, such as the one described in Chapters 2, 3 and 4. Simulated S -parameters show

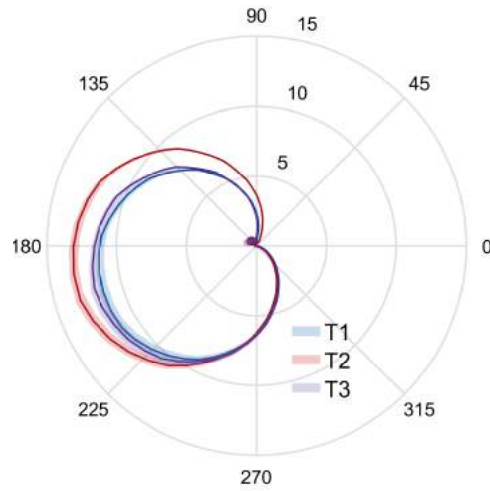


Figure 8.19: Simulated loop gain for the three transistors (T1, T2, T3) when ports are terminated with loads within the VSWR=2 circle, from DC to 20 GHz.

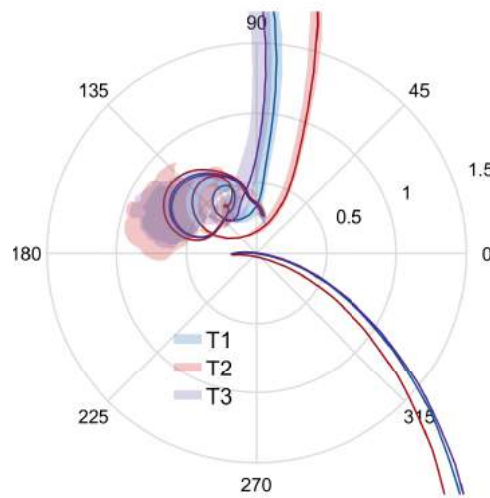


Figure 8.20: Simulated loop gain for the three transistors (T1, T2, T3) when ports are terminated with loads within the VSWR=2 circle, from DC to 20 GHz, showing in detail the behavior within a magnitude of 1.5. The shaded regions show that the phase margin for this circuit is larger than 30° for all loads that fall within the VSWR=2 circle on all three ports, with a uniform statistical distribution of impedance values.

Table 8.1: Comparison of Active MMIC Circulator Performance [124]

Ref	BW (GHz)	$ S_{31} $ (dB)	$ S_{21} $ (dB)	$ S_{11} $ (dB)	Technology	Size (mm ²)
[160]	10.2-12.6	-30	+1.5	<-17	0.25 um pHEMT	25
[161]	1.5 - 2.7	-26	+2	-10	CMOS	0.25
[134]	1.5 - 9.6	-18	-6	<-10	0.18 um CMOS	0.41
[162]	3.8 - 4.2	-22	+7.6	-15	MESFET	5
[163]	35 - 40	-30	-5	-15	0.25 um InP-HFET	3.32
[164]	6-18	-12	-2	-12	0.5 um GaAs MESFET	3.10
[128]	0.1-10	-16	-7	-13	0.5 um GaAs FET	0.9

a circulator behavior with 2.4 dB forward gain, over 20 dB isolation and better than 14 dB match from 8 to 12 GHz, which compares well to previously demonstrated devices summarized in Table 8.1. Measurements show discrepancy in isolation levels when compared to simulations, motivating the statistical analysis, which points to relevant parameters that should be taken into account in applications where variations of the port impedances can be expected. The contributions of this chapter are described in [141] and [40].

CHAPTER 9

SUMMARY, FUTURE WORK AND CONTRIBUTIONS

CONTENTS

9.1	THESIS SUMMARY	134
9.2	FUTURE WORK	135
9.3	THESIS CONTRIBUTIONS	139

9.1 THESIS SUMMARY

The thesis is organized around a 6–12 GHz 4-element, dielectric-loaded ridge horn active linear array. A broadband ridge-waveguide small-aperture horn element with transitions to microstrip enables direct MMIC integration in the antenna assembly with a low-resistance thermal path. GaAs MMIC phase shifters and GaN MMIC PAs are used as the active elements. The architecture is modular and scalable in terms of power per element and number of elements.

In the first part of the thesis, the design and measurements of the active sub-array radiating element with the microstrip-to-waveguide transition and power amplifier MMIC is discussed, followed by the 4×1 spatial power combiner array design details, including broadband Wilkinson divider feed network, expected radiation patterns, as well as measured array performance when the 4 elements are fed in phase. The analysis

and measurements of this 4-element linear array are performed over a broad frequency range (full octave), a wide range of input powers, and a wide range of PA drain voltages. Over-the-air (OTA) simulations and measurements show how these parameters affect efficiency and radiation pattern, as well as signal linearity. This study is then extended to a beam-steering phased array. The performance of the active beam-steering network and phase-shifter performance, steering angle versus progressive phase shift (PPS), and analysis of coupling effects as a function of PPS and supply-voltage amplitude tapering of the elements is presented, and an experimental array fabricated to validate the analysis.

In the second part of the thesis, simultaneous transmit-and-receive arrays are considered in terms of isolation components behind the antenna. Integration is discussed, particularly the trade-offs in component design for octave bandwidth operation, and then design and characterization is presented for three types of circulators with array integration as a goal. Ferrite circulators that use different magnetic biasing approaches to achieve miniaturization and reconfigurable bandwidth are shown, together with a comprehensive analysis of the effect of magnetization distribution on circulator design. Then, some initial results in self-magnetized circulators that can potentially be integrated with MMICs are given. Finally, a broadband GaAs MMIC circulator design, validated with measurements on a fabricated 7-13 GHz MMIC, is presented and the performance of this circulator in a phased array environment is analyzed.

9.2 FUTURE WORK

Other research topics that are initiated by this thesis are briefly introduced in this section. As mentioned, the active transmit array design is intended for scaling in number of elements, power per element, as well as number of beams and signals. A study of efficiency improvement with dynamic supply modulation for different signals, with a tradeoff between array-level and element-level integration is ongoing, e.g. [87]. The array size scaling is enabled by the modular design that includes thermal management. The modular architecture also allows element-level power scaling by inserting an additional amplifier stage, as already shown with the addition of the driver in Chapter 4, which was added together with a phase shifter in each element for beamforming. The modular architecture additionally enables straightforward modification of the

beamforming network. For example, the Wilkinson corporate feed and phase shifters can be replaced by a Butler matrix beamformer.

For power scaling at the element level, a 5-W broadband 6–12 GHz PA is designed in the WIN N15 GaN process. Specifically, broadband matching is accomplished with resonant RLC circuits. The layout of a two-stage PA is shown in Fig. 9.1(a). Reactive power combining is used in the output stage. The output, interstage and input matching networks all employ multiple resonant circuits which enable broadband operation and integrate stability networks. The layout is fully EM-simulated and allows for independent biasing of the two stages. The matching theory, simulations, design and measurements of the fabricated chip are planned for publication in 2022. Additional power scaling is planned with 20-W broadband PAs designed and fabricated in the WIN N15 GaN process as described in [165]. Fig. 9.1(b) shows another two-stage PA designed for high gain and isolation with flexible external input and output matching networks. The amplifier is designed by interconnecting two transistors of different sizes through an interstage matching network for conjugate matching when the input and output ports are directly connected to $50\ \Omega$. Bias lines are implemented on-chip. The goal of this quasi-MMIC is to have flexibility for design of off-chip specialized matching networks for different purposes in the 6–12 GHz range.

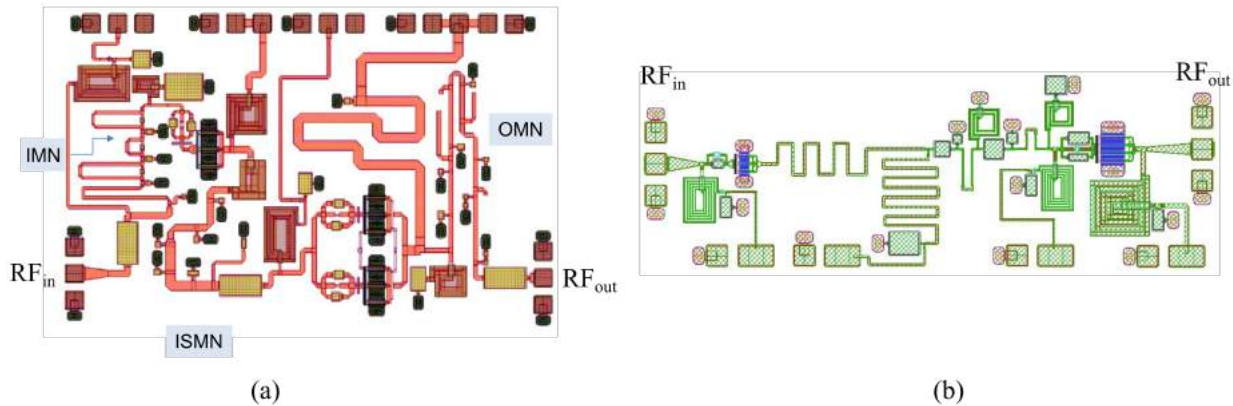


Figure 9.1: (a) Layout of a 6-W, 6–12 GHz power amplifier MMIC designed in the WIN Semiconductors NP15 GaN on SiC process, with broadband matching accomplished using multiple resonant RLC circuits. (b) Two-stage amplifier with input and output ports terminated in $50\ \Omega$ with no matching. The output of the first stage device is directly matched to the input of the second stage using resonant circuits. This quasi-MMIC has the flexibility to be matched at input and output using external matching circuits with different technical specifications from 6–12 GHz.

For increased element-level power, it is important to quantify the thermal performance of the design.

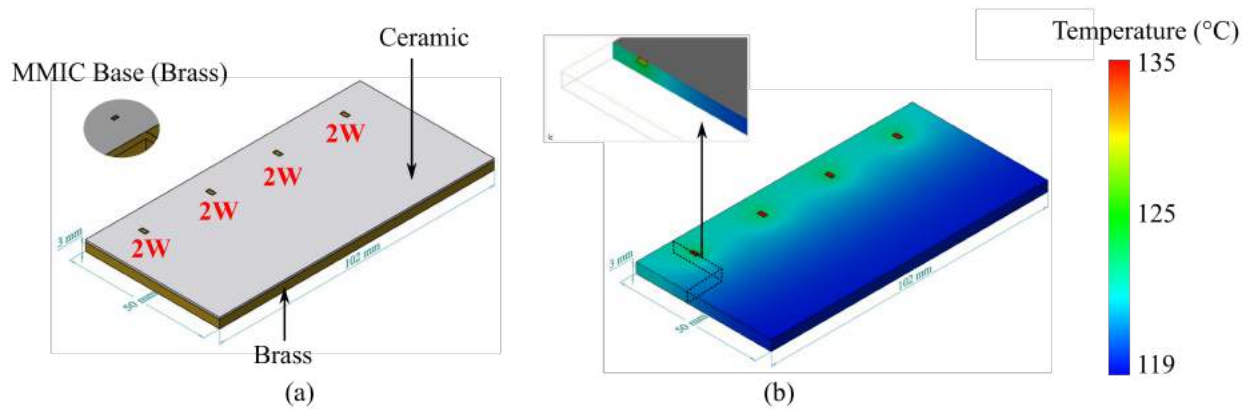


Figure 9.2: Simulated steady-state temperature throughout the brass mount when 4 heat sources the size of the 2-W MMICs are dissipating 2 W each. The brass and ceramic thermal properties are used, along with free convection coefficient of surrounding gases and dry vapors equal to 5 W/m^2 , and with an external environmental temperature of 298 K (25°C).

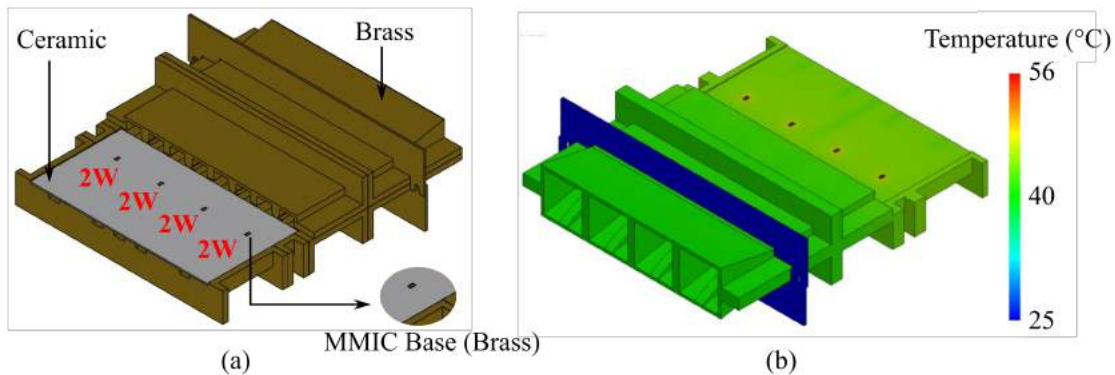


Figure 9.3: Thermal simulations using the same sources as described in Fig. 9.2 but with MMICs remounted directly to the array chassis. (a) Mechanical structure used for simulation. (b) Simulated heat map.

Some initial thermal simulations using the SolidWorks Thermal Application are shown in Fig. 9.2, where the simulated steady-state temperature throughout the brass mount is shown when 4 MMIC sources are dissipating 2 W each, assuming an output power of less than 2 W and efficiency below 50%. Brass properties are used for the metal, and an environmental temperature of 298 K (25°C) is assumed. The heat dissipation is improved when the MMICs are integrated, as shown in Fig. 9.3. The steady-state temperature of the metallic parts decreases from 119°C to 40°C , if compared to Fig. 9.2. Thermal simulations of the array were confirmed by measurements during the measurement of the supply modulate power combiner from Chapter 3, reported in [88] (accepted) .

In this thesis, many examples of co-simulations using linear and nonlinear circuit simulations and full-

wave electromagnetic simulations are shown and validated by measurements. The next step is co-simulation at the system level, e.g. using the Cadence VSS tool, which allows generation of complex signals that can be input into the circuit simulations. A simple initial co-simulation has already been done for the signals shown in Chapters 3 and 4, and over-the-air tests were used for validation, but there are many additional signals of interest, e.g. multiple simultaneous signals across the wide band, that would be useful to co-simulate.

In terms of continuing work for transmit-receive arrays, the final analysis in Chapter 8 shows limitations of the initial broadband active circulator MMIC design in terms of maintaining isolation when the antenna port impedance varies (see Fig. 8.16), as occurs with scanning and coupling variation of frequency. Therefore, an avenue of future work is to redesign the active circulator to have high isolation for mismatched conditions on the ports, by a more careful investigation of the couplers as well as amplifiers in the three branches. For example, the three couplers can have different coupling ratios, and the three amplifiers can have different gain and isolation levels. Finally, for higher power handling and linearity, an implementation in GaN as opposed to the demonstrated GaAs MMIC is desired, and this is a topic of a new NSF-funded project.

The transmit array shown in this thesis can be a part of a STAR array using active circulators, or a part of a half-duplex array using a bias-switched integrated PA and LNA, referred to as a “PALNA” [166]. A PALNA was designed in the WIN PIH110 GaAs process, and is shown in Fig. 9.4. The circuit shows a 2-stage LNA and a 2-stage PA with inputs and outputs connected in a closed-loop. The PA output is connected to the LNA input by a reactive matching network to achieve high efficiency in the transmit chain. The LNA output is connected to the PA input with a Wilkinson power divider to achieve isolation and matching. The LNA input matching networks include reflectionless filters to achieve matching outside the bands and low losses in-band, which improves noise figure. Some design challenges include: achieving high isolation between transmit and receive paths with acceptable performances in noise figure and efficiency; maintaining stability of a closed loop configuration; characterizing efficiency and noise figure of the prototyped RF front end; and understanding how antenna mismatches will affect the front-end performance. This design has been fabricated, and will be characterized for a future publication.

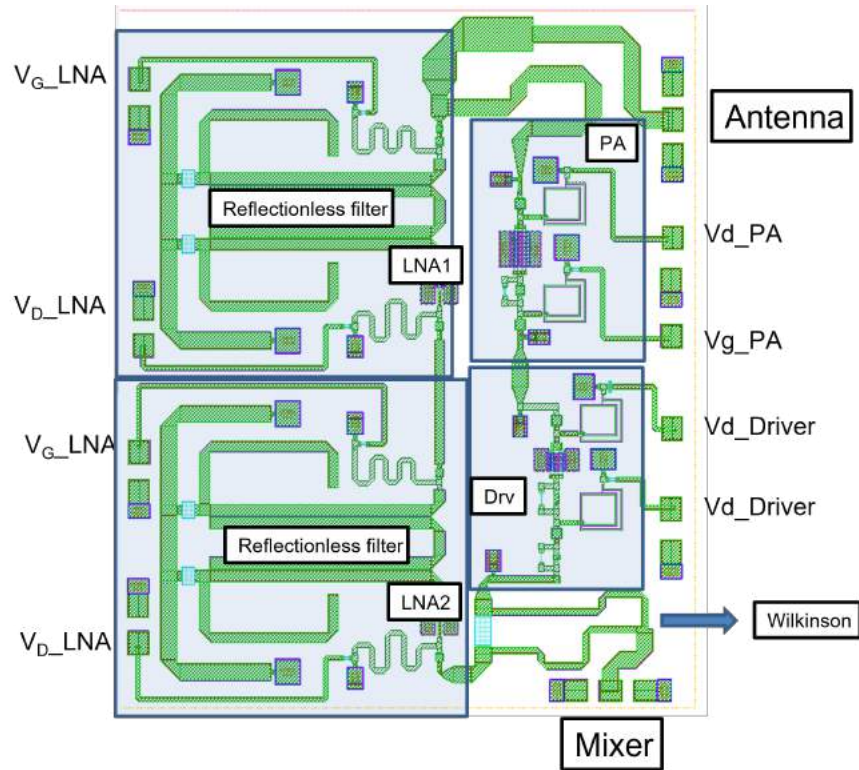


Figure 9.4: Layout of a bidirectional power–low-noise amplifier (PALNA) implemented in the WIN Semiconductors PIH110 GaAs process for the 26–30 GHz 5G frequency band. Instead of switches for T/R, one possible solution is the use of switchless front-end bidirectional amplifiers. A PA and LNA (PALNA) are connected by a specialized matching network. Switching between transmit and receive paths is done by turning ON/OFF the drain and/or gate biases. The simulated two-stage LNA gain is about 20 dB with $NF < 2.5$ dB, the class-AB PA with a drain efficiency > 40 %.

9.3 THESIS CONTRIBUTIONS

The specific contributions of this thesis can be summarized as follows:

- ◇ Developed the design procedure, prototype construction and characterization of a small octave-bandwidth linearly-polarized transmit amplified horn antenna element, suitable for array integration. The feed is implemented in ridge waveguide and includes a transition to a $50\text{-}\Omega$ microstrip line, allowing direct integration with active circuits with a common thermal and RF ground. A dielectric-slab lens extends the lower-frequency impedance matched region without significantly affecting the radiation pattern. These contributions are published in [71], [81].

- ◇ Developed a co-simulation method and calibrated over-the-air measurements for an active horn element with varying drain supply voltage of the GaN MMIC PA, showing performance trade-off between EIRP and PAE. The active element EIRP with calibrated OTA measurements depends on the power delivered to the antenna by the PA, which in turn depends on matching and nonlinear characteristics of the PA. These contributions are published in [81], [86] and [87].
- ◇ The unit active element analysis is extended to an octave-bandwidth active transmit array as a spatial power combiner (all elements in phase), including nonlinear co-simulations of EIRP, efficiency, sidelobe control and nonlinearities when the drain supply voltage is varied across amplifiers in the combiner. The co-simulations are performed with full-wave simulations (HFSS) for the passive antenna array and feed portion, Cadence MWO harmonic balance simulations for the circuit portion, and Cadence VSS system simulations for linearity under modulated signals.
- ◇ The array architecture is modular and scalable and was implemented with a broadband Wilkinson corporate feed network with excellent phase and amplitude balance over the octave. PAs are integrated with the feed. Over-the-air (OTA) measurements are performed on the prototype to validate the simulation approach, and an EIRP of 50 dBm is achieved across the 6–12 GHz octave, in agreement with simulations. The linearity is evaluated using a 64QAM 50 MHz signal, showing that the ACPR gracefully degrades when the supply voltage of the outer elements is reduced in order to improve the array sidelobe level. The measured linearity trends with frequency, supply voltage and signal follow the simulation trends. The analysis in this chapter unveils the challenges in transmit arrays that result from the complex dependence between output power, efficiency, linearity and inter-element coupling when a full octave bandwidth is considered. The contributions from this chapter are reported in [87](accepted), [86], [88](accepted), [89](accepted) and [90](to be submitted).
- ◇ The analysis is extended to a 4-element array and validated by experiment. For that, a new active module is designed and fabricated to contain GaAs phase shifters, driver amplifiers and PAs, and the accompanying control and bias circuits. The active array is analyzed in an over-the-air simulation environment starting from signal generation at the system level, following with linear and nonlinear

circuit simulations (harmonic balance in Cadence AWR MWO), with full-wave EM co-simulations in Ansys HFSS starting from the output of the final PAs to the far field of the antenna array. A large number of variables is included in the analysis to gain an understanding of array behavior: frequency (6–12 GHz); input power to each element (10–33 dBm); phase shift through control voltage in each element for beam steering (maximum value depends on frequency); drain supply voltage on each PA (for beam tapering, and later efficiency enhancement); signals transmitted through the array (single CW and two widely spaced modulated signals). The contributions of this chapter are included in [89], [86] and [87].

- ◇ For a STAR array, design of microstrip ferrite circulators by controlling the magnetic bias field (MBF) is developed. A detailed study is carried out using full-wave EM and magnetostatic co-simulations (using HFSS and Maxwell3D, respectively) and variations of the MBF are presented for several permanent magnet configurations. To the best of the author’s knowledge, the only other related work for a saturated ferrite disk is presented in [154]. The approach in this thesis includes numerical modal analysis, as well as eigenmode and driven simulations to understand the impact of magnetization levels and distribution on circulators electromagnetic performance. The contributions are published in [155], [35], [34], [141], [156].
- ◇ A graphical study for ferrite circulators is developed to characterize the real and imaginary parts of the effective permeability, as a simultaneous function of MBF intensity and frequency. It shows that the low-loss region can be avoided even with a weak MBF. On the other hand, eigenmode analysis combined with driven simulations show the effects on circulator bandwidth when applied a magnetic bias field with higher magnitudes than the ferrite magnetization saturation. The total internal field distribution changes when the same MBF is applied to different ferrite geometries, due to boundary field modification. A parametric study of the resonance and Q-factor of the disk as a function of shape and thickness quantifies this effect, and the results are confirmed with driven full-wave simulations. Finally, the nonuniformity of different PM bias geometries is characterized using magnetostatic and full-wave co-simulations in order to observe changes in the operation point (above or below FMR),

which in turn results in a shift in direction of circulation and frequency. The analysis is validated using a commercially-available ferrite disk (Skyworks TT1-105). The variations on the MBF allows design of three circulators: a 4.3 GHz device with PMs positioned to produce nearly uniform saturation; a 1.6 GHz device when the same PMs are placed further from the ferrite disk and result in weak biasing; and a 7 GHz device non-uniformly biased with a reduced-volume array of small magnets. The co-simulations match measured results. These contributions are described in [35].

- The study of ferrite circulator designs below the absorptive FMR region was motivated by self-biased circulator constraints, i.e., low volumes, nonuniform and unsaturated cavities. The same analysis was applied to investigating circulators with materials characterized by shape anisotropy, e.g. hexaferrites and magnetic nano-wires, which operate below the FMR with no external magnets and have the potential of monolithic integration with active circuits. Initial simulation and measurement results for hybrid microstrip circulators operating in the lower part of X-band with no external permanent magnets, enabled by a iron-nickel plating process of porous alumina, developed at Argonne National Labs, are presented. Proof-of-concept measurements that demonstrate non-reciprocal behavior around 7 and 8 GHz are obtained with and without external bias field, and before and after material magnetization. These demonstrations, described in [142], are the first demonstrations of self-magnetized connectorized MNC circulators below 10 GHz, to the best of the author's knowledge.
- ◇ Circulator design is extended to active circulators with gain which use transistor nonreciprocity. Simulated S -parameters show a circulator behavior with 2.4 dB forward gain, over 20 dB isolation and better than 14 dB match from 8 to 12 GHz, which compares well to previously demonstrated devices. An active circulator was implemented in GaAs and measured from 7 to 13 GHz with performance matching simulations, except for the isolation over a broad frequency range. It is determined that the circuit design is sensitive to the exact port impedances, motivating a statistical analysis which points to relevant parameters that should be taken into account in applications where variations of the port impedances can be expected, such as in the broadband phased array described in the first part of the thesis. The contributions of this chapter are described in [141] and [40].

In conclusion, this thesis has two parts with a common theme of broadband circuit co-simulation and co-design for phased array front ends, where the prefix “co-” implies linear and nonlinear circuit, as well as magneto-static and full-wave electromagnetic methods. In the first part, a 6–12 GHz active antenna array is analyzed and experimentally characterized, while the second part of the thesis details components that can enable broadband STAR operation. The research described in this thesis opens a number of avenues for exciting continuing and future work.

BIBLIOGRAPHY

- [1] K. Kibaroglu, M. Sayginer, T. Phelps, and G. M. Rebeiz, “A 64-element 28-GHz phased-array transceiver with 52-dBm EIRP and 8–12-Gb/s 5g link at 300 meters without any calibration,” *IEEE Transactions on Microwave Theory and Techniques*, vol. 66, no. 12, pp. 5796–5811, 2018. 2, 59
- [2] Y. Kawaguchi, H. Nakagawa, S. Tanaka, and T. Yamada, “Application of phased-array antenna technology to the 21 GHz broadcasting satellite for rain-attenuation compensation,” in *2002 IEEE International Conference on Communications. Conference Proceedings. ICC 2002 (Cat. No. 02CH37333)*, vol. 5. IEEE, 2002, pp. 2962–2966. 2
- [3] E. Lier, J. Huffman, W. N. Kefauver, B. Dawley, and F. Butscher, “Satellite antenna capabilities pioneered at Lockheed Martin space systems company,” in *2017 11th European Conference on Antennas and Propagation (EUCAP)*. IEEE, 2017, pp. 1506–1510. 2
- [4] S. Shahramian, M. J. Holyoak, A. Singh, and Y. Baeyens, “A fully integrated 384-element, 16-tile, W-band phased array with self-alignment and self-test,” *IEEE Journal of solid-state circuits*, vol. 54, no. 9, pp. 2419–2434, 2019. 2, 59
- [5] H. Hommel and H. Feldle, “Current status of airborne active phased array (aesa) radar systems and future trends,” in *First European Radar Conference, 2004. EURAD*. IEEE, 2004, pp. 121–124. 2
- [6] J. Schoebel, T. Buck, M. Reimann, M. Ulm, M. Schneider, A. Jourdain, G. J. Carchon, and H. A. Tilmans, “Design considerations and technology assessment of phased-array antenna systems with RF

- MEMS for automotive radar applications,” *IEEE Transactions on Microwave Theory and Techniques*, vol. 53, no. 6, pp. 1968–1975, 2005. 2
- [7] M. Dudek, I. Nasr, G. Bozsik, M. Hamouda, D. Kissinger, and G. Fischer, “System analysis of a phased-array radar applying adaptive beam-control for future automotive safety applications,” *IEEE Transactions on Vehicular Technology*, vol. 64, no. 1, pp. 34–47, 2014. 2
- [8] D. Zrnic, J. Kimpel, D. Forsyth, A. Shapiro, G. Crain, R. Ferek, J. Heimmer, W. Benner, F. T. McNellis, and R. Vogt, “Agile-beam phased array radar for weather observations,” *Bulletin of the American Meteorological Society*, vol. 88, no. 11, pp. 1753–1766, 2007. 2
- [9] E. Yoshikawa, T. Ushio, Z. Kawasaki, S. Yoshida, T. Morimoto, F. Mizutani, and M. Wada, “MMSE beam forming on fast-scanning phased array weather radar,” *IEEE Transactions on Geoscience and remote sensing*, vol. 51, no. 5, pp. 3077–3088, 2012. 2
- [10] R. Kronberger, T. Knie, R. Leonardi, U. Dettmar, M. Cremer, and S. Azzouzi, “UHF RFID localization system based on a phased array antenna,” in *2011 IEEE International Symposium on Antennas and Propagation (APSURSI)*. IEEE, 2011, pp. 525–528. 2
- [11] K. F. Warnick, R. Maaskant, M. V. Ivashina, D. B. Davidson, and B. D. Jeffs, “High-sensitivity phased array receivers for radio astronomy,” *Proceedings of the IEEE*, vol. 104, no. 3, pp. 607–622, 2016. 2
- [12] S. W. Ellingson and G. A. Hampson, “A subspace-tracking approach to interference nulling for phased array-based radio telescopes,” *IEEE Transactions on Antennas and Propagation*, vol. 50, no. 1, pp. 25–30, 2002. 2
- [13] O. M. Bucci, L. Crocco, R. Scapatucci, and G. Bellizzi, “On the design of phased arrays for medical applications,” *Proceedings of the IEEE*, vol. 104, no. 3, pp. 633–648, 2016. 3
- [14] T. Hall, B. Nukala, C. Stout, N. Brewer, J. Tsay, J. Lopez, R. Banister, T. Nguyen, and D. Lie, “A phased array non-contact vital signs sensor with automatic beam steering,” in *2015 IEEE MTT-S International Microwave Symposium*. IEEE, 2015, pp. 1–4. 3

- [15] T. Hall, D. Y. Lie, T. Q. Nguyen, J. C. Mayeda, P. E. Lie, J. Lopez, and R. E. Banister, “Non-contact sensor for long-term continuous vital signs monitoring: A review on intelligent phased-array Doppler sensor design,” *Sensors*, vol. 17, no. 11, p. 2632, 2017. 3
- [16] J. Crezee, P. Van Haaren, H. Westendorp, M. De Greef, H. Kok, J. Wiersma, G. Van Stam, J. Sijbrands, P. Zum Vörde Sive Vörding, J. Van Dijk *et al.*, “Improving locoregional hyperthermia delivery using the 3-D controlled amc-8 phased array hyperthermia system: A preclinical study,” *International Journal of Hyperthermia*, vol. 25, no. 7, pp. 581–592, 2009. 3
- [17] M. Metcalf, D. Xu, D. T. Okuda, L. Carvajal, R. Srinivasan, D. A. Kelley, P. Mukherjee, S. J. Nelson, D. B. Vigneron, and D. Pelletier, “High-resolution phased-array MRI of the human brain at 7 tesla: initial experience in multiple sclerosis patients,” *Journal of Neuroimaging*, vol. 20, no. 2, pp. 141–147, 2010. 3
- [18] B. H. Waters, B. J. Mahoney, V. Ranganathan, and J. R. Smith, “Power delivery and leakage field control using an adaptive phased array wireless power system,” *IEEE Transactions on Power Electronics*, vol. 30, no. 11, pp. 6298–6309, 2015. 3
- [19] J. Lopezf, J. Tsay, B. A. Guzman, J. Mayeda, and D. Y. Lie, “Phased arrays in wireless power transfer,” in *2017 IEEE 60th International Midwest Symposium on Circuits and Systems (MWSCAS)*. IEEE, 2017, pp. 5–8. 3
- [20] J. Navarro, “Heterogeneously-integrated phased-array antennas for line-of-sight (los) communications and sensor applications,” in *2018 IEEE/MTT-S International Microwave Symposium-IMS*. IEEE, 2018, pp. 776–778. 4
- [21] ———, “Affordable, multi-function flight-worthy airborne phased-array sensor,” in *2020 IEEE/MTT-S International Microwave Symposium (IMS)*. IEEE, 2020, pp. 829–832. 4
- [22] R. J. Mailloux, *Phased array antenna handbook*. Artech house, 1994, pp. 35–38. 4

- [23] E. Brookner, "Advances and breakthroughs in radars and phased-arrays," in *2016 CIE International Conference on Radar (RADAR)*. IEEE, 2016, pp. 1–9. 4
- [24] A. Suriani, P. Capece, and G. Mannocchi, "Developments in SAR active phased array antennas in Thales Alenia space," in *2019 IEEE International Symposium on Phased Array System & Technology (PAST)*. IEEE, 2019, pp. 1–4. 4
- [25] B. Munk, R. Taylor, T. Durharn, W. Crosswell, B. Pigon, R. Boozer, S. Brown, M. Jones, J. Pryor, S. Ortiz, J. Rawnick, K. Krebs, M. Vanstrum, G. Gothard, and D. Wiebelt, "A low-profile broadband phased array antenna," in *IEEE Antennas and Propagation Society International Symposium. Digest. Held in conjunction with: USNC/CNC/URSI North American Radio Sci. Meeting (Cat. No.03CH37450)*, vol. 2, 2003, pp. 448–451 vol.2. 4
- [26] I. Visscher, C. Roeloffzen, C. Taddei, M. Hoekman, L. Wevers, R. Grootjans, P. Kapteijn, D. Geskus, A. Alippi, R. Dekker, R. Oldenbeuving, J. Epping, R. B. Timens, E. Klein, A. Leinse, P. v. Dijk, and R. Heideman, "Broadband true time delay microwave photonic beamformer for phased array antennas," in *2019 13th European Conference on Antennas and Propagation (EuCAP)*, 2019, pp. 1–5. 4
- [27] G. Kriehn, A. Kiruluta, P. E. Silveira, S. Weaver, S. Kraut, K. Wagner, R. T. Weverka, and L. Griffiths, "Optical BEAMTAP beam-forming and jammer-nulling system for broadband phased-array antennas," *Applied Optics*, vol. 39, no. 2, pp. 212–230, 2000. 4
- [28] F. Hu and K. Mouthaan, "A 1–20 GHz 400 ps true-time delay with small delay error in 0.13 μm CMOS for broadband phased array antennas," in *2015 IEEE MTT-S International Microwave Symposium*, 2015, pp. 1–3. 4
- [29] C. Fulton, M. Yeary, D. Thompson, J. Lake, and A. Mitchell, "Digital phased arrays: Challenges and opportunities," *Proceedings of the IEEE*, vol. 104, no. 3, pp. 487–503, 2016. 4
- [30] P. K. Bailleul, "A new era in elemental digital beamforming for spaceborne communications phased arrays," *Proceedings of the IEEE*, vol. 104, no. 3, pp. 623–632, 2016. 4

- [31] J. S. Herd and M. D. Conway, "The evolution to modern phased array architectures," *Proceedings of the IEEE*, vol. 104, no. 3, pp. 519–529, 2016. 4
- [32] R. C. Hansen, *Phased array antennas*. John Wiley & Sons, 2009, vol. 213, pp. 221–276. 5, 13
- [33] M. A. Elmansouri, L. B. Boskovic, and D. S. Filipovic, "Compact wideband dual-polarized in-band full-duplex antenna subsystem," *IEEE Transactions on Antennas and Propagation*, pp. 1–1, 2021. 10
- [34] M. Pinto, L. Marzall, A. Ashley, D. Psychogiou, and Z. Popović, "Design-oriented modelling of microstrip ferrite circulators," in *2018 48th European Microwave Conference (EuMC)*. IEEE, 2018, pp. 215–218. xxii, 10, 84, 99, 101, 102, 105, 113, 141
- [35] L. Marzall, D. Psychogiou, and Z. Popović, "Microstrip ferrite circulator design with control of magnetization distribution," *IEEE Transactions on Microwave Theory and Techniques*, vol. 69, no. 2, pp. 1217–1226, 2021. 10, 84, 105, 141, 142
- [36] Y. Zhang *et al.*, "Synthesis and Properties of FeCo-Based Anisotropic Magnetic Nanocomposites," *62nd Conf. on Magnetism and Magnetic Materials, Pittsburgh, PA, USA*, 2017. 10
- [37] J. Wang *et al.*, "High-Aspect-Ratio Magnetic Nanowires by Electroplating and Electrospinning with Controlled Sizes and Compositions," *5th Nano Today Conference, Waikoloa Beach Marriott, Hawaii*, 2017. 10
- [38] a. o. Aragon, A., "Comparative magnetic studies on the ordered and disordered magnetic nanowires arrays," *62nd Conf. on Magnetism and Magnetic Materials, Pittsburgh, PA, USA*, 2017. 10
- [39] L. Marzall and Z. Popović, "An x-band quasi-circulator gaas mmic," in *2019 IEEE International Conference on Microwaves, Antennas, Communications and Electronic Systems (COMCAS)*. IEEE, 2019, pp. 1–4. 10, 84
- [40] L. Marzall, S. Verploegh, T. Cappello, M. Roberg, and Z. Popović, "Active mmic circulator performance in a phased-array-like environment," in *2020 50th European Microwave Conference (EuMC)*. IEEE, 2021, pp. 1186–1189. 10, 133, 142

- [41] C. Berrached, D. Bouw, M. Camiade, and D. Barataud, "Wideband high efficiency high power gain amplifiers using mic and quasi-mmwave technologies," in *2013 European Microwave Conference*. IEEE, 2013, pp. 1395–1398. 11
- [42] P. Zurek, "Dual-band and broadband rf power amplifiers for concurrent signal transmission," Ph.D. dissertation, University of Colorado at Boulder, 2021. 11
- [43] M. Integrated, "Adjacent channel leakage ratio acir for rf device," <https://www.maximintegrated.com/en/design/technical-documents/app-notes/3/3902.html/>, [Online; accessed 13-February-2022]. 12
- [44] M. Leffel, "Intermodulation distortion in a multi-signal environment," *RF Design*, vol. 18, no. 6, pp. 78–85, 1995. 12
- [45] N. B. De Carvalho and J. C. Pedro, "Compact formulas to relate acir and npr to two-tone imr and ip3," *Microwave Journal*, vol. 42, no. 12, pp. 70–70, 1999. 12
- [46] L. C. Nunes, P. M. Cabral, and J. C. Pedro, "AM/AM and AM/PM distortion generation mechanisms in Si LDMOS and GaN HEMT based RF power amplifiers," *IEEE Transactions on Microwave Theory and Techniques*, vol. 62, no. 4, pp. 799–809, 2014. 12
- [47] R. Quaglia, L. Piazzon, V. Camarchia, R. Giofre, M. Pirola, P. Colantonio, G. Ghione, and F. Giannini, "Experimental investigation of bias current and load modulation effects in phase distortion of GaN HEMTs," *Electronics letters*, vol. 50, no. 10, pp. 773–775, 2014. 12
- [48] R. Giofrè, P. Colantonio, and F. Giannini, "A design approach to maximize the efficiency vs. linearity trade-off in fixed and modulated load GaN power amplifiers," *IEEE Access*, vol. 6, pp. 9247–9255, 2018. 12
- [49] A. Hadjichristos, P. H. See, B. Nejadi, G. Klemens, N. L. Frederick Jr, G. S. Sahota, M. Cassia, N. M. Pletcher, Y. Zhao, T. A. Myers *et al.*, "Multi-mode multi-band power amplifier module," Mar. 3 2015, uS Patent 8,971,830. 13

- [50] A. Grebennikov, N. Kumar, and B. S. Yarman, *Broadband RF and microwave amplifiers*. CRC Press, 2015. 13
- [51] P. Asbeck and Z. Popovic, “ET comes of age: Envelope tracking for higher-efficiency power amplifiers,” *IEEE Microwave Magazine*, vol. 17, no. 3, pp. 16–25, 2016. 13
- [52] M. R. Duffy, G. Lasser, G. Nevett, M. Roberg, and Z. Popović, “A three-stage 18.5–24-GHz GaN-on-SiC 4 w 40% efficient MMIC PA,” *IEEE Journal of Solid-State Circuits*, vol. 54, no. 9, pp. 2402–2410, 2019. 13
- [53] S. K. Koul and B. Bhat, *Microwave and Millimeter Wave Phase Shifters*. Artech House Norwood, MA, 1991, vol. 2. 14
- [54] S. Barker and G. M. Rebeiz, “Distributed MEMS true-time delay phase shifters and wide-band switches,” *IEEE Transactions on Microwave Theory and Techniques*, vol. 46, no. 11, pp. 1881–1890, 1998. 14
- [55] X. Sun, J.-M. Fernández-González, M. Sierra-Pérez, and B. Galocha-Iragüen, “Low-loss loaded line phase shifter for radar application in X band,” in *2018 15th European Radar Conference (EuRAD)*. IEEE, 2018, pp. 477–480. 14
- [56] E. G. Erker, A. S. Nagra, Y. Liu, P. Periaswamy, T. R. Taylor, J. Speck, and R. A. York, “Monolithic Ka-band phase shifter using voltage tunable BaSrTiO₃ parallel plate capacitors,” *IEEE microwave and guided wave letters*, vol. 10, no. 1, pp. 10–12, 2000. 14
- [57] J. J. Venter, T. Stander, and P. Ferrari, “X-band reflection-type phase shifters using coupled-line couplers on single-layer RF PCB,” *IEEE Microwave and Wireless Components Letters*, vol. 28, no. 9, pp. 807–809, 2018. 14
- [58] A. N. Sychev, I. M. Dobush, N. Y. Rudyi, and S. M. Struchkov, “Analog phase shifter of X-band implemented with novel trans-directional coupled-line coupler,” in *2018 48th European Microwave Conference (EuMC)*. IEEE, 2018, pp. 811–814. 14

- [59] W.-T. Li, Y.-H. Kuo, Y.-M. Wu, J.-H. Cheng, T.-W. Huang, and J.-H. Tsai, "An X-band full-360 reflection type phase shifter with low insertion loss," in *2012 7th European Microwave Integrated Circuit Conference*. IEEE, 2012, pp. 754–757. 14
- [60] S. Lucyszyn and I. D. Robertson, "Two-octave bandwidth monolithic analog phase shifter," *IEEE Microwave and Guided Wave Letters*, vol. 2, no. 8, pp. 343–345, 1992. 14
- [61] M. Robinson, P. Danielson, and Z. Popović, "Continuous broadband gaas and gan mmic phase shifters," *IEEE Microwave and Wireless Components Letters*, 2021. 14
- [62] I. of Electrical and E. Engineers, "Ieee standard test procedures for antennas," *ANSI/IEEE Std 149-1979*, pp. 1–144, 1979. 15, 33, 45
- [63] M. R. Duffy, "Efficient supply modulated mmic pas for broadband linear amplification," Ph.D. dissertation, University of Colorado at Boulder, 2020. 16, 59
- [64] G. Kefalas, "Radar noise jamming calculations simplified," *IEEE Transactions on Aerospace and Electronic Systems*, no. 2, pp. 297–300, 1981. 16
- [65] "Raytheon electronic warfare quick reference guide." [Online]. Available: <https://www.raytheon.com/sites/default/files/capabilities/rtnwcm/groups/public/documents/content/ew-quick-guide-pdf.pdf> 16
- [66] D. H. Schaubert, S. Kasturi, A. O. Boryssenko, and W. M. Elsallal, "Vivaldi antenna arrays for wide bandwidth and electronic scanning," in *The Second European Conference on Antennas and Propagation, EuCAP 2007*, 2007, pp. 1–6. 21
- [67] G. Laughlin, E. Byron, and T. Cheston, "Very wide-band phased-array antenna," *IEEE Transactions on Antennas and Propagation*, vol. 20, no. 6, pp. 699–704, 1972. 21
- [68] F. F. Dubrovka, S. Y. Martyniuk, D. O. Vasylenko, and O. Postulga, "Ultrawideband tapered slot, waveguide and dipole antenna arrays," in *2017 XI International Conference on Antenna Theory and Techniques (ICATT)*. IEEE, 2017, pp. 20–25. 21

- [69] J. S. Kim, D. W. Woo, and R.-C. Jeong, "Dual-polarized open-ended waveguide with squinted beam for x-band monopulse antenna on a small diameter cylinder," in *2018 IEEE International Symposium on Antennas and Propagation & USNC/URSI National Radio Science Meeting*. IEEE, 2018, pp. 523–524. 21, 38
- [70] J. Shi, S. Weinreb, W. Zhong, X. Yin, and M. Yang, "Quadruple-ridged flared horn operating from 8 to 50 GHz," *IEEE Transactions on Antennas and Propagation*, vol. 65, no. 12, pp. 7322–7327, 2017. 21
- [71] J. R. Montejo-Garai, L. Marzall, and Z. Popović, "Octave bandwidth high-performance microstrip-to-double-ridge-waveguide transition," *IEEE Microwave and Wireless Components Letters*, 2020. xiv, 23, 28, 38, 42, 139
- [72] S. Hopfer, "The design of ridged waveguides," *IRE Transactions on Microwave Theory and Techniques*, vol. 3, no. 5, pp. 20–29, 1955. 23
- [73] W. Sun and C. A. Balanis, "Analysis and design of quadruple-ridged waveguides," *IEEE Transactions on Microwave Theory and Techniques*, vol. 42, no. 12, pp. 2201–2207, 1994. 23
- [74] A. Yaghjian, "Approximate formulas for the far field and gain of open-ended rectangular waveguide," *IEEE Transactions on Antennas and Propagation*, vol. 32, no. 4, pp. 378–384, 1984. 24
- [75] G. Tsandoulas and W. Fitzgerald, "Aperture efficiency enhancement in dielectrically loaded horns," *IEEE Transactions on Antennas and Propagation*, vol. 20, no. 1, pp. 69–74, 1972. 25
- [76] J. James, "Engineering approach to the design of tapered dielectric-rod and horn antennas," *Radio and Electronic Engineer*, vol. 42, no. 6, pp. 251–259, 1972. 25
- [77] M. Hamid, "Dielectric loaded horn antennas having improved radiation characteristics," May 8 1984, uS Patent 4,447,811. 25

- [78] S. P. Skobelev and A. Yaparova, "Modeling of horn array antennas with protruding dielectric elements," in *2007 6th International Conference on Antenna Theory and Techniques*. IEEE, 2007, pp. 409–411. 25
- [79] Y. He, N. Ding, L. Zhang, W. Zhang, and B. Du, "Short-length and high-aperture-efficiency horn antenna using low-loss bulk anisotropic metamaterial," *IEEE Antennas and Wireless Propagation Letters*, vol. 14, pp. 1642–1645, 2015. 26
- [80] R. W. Kindt and J. T. Logan, "Benchmarking ultrawideband phased antenna arrays: Striving for clearer and more informative reporting practices," *IEEE Antennas and Propagation Magazine*, vol. 60, no. 3, pp. 34–47, 2018. 31
- [81] L. F. Marzall, P. Danielson, G. Lasser, and Z. Popovic, "Broadband small-aperture high-gain ridge horn antenna array element," *IEEE Antennas and Wireless Propagation Letters*, 2021. 33, 37, 38, 40, 41, 139, 140
- [82] W. F. Moulder, K. Sertel, and J. L. Volakis, "Compact ultrawideband beam-steering horn antenna," in *Proceedings of the 2012 IEEE International Symposium on Antennas and Propagation*. IEEE, 2012, pp. 1–2. 38
- [83] A. D. Olver, P. J. B. Clarricoats, and K. Raghavan, "Dielectric cone loaded horn antennas," *IEE Proceedings H - Microwaves, Antennas and Propagation*, vol. 135, no. 3, pp. 158–162, 1988. 38
- [84] C. P. Scarborough, Q. Wu, D. H. Werner, E. Lier, R. K. Shaw, and B. G. Martin, "Demonstration of an octave-bandwidth negligible-loss metamaterial horn antenna for satellite applications," *IEEE Transactions on Antennas and Propagation*, vol. 61, no. 3, pp. 1081–1088, 2013. 38
- [85] Y. Li, L. Ge, J. Wang, S. Da, D. Cao, J. Wang, and Y. Liu, "3-d printed high-gain wideband waveguide fed horn antenna arrays for millimeter-wave applications," *IEEE Transactions on Antennas and Propagation*, vol. 67, no. 5, pp. 2868–2877, 2019. 38

- [86] L. Marzall and Z. Popović, “6–12 GHz transmit phased array efficiency with stepped static supply modulation for beam shaping,” in *2022 NRSM Conference, Boulder, CO*. URSI, 2022. 38, 57, 75, 140, 141
- [87] L. Marzall, C. Nogales, and Z. Popović, “An octave bandwidth spatial power combiner with supply voltage control,” in *2022 IEEE MTT-S International Microwave Symposium (IMS)*. IEEE, 2022. 38, 57, 75, 135, 140, 141
- [88] P. Danielson, L. Marzall, J. Molles, and Z. Popović, “6–12 ghz horn antenna array with thermal analysis for power amplifier integration,” *IEEE Antennas and Wireless Propagation Letters*, 2022. 57, 137, 140
- [89] L. Marzall and Z. Popović, “Nonlinear co-simulations for transmit broadband phased arrays,” in *2022 IEEE International Symposium on Antennas and Propagation (APSURSI)*. IEEE, 2022, submitted. 57, 75, 140, 141
- [90] L. Marzall, C. Nogales, P. Danielson, S. Verploegh, S. Schafer, G. Lasser, and Z. Popović, “Analysis of octave-band transmit phased arrays,” *IEEE Transactions on Microwave Theory and Techniques*, 2022. 57, 75, 140
- [91] J. Helszajn, *The stripline circulator: theory and practice*. Wiley, 2008. 78
- [92] D. K. Linkhart, *Microwave circulator design*. Artech house, 2014. 78
- [93] A. Fox, S. Miller, and M. Weiss, “Behaviour and application of ferrites in the microwave region,” *Bell System Technical Journal*, vol. 34, no. 1, pp. 5–103, 1955. 79
- [94] H. Bosma, “On stripline y-circulation at uhf,” *IEEE Transactions on Microwave Theory and Techniques*, vol. 12, no. 1, pp. 61–72, January 1964. 79, 92, 113
- [95] C. E. Fay and R. L. Comstock, “Operation of the ferrite junction circulator,” *IEEE Transactions on Microwave Theory and Techniques*, vol. 13, no. 1, pp. 15–27, Jan. 1965. 79

- [96] C. M. Krowne, "Cad using green's functions and finite elements and comparison to experimental structures for inhomogeneous microstrip circulators," in *Advances in imaging and electron physics*. Elsevier, 1999, vol. 106, pp. 97–184. 79, 80
- [97] H. Bosma, "On the principle of stripline circulation," *Proceedings of the IEE - Part B: Electronic and Communication Engineering*, vol. 109, no. 21, pp. 137–146, 1962. 79
- [98] J. Davies and P. Cohen, "Theoretical design of symmetrical junction stripline circulators," *IEEE Transactions on Microwave Theory and Techniques*, vol. 11, no. 6, pp. 506–512, 1963. 79
- [99] T. Miyoshi and S. Miyauchi, "The design of planar circulators for wide-band operation," *IEEE Transactions on Microwave Theory and Techniques*, vol. 28, no. 3, pp. 210–214, Mar 1980. 79
- [100] S. Yang, L. Roy, J. R. Bray, and D. Vincent, "Modeling and simulation of a partially-magnetized ferrite ltcc circulator," in *Numerical Electromagnetic and Multiphysics Modeling and Optimization (NEMO), 2015 IEEE MTT-S International Conference on*. IEEE, 2015, pp. 1–4. 79
- [101] D. C. Webb, "Design and fabrication of low-cost ferrite circulators," in *Microwave Conference, 1995. 25th European*, vol. 2. IEEE, 1995, pp. 1191–1200. 79
- [102] E. F. Schloemann, "Circulators for microwave and millimeter-wave integrated circuits," *Proceedings of the IEEE*, vol. 76, no. 2, pp. 188–200, 1988. 79
- [103] Y. S. Wu and F. J. Rosenbaum, "Wide-band operation of microstrip circulators," *IEEE Transactions on Microwave Theory and Techniques*, vol. 22, no. 10, pp. 849–856, Oct 1974. 79
- [104] J. L. Young, R. S. Adams, B. O'Neil, and C. M. Johnson, "Bandwidth optimization of an integrated microstrip circulator and antenna assembly. 1," *IEEE Antennas and Propagation Magazine*, vol. 48, no. 6, pp. 47–56, Dec 2006. 79
- [105] J. L. Young, R. S. Ada, B. O'Neil, and C. M. Johnson, "Bandwidth optimization of an integrated microstrip circulator and antenna assembly: Part 2," *IEEE Antennas and Propagation Magazine*, vol. 49, no. 1, pp. 82–91, Feb 2007. 79

- [106] T. Jensen, V. Krozer, and C. Kjaergaard, “Realisation of microstrip junction circulator using ltcc technology,” *Electronics Letters*, vol. 47, no. 2, pp. 111–113, January 2011. 79
- [107] H. How, S. Oliver, S. W. McKnight, P. Zavracky, N. McGruer, C. Vittoria, and R. Schmidt, “Theory and experiment of thin-film junction circulator,” *IEEE transactions on microwave theory and techniques*, vol. 46, no. 11, pp. 1645–1653, 1998. 79
- [108] G. T. Rado, “Theory of the microwave permeability tensor and faraday effect in nonsaturated ferromagnetic materials,” *Physical Review*, vol. 89, no. 2, p. 529, 1953. 80
- [109] E. Schlömann, “Microwave behavior of partially magnetized ferrites,” *Journal of Applied Physics*, vol. 41, no. 1, pp. 204–214, 1970. 80, 91
- [110] J. J. Green and F. Sandy, “Microwave characterization of partially magnetized ferrites,” *IEEE Transactions on Microwave Theory and Techniques*, vol. 22, no. 6, pp. 641–645, 1974. 80
- [111] E. Schlomann, “On the theory of the ferrite resonance isolator,” *IRE Transactions on Microwave Theory and Techniques*, vol. 8, no. 2, pp. 199–206, March 1960. 80
- [112] R. I. Joseph and E. Schlomann, “Demagnetizing field in nonellipsoidal bodies,” *Journal of Applied Physics*, vol. 36, no. 5, pp. 1579–1593, may 1965. 80, 93, 94, 111
- [113] H. How, S. Oliver, S. McKnight, P. Zavracky, N. McGruer, C. Vittoria, and R. Schmidt, “Influence of nonuniform magnetic field on a ferrite junction circulator,” *IEEE transactions on microwave theory and techniques*, vol. 47, no. 10, pp. 1982–1989, 1999. 80
- [114] A. Guennou, B. Della, P. Queffelec, P. Gelin, and J.-L. Mattei, “Influence of the magnetic field nonuniformity on an x-band microstrip y-junction circulator bandwidth: Theory/experiment comparison,” *IEEE transactions on magnetics*, vol. 43, no. 6, pp. 2642–2644, 2007. 80
- [115] Y. Y. Zhang, A. Aragon, M. Ahmed, Y. Xie, J. Wang, M. Puga, and K. Gao, “Synthesis and properties of feco-based anisotropic magnetic nanocomposites,” in *62nd Conf. on Magnetism and Magnetic Materials, Pittsburgh, PA.* AConf, 2017. 81

- [116] V. Harris, “The role of magnetic materials in rf, microwave, and mm-wave devices: The quest for self-biased materials,” in *Proceedings of the IEEE 2010 National Aerospace & Electronics Conference*. IEEE, 2010, pp. 1–96. 81
- [117] Metamagnetics, “Advanced microwave mm-wave circulator and isolator solutions,” <https://www.mtmgx.com/rf-microwave-smt-circulators-isolators/>, 2022, [Online; accessed 13-February-2022]. 81
- [118] W. Palmer, D. Kirkwood, S. Gross, M. Steer, H. S. Newman, and S. Johnson, “A bright future for integrated magnetics: Magnetic components used in microwave and mm-wave systems, useful materials, and unique functionalities,” *IEEE Microwave Magazine*, vol. 20, no. 6, pp. 36–50, 2019. 81
- [119] V. Laur, G. Vérissimo, P. Quéffélec, L. A. Farhat, H. Alaaeddine, E. Laroche, G. Martin, R. Lebourgeois, and J. Ganne, “Self-biased y-junction circulators using lanthanum-and cobalt-substituted strontium hexaferrites,” *IEEE Transactions on Microwave Theory and Techniques*, vol. 63, no. 12, pp. 4376–4381, 2015. 81
- [120] B. K. O’Neil and J. L. Young, “Experimental investigation of a self-biased microstrip circulator,” *IEEE transactions on microwave theory and techniques*, vol. 57, no. 7, pp. 1669–1674, 2009. 81, 113
- [121] J. Wang, R. Divan, Y. Xie, L. Ocola, Y. Zhang, A. Aragon, M. Ahmed, P. Ignacio-de Leon, and K. Gao, “High-aspect-ratio magnetic nanowires by electroplating and electrospinning with controlled sizes and compositions,” in *5th Nano Today Conference, Waikoloa Beach Marriott, Hawaii*. Institute of Bioengineering and Nanotechnology (IBN) and Elsevier, 2017. 81
- [122] A. Aragon, Y. Zhang, M. Jungfleisch, M.B. adn Ahmed, Y. Xie, J. Wang, and K. Gao, “Comparative magnetic studies on the ordered and disordered magnetic nanowires arrays,” in *62nd Conf. on Magnetism and Magnetic Materials, Pittsburgh, PA*. AConf, 2017. 81
- [123] S. Tanaka, N. Shimomura, and K. Ohtake, “Active circulators—the realization of circulators using transistors,” in *Proceedings of the IEEE*, vol. 53, no. 3, Mar. 1965, pp. 260–267. 82

- [124] S. K. Cheung, T. P. Halloran, W. H. Weedon, and C. P. Caldwell, "MMIC-based quadrature hybrid quasi-circulators for simultaneous transmit and receive," *IEEE Transactions on Microwave Theory and Techniques*, vol. 58, no. 3, pp. 489–497, 2010. xi, 82, 133
- [125] B. Tang and L. Geng, "A survey of active quasi-circulators," *Journal of Semiconductors*, vol. 41, no. 11, p. 111406, nov 2020. [Online]. Available: <https://doi.org/10.1088/1674-4926/41/11/111406> x, 82, 83
- [126] I. J. Bahl, "The design of a 6-port active circulator," in 1988., *IEEE MTT-S International Microwave Symposium Digest*, 1988, pp. 1011–1014 vol.2. 82
- [127] Y. Ayasli, "Field effect transistor circulators," in 1989 *IEEE International Magnetics Conference (INTERMAG)*, 1989, pp. AC2–AC2. 82
- [128] S. Hara, T. Tokumitsu, and M. Aikawa, "Novel unilateral circuits for mmic circulators," *IEEE Transactions on Microwave Theory and Techniques*, vol. 38, no. 10, pp. 1399–1406, 1990. 82, 133
- [129] X. Wang, Q. Cai, H. Zhu, W. Feng, Q. Xue, and W. Che, "A 28 ghz gan hemt quasi-circulator with high isolation and high power-handling capability," *Microwave and Optical Technology Letters*, vol. 64, no. 1, pp. 72–76, 2022. 82
- [130] L. Gu, W. Che, F.-H. Huang, and H.-C. Chiu, "A high power active circulator using gan mmic power amplifiers," *Journal of Semiconductors*, vol. 35, no. 11, p. 115003, 2014. 82
- [131] G. Carchon and B. Nanwelaers, "Power and noise limitations of active circulators," *IEEE Transactions on Microwave Theory and Techniques*, vol. 48, no. 2, pp. 316–319, Feb. 2000. 82
- [132] R. Vignesh, P. Gorre, H. Song, and S. Kumar, "Highly robust x-band quasi circulator-integrated low-noise amplifier for high survivability of radio frequency front-end systems," *International journal of circuit theory and applications*, vol. 49, no. 7, pp. 2170–2182, 2021. 83

- [133] A. Nagulu, T. Chen, G. Zussman, and H. Krishnaswamy, "Multi-watt, 1-ghz cmos circulator based on switched-capacitor clock boosting," *IEEE Journal of Solid-State Circuits*, vol. 55, no. 12, pp. 3308–3321, 2020. 83
- [134] S. Shin, J. Huang, K. Lin, and H. Wang, "A 1.5–9.6 ghz monolithic active quasi-circulator in 0.18 μm cmos technology," *IEEE Microwave and Wireless Components Letters*, vol. 18, no. 12, pp. 797–799, 2008. 83, 133
- [135] K. Fang and J. F. Buckwalter, "A tunable 5–7 ghz distributed active quasi-circulator with 18-dbm output power in cmos soi," *IEEE Microwave and Wireless Components Letters*, vol. 27, no. 11, pp. 998–1000, 2017. 83
- [136] C.-H. Chang, Y.-T. Lo, and J.-F. Kiang, "A 30 ghz active quasi-circulator with current-reuse technique in $0.18\ \mu\text{m}$ cmos technology," *IEEE Microwave and Wireless Components Letters*, vol. 20, no. 12, pp. 693–695, 2010. 83
- [137] T. Dinc and H. Krishnaswamy, "17.2 a 28ghz magnetic-free non-reciprocal passive cmos circulator based on spatio-temporal conductance modulation," in *2017 IEEE International Solid-State Circuits Conference (ISSCC)*. IEEE, 2017, pp. 294–295. 83
- [138] B. Tang, J. Xu, and L. Geng, "Integrated active quasi-circulator with 27 db isolation and 0.8–6.8 ghz wideband by using feedback technique," in *2018 IEEE MTT-S International Wireless Symposium (IWS)*. IEEE, 2018, pp. 1–4. 83
- [139] B. Tang, X. Gui, J. Xu, Q. Xia, and L. Geng, "A dual interference-canceling active quasi-circulator achieving 36-db isolation over 6-ghz bandwidth," *IEEE Microwave and Wireless Components Letters*, vol. 29, no. 6, pp. 409–411, 2019. 83
- [140] B. Tang, X. Gui, J. Xu, Q. Xia, H. Yang, and L. Geng, "A wideband active quasi-circulator with 34-db isolation and insertion loss of 2.5 db," *IEEE Microwave and Wireless Components Letters*, vol. 30, no. 7, pp. 693–696, 2020. 83

- [141] L. F. Marzall, M. Pinto, A. Ashley, D. Psychogiou, and Z. Popović, “Co-simulations of dc magnetic bias fields and rf performance for microwave ferrite circulators,” in *2018 International Applied Computational Electromagnetics Society Symposium (ACES)*. IEEE, 2018, pp. 1–2. 84, 105, 133, 141, 142
- [142] L. Marzall, Y. Zhang, M. Pinto, A. Ashley, K. Gao, J. Hryn, D. Psychogiou, and Z. Popović, “Analysis of self-biased nano-composite microstrip circulators,” in *Government Microcircuits Applications & Critical Technology Conference*. Department of Defense, 2019. 84, 114, 142
- [143] L. Marzall, M. Robinson, P. Danielson, A. Robinson, N. Ehsan, and Z. Popović, “Active and passive components for broadband transmit phased arrays: Broadband transmit front-end components,” *IEEE Microwave Magazine*, vol. 23, no. 2, pp. 56–74, 2022. 84
- [144] Ü. Özgür, Y. Alivov, and H. Morkoç, “Microwave ferrites, part 1: fundamental properties,” *Journal of Materials Science: Materials in Electronics*, vol. 20, no. 9, pp. 789–834, Sep 2009. [Online]. Available: <https://doi.org/10.1007/s10854-009-9923-2> 87
- [145] “Tt1-105 parameters.” [Online]. Available: <https://www.skyworksinc.com/products/technical-ceramics/tt1-105> 88
- [146] R. E. Collin, *Foundations for microwave engineering*. John Wiley & Sons, 2007. 88
- [147] B. Lax and K. J. Button, *Microwave ferrites and ferrimagnetics: Benjamin Lax Kenneth J. Button*. McGraw-Hill, 1962, pp. 149-159. 90
- [148] V. Voronkov, “Microwave ferrites : the present and the future,” *Le Journal de Physique IV*, vol. 07, no. C1, pp. C1–35–C1–38, mar 1997. 91
- [149] J. J. Green, C. Patton, and F. Sandy, “Microwave properties of partially magnetized ferrites,” RAYTHEON CO WALTHAM MA RESEARCH DIV, Tech. Rep., 1968. 91
- [150] E. Schlömann, “Behavior of ferrites in the microwave frequency range,” *Le Journal de Physique Colloques*, vol. 32, no. C1, pp. C1–443, 1971. 91

- [151] B. K. O’Neil and J. L. Young, “Experimental investigation of a self-biased microstrip circulator,” *IEEE Transactions on Microwave Theory and Techniques*, vol. 57, no. 7, pp. 1669–1674, July 2009. 94
- [152] C. Kittel, “On the theory of ferromagnetic resonance absorption,” *Phys. Rev.*, vol. 73, pp. 155–161, Jan 1948. [Online]. Available: <https://link.aps.org/doi/10.1103/PhysRev.73.155> 94
- [153] H. Engineering. [Online]. Available: <https://www.hkcm.de/desk.php/> 97, 99
- [154] V. VK Thalakkatukulathil, A. Chevalier, V. Laur, G. Verissimo, P. Queffelec, L. Qassym, and R. Lebourgeois, “Electromagnetic modeling of anisotropic ferrites—application to microstrip y-junction circulator design,” *Journal of Applied Physics*, vol. 123, no. 23, p. 234503, 2018. 105, 141
- [155] L. F. Marzall, M. Pinto, A. Ashley, D. Psychogiou, and Z. Popović, “Co-simulations of DC magnetic bias fields and RF performance for microwave ferrite circulators,” in *Proc. Int. Applied Computational Electromagnetics Society Symp. (ACES)*, Mar. 2018, pp. 1–2. 105, 141
- [156] A. Ashley, L. F. Marzall, Z. Popovic, and D. Psychogiou, “Frequency selective ferrite circulators with quasi-elliptic transmission response,” in *2018 48th European Microwave Conference (EuMC)*. IEEE, 2018, pp. 211–214. 105, 106, 141
- [157] V. G. Harris, “Modern microwave ferrites,” *IEEE Transactions on Magnetics*, vol. 48, no. 3, pp. 1075–1104, March 2012. 107
- [158] Y. Cui, Y. Zhang, L. Witkowski, S. D. Yoon, S. Pilla, E. Beam, A. Xie, S. Chen, A. Ketterson, C. Lee, Y. Xie, K. Gao, J. Hryn, and Y. Cao, “Monolithic integration of self-biased C -band circulator on sic substrate for gan mmic applications,” *IEEE Electron Device Letters*, vol. 40, no. 8, pp. 1249–1252, Aug 2019. 107

- [159] M. Roberg, "Loop gain envelope evaluation for rapid mmic amplifier stability analysis," in *2019 IEEE Texas Symposium on Wireless and Microwave Circuits and Systems (WMCS)*. IEEE, 2019, pp. 1–4. 129
- [160] S. Cheung, T. Halloran, W. Weedon, and C. Caldwell, "Active quasi-circulators using quadrature hybrids for simultaneous transmit and receive," in *2009 IEEE MTT-S International Microwave Symposium Digest*, 2009, pp. 381–384. 133
- [161] Y. Zheng and C. E. Saavedra, "Active quasi-circulator mmic using otas," *IEEE Microwave and Wireless Components Letters*, vol. 19, no. 4, pp. 218–220, 2009. 133
- [162] A. Gasmi, B. Huyart, E. Bergeault, and L. Jallet, "Noise and power optimization of a mmic quasi-circulator," *IEEE transactions on microwave theory and techniques*, vol. 45, no. 9, pp. 1572–1577, 1997. 133
- [163] M. Berg, T. Hackbarth, B. Maile, S. Kossowski, J. Dickmann, D. Kother, B. Hopf, and H. Hartnagel, "Active circulator mmic in cpw technology using quarter micron inalas/ingaas/inp hfets," in *Proceedings of 8th International Conference on Indium Phosphide and Related Materials*. IEEE, 1996, pp. 68–71. 133
- [164] P. Katzin, Y. Ayasli, L. D. Reynolds Jr, and B. E. Bedard, "6 to 18 ghz mmic circulators," *Microwave Journal - MICROWAVE J*, vol. 35, 01 1992. 133
- [165] V. G. Posadas, "Stability, mounting and measurement considerations for high power gan mmic amplifiers," private communication, Jan 2022. 136
- [166] D. Lu, D. Rutledge, M. Kovacevic, and J. Hacker, "A 24-ghz patch array with a power amplifier/low-noise amplifier mmic," *International Journal of Infrared and Millimeter Waves*, vol. 23, no. 5, pp. 693–704, 2002. 138

